OPTIMAL PHASING AND PERFORMANCE MAPPING FOR TRANSLUNAR SATELLITE MISSIONS ACROSS THE EARTH-MOON NODAL CYCLE

A Thesis
Presented to
The Academic Faculty

By

Richard A. J. Hunter

In Partial Fulfillment
of the Requirements for the Degree
Master of Science in the
Daniel Guggenheim School of
Aerospace Engineering

Georgia Institute of Technology

May 2020

**OPTIMAL PHASING AND PERFORMANCE MAPPING FOR
TRANSLUNAR SATELLITE MISSIONS ACROSS THE EARTH-MOON
NODAL CYCLE**

Approved by:

Dr. Brian C. Gunter
Daniel Guggenheim School of
Aerospace Engineering
Georgia Institute of Technology

Dr. Edgar G. Lightsey
Daniel Guggenheim School of
Aerospace Engineering
Georgia Institute of Technology

Dr. Koki Ho
Daniel Guggenheim School of
Aerospace Engineering
Georgia Institute of Technology

Date Approved: January 08,
2020

"Exploration is in our nature.

We began as wanderers, and we are wanderers still.

We have lingered long enough on the shores of the cosmic ocean.

We are ready at last to set sail..."

Carl Sagan

To my mother and father, whose strong work ethic, intelligence, and boundless support has placed within reach a profession that brings challenge and wonder.

ACKNOWLEDGEMENTS

TABLE OF CONTENTS

LIST OF TABLES

LIST OF FIGURES

SUMMARY

NASA has declared the Moon a strategic focal point for the US space program in the coming decade. This resurgent interest in lunar exploration seeks to advance scientific knowledge, deep-space technology, and "beyond-Earth" industry.

Specifically, humanity's motivation for returning to the Moon in the 2020's rests upon four fundamental pillars as articulated by the NASA 2018 Strategic Plan. The first is solar system science. Without the shield of a dense atmosphere and magnetic field, the unprotected lunar surface has been bombarded by eons of meteorite impacts and solar radiation. These unique conditions are ideal for studying the impact history of the early solar system, and the composition of the stellar winds.

The second is lunar prospecting. This constant bombardment by meteorites and stellar wind make the lunar regolith a likely home to deposits of valuable elements that may be extracted and used to bolster lunar, Earth obit, and deep space infrastructure. Furthermore, with the discovery of water ice at the lunar poles, there exists potential to harvest oxygen, hydrogen and liquid water to support permanent human outposts. The off-world extraction, processing, and transportation of these materials by commercial companies represents a new opportunity for economic growth with minimal impact to Earth's environment.

The third is technology validation. Lunar orbit represents a valuable testing ground for deep-space technologies beyond the shielding effect of Earth's magnetic field, the GNSS constellations, and the range of standard, low power UHF and S-Band communications systems.

The fourth is inter-planetary exploration. The development of orbital infrastructure for in-space refuelling of inter-planetary spacecraft may provide a launch point for the missions to Mars and the outer solar system.

The importance of these advancements is evidenced through significant invest-

ments in the Artemis, Lunar Gateway, and the Commercial Lunar Payload Services (CLPS) programs. Unlike Apollo, these programs are built around long term, sustainable science and exploration. Within this new Lunar era, there is opportunity for small satellites to play a valuable role as pathfinders. When compared to traditional New Frontiers, Discovery, and Flagship class science missions, small satellite architectures can be developed at low cost, on short time scales. Thus, they are accessible to academic researchers and small technology companies. This ease of development provides a platform for the iterative testing of innovative instrumentation with potential for high scientific and commercial yield.

To be viable as pathfinders, small satellite lunar missions must limit translunar flight time to make best use of finite spacecraft lifespans and minimize Van Allen radiation exposure. This is possible through a high-thrust, direct injection translunar trajectory from an Earth parking orbit similar to the Apollo missions. However, such an architecture is not currently achievable with small satellite onboard propulsion, and dedicated lunar transfers from the world's space agencies are expensive and exceedingly rare. To solve this problem affordably, small satellite lunar missions must ideally fit within the current commercial launch framework of ride share opportunities, or dedicated missions aboard small, low-cost launch vehicles.

Compatibility with commercial launch vehicles is driven by the performance demand of direct injection lunar missions from an Earth parking orbit - a highly dynamic, multi-parameter astrodynamics problem. Mission performance is a function of departure and arrival Keplerian orbital elements, and the relative states of Earth, Moon, and Sun across the various cycles of the Earth-Moon system. Presently, there is no reference to accurately quantity these dependencies.

This research bridges that knowledge gap with a global characterization of performance demands for lunar flyby, orbit insertion, and landing missions with 0-24 kg payloads over an 18.6 year Earth-Moon nodal cycle. By the simulation and sta-

tistical analysis of over 640,000 trajectories with high-fidelity orbital dynamics, the performance demands of optimal monthly departures from 2020 to 2038 have been identified and catalogued.

Through a study of periodic and secular performance trends, this thesis quantifies the dependencies between mission performance and 1) departure epoch, 2) lunar arrival Keplerian elements, and 3) payload mass. Finally, it demonstrates 4) the viability of low-cost, high-cadence small satellite missions by mapping the mass requirements of mission payload, propellant, and the subsystems of a translunar injection stage against the lift capacity of modern commercial launch vehicles.

It is hoped that this research will serve as a useful reference for lunar mission designers, enabling a performance comparison across payloads, departure windows, and arrival conditions. In so doing, it might in some small way contribute to the exciting new age of lunar exploration that lies ahead.

CHAPTER 1

MOTIVATION AND BACKGROUND

1.1 Motivation

1.1.1 Lunar Exploration: A New Focus

The *NASA 2018 Strategic Plan* defines a clear shift in operational focus beyond Low Earth Orbit (LEO), to pursue "a broader strategy to explore and utilize the Moon and its surface" [1]. By leveraging the lunar orbit and surface as a rich source of scientific insight, a repository of volatile materials, a challenging testing ground for the validation of deep-space technologies, and the launch point for interplanetary exploration, NASA aims to advance its planetary, heliophysics, and astrophysics scientific objectives whilst unlocking economic growth through the enabling of "beyond-Earth" industries.

This new strategic direction is best evidenced by NASA's Artemis Program. This national-scale spaceflight campaign pays homage to the pioneering feats of Apollo in the 1960's. Like Apollo, Artemis has spurred the development a new heavy lift rocket, a deep space vehicle, and an ambitious, detailed timeline to establish a human presence on the moon in the 2020's. However, Artemis also takes NASA in an entirely new direction - one in which technology and the new commercial space industry are enabling sustainable, long duration lunar exploration. Beyond the eventual construction of the Lunar Gateway orbital platform and a permanent surface settlement, NASA's Moon-centric focus creates new opportunities for high impact science, resource prospecting, and technology validation from the academic and entrepreneurial space sectors for years to come. Specifically, the long term motivations behind the Artemis program's sustainable return to lunar space

rests upon four fundamental pillars.

First is the solar system science and missions to characterize the lunar surface and the surrounding space environment. *Vision and Voyages*, the 2013-2022 Planetary Science Decadal Study by the National Research Council, specifically identifies the moon as an important strategic objective, calling for future missions to address a range of science questions [2]. Without the shield of a dense atmosphere and magnetic field, the unprotected lunar surface has been bombarded by eons of meteorite impacts and solar radiation. These unique conditions are ideal for studying the impact history of the early solar system, and the composition of the stellar winds. Additionally, there is a interest around recent activity at potential surface vent sites, and the reconstruction of a thermal-tectonic-magmatic history of the Moon [2]. This foundational study establishes NASA's specific scientific priorities and clearly places the moon as a prime research destination.

Second is orbital prospecting to characterize the nature and abundance of surface volatiles (most notably hydrogen and oxygen) with potential for In-Situ Resource Utilization (ISRU) to support future human exploration missions and the development of lunar, Earth-orbit, and deep space infrastructure. Per Sacksteder and Sanders, the Moon is approximately 40 percent oxygen, stored in silicate materials within the lunar rock and regolith [3]. While samples gathered from the equatorial Apollo landing sites demonstrate only trace amounts of hydrogen, orbital analysis from the 1998 Lunar Prospector mission has revealed high concentrations of water ice at the poles - an immensely valuable, harvestable resource. If hydrogen, oxygen and liquid water were extracted, separated, and stored, they could serve as viable power generation and life support resources for human lunar surface operations. Detailed research into extraction, processing, storage, and transportation of hydrogen and oxygen by Stancati, Jacobs, and Rauwolf [4] demonstrate the viability of this lunar surface ISRU given adequate local supply. Orbital prospecting missions

could identify high concentrations of volatiles, thus guiding site-selection for future lander, sample return, and manned missions.

Third is the use of lunar space for technology validation of deep-space instrumentation and subsystems in the punishing environment beyond LEO. Without the shielding effect of Earth's magnetic field, a lunar small satellite will be exposed to ionizing (high energy) radiation from the stellar winds, Galactic Cosmic Radiation (GCR), Solar Particle Events (SPE's), and during passage through the Van Allen belts. As such, any subsystems must be appropriately shielded against both long term degradation and Single Event Upsets (SEU's). Additionally, translunar missions must incorporate high-frequency X-Band, Ka-Band, or DSO (Deep Space Optical) communications systems to ensure reliable connectivity with ground stations at extreme ranges, and operate autonomously through sustained communications blackout while passing around the dark side of the moon. Real-world testing and development in this environment will enable the qualification of interplanetary hardware to explore compelling scientific destinations throughout the solar system.

Fourth is the development of an in-space refueling and launch point to enable exploration of Mars and the outer planets. The Lunar Gateway orbital platform (a primary component of the Artemis program) shall support docking by multiple spacecraft for the transfer of crew between a lunar lander/ascent vehicle and an Orion spacecraft. A similar methodology may be applied to the in-space refueling of interplanetary spacecraft in lunar orbit. The hydrogen and oxygen harvestable from water ice on the lunar surface may be used as propellant for deep space exploration missions that leverage advanced hybrid cycle H_2/O_2 rocket engines. Transporting this propellant to an lunar orbiting fueling platform will require significantly less energy than it takes to reach LEO from Earth's surface. Once refueled after its translunar injection and lunar orbit insertion, an interplanetary spacecraft shall require significantly less energy to escape lunar gravity and achieve a heliocentric

interplanetary transfer orbit than it would to achieve the same transfer directly from LEO. Such an architecture shall allow reduced wet/dry mass ratios for departure of the Earth-Moon system, and thus more useable payload upon arrival at an interplanetary destination.

All four of these advancements may be supported by pathfinder missions with small satellites. When compared to traditional New Frontiers, Discovery, and Flagship class science missions, the versatility of small satellite architectures allow the application of new, innovative instrumentation at lower cost, lower development time, lower mission assurance demands, and - through launch vehicle ride-share options - higher launch cadence. These conditions enable the application and iterative testing of technologies deemed too high-risk for traditional high-cost, long duration satellite missions. This process is essential to raising Technology Readiness Levels (TRL's) and enabling the future pursuit of more ambitious scientific and commercial objectives. Indeed, the NASA CubeSat Launch Initiative has funded and launched 54 cube satellites since 2010 with an additional 47 on manifest, 64% of which have a technology development objective.

However, current small satellite missions are almost exclusively constrained to LEO operations, leaving translunar deployment an unexplored sector.

1.1.2   Pathfinders: Small Satellite Lunar Applications

Demand for lunar bound scientific, prospecting, and technology validation small satellite missions is perhaps best demonstrated by the architecture of NASA's Exploration Mission One (EM1). This mission is an autonomous test flight of the Orion spacecraft launched aboard the Space Launch System (SLS). NASA has selected thirteen 6U cube satellite missions to fly aboard the SLS Interim Cyrogenic Propulsion Stage (ICPS) as secondary payloads, deploying at various points along the translunar trajectory.

Table 1.1: EM1 secondary payload small satellite missions

Mission	Operator	Objective
Lunar IceCube	MSU	Characterize water ice deposits for future robotic and manned surface prospecting.
SkyFire	Lockheed	Surface imaging for surface characterization, landing site selection, and deep space orbital remote sensing.
BioSentinel	NASA Ames	Biological payload to heliocentric orbit via lunar flyby to measure the effect of deep space radiation on DNA.
NEA Scout	NASA Marshall, JPL	Solar sail propulsion to image a near Earth asteroid, studying orbit, rotation, composition, and presence of volatiles.
Lunar Flashlight	NASA Marshall, JPL	Map the lunar south pole for water ice to assess potential for extraction by future lander missions.
CuSP	Southwest RI	Enter heliocentric orbit via lunar gravity assist to measure the "solar weather" of dynamic particles and magnetic fields emanating into deep space.
LunaH Map	ASU	Employ neutron detector to develop a detailed map of water deposites at the lunar south pole for future human operations.
Cislunar Explorers	Cornell	Perform a gravity assist maneuver with on-board water electrolysis propulsion.
CU E^3	UC Boulder	Use lunar gravity assist to enter a heliocentric orbit and achieve greatest cube satellite comm's distance, longevity, and largest aggregate data volume.
Team Miles	Fluid and Reason LLC	Deploy Model-H ion thruster to reach a heliocentric orbit with target Earth distance of 96 million km.
EQUULEUS	Tokyo University, JAXA	Characterize the radiation environment in the space around Earth for protection of electronics and humans aboard long duration missions.
OMOTENASHI	JAXA	Validation of small, low cost spacecraft for lunar surface exploration
ArgoMoon	Italian Space Agency	Short range ProxOps with the ICPS and testing of optical communications.

These cube satellite missions, as detailed in table 1.1, were selected to balance a range of strategic objectives by five NASA initiatives - the Next Space Technologies for Exploration Partnership (NextSTEP), the Human Exploration and Operations Directorate, the Science Mission Directorate, the Cube Quest Challenge, and the on-going collaboration with NASA's international partner agencies.

The broad range of missions presented in table 1.1 is indicative of the growing value placed on lunar small satellite operations for their scientific, prospecting, and technology validation potential. This trend is set to continue as the capability and cost of on-board systems miniaturized for smaller spacecraft buses improves over time. However, EM1 represents a rare opportunity for lunar passage that small satellite missions are rarely afforded.

1.1.3   The Barrier of Translunar Injection

Small satellites transported into orbit as secondary payloads aboard governmental space agency or commercial rockets are limited to the destination orbit of a primary mission. Rarely does this extend beyond a geostationary transfer orbit into lunar space, thus secondary payload small satellite missions currently lack the requisite velocity to reach the moon upon deployment from the launch vehicle. Indeed, the primary barrier to lunar missions is the translunar injection - an obstacle yet to be overcome by on-board propulsion.

The NASA Ames Research Center State of the Art Report for Small Satellite Technology [5] details the current type, performance characteristics, and development stage of small satellite on-board propulsion systems. The highest Technology Readiness Level (TRL) of 9 indicates that a mature technology that is flight proven, thus representing a viable option for mission designers. TRL 9 systems are detailed in table 1.2

Note that while many promising low-thrust technologies such as the Hall ef-

Table 1.2: TRL 9 small satellite propulsion technologies

Type	Thrust	Specific Impulse
Pressurized Cold Gas	0.001N - 10N	65s - 70s
Mono-propellant: Hydrazine	0.5N - 30.7N	200s - 235s
Mono-propellant: Green	0.1N - 27N	220s - 250s
Solid Rocket Motor	Tailored Sizing	210s
Resistojet	100mN	48s - 99s

fect thruster, electron spray propulsion, and ion engines demonstrate high specific impulse and Δv performance over long mission durations, these technologies have yet to be scaled to small satellite form factors and thus require further development before application on feasible lunar missions.

Pressurized cold gas thrusters are a mature, low complexity, and reliable technology by which thrust is provided through the controlled expulsion of a pressurized gas. This technology has been applied to small satellite compatible form factors such as the Butane powered GomSpace NanoProp 6U. Whilst this system is well suited to attitude control, the low specific impulse of 60 s - 110 s offers relatively low Δv performance under the limited propellant volume offered by a small satellite bus when compared to mono-propellant alternatives.

Mono-propellant propulsion systems involve a single reactant mix exposed to a catalyst, causing rapid expansion of a directed exhaust gas to provide thrust. Hydrazine (N_2/H_4) is a common mono-propellant reactant with ample flight heritage. Whilst the high volatility and toxicity make hydrazine difficult to handle and store, it offers significantly higher specific impulse than cold gas thrusters. In recent years, advancements have been made in the field of "green" reactants for mono-propellant systems. Green propulsion mitigates some hazards associated with hydrazine by employing less flammable, lower toxicity fuels such as Ammonium DiNitrimide (ADN) or HydroxlAmmonium Nitrate (HAN). Green propulsion can also offer a greater fuel density for improved specific impulse.

Bi-propellant space propulsion traditionally stores a liquid fuel and a liquid oxidizer in separate tanks, combining them inside a combustion chamber of a rocket engine for either a catalyst induced or automatic (hypergolic) explosive reaction. Storeable liquid bi-propellants offer higher performance than mono-propellants, but the additional mass and complexity of multiple propellant tanks and lines precludes application to small satellite systems.

Cryogenic bi-propellants make use of the high energy density of super-cooled propellants and/or oxidizers stored in liquid form. These include H_2/O_2, $RP1/O_2$ and CH_4/O_2 engines that offer very high performance and have a rich flight heritage in launch vehicles since the dawn of rocketry. However, it is a substantial technical challenge to maintain the propellants at a super cooled liquid state. Furthermore, the intense heat and pressure of the reaction requires a robust thrust chamber, hence, increased mass. These challenges make cyrogenics poorly suited to small satellite lunar missions.

Solid rocket motors offer a relatively low weight, low complexity system with both the fuel and the oxidizer stored in a highly stable solid state. However, restrictions placed upon secondary payloads limit the use of pyrotechnics to mitigate risk of an uncontrolled ignition destroying the launch vehicle and primary payload. Whilst some newly developed systems such as the CAPS-3 by Digital Solid State Propulsion (DSSP) offer non-pyrotechnic, electrically ignited solid propellants, these technologies do not yet offer a thrust comparable with mono-propellant alternatives. Were the risk of a pyrotechnic system to be deemed permissible, the Orbital ATK Star-4G Solid Rocket is being developed specifically for a nanosatellite scale and offers a high specific impulse of 270 s. However, this system is currently at TRL 6 and not yet flight qualified.

Finally, Resistojet drives are the most rudimentary form of electric spacecraft propulsion, leveraging an electric current to heat a propellant gas causing directed

high velocity expansion. The most developed Resistojet technology is the Surrey Satellite Technology Ltd. (SSTL) Resistojet Propulsion System with a 100 mN thrust, and a maximum specific impulse of 99 s with a non-toxic, non-volatile nitrogen propellant. Similar to cold gas and DSSP Solid Rockets, this system lacks the propulsive performance of mono-propellant thrusters.

A basic performance analysis under ideal conditions can be used to determine the high level feasibility of translunar injection using the current TRL 9 state of the art on-board propulsion systems. Given a favourable balance of propulsive performance, low system mass, and high technology readiness, a mono-propellant system will be applied with both hydrazine and green propellant alternatives.

To present an ideal case for TLI, a planar Hohmann Transfer is assumed, with the departure point at Hohmann ellipse periapsis, and lunar arrival occurring at Hohmann ellipse apoapsis. Initial insertion into a 400km altitude circular parking orbit is assumed. This initial condition is commensurate with a secondary payload mission to ISS orbit, and allows the satellite to be considered free from the effects of atmospheric drag during the short time span of the maneuver. Only the departure TLI maneuver is considered, thus allowing a lunar flyby with no orbit insertion maneuvers to be minimized through application of a bi-elliptic transfer. Simple 2-Body dynamics with Earth gravity are also assumed - no lunar gravity or additional perturbing effects are considered. The TLI burn is considered impulsive. The analysis payload adopts a 6U form factor to match the EM1 secondary payloads - a small satellite size and mass proven to be capable of high value lunar science.

A planar Hohmann Transfer represents the minimum possible energy required to reach the moon from the specified parking orbit. As the lunar orbital motion transects the apoapsis of the transfer ellipse, any lower Δv would fall short of the lunar orbital radius. This is an ideal model for assessing viability of on-board mono-propellant systems - if an on-board system cannot achieve this Hohmann transfer,

9
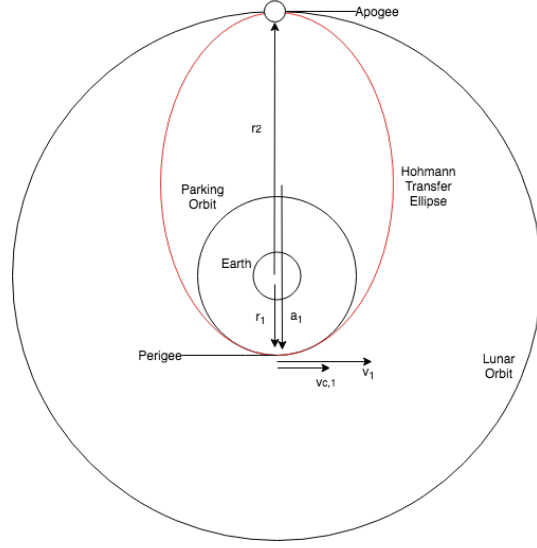
Figure 1.1: Simplified lunar Hohmann transfer

it cannot achieve a lunar approach under any trajectory.

To determine the required Δv for the Hohmann transfer, one must first characterize both departure and arrival points based on the 400 km parking orbit assumption and mean Earth radius per NASA Goddard Space Flight Center (NASA GSFC) Planetary Fact Sheet.

$$r_{earth} = 6,371 km$$

$$alt_1 = 400 km$$

$$r_1 = r_{earth} + alt_1$$

$$= 6,771 km$$

The lunar orbit is considered circular, at its minimum observed monthly orbital radius.

$$r_2 = 357,000 km$$

The position magnitudes allow computation of the semi-major axis for both the

parking orbit and the Hohmann transfer ellipses:

$$a_{c,1} = r_1$$

$$= 6,771km$$

$$a_1 = \frac{r_1 + r_2}{2}$$

$$= 181,886km$$

The Vis-Viva equation defines the velocity of a spacecraft as a function of position and the semi-major axis of it's orbit ellipse assuming 2-Body dynamics:

$$v = \sqrt{\mu(\frac{2}{r} - \frac{1}{a})}$$

Where the standard gravitational parameter for Earth is:

$$\mu_e = 389,600km^3s^{-2}$$

Using the Vis-Viva equation allows computation of the parking orbit velocity $v_{c,1}$, and the required Hohmann Transfer perigee velocity v_1:

$$v_{c,1} = \sqrt{\mu_e(\frac{2}{r_1} - \frac{1}{a_{c,1}})}$$

$$= 7.67kms^{-1}$$

$$v_1 = \sqrt{\mu_e(\frac{2}{r_1} - \frac{1}{a_1})}$$

$$= 10.75kms^{-1}$$

11

Thus, the ideal case translunar injection (TLI) Δv can be determined:

$$\Delta v_{TLI} = v_1 - v_{c,1}$$

$$= 3.08 kms^{-1}$$

This Δv_{TLI} can now be directly compared to velocity changes achievable through small satellite based mono-propellant engines. The Aerojet Rocketdyne MPS-120XW CubeSat High Impulse Adaptable Modular Propulsion System (CHAMPS) leverages 4 MR-142 hydrazine engines with a propellant storage and delivery system. Each hydrazine engine produces 0.26 N - 2.79 N of thrust, offering an overall specific impulse range of 206 s - 217 s. CHAMPS offer three configurations - a base 1U version with a 1.48 kg engine wet mass, a longitudinally configured 2U x 1U XL version, and a laterally oriented 1U x 2U XW verison. Both 2U options provide additional propellant storage with a 2.38 kg engine wet mass. For the purpose of a 6U mission, a larger 2U unit will be applied, offering 0.98 kg of useable propellant. To present an ideal performance case for the MPS-120 engine, the highest specific impulse of 217 s is assumed.

$$m_{drive,mono} = 2.38 kg$$

$$m_{prop,mono} = 0.98 kg$$

$$I_{sp,mono} = 217 s$$

Per the NASA CubeSat Launch Inititate Overview, a single cube satellite unit (1U) typically weighs less than 1.33 kg. This mass shall be applied for the remaining 4U to make up a 6U bus. This additional mass shall encompass the vehicle subsystems required for a lunar mission, including the scientific instrumentation payload, an attitude control system (ACS), a Guidance, Navigation, and Control system (GNC),

an on-board computer (OBC), a communications system, and a power supply. Thus, the total vehicle wet (initial) mass is assumed to be:

$$m_{wet} = m_{drive,mono} + 4m_{1U}$$

$$= 7.70kg$$

The total vehicles dry (final) mass after complete propellant expenditure is assumed to be:

$$m_{dry} = m_{wet} - m_{prop,mono}$$

$$= 6.72kg$$

The rocket equations defines the achievable Δv as a function of I_{sp} and mass ratio. Assuming field free space and constant magnitude and direction of exhaust velocity (a valid assumption for high-thrust chemical engines per Prussing and Conway [6]:

$$\Delta v = gI_{sp}ln(\frac{m_{wet}}{m_{dry}})$$

Where g is the 0.0098 km/s^2 acceleration due to gravity at Earth surface.

Thus, a 6U CubeSat powered by a 2U MPS-120 hydrazine mono-propellant engine is capable of:

$$\Delta v_{mono} = 0.29kms^{-1}$$

Under ideal assumptions, the best-in-class MPS-120 only achieves 9.4% of the Δv required for TLI of a 6U small satellite under ideal conditions - a significant shortfall.

Select green mono-propulsion options offer an improved propellant density to

the hydrazine thruster. The Bradford Engineering 1N High Performance Green Propulsion (HPGP) is powered by Ammonium DiNitrimide (ADN) and capable of 0.25 N - 1 N of thrust, with a 204 s - 209 s specific impulse range. Unlike the hydrazine MPS-120, this thruster has not been specifically discretized into a cube satellite compatible configuration. However, the 178 mm overall length and a low thruster mass of 0.38 kg enable integration into a 2U x 2U package assuming 1U x 2U for propellant storage tanks. For a comparative analysis, this engine is assumed to offer the same propellant storage dry mass and volume as the MPS-120 hydrazine thruster (an assumption based on similar propellant storage geometry), with a greater propellant mass due to the 22% density difference between hydrazine and ADN. Thus, the mass of the 1N HPGP drive system is derived as follows:

$$m_{thruster,green} = 0.38 kg$$

$$m_{tanks,green} = m_{drive,mono} - m_{prop,mono}$$
$$= 1.40 kg$$

$$m_{drive,green} = m_{thruster,green} + m_{tanks,green}$$
$$= 1.78 kg$$

The propellant mass is given by the relative density of hydrazine to ADN:

$$m_{prop,green} = 1.22(m_{prop,mono})$$
$$= 1.20$$

Thus, a 6U spacecraft mass can be calculated under the 1.33 kg assumption for the

remaining 1U x 2U sections:

$$m_{wet} = m_{drive,green} + 2m_{1U}$$

$$= 4.44kg$$

$$m_{dry} = m_{wet} + m_{prop,green}$$

$$= 5.64kg$$

For the ideal case, one assumes the maximum 1N HPGP specific impulse of 209 s. Per the Rocket Equation:

$$\Delta v_{green} = 0.49 kms^{-1}$$

The low-mass construction and improved propellant density of ADN result in a demonstrable performance increase when compared to hydrazine. However, the 1N HPGP engine provides only 16% of TLI Δv demand for a 6U small satellite under ideal conditions.

Based on this analysis, it was concluded that no current TRL 9 small satellite on-board propulsion systems are yet capable of achieving TLI. In order to open new opportunities for translunar missions, a supplementary TLI stage is required to provide significantly higher propulsive performance and greater flexibility than rare and highly specific ride share trajectories.

The *NASA 2018 Strategic Plan* [1] provides a clear mandate for greater presence in lunar space. Through the Commercial Lunar Payload Services (CLPS) program, NASA aims to invest $2.6 Billion from 2018-2028 to leverage the growing capabilities of the commercial space sector to improve lunar access. An economic opportunity therefore exists to develop mission architectures that use a TLI stage based

on proven propulsion technology and the competitive commercial launch vehicle market.

However, with different scientific and commercial objectives requiring unique launch dates and lunar orbital elements, an essential prerequisite to this vision of increased lunar access is a global characterization of key performance metrics. Specifically this characterization must quantify the impact of payload mass, lunar arrival orbital elements, and departure epoch upon mission performance demand.

1.2 Background

Translunar space is a highly dynamic navigational environment with interrelations between the positions and velocities of numerous celestial bodies, and orbital perturbations such as non-spherical gravity, atmospheric drag, solar radiation pressure and general relativity. This complex balance of forces must be accurately applied in the design of lunar trajectories. Given the vast distance between Earth and Moon, small inaccuracies or simplifications to the force model can lead to large errors in a spacecraft's arrival state.

Fortunately, these dynamics are well defined in literature and can be distilled into a detailed mathematical description of the Earth-Moon system.

1.2.1 The Lunar Orbit

The most important factor to consider when designing the Earth-Moon trajectory is the relative position between Earth, Moon, and Sun. The lunar orbit demonstrates complex kinematics due to several periodic and secular cycles within the Earth-Moon system. Periodic cycles include the monthly lunar orbit about Earth, the fluctuation in lunar orbit eccentricity. Secular cycles include the annual Earth orbit about the sun, and two long term precessions in the lunar orbit caused predominantly by the perturbing effects of solar gravity. The first is the apisidal precession,

by which the major axis of the orbit ellipse rotates about Earth within the lunar orbital plane. The second is the nodal precession, whereby the line of nodes of the orbit ellipse - the points where the lunar orbit cross the ecliptic - rotates about Earth upon the ecliptic. These cycles result in a time dependency in both lunar range, and lunar declination, with important implications for transfer trajectories. In order to model a translunar mission, the range and declination must be accurately characterized for a given mission epoch.

This characterization was achieved through Horizons system - a tool developed by the NASA Jet Propulsion Laboratory (JPL) for the generation of highly accurate ephemerides for planetary bodies within the solar system. Lunar ephemerides were generated for a full 18.6 year declination cycle from 01 January 2020 to 01 July 2038. These ephemerides provided orbital elements for the Moon with respect to Earth's center, expressed in both ecliptic and equatorial coordinate frames using the mean equinox at the J2000 reference epoch.
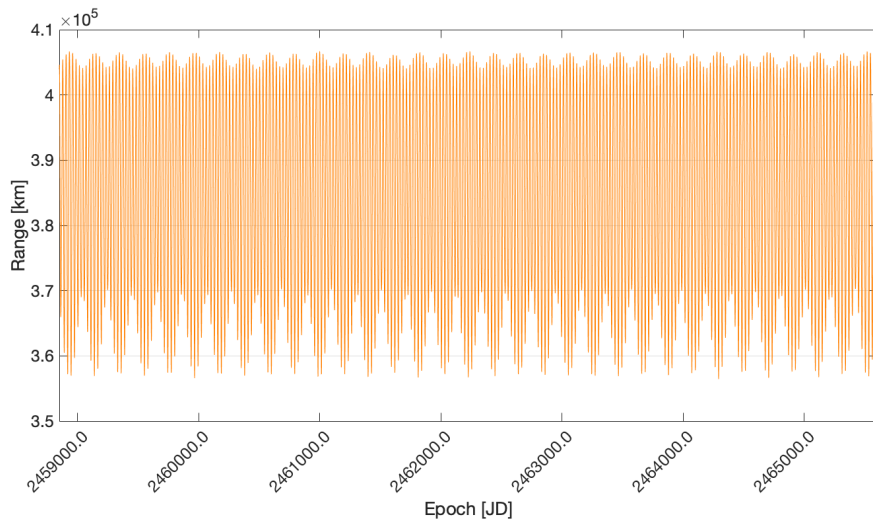
Figure 1.2: Lunar range

On the shortest time scale, the periodic cycles may be observed. Range oscillates with a 27.3 day period as the Moon travels around its month long Earth orbit. The maximum and minimum monthly ranges occur at apogee and perigee passage

17

respectively. Due to solar gravity, third body gravity, and tidal forces, the Lunar orbit has a time varying eccentricity. This is observed by the oscillation in minimum and maximum apogee and perigee radius over a period of 7 months.
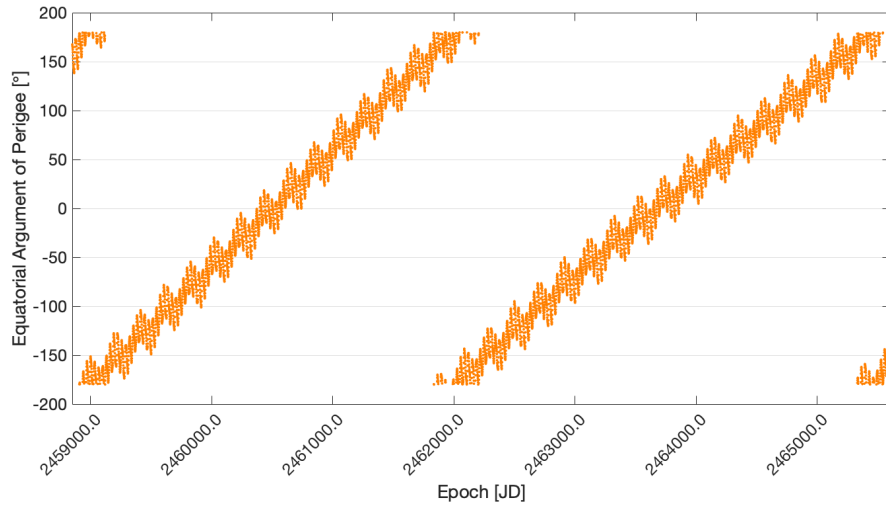
Figure 1.3: Lunar argument of perigee, equatorial, J2000 mean equinox

On a medium time scale, the equatorial argument of perigee for the can be seen to pass through a full 360 degree revolution every 8.9 years - a demonstration of the secular apisidal precession cycle. Thus, the instantaneous Earth-Moon distance is a function of the true anomaly of the Moon in its Earth orbit (27.3 day period), the lunar eccentricity (7 month period), and the orientation of the line of apisides (8.9 year period). The magnitude of this position vector drives the semi-major axis of the minimum ellipse required to reach the moon.

Per the Vis-Viva equation - the greater the semi-major axis of the transfer ellipse, the higher the required earth departure velocity becomes.

On a long time scale, the Moon's ecliptic Right Ascension of the Ascending Node (RAAN) is observed to pass through a full 360 degree revolution every 18.6 years - a demonstration of the secular nodal precession cycle. The obliquity of Earth's axis of rotation places the celestial equator at a 23.5° inclination to the ecliptic, with the two planes transecting along the vernal equinox. The lunar dec-
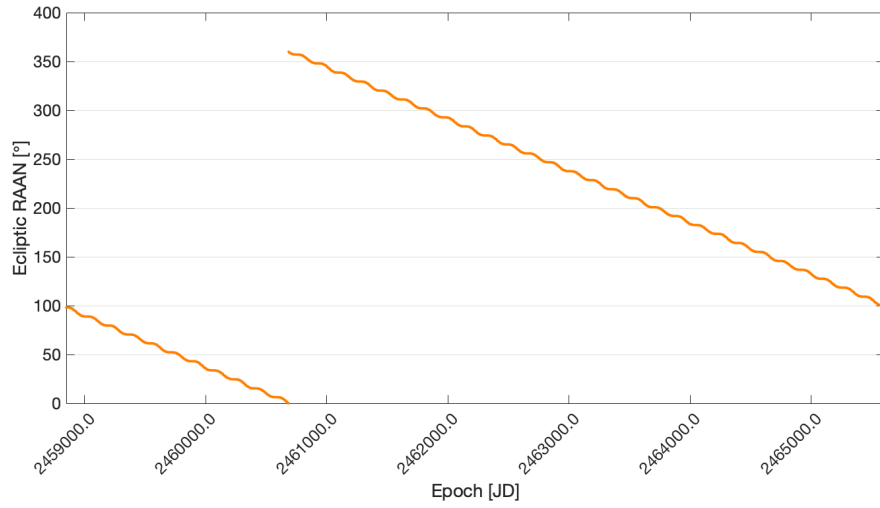
Figure 1.4: Lunar RAAN, ecliptic, J2000 mean equinox

lination - the angle between the Moon and the celestial equator - is driven Earth's obliquity, the lunar RAAN, and the Moon's ecliptic inclination. As demonstrated, the ecliptic inclination oscillates between 5° and 5.3°.
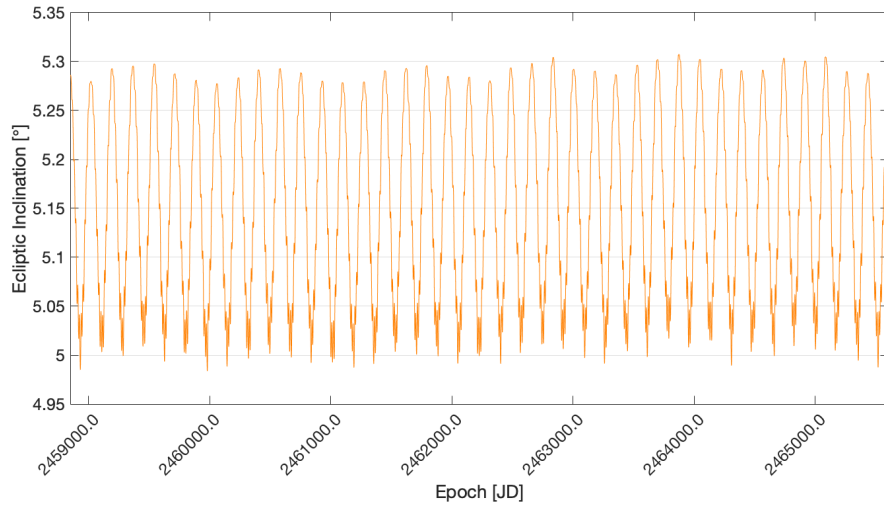
Figure 1.5: Lunar inclination, ecliptic, J2000 mean equinox

The minimum declination of 0° occurs when the Moon passes through an ascending or descending node. The maximum declination fluctuates between low and high values. The low maximum occurs when the line of nodes of the celestial equator and the lunar orbit plane are aligned. The angular difference in the inclinations

is thus 23.5° - 5.3° = 18.2°. The high maximum occurs when the line of nodes of the celestial equator and the lunar orbit plane are 180° out of alignment (co-linear line of nodes, with opposite ascending nodes). The angular difference in the inclinations is thus 23.5° + 5.3° = 28.8°. Thus, the monthly minimum and maximum lunar declination oscillates over the 18.6 year nodal cycle.
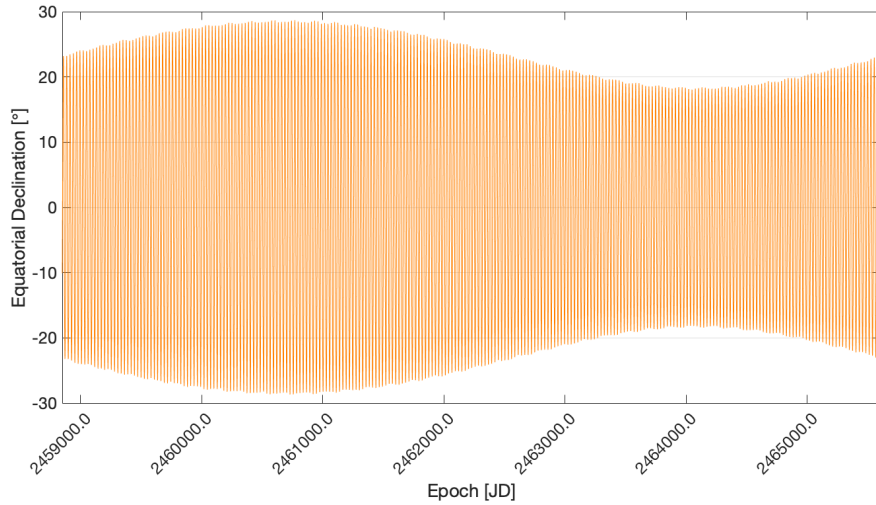
Figure 1.6: Lunar declination, equatorial, J2000 mean equinox

This pattern corresponds to an oscillation in the Moon's equatorial inclination.
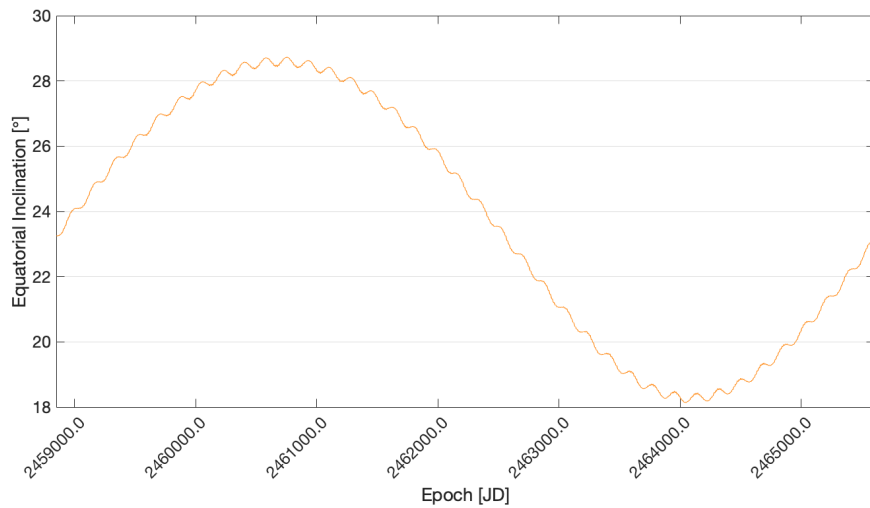
Figure 1.7: Lunar inclination, equatorial, J2000 mean equinox

The performance demand for efficient lunar trajectories is reliant upon lunar

20

range and declination at the departure epoch. Given a fixed parking orbit radius and inclination, the mission epoch will dictate the required parking orbit RAAN, and the true anomaly of the TLI burn. These parameters may be used to align the transfer trajectory to intersect the Moon at any epoch. Upon arrival, relative velocity between the spacecraft will be driven by the lunar orbital radius and the angle between transfer and lunar orbital planes. Thus, the relative positions at departure also dictate the Δv necessary for orbit insertion upon arrival.

To understand the approximate Δv and time of flight magnitudes required for lunar trajectories, it is beneficial to analyze the data from a range of unique translunar mission architectures that have successfully flown, or have reached a mature stage in design with high fidelity analysis.

1.2.2 Apollo Architecture

A rich source of information for comparative analysis are the Apollo missions. The Apollo 10, 11, and 12 Mission Reports [7][8][9] accurately detail mission operations including burn times, durations and Δv's for TLI, orbit insertion, and landing maneuvers performed by the Saturn-IVB, the Command/Service module, and the lunar lander, as well as the properties of Earth departure and lunar arrival parking orbits.

The architecture for these missions includes a circular parking orbit with an average altitude of approximately 170 km. From this parking orbit, a single TLI burn places the spacecraft into a free return transfer. Upon arrival, the spacecraft is directly inserted into a parking orbit of approximately 100 km altitude circular. The advantages of this architecture is that a circular parking orbit that allows the adaptable, on-the-fly selection of transfer orbit argument of perigee and is well suited to ride share opportunities. The disadvantage is that a free return trajectory has an apogee beyond the lunar radius, therefore, the transfer orbit is not optimally
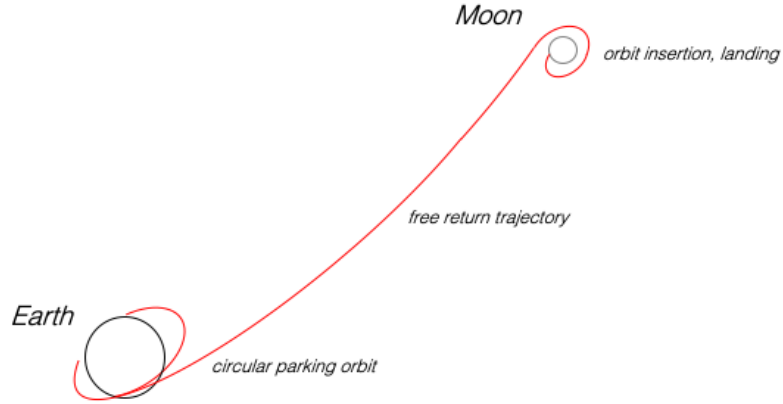
Figure 1.8: Apollo trajectory, circular parking orbit, free return

energy efficient.

Presented below are the outbound mission metrics of Apollo 10, 11, and 12.

Table 1.3: Earth-Moon segment characteristics for the Apollo 10, 11, 12 [7][8][9]

Metric	Mission		
	Apollo 10	Apollo 11	Apollo 12
Earth Dep. Orbit [km]	160.3 x 165.1	159.6 x 162.1	185.1 x 189.7
Lunar Arr. Orbit [km]	95.3 x 98.2	86.6 x 105.7	87.4 x 106.4
Translunar Inj. Δv [m/s]	3049	3182	3205
S-IVB Sep Burn Δv [m/s]	6	6	-
Mid-Course 1 Δv [m/s]	15	6	19
Total Flyby Δv [m/s]	3070	3194	3224
Lunar Orbit Ins. Δv [m/s]	909	889	881
Lunar Orbit Corr. Δv [m/s]	42	48	50
Total Orbit Ins. Δv [m/s]	4021	4131	4155
Com. Mod. Sep Δv [m/s]	-	1	1
Descent Burn Δv [m/s]	-	23	19
Landing Burn Δv [m/s]	-	2112	2003*
Total Landing Δv [m/s]	-	6267	6178
Translunar Time [hh:mm:ss]	80:25:08	80:11:36	87:48:48

* Δv **not presented. Extrapolated from burn time and engine parameters.**

The translunar (all pre-lunar arrival) segments of Apollo 10, 11, and 12 have Δv

22

expenditures of 3.07 km/s, 3.19 km/s, 3.22 km/s respectively. These numbers provide a sample for the expected mission performance demands of a direct approach free return trajectory from a circular parking orbit within the 159.6 km - 189.7 km altitude range. The post LOI and LOC Δv values of 4.02 km/s, 4.13 km/s, 4.16 km/s demonstrate the performance demand for lunar orbit insertion. Likewise the Apollo 11 and 12 post descent and landing burn Δv values of 6.27 km/s, and 6.18 km/s demonstrate the performance demand for lunar landing.

1.2.3   Exploration Mission 1 Architecture

Another valuable data point is the trajectory design for Exploration Mission 1 (EM1) - the first mission of the Artemis program. Whilst this mission is yet to fly, it has been modelled with the NASA Johnson Space Flight Centre Copernicus mission optimization software and represents a high-fidelity, flight ready mission design. *Trajectory Design Considerations for EM1* by Dawn et. al. [10] details the arrival and departure conditions, along with detailed performance metrics for the ICPS and Orion maneuvers.
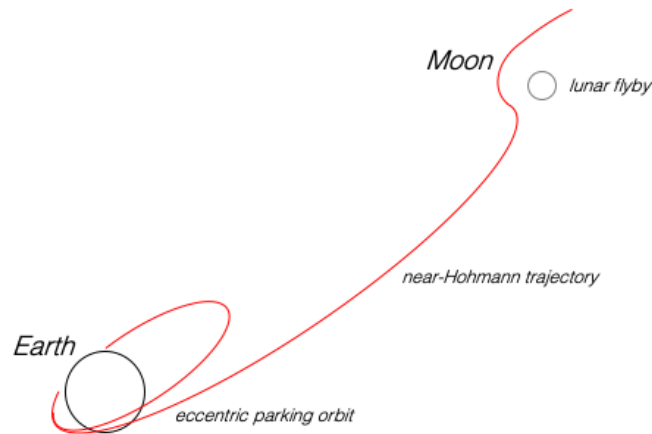
Figure 1.9: EM1 trajectory, eccentric parking orbit, near-Hohmann

This mission provides an interesting contrast to the Apollo trajectories as it per-

forms a powered lunar flyby rather than lunar insertion. Furthermore, the translunar segment of EM1 has two significant departures from the Apollo model. First, it makes use of an eccentric Earth parking orbit (1800 km x 185 km apogee/perigee altitudes). Second, it makes use of a near-Hohmann transfer rather than a free return trajectory (in the context of this research, near-Hohmann means departure at periapsis, arrival at apoapsis, without any further simplifying assumptions).

The advantage of this trajectory is increased energy efficiency by applying more mechanical energy to the parking orbit before TLI, and departing upon a more efficient near-Hohmann transfer to minimize performance demand. The disadvantage is that a high apogee departure orbit is very specific, requiring a powerful launch vehicle and very specific launch window (potentially instantaneous). As such, this architecture does not fit well with small commercial launch vehicles, or with ride share opportunities (the market for which are predominantly circular orbits).

Presented below are the outbound mission metrics of EM1.

Table 1.4: Earth-Moon segment characteristics for EM1 [10]

Metric	Mission
	EM1
Earth Dep. Orbit [km]	185 x 1806
Lunar Arr. Perilune [km]	100
Translunar Inj. Δv [m/s]	2864.3
Vehicle Sep Burn Δv [m/s]	2
Total Δv [m/s]	2866
Translunar Time [hh:mm:ss]	140:00:00

A lower Δv of 2.87 km/s can be observed, demonstrating the effects of departure and arrival conditions on the overall Δv requirement. Firstly, the high Earth parking orbit apogee of 1806 km ensures a comparatively large perigee velocity when the TLI burn is initiated. Secondly, EM1 does not follow an Earth free return trajectory. The spacecraft arrives at the moon close to the apogee of its transfer orbit, thus, the transfer orbit has a lower semi-major axis and correspondingly, a

lower target perigee velocity for the TLI burn.

1.2.4   Beresheet/Chandrayaan 2 Architecture

At the time of writing, the most recent lunar missions were those of Beresheet and
Chandrayaan 2. The Beresheet lander was launched by Israel's SpaceIL aboard a
SpaceX Falcon 9 on 22 February 2019. Though the failed landing attempt resulted
in loss of the craft, the Beresheet successfully achieved lunar orbit insertion. Whilst
no detailed analysis of achieved performance was found in current literature, it is
interesting to view the qualitative advantages and disadvantages of these trajecto-
ries. In contrast to Apollo and EM-1 trajectories which make use of powerful cryo-
genic translunar S-IVB and ICPS stages, the 585 kg Beresheet lander was propelled
by a smaller 400 N Leros 2B Hydrazine/Mixed Oxides of Nitrogen thruster. This
comparatively low thrust-to-weight ratio meant a longer burn duration. To improve
efficiency (as discussed below) the translunar injection was split into four shorter
apogee raising burns. The final apogee was equivalent to the lunar orbital radius
and was correctly phased to allow lunar capture on 04 April 2019.
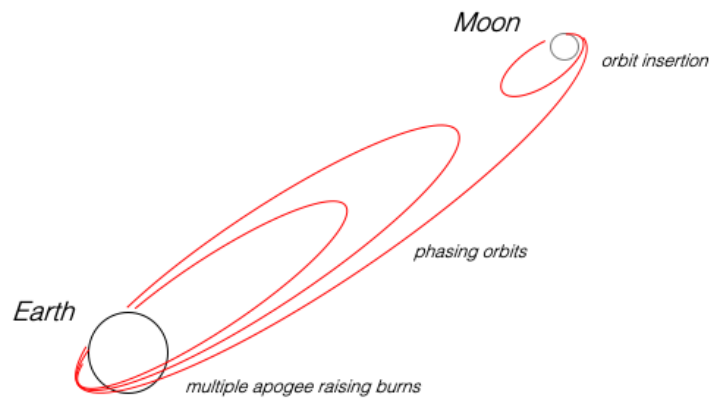
Figure 1.10: Beresheet/Chandrayaan 2 trajectory, multiple apogee raising burns,
phasing orbits

The Chandrayaan 2 mission was launched by the Indian Space Research Orga-

nization aboard a GSLV on 14 July 2019. In the same fashion as Beresheet, Chandraayan 2 applied six successive apogee raising maneuvers to reach lunar radius. Though the Vikram lander crashed during descent to the lunar surface, the spacecraft successfully achieved insertion on 20 August 2019, and the orbital portion of the vehicle remains functional.

These trajectories both made use of the Oberth effect as proposed by Hermann Oberth in *Ways to Space* [11] by burning in short segments as close as possible to perigee in order to maximize the increase in specific kinetic energy from each maneuver. The trade off for this efficiency is an increase in flight times from the direct approach taken by EM-1, (5.8 days vs. 42 days for Beresheet and 37 for Chandrayaan 2), and multiple passes through the Van Allen radiation belts.

1.2.5   Gravity Recovery and Interior Laboratory Architecture

The JPL Gravity Recovery and Interior Laboratory (GRAIL) mission launch from Cape Canaveral aboard a Delta II rocket on 10 September 2011. As presented by Parker and Anderson in JPL's *Low Energy Lunar Trajectory Design* [12], the two spacecraft (GRAIL A and GRAIL B) achieved translunar injection via a low energy, weak stability boundary transfer (WSBT). The WSBT architecture required a TLI burn that overshot the lunar radius. Gravitation due to a precise orientation of Earth, Moon, and Sun altered the shape of the orbit such that when each spacecraft fell back towards Earth after apogee, they intercepted the Moon at perigee for a reduced relative velocity, therefore optimal orbit insertion.

The advantage of this trajectory is a lower orbit insertion Δv compared with a direct injection such as Apollo. Furthermore, the arrival vector and timing can be tailored with minor course correction maneuvers to achieve any arrival inclination or RAAN. The disadvantage are a long flight time of 70-120 days and a precise departure epoch that limits adaptability to commercial rise share opportunities.
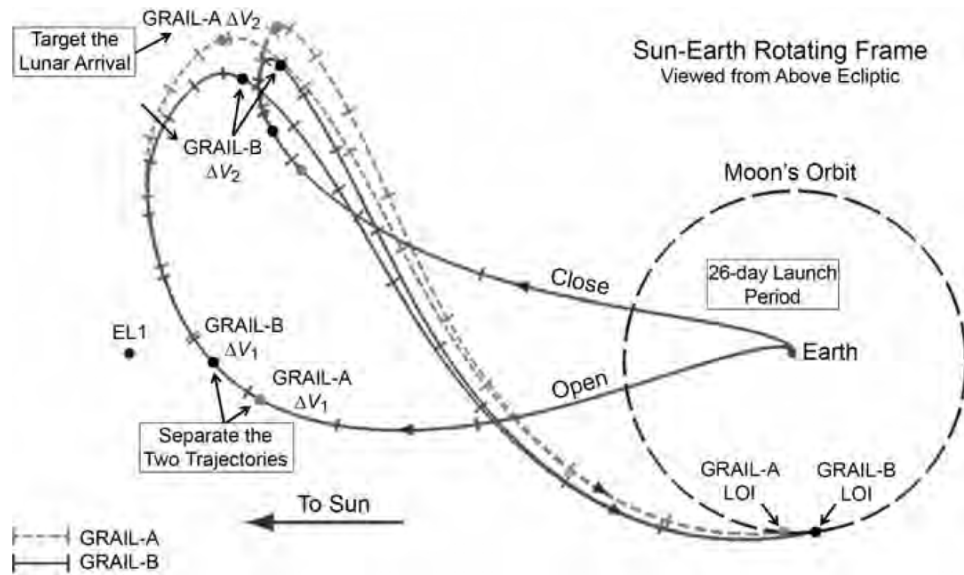
Figure 1.11: GRAIL trajectory, weak stability boundary transfer [12]

The advantage of this trajectory is a lower orbit insertion Δv compared with a direct injection such as Apollo. Furthermore, the arrival vector and timing can be tailored with minor course correction maneuvers to achieve any arrival inclination or RAAN. The disadvantage is a long flight time of 70 to 120 days and tight limitations on launch epoch.

1.2.6 Optimal Lunar Pathfinder Architecture

To select an optimal mission architecture for lunar pathfinders, the advantages and disadvantages of each unique architecture reviewed above were compared in the context of small satellite missions.

An important factor for small satellite missions is translunar flight time, and the additional mission assurance that long flight times demand. Traditional Discovery and Flagship class vehicles designed for the rigors of long periods in deep space undergo years of analysis, environmental testing and qualification before flight. The associated costs rightly foster an aversion to technical risk, but such conservatism

27

comes at the expense of innovation. These missions rarely push the boundaries of space technology by trialing high performance, less proven on-board instruments, or by adopting challenging, high-risk, high-yield mission architectures.

Pioneering small satellite missions provides an avenue for rapid advancement in lunar science and deep space technology with little consequence in the event of individual mission failure. This prospect does, however, come with limitations. When compared to Discovery and Flagship class counterparts, small satellites are inherently more vulnerable to the ionizing radiation of the deep space environment. Furthermore, decay in the performance of low-weight, low-cost batteries and solar cells are provide an additional time limiting factor. To account for this, a direct translunar trajectory similar to Apollo or EM1 would be favourable for pathfinder missions. This approach maximizes the portion of operational life a satellite spends collecting data in lunar orbit or on the surface, rather than in transit.

The corresponding flight time of 3 - 5 days would enable satellites with month-long deep space lifetimes to be viably applied on lunar missions. Adopting phasing loops such as those of the recent Beresheet and Chandrayaan 2 missions, or adopting a weak stability boundary transfer similar to GRAIL may add weeks or even months to the translunar travel time. Though more mass efficient, these trajectories limit access to spacecraft with a design life sufficient to endure the long voyage, and risk reduction to justify the human capital required to support extended operation. Though not an intractable problem, it dulls the unique advantage of rapid, low cost iteration.

Another important factor in enabling increased mission volume is access to cost competitive commercial launch vehicles, either by dedicated launch aboard a small, low cost rocket, or through ride share aboard a larger rocket with a high payload capacity and lower cost-per-kilogram ($/kg) performance. Ride share places two restrictions upon a lunar mission. Firstly, the translunar injection must occur from a

standard, readily available LEO parking orbit that services other satellite customers. The market for ride share is predominantly to circular orbits, not a mission specific high eccentricity transfer orbit with dedicated alignment and phasing. Secondly, the vehicle required to complete the mission must fit within the mass limitations and fairing form factor of the cost competitive launch vehicles of the current and near-future commercial launch market.

The mission architecture selected for this research was a circular Earth parking orbit (similar to Apollo), a single TLI burn for direct injection into a near-Hohmann transfer (similar to EM1), insertion into circular parking orbit, then a half-orbit descent and landing sequence. As discussed in Chapter 2, this configuration serves as a sound architectural "baseline" that limits translunar flight time and Van Allen exposure, adopts a near-Hohmann transfer for the most efficient direct injection trajectory, and utilizes a versatile parking orbit that is compatible with small commercial launch vehicles and ride share opportunities.

1.2.7   Lunar Arrival Conditions

Further important drivers for mission performance are the conditions at the lunar arrival. A small satellite pathfinder mission is likely to require objective-dependant lunar orbit parameters. Potential objectives include using Earth, lunar, and solar gravity to maintain a specific orbital geometry, insertion into a particular post-flyby geocentric or heliocentric trajectory, ensuring the ground trace transects a geographic region of interest for orbital imaging, or landing at a precise lunar latitude and longitude.

Consider a Lunar Centered, Lunar Fixed (LCLF) rotating frame with the lunar prime meridian and equator as fixed datums. The geometry of the arrival trajectory, be it a flyby, orbit insertion, or landing architecture, may be characterized through the Keplerian orbital elements. By utilizing a lunar fixed rotating frame, the ground

trace can be made to transect a particular region of geographic interest for imagining or landing by tailoring select orbital elements.

The adjustment of lunar orbital elements determine the required velocity vector upon arrival at the lunar sphere of influence (driven by departure parameters at the TLI burn phase), as well as subsequent orbit insertion, orbit adjustment, and landing maneuvers. Therefore, variation in the lunar orbital elements will, like the departure epoch and trajectory architecture, affect the cumulative mission Δv, and thus, performance demand.
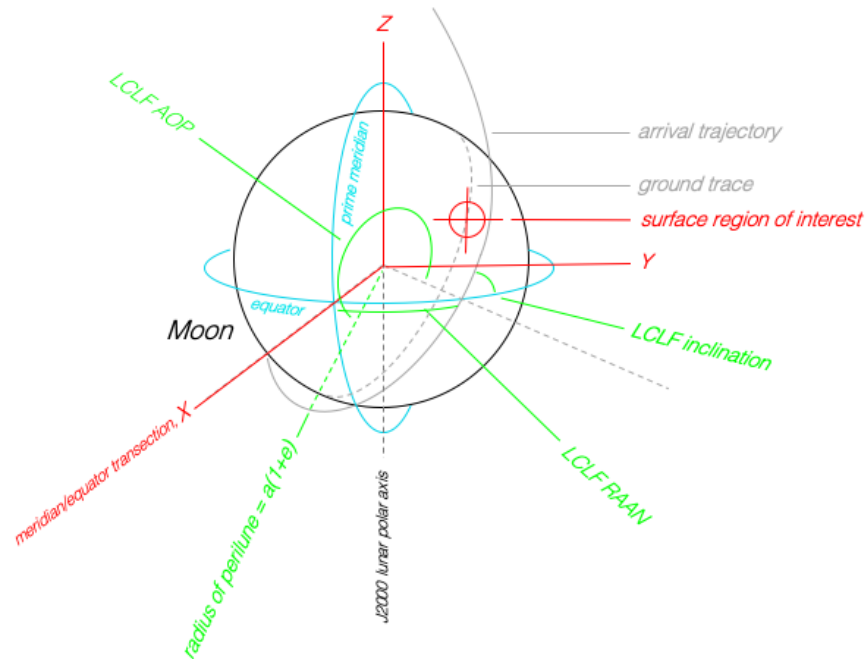
Figure 1.12: Ground trace targeting with lunar orbit Keplerian elements

1.2.8 Knowledge Gap

Through a review of past and future missions (Apollo 10 [7], Apollo 11 [8], Apollo 12 [9] EM1 [10], Beresheet, and Chandrayaan 2), along with holistic guidance on lunar trajectory design per Parker and Anderson, it was observed that the performance demands of lunar missions are highly case dependant, or subject to simpli-

fied assumptions with limited variable parameters.

No reference currently exists to accurately characterize the dependency of performance demand upon four important variable parameters. First is the dependency upon variability in payload mass to cover a range of small satellite form factors and masses that would prove viable as lunar pathfinder vehicles. Second is the dependency upon the periodic and secular cycles of the Earth-Moon system (including lunar orbit, eccentricity fluctuation , the characterization of which would allow the identification of optimal departure phasing. Third is the dependency upon lunar arrival Keplerian elements to target specific post flyby trajectories, specific orbital geometries, or ground trace intersections with geographic regions of interest. Fourth is the dependency upon arrival architecture to cover lunar flyby, orbit insertion, and landing scenarios.

Finally, no reference exists to compare a multi-parameter performance map to gauge compatibility of small satellite pathfinders with cost-competitive commercial launch vehicles as a dedicated or ride share mission.

1.3 Objectives

The value proposition of this thesis is to fill the aforementioned knowledge gap by leveraging high-performance computing to map the performance demand for direct injection lunar pathfinder missions. This map characterizes variability over a broad range of small satellite payload masses, departure epochs, arrival elements, and arrival architectures over a complete 18.6 year Earth-Moon nodal cycle. The results of this analysis are to provide lunar mission designers with a versatile reference for preliminary planning, including optimal phasing and compatibility with commercial launch vehicles in the current and near-future market.

To define performance this study focuses primarily on three mission metrics most relevant to mission designers:

Translunar Flight Time: the elapsed time between TLI and passage through lunar periapsis (perilune).

Delta Velocity (Δv): the cumulative total velocity change required to achieve all maneuvers. Used for cross mission comparison.

Mission Mass: the cumulative total mass of payload, spacecraft, and propellant - the total mass that must be lifted into an Earth parking orbit by a launch vehicle. Used for vehicle scoping.

Specifically, this thesis sought to answer four questions.

1.3.1   Research Question 1: Payload Mass Dependency

What is the relationship between mission mass and payload mass for lunar flyby, orbit insertion, and landing trajectories?

Hypothesis 1: Payload Mass Dependency

Without gravity losses, the Δv demand does not change with overall vehicle mass. Based on the rocket equation, it is hypothesized that propellant consumption, and therefore mission mass, must increase in proportion to payload mass such that the wet/dry mass ratio is maintained.

1.3.2   Research Question 2: Arrival Orbital Element Dependency

What is the relationship between mission mass and the arrival LCLF inclination and right ascension of the ascending node for lunar flyby, orbit insertion, and landing trajectories?

Hypothesis 2: Arrival Orbital Element Dependency

Arrival at a $0°$ inclination corresponds to entry into the lunar sphere of influence at the shortest possible orbital radius from Earth. Given this requires a marginally less

energetic transfer orbit, it is hypothesized that a 0° arrival corresponds to the lowest propellant consumption, therefore mission mass, and that increasing or decreasing inclinations progressively increase mission mass. Upon insertion into a lunar orbit, it is predicted that a specific LCLF RAAN can be achieved by waiting for the moon to turn beneath the orbit over its 27.3 day rotation, thus RAAN has no effect on mission mass. RAAN is only defined upon orbit insertion, therefore does not pertain to flyby missions

1.3.3 Research Question 3: Departure Epoch Dependency

What is the relationship between mission mass and the departure (TLI ignition) epoch for lunar flyby, orbit insertion, and landing trajectories?

Hypothesis 3: Departure Epoch Dependency

Transfer orbit energy is driven by lunar range (defining travel distance), and declination (defining relative inclination and velocity upon arrival). It is hypothesized that flyby mission mass is optimized at minimum lunar range, and that orbit insertion and landing mission mass is minimized at the lowest relative inclination between the transfer orbit and lunar orbit at major standstill (the point of highest lunar inclination with respect to the equator).

1.3.4 Research Question 4: Launch Vehicle Compatibility

Are direct injection, translunar missions for 0 - 24 kg small satellite payloads compatible with cost-effective launch vehicles in the near-future commercial market?

Hypothesis 4: Launch Vehicle Compatibility

It is hypothesized that the mission mass required for all direct injection, translunar missions within the parameter space can be delivered to the required parking

orbit by the SpaceX Falcon 9 and Blue Origin New Glenn heavy lift vehicles. Furthermore, it is hypothesized that smaller, low-cost commercial launch vehicles can provide frequent, dedicated parking orbit delivery to a subset of translunar missions for flyby and orbit insertion missions at lower payload masses.

CHAPTER 2

TECHNICAL APPROACH

In order to answer the research questions posed in chapter 1, this research followed
a technical methodology made up of three progressive steps.

First, a parameter space of lunar pathfinder payload masses, departure epochs,
arrival elements, and arrival architectures was designed to encompass a wide range
of scientifically/commercially compelling pathfinder mission configurations. Second, a translunar trajectory design algorithm was designed to generate optimal mission architectures for each parameter set within the parameter space. This algorithm
was based upon a high-fidelity dynamics for the Earth-Moon system to ensure accurate solutions. Finally, the trajectory design algorithm was used to derive precise,
optimal, direct lunar trajectories for comparative analysis.

2.1 Parameter Space

2.1.1 Fixed Parameters

Earth Parking Orbit Geometry

A fixed 400km altitude circular orbit is far from optimized for minimizing the TLI
burn - it was instead selected for its ubiquity. 400km is an arbitrary LEO orbit
readily accessible to current commercial launchers and flies underneath the South
Atlantic Anomaly and Van Allen Belts, ensuring the critical TLI burn occurs when
the chance of a single event failure due to TIR is minimal. The assumption of
a standard circular orbit at deployment from the payload plate (as opposed to a
tailored high apogee elliptical orbit with a perigee carefully aligned for the TLI
burn) is conducive to ride-share opportunities aboard heavy lift vehicles that offer

competitive $/kg to orbit performance.

Earth Parking Orbit Inclination

The fixed Earth parking orbit inclination of 28.5° was selected as the latitude, therefore minimum directly accessible inclination achievable from Kennedy Space Center. This is the same parking inclination selected for the Apollo missions. KSC was selected for its ability to support a wide range of cost-competitive commercial rockets. According to the FAA's *Annual Compendium of Commercial Space Transportation, 2018*, flight tested launch vehicles supported at KSC (available for non-defense applications) are the Space X Falcon 9, Orbital ATK Minotaur C, Orbital ATK Pegasus XL, and the Rocket Lab Electron. Vehicles at an advanced stage of development and likely supported at KSC in the near-future are the Blue Origin New Glenn, Firefly Alpha, and Virgin Orbit LauncherOne. Furthermore, it offers the lowest inclination direct insertion from US soil - a favourable characteristic for maximum mass-to-orbit. For these reasons, Kennedy was considered the optimal US based launch site for a lunar mission aboard a cost-competitive commercial rocket. Given that launch site selection is not a flexible decision for mission designers, and that any alternative US-based site will not out-perform KSC, the launch site inclination was considered a fixed parameter.

Lunar Parking Orbit Geometry

A fixed 100km was chosen as the lunar arrival perigee for its practical relevance to scientific mission design. Parker and Anderson adopted the same approach, stating that "many spacecraft have been inserted into very similar orbits, including Lunar Prospector, Kaguya/ Selenological and Engineering Explorer (SELENE), Chang'e 1, LRO, and GRAIL"[12]. Furthermore, a 100 km lunar parking orbit also closely matches the arrival altitude of the Apollo missions for ease of comparative analysis.

2.1.2   Variable Parameters

Payload Mass

The first variable parameter is payload mass. The miniaturization of spacecraft sensors and subsystems allows high-impact science in low-weight, low-volume buses. Given part standardization, low mass, and growing flight heritage, the standard cube satellite form factor was considered the most efficient payload focal point. Centered upon on the nominal form factor of 6U cube satellite (proven to yield high scientific value through the secondary payloads selected for EM1), a payload variability of 0 - 12U (0 - 24 kg at 2 kg/U per chapter 1) was deemed reasonable to provide a viable range of options for small satellite pathfinder spacecraft.

Departure Epoch

To ensure the parameter space encompassed the performance dependencies of the full periodic (lunar orbit, and lunar eccentricity fluctuation), and secular (Earth orbit, apisidal precession, and nodal precession) cycles, an 18.6 year analysis period from 01 Jan 2020 00:00:00.000 to 01 Jul 2038 00:00:00.000 at 2 day intervals was selected as the range and resolution of departure epochs.

Arrival Keplerian Elements

With the lunar parking orbit fixed at 100 km circular, targeting a ground trace transection with a geographic region of interest for orbital fly-over or landing may be achieved by tailoring two Keplerian elements - the Lunar Centered Lunar Fixed (LCLF) Right Ascension of the Ascending Node (RAAN) and inclination. To encompass a broad range of targeted longitudes and latitudes, LCLF inclinations of -135° to 135° at 45° intervals (180° is a less efficient retrograde equatorial orbit than the 0° prograde alternative therefore is not included).

As arrival LCLF RAAN for a direct injection transfer is dictated by departure epoch, a specific RAAN must be achieved by waiting in lunar orbit as the tidally locked Moon rotates beneath the spacecraft for a maximum coast period of one rotation period (27.3 days). As this coast period does not effect mission performance, it is not considered a variable parameter within the trajectory design algorithm.

Arrival Architecture

To encompass a range of pathfinder mission options, lunar flyby, orbit insertion, and landing arrival architectures are applied.

2.1.3 Parameter Space Summary

Table 2.1: Parameter space summary

Variable Parameter	Min:Res:Max
Payload Mass	0 : 3 : 24 kg
Departure Epoch	01 Jan 2020 : 2 days : 01 July 2038
Arrival Inclination	-135 : 45 : 135°
Arrival Architecture	Flyby, Orbit Ins. Landing
Total number of cases	642,033

2.2 The General Mission Analysis Tool: GMAT

A high-fidelity mission trajectory was required for each unique combination of parameters. This trajectory and the associated performance characteristics were computed for each parameter set using the General Mission Analysis Tool (GMAT) developed by NASA GSFC.

GMAT was selected for five reasons. First, it supports high-fidelity modelling of the relevant orbital dynamics. Second, it contains differential correction and optimization tools required to solve trans-lunar trajectories based on variable inputs.

Third, the efficiency of the underlying ANSI C++ code allows fast computation, enabling a wide parameter space. Fourth, the software is open source, with open guidance documentation for easy validation of the underlying mathematical model and the quality control that comes from a widely tested and updated software. Fifth, GMAT is independently validated by over 13,000 core code tests run nightly [13] at GSFC and certified as a TRL 9 software. Finally, it has proven heritage in real-world application, having contributed to 9 NASA missions.

A GUI version of the application was used for algorithm design, testing, and for automated script generation. The Linux based GMAT console version was then used for actual analysis due to a significantly faster run time without the GUI over-head. A simple shell script was written to automatically cycle input parameters through the GMAT script, appending solutions as a single line 'string' to an output text file for data processing.

The subsequent sections provide definitions of applied time scales and coordinate systems, a description of the underlying mathematical architecture for the orbital dynamics, and a detailed characterization of the trajectory design algorithm applied using the NASA GMAT source code.

2.3 Time Scales

2.3.1 International Atomic Time: TAI

International Atomic Time defines the uniform passage of time as observed upon the Earth geoid, and is discretized into standard international seconds. SI seconds are precise temporal units based upon the radioactive decay of Cesium-133 as measured and averaged across a global network of atomic clocks. Due to its precision, TAI serves as the basis for numerous time scales.

2.3.2   Terrestrial Time: TT

Dynamical times are defined as the independent variable of planetary and lunar ephemerides, thus, they are measured through observations of the sun, planets, and moons. TT is the dynamical time specific to geocentric ephemerides. Per Montenbruck and Gill [14], it is the time in 86400 SI second days that would be measured by an ideal clock upon the surface of the geoid. TT agrees with TAI at a constant positive offset of 32.184s:

$$TT = TAI + 32.184s \tag{2.1}$$

TT is important as the defining time scale of the fundamental astrodynamical J2000 reference epoch 01 January 2000 12:00:00 TT.

2.3.3   Universal Time: UT1

Solar time is based upon a day marked by successive passages of the sun across the prime meridian in the geocentric celestial sphere. However, due to the eccentric orbit of Earth about the sun, the length of a solar day is subject to seasonal drift as Earth passes between perihelion and apohelion. Therefore, it is not a suitable datum for accurate time keeping. Instead, mean solar time is based upon the meridian passage of a fictitious "mean sun" which undergoes a constant daily shift in its Earth Fixed RAAN at a rate determined through observations and analytical methods. Universal Time UT1 is a mean solar time determined through observation of the Greenwich Mean Sidereal time - the measurable Greenwich hour angle of the vernal equinox.

2.3.4   Coordinated Universal Time: UTC

UTC is a realization of the mean solar time based upon the atomic time scale. It is based upon TAI with its accurate SI second, but includes a constant offset of "leap seconds" such that UTC always matches UT1 to within 0.9s. The annual leap offset between UT1 and UTC ($\Delta UT1$), and the cumulative leap seconds between UTC and TAI (ΔTAI) are catalogued by the International Earth Rotation and Reference Systems Service (IERS), whereby:

$$UTC = UT1 + \Delta UT1 \tag{2.2}$$

and

$$UTC = TAI + \Delta TAI = TT - 32.184s + \Delta TAI \tag{2.3}$$

UTC is the standard scale of time used across this analysis to define all departure and arrival epochs, burn times, and coast times. The UTC time of the fundamental J2000 epoch (defined in the TT scale as 01 January 2000 12:00:00.000) is 01 January 2000 11:58:55.815986276 [15].

2.4   Time Formats

2.4.1   Julian Date: JD

The Julian Date (JD) is the number of days elapsed since a reference epoch of noon, 01 January 4713 BC in the Julian calendar [15]. Thus, the J2000 epoch occurs at JD 2451545 TT, or JD 2451544.999257130 UTC.

2.4.2   Modified Julian Date Format: MJD

To reduce the numerical size of the epoch variable, the Modified Julian Date is appiled. MJD is the number of days elapsed since a second, more recent JD format

reference epoch. GMAT uses 05 January 1941 12:00:00.000 as this reference, thus:

$$MJD = JD_{day} - 2430000 \qquad (2.4)$$

Therefore, the J2000 epoch occurs at MJD 21545 TT, or MJD 21544.999257130 UTC. MJD is the numerical input applied by GMAT for ease of epoch based calculations. It is important to note that the GMAT form of MJD differs from the standard convention that utilizes a reference epoch of 17 November 1858 12:00:00.000.

2.4.3   Gregorian Date: GD

Whilst MJD is convenient for computation, all important mission epoch results are processed into the recognizable and intuitive Gregorian form of "dd MM yyyy HH:mm:ss.SSS" UTC.

2.5 Coordinate Frames

2.5.1 Earth Centered Inertial Frame: ECI

Earth Centered Inertial (ECI) is fixed with respect the celestial field, with its origin at Earth's center of mass. The X axis lies upon the mean vernal equinox - the intersection of the J2000 mean equatorial plane and the J2000 mean ecliptic - in the direction of the constellation Aries. The Z axis is aligned with Earth's polar axis of rotation at the J2000 epoch, whilst the Y axis lies on the equatorial plane, counter-clockwise positive of the X-axis, to complete a right handed set.
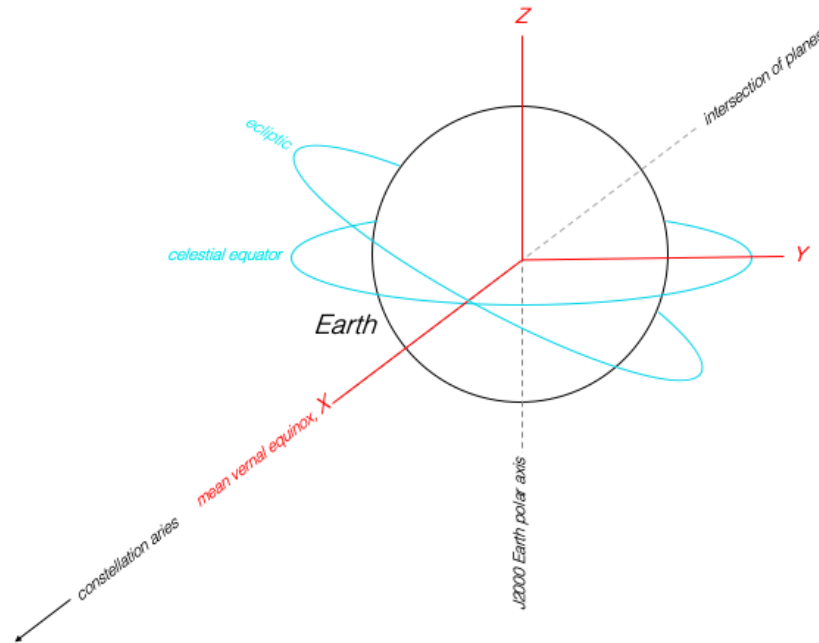
Figure 2.1: ECI frame

2.5.2 Earth-Moon Rotating Frame: EMR

The Earth Moon Rotating frame (EMR) is formed by a set of object referenced axes defined by the relative position of Earth and Moon. These axes are characterized by 6 vectors within the ECI inertial frame. The first is the position vector R of the

center of mass of the moon relative to the center of mass of Earth. The second is the velocity vector V of the Moon's motion within the ECI frame (ie. its velocity with respect to Earth). The third, N, is the cross product of the R and V vectors, forming a right handed set. The remaining three vectors are opposite and equal to the first three.
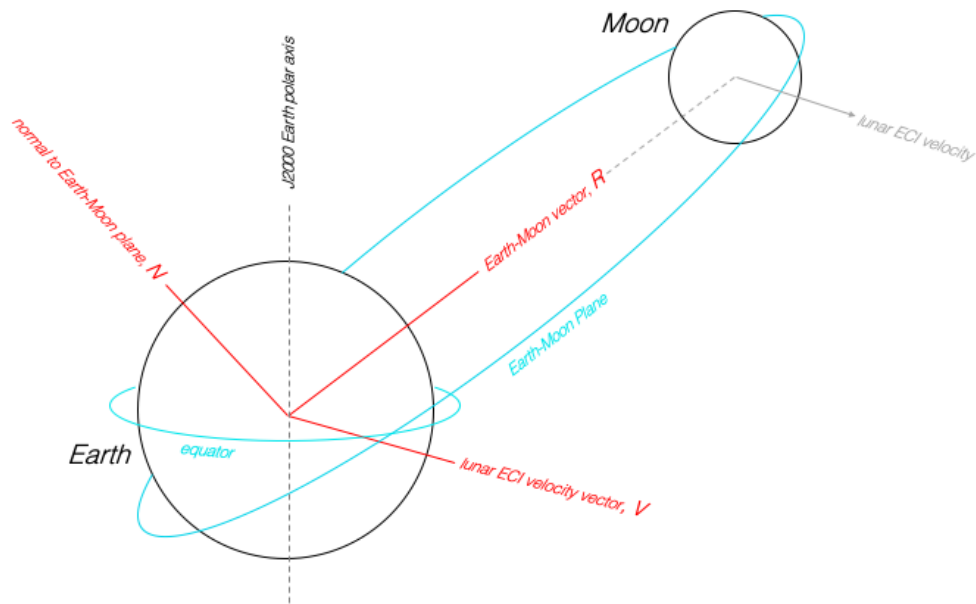
Figure 2.2: EMR frame

2.5.3   Lunar Centered Inertial Frame: LCI

Lunar Centered Inertial (LCI) is fixed with respect to the celestial field, with its origin at the Moon's center of mass. The X axis is aligned with the intersection of the Moon's equator and Earth's equator at the J2000 epoch. The Z axis is aligned with the Moon's axis of rotation, whilst the Y axis lies upon the equator, counter-clockwise positive from the X axis, to complete a right handed set.
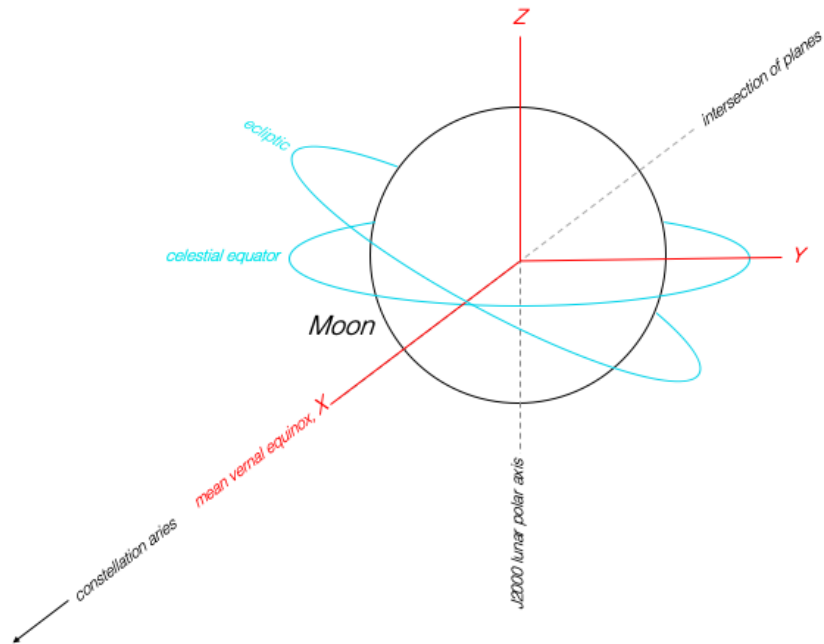
Figure 2.3: LCI frame

2.5.4 Lunar Centered Lunar Fixed Frame: LCLF

Lunar Centered Lunar Fixed (LCLF) originates at the Moon's center of mass. The X axis lies upon the lunar equatorial plane, aligned with the Lunar prime meridian (0 degrees longitude) as defined by JPL's Development Ephemeris model DE405 included with the GMAT source code. The Z axis is aligned with the Moon's axis of rotation. The Y axis lies upon the equatorial plane, east-positive of the X-axis, to complete a right handed set. The LCLF frame is used to define the orbital elements and Cartesian states for lunar observation orbits and precision landing operations dependant upon specific lunar latitudes and longitudes.
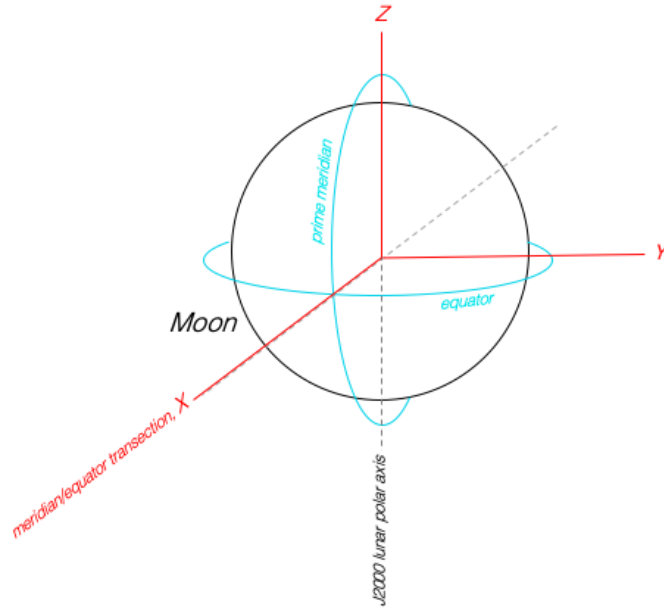
Figure 2.4: LCLF frame

2.5.5   Velocity Normal Bi-Normal Frame: VNB

The Velocity Normal Bi-Normal Frame (VNB) is fixed with respect to the instantaneous spacecraft motion and centered upon the spacecraft center of mass. The V axis is aligned with the spaceraft velocity vector. The N axis is aligned with the orbit normal (the angular momentum, or cross product of the radial position and velocity). The B axis completes the right handed set.

2.6   Orbital Dynamics: The Equations of Motion

This section details the underlying mathematical model used to characterize the forces of the Earth-Moon System, and the equations of motion that describe the passage of a spacecraft passing through it. A high-fidelity dynamics model was considered a fundamental requirement of this research in order to provide a meaningful assessment of mission performance for lunar mission designers.

Including higher-order acceleration terms into the equations of motion (for improved fidelity) comes at a cost to computational speed. A test run of the GMAT algorithm applied to a simple lunar landing trajectory was used to compare speeds with simple three body equations of motion (accounting for Earth and lunar gravity), and a complex equations of motion with higher order terms. The run times on a quad core Macbook were 25.763683 seconds versus 36.779985 seconds - an 11 second difference. Whilst not an issue for a single test case, this increased duration adds 12.7 days of computation for every 100,000 parameter combinations that are run through the algorithm.

Access to the Georgia Institute of Technology's super-computing capability through the Partnership for an Advanced Computing Environment (PACE) network made the implementation of a high-fidelity propagator possible by running multiple analyses in parallel across 80 cores.

The underlying differential equations of motion applied by the numerical propagator to describe the trajectory of a spacecraft flying through the Earth-Moon system are constructed from accelerations due to all significant forces acting upon the spacecraft in Earth and lunar spheres of influence.

These accelerations are central body gravitation $\ddot{r}_{CB}$, third-body gravitation $\ddot{r}_{TB}$, and the perturbing accelerations due to central-body non-spherical gravity $\ddot{r}_{NS}$, atmospheric drag $\ddot{r}_{AD}$, solar radiation pressure $\ddot{r}_{SR}$, relativistic correction $\ddot{r}_{RC}$, and spacecraft thrust $\ddot{r}_{ST}$ thus:

$$\ddot{r}_{spacecraft} = \ddot{r}_{CB} + \ddot{r}_{TB} + \ddot{r}_{NS} + \ddot{r}_{AD} + \ddot{r}_{SRP} + \ddot{r}_{RC} + \ddot{r}_{ST} \qquad (2.5)$$

The relative magnitudes of the various contributing accelerations are demonstrated by Montenbruck and Gill in *Satellite Orbits* chapter 3, figure 3.1 [14]. The precise formula of each acceleration as defined within the GMAT Mathematical Specification [15] is detailed in the following sections.
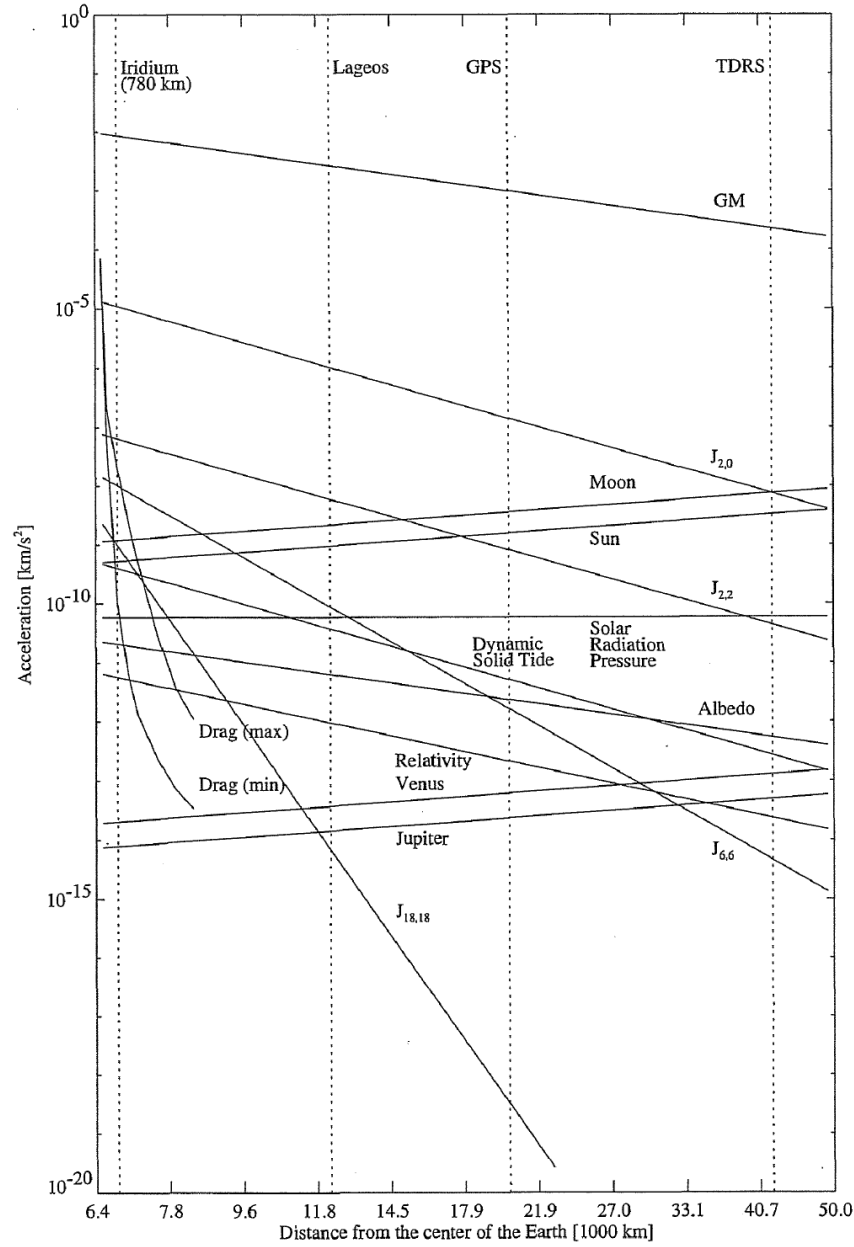
Figure 2.5: Relative acceleration of perturbing effects in Earth Orbit, *Satellite Orbits*, Figure 3.1 [14]

2.7   Central-Body and Third-Body Gravity

Each reference frame with which the spacecraft Cartesian state is defined originates at the centre of mass of the predominant gravity well. As a result, the instantaneous acceleration acting upon a spacecraft due to the gravitational attraction of planetary

48

bodies is purely a function of spacecraft and third body positions relative to the central body about which the reference frame is defined.

As detailed by Prussing and Conway in *Orbital Mechanics* section 1.3 [6], it is appropriate to represent each planetary body is a point mass under two conditions. Firstly, the spacecraft must always lie outside of the external sphere of all attracting planetary bodies. This condition is obviously met - no trajectory resulting in an impact event with Earth or Moon would be considered a particularly promising basis for a lunar mission. Secondly, the mass distribution within the planets must be spherically symmetric. This condition is perfectly valid for all planetary bodies beyond the Earth-Moon system. Given the extreme distance, the vectors between the spacecraft and the centers of multiple non-spherically symmetric mass concentrations inside the planet converge beyond any meaningful error. Earth and Moon are however, a different matter. As presented in figure 2.5, the perturbing effects of spherical asymmetry exert a significant influence when a spacecraft is in close proximity to a non-spherical planetary body. To account for this, these effects are managed as separate perturbations.

Thus, the assumption of point-mass gravity sources valid, and accelerations due to central and third body gravitation is derived from two of Newton's laws as set forth in *Principia Mathematica Philosophiae Naturalis*. These are the second law of motion, and the law of gravitation.

The second law of motion states that the external force applied to a body is equal the rate of change of the linear momentum of the body. Thus, per Prussing and Conway [6]:

$$\Sigma F_{external} = \frac{d}{dt}(m\bar{v})$$

$$= m\frac{d\bar{v}}{dt} \tag{2.6}$$

49

Newton's law of gravitation states that the force due to the gravitational attraction between two point-mass bodies is proportional to the product of their masses, inversely proportional to the square of their separation distance, and acts in the direction defined by the unit vector aiming from the first mass to the second. Thus, per Prussing and Conway [6]:

$$F_{gravity} = G\frac{m_1 m_2}{r^2}\frac{\bar{r}}{r} \tag{2.7}$$

where coefficient G is the empirically determined Constant of Gravitation:

$$G = 6.67259 \times 10^{-11} m^3 kg^{-1} s^{-2}$$

To determine the acceleration acting upon the spacecraft, equations 2.6 and 2.7 must be applied to the spacecraft (mass m_s), the central-body (mass m_j), and n third-bodies (mass m_k where $k = 1...n$) within an inertial frame. Consider the system in figure 2.6:
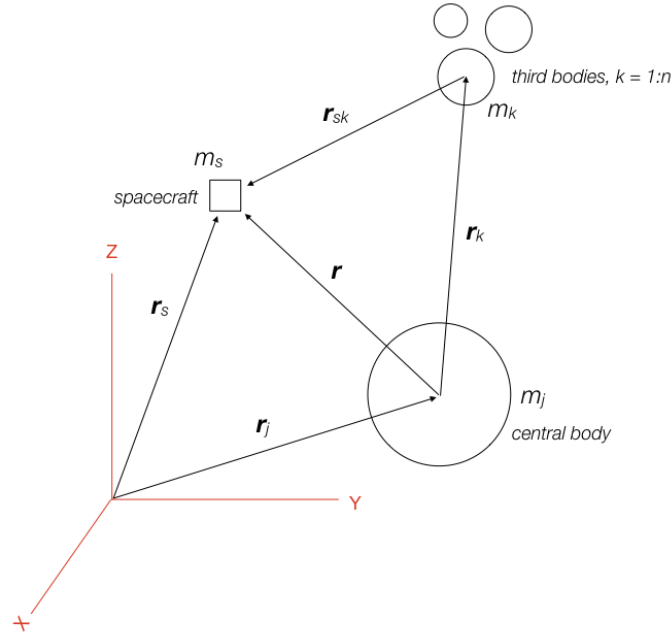
Figure 2.6: N-Body inertial reference frame

50

The position of the spacecraft relative to the central body is given by:

$$\bar{r} = \bar{r}_s - \bar{r}_j \tag{2.8}$$

The second time derivative of equation 2.8 (refer to Prussing and Conway [6] for full derivation) provides the acceleration of the spacecraft with respect to the central body expressed in terms of spacecraft and central-body inertial accelerations.

$$\ddot{\bar{r}} = \ddot{\bar{r}}_s - \ddot{\bar{r}}_j \tag{2.9}$$

Solving equation 2.9 requires expressions for $\ddot{\bar{r}}_s$ and $\ddot{\bar{r}}_j$. These terms are obtained by applying Newton's Second Law of Motion and Law of Gravitation. Applying 2.6 and 2.7 to the spacecraft inertial acceleration $\ddot{\bar{r}}_s$ yields:

$$m_s \ddot{\bar{r}}_s = \sum F_{s,external}$$

$$= G \frac{m_s m_j}{r^3} \bar{r} + \sum_{k=1}^{n} G \frac{m_s m_k}{r_{sk}^3} \bar{r_{sk}}$$

$$= G \frac{m_s m_j}{r^3} \bar{r} + G \sum_{k=1}^{n} \frac{m_s m_k}{|r_k - r|^3} (\bar{r}_k - \bar{r})$$

$$\ddot{\bar{r}}_s = G \frac{m_j}{r^3} \bar{r} + G \sum_{k=1}^{n} \frac{m_k}{|r_k - r|^3} (\bar{r}_k - \bar{r}) \tag{2.10}$$

Similarly, applying 2.6 and 2.7 to the central body inertial acceleration $\ddot{\bar{r}}_j$ yields:

$$m_j \ddot{\bar{r}}_j = \sum F_{j,external}$$

$$= G\frac{m_j m_s}{r^3}\bar{r} + \sum_{k=1}^{n} G\frac{m_j m_k}{r_k^3}\bar{r}_k$$

$$\ddot{\bar{r}}_j = G\frac{m_s}{r^3}\bar{r} + G\sum_{k=1}^{n} \frac{m_k}{|r_k|^3}(\bar{r}_k) \tag{2.11}$$

Substituting equations 2.10 and 2.11 into 2.9, yields:

$$\ddot{\bar{r}} = G\frac{m_j}{r^3}\bar{r} + G\sum_{k=1}^{n} \frac{m_k}{|r_k - r|^3}(\bar{r}_k - \bar{r}) - G\frac{m_s}{r^3}\bar{r} - G\sum_{k=1}^{n} \frac{m_k}{|r_k|^3}\bar{r}_k$$

By simplification, we arrive at the n-body equation of motion:

$$\ddot{\bar{r}} = -\frac{\mu}{r^3}\bar{r} + G\sum_{k=1}^{n} \left(\frac{\bar{r}_k - \bar{r}}{|r_k - r|^3} - \frac{\bar{r}_k}{|r_k|^3} \right) \tag{2.12}$$

where $\mu = G(m_s + m_j)$. Thus, we have terms for accelerations acting upon the spacecraft from central body gravitation:

$$\ddot{\bar{r}}_{CB} = -\frac{\mu}{r^3}\bar{r} \tag{2.13}$$

and third-body gravitation:

$$\ddot{\bar{r}}_{TB} = G\sum_{k=1}^{n} \left(\frac{\bar{r}_k - \bar{r}}{|r_k - r|^3} - \frac{\bar{r}_k}{|r_k|^3} \right) \tag{2.14}$$

It can be observed in figure 2.5 that perturbing accelerations due to third-body gravitation is low in comparison to central-body, atmospheric drag and non-spherical gravity whist in LEO. However, as altitude increases, these Earth-based perturbations decline whilst third-body acceleration steadily increases. Given the approximately 400,000 km Earth-Moon distance, third-body gravitation represents the primary acceleration after central-body gravitation for much of the trans-lunar trajectory once the spacecraft departs LEO and enters translunar space.

Planetary positions at each analysis epoch are generated from JPL's Planetary and Lunar Development Ephemeris 405 (DE405). This ephemeris is provided with the GMAT source code through the NASA SPICE binary file *DE405AllPlanets.bsp*. The JPL ephmerides are sets of Chebyshev polynomials fit to planetary Cartesian states at fixed time steps. The polynomials are derived from integrating the n-body equations of motion for all planetary bodies in the solar system with corrections to fit observation data from laser ranging of the moon, radar ranging of the inner planets and select asteroids and DSN satellite ranging to deep space probes and orbital spacecraft. It is noted by Standish in the JPL Planetary and Lunar Ephemerides, DE405/LE405 Memorandum that "the ephemerides of the four innermost planets along with the moon and the sun are all well-known with respect to each other because of the accurate ranging observations to which the ephemerides are adjusted" [16]. It is pertinent to note that the Moon in particular is very well defined due to accurate and frequent laser ranging made possible by reflectors at the Apollo landing sites. The accuracy of DE405 for inner planets is considered 0.001 arcseconds, which was verified "by the arrival of the Pathfinder Spacecraft at Mars in July 1997, where the ephemeris error was about 0.001 arcseconds, corresponding to 1 km at that distance" [16]. The outer planets are considered less accurate due to the reliance on optical measurements for range and range rate measurements, however, given the extreme distance between the outer planets and the Earth-Moon system, even large positional errors of hundreds of thousands of kilometers for Jupiter and Saturn have a negligible effect on the spacecraft-to-planet relative position vector and thus, the resulting acceleration.

2.7.1 Non-Spherical Gravity

In the previous section, the n-body equations of motion was derived to describe pure Keplerian motion without perturbing effects. It was assumed that all bodies

within the system were spherically symmetric. Physically, this means that the gravitational pull of each body must be accurately represented by a single mass acting at a point source. In reality, the non-spherical shape of Earth causes significant perturbations on the motion of spacecraft in Earth orbit as demonstrated by the multiple J term accelerations in figure 2.5. The magnitude of this perturbation is driven by the geodetic position and altitude of the spacecraft, and a geopotential model that accurately describes the mass distribution of the planet, including equatorial bulge, polar contraction, mountains, and oceans.

To handle non-spherical gravity, one must define the inertial acceleration induced by a planet as the gradient of the gravitational potential U, that describes the planet's distribution of mass [15]:

$$\ddot{\bar{r}} = \nabla U \tag{2.15}$$

This gravitational potential for an arbitrary mass distribution is expressed as the sum of individual mass elements that make up a planet [14]:

$$U = G \int \frac{\rho(s) d^3 \bar{s}}{|\bar{r} - \bar{s}|} \tag{2.16}$$

where $\bar{s}$ is the vector between the planets center of mass and a contributing mass element, $\rho(s)$ is the element density, $|\bar{r} - \bar{s}|$ is the distance between the element and the spacecraft.

This expression can be expanded using spherical harmonics to describe gravitational potential as a distribution over the surface of a sphere. This is achieved by representing equation 2.16 as a summation of Legendre polynomials on a spherical basis. First, one defines the conversion between Cartesian and spherical coordi-

nates:

$$x = r \cos \phi \cos \lambda$$

$$y = r \cos \phi \sin \lambda \qquad (2.17)$$

$$z = \sin \phi$$

where ϕ is latitude (positive north), λ is longitude (positive east), and r is range from the planets center of mass:

$$r = \sqrt{(x^2 + y^2 + z^2)}$$

As presented by Pines in *A Uniform Representation of Gravitational Potential and its Derivatives* [17], gravitational potential may be expressed in spherical terms of ϕ, λ, and r through the spherical harmonic expression:

$$U = \frac{\mu}{r} \left(1 + \sum_{n=1}^{\infty} \left(\frac{R}{r} \right)^n \sum_{m=1}^{n} P_{nm}(sin\phi)(C_{nm} \cos m\lambda + S_{nm} \sin m\lambda) \right) \qquad (2.18)$$

where μ and R are the gravitational parameter and radius of the central planet, P_{nm} are the Legendre polynomials of degree n, order m. C_{nm} and S_{nm} are the corresponding empirically derived gravitational coefficients that describe the mass distribution of the planet, representing the density term $\rho(s)$ in equation 2.16.

The Legendre polynomials are defined by Rodrigues' formula in Lundberg's *Recursion Formulas of Legendre Functions for Use with Nonsingular Geopotential*

55

Models [18]:

$$P_{n0}(u) = P_n(u) = \frac{1}{2^n n!} \frac{d^n}{du^n} (u^2 - 1)^n \tag{2.19}$$

$$P_{nm}(u) = (1 - u^2)^{m/2} \frac{d^m}{du^m} P_n(u) \tag{2.20}$$

The partial derivatives of the gravitational potential must be taken to determine the gravity gradient. In the form of equation 2.18, the partial derivatives yield a singularity at zero degree latitudes. Thus, a spacecraft positioned directly over a pole has an undefined gravitational potential. To correct this, GMAT adopts Pines' expression for gravitational potential [17]. This method applies a new basis of modified Cartesian terms:

$$s = \frac{x}{r} \qquad t = \frac{y}{r} \qquad u = \frac{z}{r} = sin(\phi)$$

By substituting trigonometric terms $\sin m\lambda$ and $\cos m\lambda$ for real and and imaginary terms $r_m(s,t)$ and $i_m(s,t)$, Pines converts equation 2.18 to [17]:

$$U = \frac{\mu}{r} \left(1 + \sum_{n=1}^{\infty} \left(\frac{R}{r} \right)^n \sum_{m=1}^{n} A_{nm}(u) |C_{nm} r_m(s,t) + S_{nm} i_m(s,t)| \right) \tag{2.21}$$

where $A_{nm}(u)$ is the derived Legendre function - the mth derivative of the degree n Legendre polynomial of variable $u = \sin(\phi)$ [17]:

$$A_{nm}(u) = \frac{d^m}{du^m} (P_n(u)) = \frac{1}{2^n n!} \frac{d^{n+m}}{du^{n+m}} (u^2 - 1)^n \tag{2.22}$$

Continuing with Pines' uniform method, GMAT applies recursive formulas to

compute the real and imaginary positional terms $r_m(s, t)$ and $i_m(s, t)$ [17]:

$$r_0 = 1 \qquad\qquad i_0 = 1$$

$$r_1 = s \qquad\qquad i_1 = s$$

$$r_m = sr_{m-1} - ti_{m-1} \qquad\qquad i_m = si_{m-1} + tr_{m-1}$$

For numerical stability, the mass coefficients C_{nm} and S_{nm} and Legendre function A_{nm} are normalized, thus preventing inaccuracies due to poorly scaled coefficient arrays. GMAT employs the normalization function N_{nm} [15]:

$$N_{nm} = \left[\frac{(n-m)!\,(2n+1)!}{(n+m)!} \right]^{1/2} \tag{2.23}$$

to compute the normalized spherical harmonic harmonic coefficients $\bar{C}_{nm}$ and $\bar{S}_{nm}$ [15]:

$$\bar{C}_{nm} = \frac{C_{nm}}{N_{nm}} \qquad\qquad \bar{S}_{nm} = \frac{S_{nm}}{N_{nm}} \tag{2.24}$$

Likewise, the derived Legendre function is normalized by:

$$\bar{A}_{nm} = N_{nm} A_{nm} \tag{2.25}$$

Like the r_m and i_m terms, $\bar{A}_{nm}$ can be computed through the use of recursive formulas. GMAT initializes these recursions with the diagonal terms $\bar{A}_{11}$ and $\bar{A}_{nn}$:

$$\bar{A}_{11} = \sqrt{3}\cos(\phi) \tag{2.26}$$

$$\bar{A}_{nn} = \cos\phi \sqrt{\frac{2n+1}{2n}} \bar{A}_{n-1,n-1} \tag{2.27}$$

The remaining non-diagonal terms can then be found via the recursive formula [15]:

$$\bar{A}_{nm} = u \left[\frac{(2n+1)(2n-1)}{(n-m)(n+m)} \right]^{1/2} \bar{A}_{n-1,m}$$
$$- \left[\frac{(2n+1)(n-m-1)(n+m-1)}{(2n-3)(n+m)(n-m)} \right]^{1/2} \bar{A}_{n-2,m} \qquad (2.28)$$

With elements of equation 2.21 now defined and normalized, accelerations may now be derived through its partial derivatives.

2.7.2   Atmospheric Drag

As demonstrated in figure 2.5, atmospheric drag acts as the dominant perturbation for orbital altitudes below 200km. Though drag reduces exponentially with altitude as the atmosphere thins, it continues to have a measurable impact on an orbiting space craft throughout LEO altitudes up to 1000km.

Acceleration due to drag acts in the direction opposite to the spacecraft velocity relative to the atmosphere. Thus, this acceleration always acts to slow the spacecraft, and is defined by:

$$\ddot{\vec{r}}_{AD} = -\frac{1}{2} \rho v_{relative}^2 \frac{C_D A_D}{m_s} \hat{v}_{relative} \qquad (2.29)$$

where ρ is the atmospheric density at the current altitude, C_D is the aerodynamic drag coefficient describing the interaction of the atmosphere with the spacecraft materials, m_s is the spacecraft mass, and A_D is the cross sectional area normal to the velocity relative to atmosphere $v_{relative}$. This cross sectional area is considered constant - a valid assumption for a spacecraft whose orientation is maintained by an active attitude control system.

$v_{relative}$ requires that spacecraft velocity be converted from the inertial frame,

to the Earth fixed frame to define its flight through a "still" atmosphere, with a correction then applied for local wind speed. It is assumed that the atmosphere rotates with Earth

$$v_{relative} = v - \omega_E \times r + v_w \tag{2.30}$$

where v is the spacecraft velocity in the intertial frame, $\omega_E = 0.729 \times 10^{-4} rads^{-1}$ is the angular velocity of Earth's rotation, r is the orbital radius, and v_w is the local wind-speed. Note that for the altitudes studied herein, the low atmospheric density and the extreme velocity of the spacecraft when compared to wind speed, the v_w term is negligible.

The atmospheric density as applied in equation 2.29 is a complex function of altitude, temperature, and atmospheric dynamics. As altitude increases, the density of atmospheric constituents naturally decreases, though this occurs at different rates. At various strata throughout the Homosphere, Thermosphere, and Exosphere, the atmosphere transitions from a turbulent mix of constituents, to nitrogen dominant, molecular oxygen dominant, then molecular hydrogen dominant states.

These density strata are not, however, driven by altitude alone. Temperature has a significant effect on atmospheric density, and is itself a function of many parameters, typically ranging between 200K and 2000K. The sun is the cause of variation in atmospheric temperature. As described by Montenbruck and Gill [14], there are three primary effects of solar radiation on the upper atmosphere. First, the diurnal exposure to solar ultraviolet radiative heating [14] produces a day-night density cycle. Due to Earth's obliquity, these densities are a function of time, and geographic latitude. Second, is heating due to extreme ultraviolet radiation [14]. Essentially, this is a cyclical variation in radiation magnitude described by a 27 day short-term cycle driven by the rotation of the Sun, and an 11 year long-term cycle driven by Sun spot fluctuations. The third solar influence comes in the form of solar

wind [14]. Waves of solar particles collide with molecules in the upper atmosphere and Earth's magnetic field. The resulting geomagnetic storms have been observed to alter temperature and total upper atmospheric density for multiple days.

The dependencies of atmospheric density upon a multitude of parameters make it notoriously difficult to model, and current methods rely on thermodynamic modelling augmented by empirical measurements of satellite orbital decay through the upper atmosphere. Jacchia 1971 is widely used in literature after its adoption by the Committee on Space Research as the International Reference Atmosphere [14]. This model is based on an analytical model for density as a function of temperature and altitude (originally Jacchia 1965), improved through analysis of real-world satellite orbital decay through the upper atmosphere.

The Jacchia-Roberts model is a further development. As described by Montenbruck and Gill [14], this variant uses the Jacchia 1971 equations for altitudes between 90 km and 125 km. Above 125km, a different temperature model is applied such that the underlying equations can be integrated analytically. This approach eases computational demand through a closed form solution that avoids the need for numerical integration between each propagation step or large coefficient arrays, whilst agreeing closely with the original yet computationally expensive Jacchia 1971. Due to the industry validation of Jacchia 1971 and the performance of the Roberts variation, Jacchia-Roberts has been selected for implementation within GMAT as the atmospheric density model for this analysis. The model is defined in full by Long et. al. [19].

2.7.3   Solar Radiation Pressure

Solar radiation pressures results from the transfer of momentum as the spacecraft is continually impacted by photons emitted from the sun in the form of stellar wind. As demonstrated in figure 2.5, the induced acceleration is in the order of 10^{-10} km/s

- significantly less than other perturbations in LEO. However, solar radiation pressure remains constant regardless of altitude, thus in translunar space, it eventually exerts a greater comparative influence than Earth non-spherical and atmospheric drag terms.

The acceleration always acts in the direction of the Sun-to-spacecraft vector $\bar{r}_{SRP} = \bar{r}_{sol} - \bar{r}_s$, provided the spacecraft is not eclipsed by Earth, Moon, Venus, or Mercury. The magnitude of the solar radiation pressure is a function of solar flux ϕ - a measure of energy passing through an area over a given time interval:

$$\phi = \frac{\Delta E}{A \Delta t} \tag{2.31}$$

The force exerted upon a spacecraft by this flux is [14]:

$$F_{SRP} = \frac{\Phi}{c} A_S \tag{2.32}$$

where c is the speed of light, and A_S is the projected spacecraft area normal to the solar flux. Per Montenbruck and Gill [14], solar flux at 1 AU from the sun is approximately constant at 1367 Wm^{-2}. The solar radiation pressure is therefore:

$$P_{SRP} = \frac{F_{SRP}}{A_S} = \frac{\Phi}{c} = 4.56 \times 10^{-6} \quad Nm^{-2} \tag{2.33}$$

Applying the above pressure term, the perturbation due to solar flux is characterized by:

$$\ddot{\bar{r}}_{SRP} = -P_{SRP} \frac{C_R A_S}{m_s} \hat{\bar{r}}_{SRP} \tag{2.34}$$

where m is the spacecraft mass and $\hat{\bar{r}}_{SRP}$ is the unitized Sun-spacecraft vector. C_R is this the radiation pressure coefficient equivalent to $1 + \epsilon$, where ϵ is the reflectively of the spacecraft surface, ranging from zero (completely absorbent) to one (completely reflective).

2.7.4 Relativistic Correction

In accordance with the theory of general relativity, the acceleration of a spacecraft is perturbed whilst in the vicinity of a planetary body. Unlike the other perturbing factors presented above, relativistic error manifests not through an applied force, but through a deviation in the passage of time as measured aboard the spacecraft, and at the geocenter of the local planetary body. This temporal dilation - whereby time passes more slowly for an observer closer to a gravity source - is induced by the curvature in four-dimensional space-time due to a planetary body's mass. For high precision orbit determination, a correction may be applied to spacecraft acceleration to account for such relativistic effects.

It is worth noting that errors due to general relativity are small. It may be observed in figure 2.5 that near Earth's surface, the perturbation in spacecraft acceleration due to relativity induced error is in the order of 10^{-10} km/s^2, and reduces linearly with altitude. This magnitude is lower than that of dynamic solid tide and albedo radiation perturbations, both of which are omitted due to their negligible effect on a trans lunar mission duration. However, GMAT allows the inclusion of an analytical relativistic correction term that requires no numerical integration between propagation steps or external coefficient arrays. Given that the inclusion of this term provides an increase in accuracy at little computational expense, the decision was made to include it with the force model.

Per the GMAT Mathematical Specification [15], relativistic correction is computed via:

$$\ddot{\bar{r}}_{RC} = \frac{\mu}{c^2 r^3} \left(\left(\left(4\frac{\mu}{r} - v^2 \right)\bar{r} + 4(\bar{r} \cdot \bar{v})\bar{v} \right) \right.$$

$$+ 2\left(\left(\frac{3}{2}\bar{v}_{CB/Sol} \times \left(\frac{-\mu\bar{r}_{CB/Sol}}{c^2 r_{CB/Sol}^3} \right) \right) \times \bar{v} \right)$$

$$\left. + 2\frac{\mu}{c^2 r^3} \left(\frac{3}{r^2}(\bar{r} \times \bar{v})(\bar{r} \cdot \bar{J}) + (\bar{v} \times \bar{J}) \right) \right) \qquad (2.35)$$

where c is the speed of light, μ and J are respectively the gravitational parameter and specific angular momentum of the central body, $\bar{r}$ and $\bar{v}$ are respectively the position and velocity of the spacecraft within the central body J2000 inertial coordinate frame, and $\bar{r}_{CB/Sol}$ and $\bar{v}_{CB/Sol}$ are respectively the position and velocity of the central body with respect to the sun.

The vector for central body specific angular momentum, J, is derived via:

$$\bar{J} = R_{CB}^{I/F} = \begin{bmatrix} 0 & 0 & \frac{2}{5}R_{CB}^2 \omega_{CB} \end{bmatrix} \qquad (2.36)$$

where R_{CB} is the central body equatorial axis, ω_{CB} is the central body angular velocity, and $R_{CB}^{I/F}$ is the rotation matrix for body-fixed to inertial frame transformations.

2.7.5 Spacecraft Thrust

Real-world thrusters exhibit a mass flow gradient once the propellant feed valves are opened as the engine ramps up from static, to full mass flow rate $\dot{m}$. Similarly, there is a gradient in the combustion chamber temperature from a cold start to a stable, sustained burn.

From *Space Mission Design and Analysis* by Larson and Wertz [20], specific impulse of a chemical rocket I_{sp} is proportional to the square root of the chamber

temperature $T_{chamber}$ and average molecular weight of the exhaust gases $M_{exhaust}$:

$$I_{sp} = K\sqrt{\frac{T_{chamber}}{M_{exhaust}}} \qquad (2.37)$$

The engine thrust is equivalent to the product of specific impulse and mass flow rate of propellant:

$$F_{thrust} = I_{sp}\dot{m}g \qquad (2.38)$$

Examining equations 2.37 and 2.38, it may be observed that variability in $T_{chamber}$ or $\dot{m}$ will result in variability in an engine's thrust and specific impulse. However, for the selected pressure regulated propellant system, the high pressure helium tank driving a 2.6 MPa feed pressure to the propellant tanks ensures a fast build up in mass flow rate to the engine (and subsequently combustion chamber temperature) such that any latency is in the order of seconds. This is comparatively short compared to the proposed TLI burn duration's (in the order of hundreds of seconds), and LOI burn duration's (in the order of tens of seconds).

Driving additional accuracy into engine performance would require a polynomial thrust profile reflecting detailed mass flow and temperature data from hot fire testing of the selected engine. Such an undertaking would be an unjustified complexity - the intent of the engine model is not to fully characterize a specific engine. Instead, it is to approximate a viable high-thrust chemical engine and capture the effects of finite burn maneuvers (and corresponding efficiency losses) on the overall performance.

Therefore, for the purpose of this analysis, spacecraft propulsion has been modelled as constant thrust, constant specific impulse. In practical terms, this is synonymous with an ideal high-thrust engine with a step change from "on" to "off", and no latency or variability in its mass flow rate or chamber temperature. Under this model, GMAT takes thrust force and I_{sp} parameters as constants whereby no

temperature or pressure dependencies need be computed [15].

With the full engine thrust magnitude considered active (and at full mass flow rate) for the full duration of each burn, the thrust scale factor f_s and duty cycle f_d are both at unity. The thrust vector is computed by [15]:

$$\bar{F}_{thrust} = f_s f_d F_{thrust} \bar{R} \hat{\bar{T}}$$
$$= F_{thrust} \bar{R} \hat{\bar{T}} \tag{2.39}$$

where $\bar{R}$ is the rotation matrix between spacecraft VNB and body-centered inertial frames, and $\hat{\bar{T}}$ is the spacecraft VNB frame thrust direction unit vector.

The total mass flow rate of fuel and oxidiser is thus:

$$\dot{m} = \frac{F_{thrust}}{I_{sp}g} \tag{2.40}$$

The acceleration induced by spacecraft thrust is a function of the thrust force, and mass. As a thrusting burn expends mass in the form of exhausted propellant, the mass term is time dependant throughout the burn duration of time t:

$$\ddot{\bar{r}}_{thrust} = \frac{1}{m_s(t)} F_{thrust} n \bar{R} \hat{T} \tag{2.41}$$

The time dependent spacecraft mass is a function of fixed mass m_{fixed}, and the consumable fuel mass m_f, and oxidizer mass m_o:

$$m_s(t) = m_{fixed} + m_f(t) + m_o(t) \tag{2.42}$$

The overall mass flow rate of consumables passing through the engine is computed in equation 2.40. This value may be discretized into fuel and oxidizer mass

flow rates using the oxidizer/fuel ratio o/f:

$$\dot{m} = \dot{m}_o + \dot{m}_f$$

$$\dot{m}_o = \frac{o/f}{1+o/f}\dot{m} \qquad (2.43)$$

$$\dot{m}_f = \frac{1}{1+o/f}\dot{m} \qquad (2.44)$$

As constant mass flow is assumed, the time dependent mass terms applied in equation 2.42 may be derived through a linear relationship. Combining mass flow rates from equations 2.43 and 2.44 with pre-burn masses $m_{f,0}$ and $m_{o,0}$, the fuel and propellant mass after burn duration t is derived via:

$$m_o(t) = m_o - \frac{o/f}{1+o/f}\dot{m}t \qquad (2.45)$$

$$m_f(t) = m_f - \frac{1}{1+o/f}\dot{m}t \qquad (2.46)$$

2.8 Numerical Propagators

Two propagators were constructed in GMAT to transition the spacecraft state forward and backward in time by numerically integrating the equations of motion - Near Earth Propagator (NEP) and Near Moon Propagator (NMP). The Ordinary Differential Equation solver used in the propagators was the Runge-Kutta 8th order integrator with 7th order error correction using the Prince and Dormand coefficients - the Prince Dormand 78 method for short. Prince Dormand was selected for its favourable computational accuracy for lunar trajectories when compared with 6 alternative integrators that may be applied within a GMAT simulation. In *Verifica-*

tion and Validation of the General Mission Analysis Tool (GMAT), Hughes et. al. apply a "loop test" by propagating 6 unique control case orbits (ISS LEO, Molniya, Lunar flyby, Mars transfer, and two finite burns) as defined in figure 2.7.

Orbit	Dynamics Model	Duration
LEO	Earth 20x20, Sun, Moon, MSISE90 density, SRP	1 day
Molniya	Earth 20x20, Sun, Moon, Jacchia Roberts, SRP	3 days
Mars Transfer	Near Earth: Earth 8x8, Sun, Moon, SRP Deep Space: All planets as point mass perturbations Near Mars: Mars 8x8 SRP	333 days
Lunar Transfer	Earth central body with all planets as point mass perturbations	5.8 days
Finite Burn (case 1 and 2)	Point mass gravity. (1) Blow down, (2) Pressure Regulated.	7200 sec.

Figure 2.7: GMAT integration test cases, *Verification and Validation of the General Mission Analysis Tool (GMAT)*, table 8 [13]

Each test case was propagated with all 7 available integrators, then back-propagated for the same number of time steps. The initial and final positions were then compared as a measure of accuracy. Though Prince Dormand 78 had the longest run time for the lunar flyby case, it also demonstrated the greatest accuracy with zero integration error to the mm level as shown in figure 2.8.

Orbit	Data	RKV89	RKN68	RK56	PD45	PD78	ABM
ISS	Run Time	1.53	**1.00**	2.14	2.78	1.46	3.41
	Error (m)	0.003	64.060	0.022	0.002	0.006	0.012
Molniya	Run Time	1.32	1.47	1.99	3.08	**1.00**	3.35
	Error (m)	0.007	0.601	0.059	0.032	0.043	380.125
Lunar Flyby	Run Time	**1.00**	1.01	2.26	2.98	2.21	3.30
	Error (m)	0.063	0.017	0.002	0.023	0.000	0.236
Mars Transfer	Run Time	1.02	1.04	1.14	1.40	**1.00**	3.07
	Error (m)	0.030	0.001	0.043	0.194	0.009	25.231
Finite burn 1	Run Time	1.27	**N/A**	1.24	1.26	**1.00**	1.45
	Error (m)	0.002	N/A	0.006	0.002	0.002	0.000
Finite burn 2	Run Time	1.03	**N/A**	1.18	1.31	**1.00**	1.54
	Error (m)	0.002	N/A	0.000	0.000	0.001	0.003

Figure 2.8: Comparison of GMAT integrator performance, *Verification and Validation of the General Mission Analysis Tool (GMAT)*, table 9 [13]

NEP and NMP are similar in architecture, with each applying the following

integration configuration:

- Integrator: Prince Dormand 78

- Min time step: 0

- Max time step: 86400

- Accuracy: 10^{-12}

The force model applied by each propagator was driven by the configuration of the equations of motion. Both NEP and NMP applied the following common elements:

- Third body gravitation from the Sun , Venus, Mars, Jupiter, and Saturn, $\ddot{\vec{r}}_{TB}$

- Solar radiation pressure, $\ddot{\vec{r}}_{SRP}$

- Relativistic correction, $\ddot{\vec{r}}_{RC}$

- Spacecraft thrust, $\ddot{\vec{r}}_{ST}$

In addition to these shared accelerations, the NEP propagator has the following unique elements:

- Central body gravitation from Earth, $\ddot{\vec{r}}_{CB,earth}$

- Third body gravitation from the Moon, $\ddot{\vec{r}}_{TB,moon}$

- Degree 10, order 10 gravitational harmonics with JGM3 coefficients, $\ddot{\vec{r}}_{NS,earth}$

- Atmospheric drag, $\ddot{\vec{r}}_{AD}$

Likewise, the NMP propagator has the following unique elements:

- Central body gravitation from the Moon, $\ddot{\vec{r}}_{CB,moon}$

- Third body gravitation from Earth, $\ddot{\vec{r}}_{TB,earth}$

- Degree 10, order 10 gravitational harmonics with LP165P coefficients, $\ddot{\vec{r}}_{NS,moon}$

The selected force models inherent to NEP and NMP have two notable sets of exclusions. First are JGM3 and LP165 geopotential spherical harmonics of degree and order greater than 10. The second are n-body gravitational acceleration from Mercury, Saturn, Uranus, Neptune, and Pluto. These exclusions were made to simplify the equations of motion and improve computational speed on the condition

that they did not significantly decrease accuracy on lunar mission time scales. To validate this assumption, a GMAT analysis was run to compare the "applied" force model (NEP) to a "complete" model of JGM3 degree and order 70, and all nine planets considered for n-body gravitation.

The analysis used the Prince Dormand 78 integrator to propagate identical spacecraft from an identical initial state and epoch, though acted upon by the two different force models. To best reflect the primary analysis, each spacecraft had a 41.5 kg dry mass, a constant 635 N thrust, 317 s specific impulse chemical thruster, and a 100 kg propellant load. The spacecraft was placed in a 400 km altitude, 28.5 degree inclination circular parking orbit with zero RAAN, TA, and AOP, at an epoch 01 Jan 2020 00:00:00.000 UTC. A boundary value solver was used to apply a finite burn, varying its duration until, at cut-off, each spacecraft would coast to an apogee of 400,000 km with a tolerance of 0.1 km - an approximation of lunar distance.

Below is presented the apogee radius, burn duration, residual propellant, and a positional deviation from the "complete" model solution.

Table 2.2: Force model comparison

Parameter	Complete Model	Applied Model
Apogee radius [km]	399999.950717	399999.998886
Burn duration [s]	437.587372	437.587394
Residual propellant [kg]	10.646774	10.646769
Δ x	0	0.073723
Δ y	0	0.400397
Δ z	0	0.190650
Normalized Δ	0	0.449556

As evidenced by these results, the final spacecraft positions deviate by 449.56 m between the complete and applied force models after a 5 day, 6 hour, 58 minute flight time. This is equivalent to a 0.0002% deviation in lunar orbital radius upon arrival at the nominal 100km perilune altitude. Burn duration's differ by 0.00002 s, resulting in a negligible deviation in efficiency loss during the finite burn maneuver.

The residual propellant masses differ by 0.000004 kg, resulting in negligible deviation the spacecraft mass during the propagation. The comparative computation times between applied and complete running on a quad-core Macbook were 2.7180 s and 4.2260 s - thus the applied model offered a 40% reduction. For an analysis with hundreds of thousands of runs required to cover all combinations of input parameters, it was judged that the observed computational performance improvement justified the minor reduction in accuracy.

2.9 Solver

Each mission trajectory was constructed in stages using a differential correction solver. This numerical technique solves a boundary value problem in order to determine the specific control variables that satisfy defined arrival condition constraints for a given trajectory segment. The Newton-Raphson method was selected as the solver algorithm after several GMAT test runs demonstrated a more robust convergence than the Broyden and Modified Broyden alternatives. Furthermore, the Newton-Rapshon method demonstrates quadratic convergence when appropriate initial values are provided.

$$x_{i+1} = x_i + J_{y_i}(x_i)^{-1}y_i$$
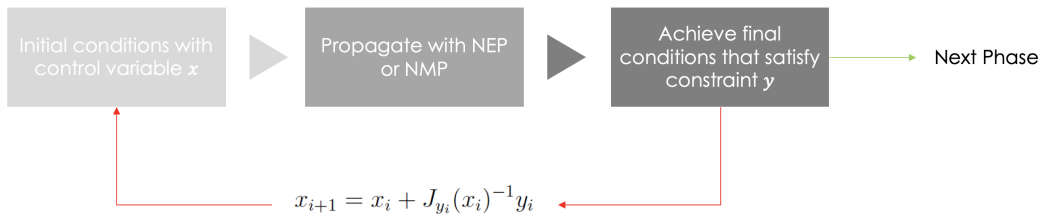
Figure 2.9: Newton-Raphson method differential correction

Where $x_{1..m}$ are control variables, $y_{1..n}$ are control variable dependent constraints placed upon a certain arrival conditions. Thus $y_1 = f_1(x_{1..m})$, $y_2 = f_2(x_{1..m})$,

... , $y_n = f_n(x_{1..m})$. Expressed in matrix form:

$$x = \begin{bmatrix} x_1 \\ x_2 \\ \vdots \\ x_m \end{bmatrix}, \qquad y = \begin{bmatrix} y_1 \\ y_2 \\ \vdots \\ y_n \end{bmatrix} = \begin{bmatrix} f_1(x_{1..m}) \\ f_2(x_{1..m}) \\ \vdots \\ f_n(x_{1..m}) \end{bmatrix} \tag{2.47}$$

The Newton-Raphson method computes the partial derivatives of y with respect to x via forward finite differencing with a defined control variable perturbation Δx:

$$\frac{\partial y_1}{\partial x_1} = \frac{y_1(x_1 + \Delta x_1) - y_1(x_1)}{\Delta x_1} \tag{2.48}$$

Thus, the algorithm may compute the Jacobian matrix of the control variables and constraints:

$$J_y(x) = \begin{bmatrix} \frac{\partial y_1}{\partial x_1} & \frac{\partial y_1}{\partial x_2} & \cdots & \frac{\partial y_1}{\partial x_m} \\ \frac{\partial y_2}{\partial x_1} & \frac{\partial y_2}{\partial x_2} & \cdots & \frac{\partial y_2}{\partial x_m} \\ \vdots & \vdots & \ddots & \vdots \\ \frac{\partial y_n}{\partial x_1} & \frac{\partial y_n}{\partial x_2} & \cdots & \frac{\partial y_n}{\partial x_m} \end{bmatrix} \tag{2.49}$$

For the remainder of section 2.9, numerical subscripts refer to Newton-Raphson iteration.

By generating a Jacobian in this fashion, the Newton-Raphson method performs a series of iterations until converging upon a set of control variables that meet the constraints targeted by the solver. Given control variables x_i (for iteration i) and perturbation Δx, finite differencing is applied to generate a new estimate, x_{i+1}, via:

$$x_{i+1} = x_i + J_{y_i}(x_i)^{-1} y_i \tag{2.50}$$

The solver is initialized by defining:

– Constraint targets y^*

71

- Constraint tolerances Δy_{max}

- Control variable initial values x_0

- Control variable perturbation Δx

- Control variable upper limit x_{upper}

- Control variable lower limit x_{lower}

- Solver maximum step-size x_{max}

Once these attributes are chosen, the solver will run through the following control loop:

1. Using the initial control variable (eg. duration of TLI burn and true anomaly in Earth parking orbit), propagate the spacecraft from the departure point using the appropriate NEP or NMP propagator until the targeted arrival condition is met (eg. arrival at perilune), or a time limit is reached.

    - Input: x_0

    - Output: $y_0 = f(x_0)$

2. Returning to the departure point, adjust the control variables by the perturbation. This becomes the control variable for iteration $i = 1$.

    - Input: x_0, Δx

    - Output: $x_1 = x_0 + \Delta x$

3. Propagate spacecraft for a set duration, or until the targeted arrival condition is met (eg. arrival at perilune). GMAT computes constraint value at final spacecraft location (eg. deviation from a targeted 100 km perilune), and applies the finite difference method to compute the Jacobian.

    - Input: x_1, y^*

    - Output: $y_1 = f(x_1)$, $J_{y_1}(x_1)$

4. Achieve convergence criteria;

    (a) If the constraint falls within tolerance of its specified target (eg. +/- 1 km from a targeted 100 km perilune), the current estimates for control

72

variables are output as solutions:

    – Input: y_1, Δy_{max}

    – Output: x

(b) If the constraint does not meet tolerance, the Newton-Raphson method is applied, using the constraint value and Jacobian to generate a new estimate for the control variables. The entire control loop is repeated until either convergence or the maximum number of iterations is reached.

    – Input: y_1, Δy_{max}, $J_{y_1}(x_1)$

    – Output: x_{i+1}

Due to quadratic convergence, the differential correction solver can build trajectories faster than an optimizer, however, convergence using the Newton-Raphson method relies upon sound initial values for the control variables. In the example given above, the control parameters are TLI burn duration and parking orbit true anomaly, whilst the targeted arrival condition is a perilune altitude of 100 km with a +/- 1 km tolerance constraint. For the burn to be optimal, it must occur slightly ahead of the perigee of a near-Hohmann transfer ellipse between Earth and moon. Thus the initial true anomaly estimate must place the spacecraft close to this point in Earth parking orbit. Similarly, for the TLI burn to accurately reach a 100 km perilune approximately 400,000 km away (a very tight target) its duration must be initialized to provide a Δv closely matching the true value for any hope of convergence.

Furthermore, the initial burn duration must be placed slightly below the duration required to reach the targeted arrival. This ensures the solver gradually increases the burn duration control variable, bound by the maximum iterative step size, until converging at the lowest viable value, the solution corresponding to minimum propellant consumption.

This example highlights the need for intelligent initial estimates. Without robust

inputs, the solver will not converge, or will converge onto a sub-optimal solution. To ensure robust performance, a succession of solver loops were applied in the design of maneuvers. The initial loop allows broad variation in limited input parameters with a coarse constraint tolerance. Each loop progressively tightens this tolerance and introduces more input parameters to build initial conditions for the next, more accurate loop.

2.10   Spacecraft Model

The equations of motion detailed in the sections above draw upon several spacecraft driven parameters, namely:

- Spacecraft mass, m_s
- Fixed mass, m_{fixed}
- Fuel mass, m_f
- Oxidizer mass, m_o
- Drag area, A_D
- Drag coefficient, C_D
- Solar flux area, A_D
- Solar radiation pressure coefficient, C_S
- Thrust force, F_{thrust}
- Specific impulse, I_{sp}

In order to quantify these performance and mass characteristics, it was necessary to make a series of estimates based upon a basic systems level design of a TLI stage. This section details that design process, cataloguing the underlying assumptions and sources for component characteristics.

Recognizing that navigation, communication, power, and environmental endurance are non-trivial factors beyond LEO, the design of the TLI stage assumes a "baseline" mission model that employs direct lunar transfer and orbit insertion with

single burns at optimal locations. This architecture, discussed in chapter 1, ensures faster transfer times to maximize scientific return and minimize passage through the Van Allen belts.

This model provides a robust upper bound for propellant demand for a given payload departing on a given epoch to a given lunar arrival condition. If a long flight times and multiple Van Allen belt passages are considered viable for a certain mission, designers may use this result as a starting point for further optimization with mission specific parameters. Propellant mass may be further reduced with the introduction of multiple phasing loops that minimize inefficiency due to the Oberth Effect during TLI and LOI burns.

The assumptions of this baseline model are summarized in table 2.3 and provide design guidance for the TLI stage.

Table 2.3: Baseline mission assumptions

	Flyby	Orbit Insertion	Landing
Form factor compatible with contemporary commercial launcher fairings	x	x	x
Self contained TLI capability from circular parking orbit	x	x	x
Storeable, hypergolic, bipropellant with proven flight heritage	x	x	x
Thrust always applied along spacecraft longitudinal axis	x	x	x
Single burn TLI maneuver directly to perilune	x	x	x
Single burn LOI maneuver directly to a circular parking orbit		x	x
Constant thrust descent and landing maneuvers			x

To size the spacecraft envelope, fairing sizes for current or soon to be available cost-competitive commercial launch vehicles were used as a benchmark. The

FAA's 2018 Annual Compendium of Commericial Space Transportation[21] details specifications for commercial US launchers compatible with KSC operations. The launch vehicles detailed below are currently available, or are in production for flight testing by 2020. Vehicles exclusive to government or military customers are excluded.

Table 2.4: Kennedy Space Center compatible launch vehicles

Launch Vechicle	Company	Fairing diameter [m]	Fairing Length [m]
New Glenn	Blue Origin	7	Undisclosed
Falcon 9	Space X	5.2	13.2
Alpha	Firefly	2	5
Minotaur C	Orbital ATK	1.6	2.2
Launcher One	Virgin Orbit	1.4	3.6
Pegasus XL	Orbital ATK	1.2	2.1
Electron	Rocket Lab	1.2	2

The most compact envelope of 1.2 x 2 m was selected as an upper envelope limit to ensure compatibility across the full range of viable near-term launch options.

A storeable, hypergolic, bi-propellant engine has been selected as the propulsion architecture for its proven heritage aboard missions with long durations and requirements for multiple burns. The technology began in the Apollo era with Aerozine 50/Nitrogen Tetroxide used as the fuel/oxidizer combination for the Command and Service Module and Lunar Module main engines and RCS thrusters. The technology has since developed into a mature system with significantly greater performance than TRL 9 monopropellant, hot gas, and cold gas alternatives, whilst offering greater long duration operability than cryogenics.

Of particular applicability to lunar mission architectures is the Leros engine developed in England by Royal Ordnance. The Leros line has successfully flown multiple interplanetary missions, including NASA's NEAR Shoemaker, Mars Global Surveyor, Mercury MESSENGER, and Juno. It has also achieved TLI and LOI for

SpaceIL's Beresheet lunar lander.

The 635 N thrust, 317 s specific impulse Leros 1B Hydrazine/Mixed Oxides of Nitrogen (MMO) engine [22] was used as the model for spacecraft propulsion for this analysis. This selection was based on multiple favourable characteristics. First, through a simple GMAT validation, its thrust performance proved capable of performing a single TLI burn from a 400 km parking orbit given a mission mass of 490.50 kg (the maximum mission mass for the spacecraft configuration defined in this section) with propellant remaining for LOI and landing.

Second, the engine line has a proven track record in deep space (Juno, Mercury MESSENGER - Leros 1B) and lunar (Beresheet - Leros 2B) applications, making it a feasible, well-tested option for lunar mission designers using this study to scope a preliminary TLI stage.

Third, the engine can accomodate long burn durations and multiple restarts - both crucial factors for a translunar mission. Leros 1B has achieved a 3,426 s maximum single burn, 6,797 s cumulative burn duration, and 18 restarts through trajectory correction and momentum dumping maneuvers throughout the MESSENGER mission [23].

Fourth, the 635 N Leros 1B mass is only slightly higher than the 4.3 kg, 458 N Leros 1C alternative. Though 458 N may indeed offer sufficient thrust for the 0 - 24kg payload range, without significant mass or volumetric penalties, the higher thrust option was preferred.

Based on the Leros 1B, the TLI stage main engine characteristics are:

– Thrust = 635 N [22]

– Specific impulse = 317 s [22]

– O/F ratio = 0.541:0.459 [22]

– Max restarts = 18

– Max single burn duration = 3,426 s [23]

– Max single cumulative burn duration = 6,797 s [23]

The choice of a hydrazine is another baseline assumption that may be further optimized by mission designers. As demonstrated in chapter 1 - safer, green propellants may soon offer higher I_{sp} than hydrazine. A designer may therefore consider hydrazine a conservative approximation, and later apply the improved performance characteristics of a green engine system as the technology matures to TRL 9 status.

The spacecraft was configured following the mission design architecture laid forth by Wiley and Wertz[20]. The vehicle was discretized into subsystems as follows:

Propulsion
- Main Engine
- Fuel tank
- Oxidizer tank
- Press. tanks
- Lines, valves, regulators

GNC
- Inertial measurement unit
- Star tracker
- Processor

CDH
- Command unit

Spacecraft

ADCS
- Control actuators

Communications
- Antenna
- Transceiver

Power
- Solar panel array
- Batteries
- Controller
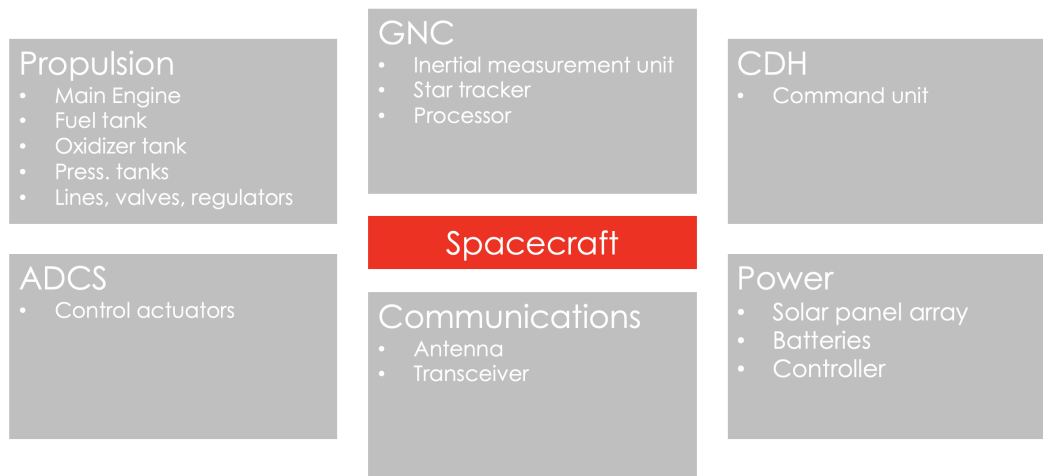
Figure 2.10: TLI stage subsystems architecture

The propulsive elements - most notably the propellant storage and management hardware - are the primary driver of mass on the vehicle. As previously described, the Leros-1B hydrazine/MON thruster was selected as the main engine.

The propulsive architecture was based upon NASA's Mercury MESSENGER spacecraft. MESSENGER was a successful Discovery Class science mission to Mercury orbit. The core architecture was an interplanetary vehicle consisting a Leros-1B main engine with a pressure regulated propellant management system to feed the engine. Within this system, a small reservoir of pressurized helium supplies gas for injection into the propellant tanks. The helium maintains positive

internal pressure, forcing fuel and oxidizer into the combustion chamber of the main engine. The hypergolic nature of hydrazine and MON causes violent instantaneous combustion without the need for a catalyst.

An on-board attitude determination and control system (ADCS) maintains spacecraft thrust direction either directly aligned or opposed to the spacecraft velocity vector during burn phases. A cold gas ADCS propellant such as nitrogen was considered as an alternative for its low cost and complexity, but given a large reservoir of high energy density hydrazine on board, hot gas thrusters where selected to eliminate an additional nitrogen tank system. For inertial pointing control, a 12 thruster configuration was selected to provide 3-axis control (4 for pitch, 4 for roll, 4 for yaw). Given the shared propellant and lines, the ACDS thrusters were considered a part of the propulsion system for mass estimation.

Wiley et. al. [24] detail the mass and performance metrics of the MESSENGER propulsion system. The vehicle was designed to carry a large suite of scientific instruments for a long duration mission to orbit around Mercury. MESSENGER has a wet mass of 1130 kg and a propellant load of 600 kg[24]. Using the rocket equation, MESSENGER's Δv capacity can be computed assuming a Leros I_{sp} of 317 s.

$$\Delta v = gI_{sp}ln\frac{m_{wet}}{m_{wet} - m_{propellant}}$$
$$= 2.354km/s$$

Based on the Apollo 11 mission report[8], a direct approach lunar landing mission from an Earth parking orbit requires a Δv in the order of 6.269 km/s. To achieve this performance increase, significant improvements were required to MESSENGER's mass ratio. This was achieved by through a significantly lighter maximum payload mass (24 kg vs. MESSENGER's 47.2 kg [25]), tank design safety

margins commensurate with the reduced mission assurance requirments of a non-Discovery Class mission, reduced thermal and radiation shielding proportional to solar distance and mission life (including the exclusion of a large ceramic and titanium sunshade), body mounted solar panels, and the use of modern, low mass satellite subsystems.

For ease of design and validation, the lunar craft will adopt similar 200 l titanium oxidizer and fuel tanks to those used by MESSENGER, placed symmetrically about the spacecraft centerline (thrust direction) for mass balance. To fit within the defined envelope diameter of 1.2 m when positioned side by side, the radius of the propellant tanks will be restricted to 0.25 m. Per Wiley and Wertz[20], space grade Ti-6AI-4V Titanium alloy has the following mechanical properties:

Table 2.5: Ti-6AI-4V Titanium mechanical properties

Density ρ_{ti}	4.43×10^3 kg/m^3
Ultimate Tensile Strength $\sigma_{u,ti}$	900×10^3 N/m^2
Tensile Yield Strength $\sigma_{y,ti}$	830×10^3 N/m^2

Each tank consists of two hemispherical end caps and a cylindrical center section sized to achieve the tank volume of 0.2 m^3. With a tank radius limited to 0.25 m, the resulting tank height is 1.185 m. Wall thicknesses for the cylindrical and spherical sections were determined per Larson and Wertz [20] using the material stress relationships:

$$\sigma = \frac{pr}{t} \quad (cylindrical) \tag{2.51}$$

$$\sigma = \frac{pr}{2t} \quad (spherical) \tag{2.52}$$

The tank operating pressure p matches that of MESSENGER. From Wiley et al

[24], the maximum expected operating pressure was 2.24 MPa. In accordance with table 11-48 of Larson and Wertz [20], a design factor of safety of 25% was applied to the titanium yield strength, reflecting that all flight units would be hydrostatically proof tested. Thus, the tank wall thicknesses are computed using equations 2.51 and 2.52.

$$t_{tank,cyl} = 1.25 \frac{pr}{\sigma_{y,ti}} = 0.844mm$$

$$t_{tank,end} = 1.25 \frac{pr}{2\sigma_{y,ti}} = 0.422mm$$

These thicknesses can be directly compared to equivalent sections of the MESSENGER tanks[24] which were designed at 1 mm and 0.5 mm - a slight increase reflective of the more conservative design approach befitting a Discovery-Class mission. The wall thickness values was used to derive a total titanium volume $v_{tank,ti}$. As recommend by Larson and Wertz [20], a 30% factor was applied to the subsequent tank mass calculation to account for tank systems (lines, valves, regulators, attachment hardware etc). The resulting mass for each of the two propellant tanks was therefore:

$$m_{tank} = 1.3v_{tank,ti}\rho_{ti} = 7.127kg$$

The MESSENGER tanks are pressurized by a reservoir of gaseous helium stored at a maximum expected operating pressure of 25.55 MPa. The mass of helium required to maintain the propellant tanks at operating pressure is given by Larson and Wertz [20]:

$$m_{he} = \frac{p_{prop}v_{prop}}{RT_i} \left[\frac{k}{1 - \frac{p_h e}{p_i}} \right] \tag{2.53}$$

where p_{tank} and v_{tank} are the propellant tank pressure (2.24 MPa) and volume (0.2 m^3) respectively. R is the helium gas constant of 2077.3 J/(kg K) [20], T_i is the

initial gas temperature of 300 K[20], and k is the helium specific heat ratio of 1.67 [20]. p_{he} is the initial gas pressure of 25.55 MPa, and p_i is the instantaneous gas pressure - considered to be the propellant tank operating pressure. The pressurant helium mass was thus found to be 2.633 kg. The pressurant tank was considered a small, spherical, titanium design of radius 0.1 m placed atop the propellant tanks. With a supplementary systems factor of 20%, the pressurant tank mass m_{press} was computed to be 1.259 kg through the same method as detailed for the propellant tank masses.

The 4.1 kg Leros 1B [26] was allocated an additional 10% mass for attachment hardware bringing the total main engine mass estimate to 4.5 kg. Per Larson and Wertz table 10-12 [20], each of the 12 attitude control thrusters was estimated at 0.35 kg. The total mass of the spacecraft propulsion system was therefore considered:

$$m_{prop} = m_{engine} + 12m_{ADCS} + 2m_{tank} + m_{press} + m_{he} = 26.84 kg \qquad (2.54)$$

To guide the spacecraft along its nominal trajectory, and to achieve accurate inertial pointing control during main engine burns, the spacecraft required a GNC system for attitude determination with respect to the celestial field, and state propagation within a defined coordinate frame. Upon the guidance of Larson and Wertz, table 11-6 [20], this was achieved using a star tracker and inertial measurement unit (IMU). Accurate navigation was assumed to be possible with a Kalman filter using range and range rate measurements between Earth-based ground stations and the on board communications system. Control logic for the main engine and ADCS system will be run directly by the on board computer. The NASA *State of the Art Small Satellite Technology* report [5] was used to select modern, high performance instrumentation with optimized mass and form factors. A 0.185 kg ST-16RT2 star

tracker from Sinclair Interplanetary, and a 0.75 kg LN-200S fibre optic gyro were used to estimate the mass of the GNC subsystem:

$$m_{GNC} = m_{startracker} + m_{IMU} = 0.935 kg \quad (2.55)$$

Deep space communications typically require a high system mass given the need for large antenna arrays. This mass was limited by selection of JPL's 1.2 kg Iris V2 X-Band transceiver and 0.998 kg folding high-gain X-Band antenna[27]. This combination was optimized for deep space small satellite operations and offers proven performance after successful operation aboard NASA's 6U MarCO mission to Mars flyby. The system provides communications for navigation and telemetry in translunar space. The mass estimate for the communication system is therefore:

$$m_{comms} = m_{transceiver} + m_{antenna} = 2.198 kg \quad (2.56)$$

Attitude control, guidance, and navigation processing, as well as command and data handling functions are enabled by a space rated 0.130 kg AAC Sirus on board computer. For redundancy in the case of an SEU, two Sirius units (one primary, one back up) were considered in the command and data handling subsystem mass estimate:

$$m_{CDH} = 2m_{OBC} = 0.260 kg \quad (2.57)$$

The power system mass was a function of the spacecraft's power demand. Operational power for the propulsion system was drawn from Wiley's characterization of MESSENGER [24] (linearly interpolated for a two tank configuration), whilst power for subsystems selected from the SOASST report were sourced from supplier data. Total power P was derived as follows:

Solar arrays with storage batteries are a simple power system architecture with

Table 2.6: Spacecraft subsystem power demand

System	Power Draw [W]
Propellant tank heaters	41.06
Pressurant tank heater	10.10
Propellant line heaters	43.40
Main engine heater	16.00
Startracker	0.50
IMU	12.00
Transceiver	35.00
Antenna array	5.00
OBC's	2.60
Total Power	165.67

proven operational heritage. The NanoPower BPX Li-ion batteries were selected from the SOASST report [5] for a high energy density ρ_E of 154 Wh/kg. 29.5% - 30.7% efficiency SolAero XJT cells were chosen for the solar arrays. Like the X-Band antenna, these cells were flight proven in deep space aboard the MarCo mission, achieving a 72 W production from a 0.6 kg array mass. To ensure sufficient battery charge during passage through Earth or lunar eclipse, the battery capacity C was scoped to provide a full 165.67 W for two hours. Panels are considered fixed rather than articulating - a low mass design. Correct panel orientation can be maintained during trans lunar cruise by the ADCS system. From Larson and Wertz table 10-27 [20], the mass of the power control unit (PCU) required to regulate power distribution across the spacecraft can be estimated by 0.02 kg/W of the total power demand. Based on these assumptions, the mass of the power system was

derived:

$$C = 2P = 331.33Wh$$

$$m_{batteries} = \frac{C}{\rho_E} = 2.152kg$$

$$m_{array} = \frac{0.6}{72}P = 1.38kg$$

$$m_{PCU} = 0.02P = 3.313kg$$

$$m_{power} = m_{batteries} + m_{array} + m_{PCU}$$

$$= 6.845kg \tag{2.58}$$

In accordance with Larson and Wertz table 10-10 [20], an additional allowance for structural mass may be estimated as 8% to 12% of the overall subsystems mass. The mean value of 10% was assumed, which encompasses a small aluminium vault for the avionics, and landing skids capable of withstanding a soft touchdown with minimal residual propellant mass at lunar surface gravity. Finally, from Larson and Wertz table 10-27 [20], the electrical harness must be assumed as 1% to 4% of the vehicle. Given the simplicity of the electrical systems onboard, the harness mass was assumed at to be 2%. With a maximum payload of 24 kg, spacecraft dry mass

could now be computed:

$$m_{subsystems} = m_{prop} + m_{GNC} + m_{comms} + m_{CDH} + m_{power}$$
$$= 37.084 kg$$

$$m_{structural} = 0.1 m_{subsystems}$$
$$= 3.708 kg$$

$$m_{harness} = 0.02(m_{subsystems} + m_{structural})$$
$$= 0.741 kg$$

$$m_{dry} = m_{subsystems} + m_{structural} + m_{harness} + m_{payload}$$
$$= 65.5 kg$$

By leveraging a lower payload mass, thin tanks, and state of the art subsystem components, the spacecraft dry mass has been kept to a minimum. The total stack height can be estimated by addition of the major volumetric components that must be longitudinally positioned. Assuming a 0.4 m vacuum optimized nozzle for the main engine, the derived tank height of 0.879 m, and a 0.3 m tall 12U cube sat payload, the total stack height is 1.679. With a total diameter of 1.2 m (driven by the tank radius), the spacecraft fits within the targeted 1.2 m x 2.0 m form factor.

The tank volume, propellant density and o/f ratio drives a maximum propellant mass of 425 kg. Therefore:

$$m_{wet} = m_{dry} + m_{prop} = 490.50 kg \qquad (2.59)$$

Thus, an estimate for potential Δv may be derived using the rocket equation:

$$\Delta v = gI_{sp}ln\frac{m_{wet}}{m_{dry}} = 6.261km/s \tag{2.60}$$

The spacecraft design yields a significantly higher Δv potential than MESSENGER, and is comparable to that of Apollo 11.

This completes the description of the design ethos and underlying assumptions used to generate the physical characteristics of the TLI stage for application to the mathematical model.

2.11 Summary of the Mathematical Architecture

The previous sections have defined the constituent parts of the mathematical architecture for this analysis. Atomic Time, Terrestrial Time, Coordinated Universal Time and the J2000 epoch provide a universal temporal reference point for defining events within a time varying celestial field of moving gravitational sources. The inertial, body-fixed, and body-relative reference frames allow the characterization of position and velocity in space.

The equations of motion accurately describe the dynamics acting upon a spacecraft during its passage through the Earth-Moon system. These dynamics encompass central body and non-spherical gravitation from Earth and Moon, n-body gravitation from the Sun, Venus, Mars, and Jupiter, atmospheric drag, solar radiation pressure, relativistic correction, and finite duration spacecraft thrust.

Earth and Moon centered propagators apply the equations of motion though the Runge-Kutta Prince Dormand 78 numerical integration method. This technique allows propagation of a spacecraft state over mission phases with respect to a reference frame centered upon a central body center of mass.

The Newtown-Raphson boundary value solver applies finite differencing to solve

input parameters necessary for a targeted end state after propagation. This solver will be used to build mission trajectories.

2.12 Trajectory Design Algorithm

The GMAT algorithm is one of the key innovations of this research. It was written to design direct translunar flyby, orbit insertion, and landing trajectories using the mathematical components demonstrated in the previous section. The complete algorithm is provided in appendix G, and provides a robust tool for the design of direct injection translunar trajectories based upon any compination of input parameters within the defined parameter space.

Each phase of this algorithm builds the initial conditions for the next, more accurate phase, until convergence to viable mission architecture. This method culminates in the design of translunar injection (TLI), lunar orbit insertion (LOI), inclination adjustment (IAB), perigee lowering (PL), circularization (C), deorbit (DO), braking (B), and landing (L) burns.

Note that due to the structuring of the NEP and NMP propagators, the problem is not broken into a piece-wise structure with spheres of influence centered around a single gravitational point source. Instead, all gravitational point sources are active for all phases of the trajectory, even when close to Earth or lunar surface. This method is computationally slower than a piece-wise approach, but provides greater accuracy and ensures no convergence failures at sphere of influence transitions. Sensitivities to lunar and solar gravity that are normally a concern at the sphere of influence boundary are already accounted for by the equations of motion.

The only differences between NEP and NMP are Earth atmosphere (included for NEP), and the gravitational harmonics model (Earth JGM3 for NEP, and Lunar LP165 for NMP). As the non-spherical lunar gravity components have minimal effect on an inbound arrival trajectory, the switch between NEP and NMP occurs at

lunar periapsis (perilune) arrival. Therefore, the lunar gravitational harmonics are included through lunar orbit and landing phases.

The following section provides an overview of the algorithm.

2.12.1 Phase 1: Coarse TLI to Target Moon

Solver Control Variables

- ECI RAAN
- ECI AOP

Solver Constraints

- EMR right ascension = $0°$
- EMR declination = $0°$

2.12.2 Phase 2: Fine Impulse TLI and LOI

Solver Control Variables

- ECI RAAN
- ECI AOP
- TLI Δv
- LOI Δv
- IAB Δv

Solver Constraints

- LCI B-Vector angle = Target Inclination
- LCI Perilune altitude = 100 km +/- 10 km

2.12.3 Phase 3: Coarse Finite TLI Burn

Solver Control Variables

- TLI duration
- ECI true anomaly
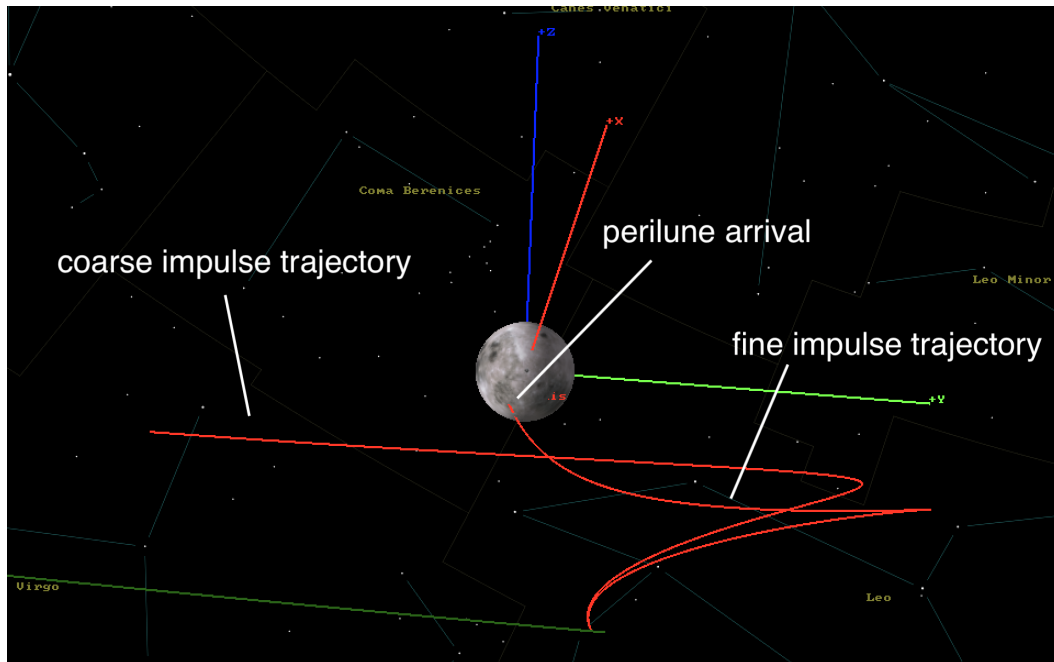
Figure 2.11: Algorithm phases 1 and 2

Solver Constraints

  – ECI right ascension = Phase 2 ECI right ascension

  – ECI orbital radius = 350,000 km

2.12.4 Phase 4: Fine Finite TLI Burn

Solver Control Variables

  – TLI duration

  – ECI true anomaly

Solver Constraints

  – LCI B-Vector angle = Target inclination

  – LCI perilune altitude = 100 km +/- 10 km

  – ECI right ascension = Phase 3 ECI right ascension

2.12.5 Phase 5: Fine Finite LOI and IAB Burns

Solver Control Variables
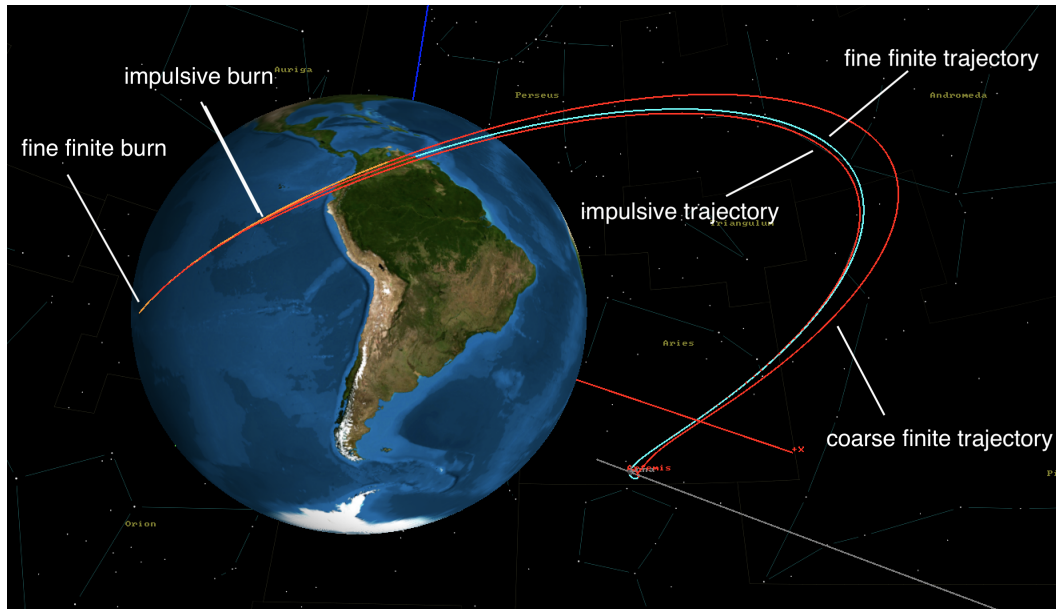
Figure 2.12: Algorithm phases 3 and 4

  – LOI duration

  – IAB duration

Solver Constraints

  – LCI eccentricity = 0

  – LCLF Inclination = Target inclination

2.12.6   Phase 6: RAAN Coast

Solver Control Variables

  – Coast duration

Solver Constraints

  – LCLF RAAN = Target RAAN

2.12.7   Phase 7: Fine Tune Parking Orbit for Landing

Solver Control Variables

  – PL duration

  – C duration
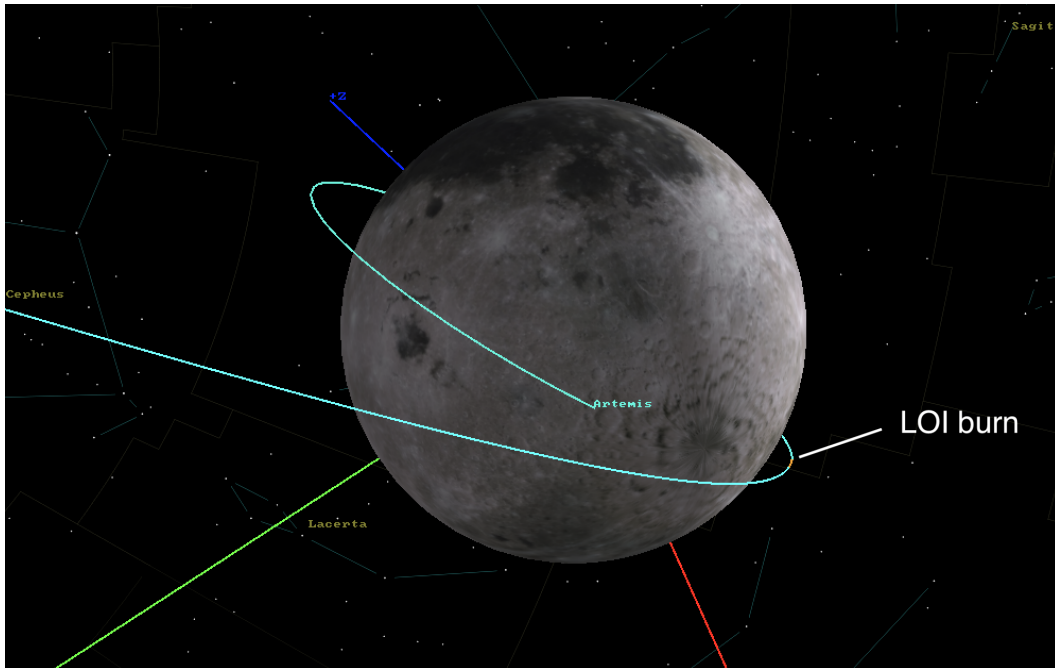
Figure 2.13: Algorithm phase 5
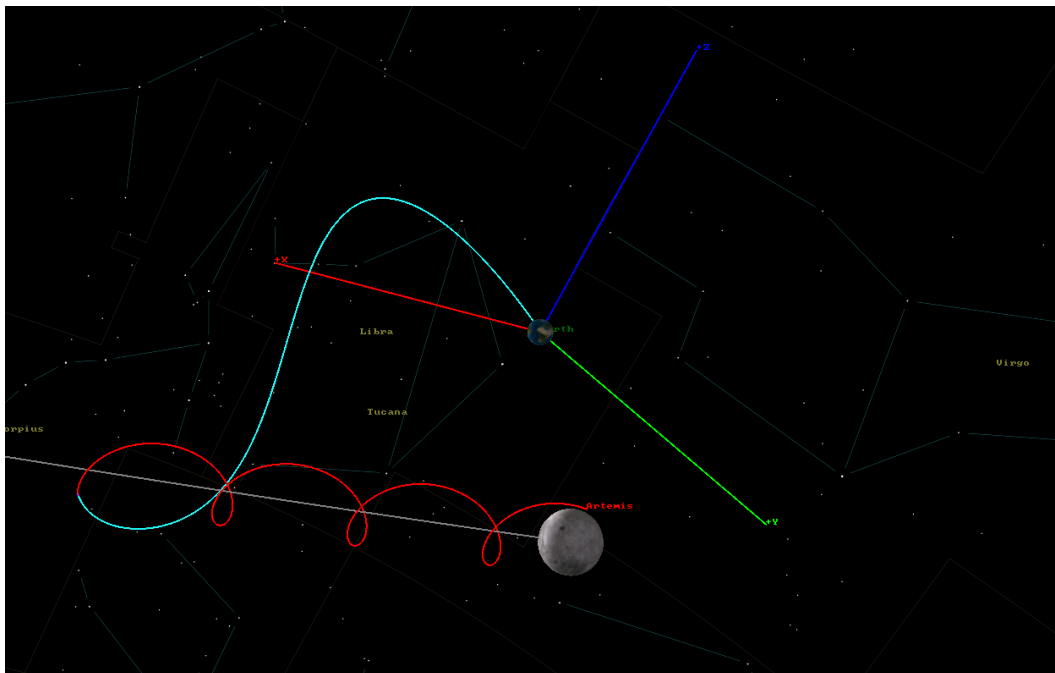
Figure 2.14: Algorithm phase 6

Solver Constraints

  – LCI perilune altitude = 100 km +/- 1 km

  – LCI eccentricity = 0

2.12.8   Phase 8: Initiate Descent

Solver Control Variables

- DO duration

Solver Constraints

- LCI perilune altitude = 22 km
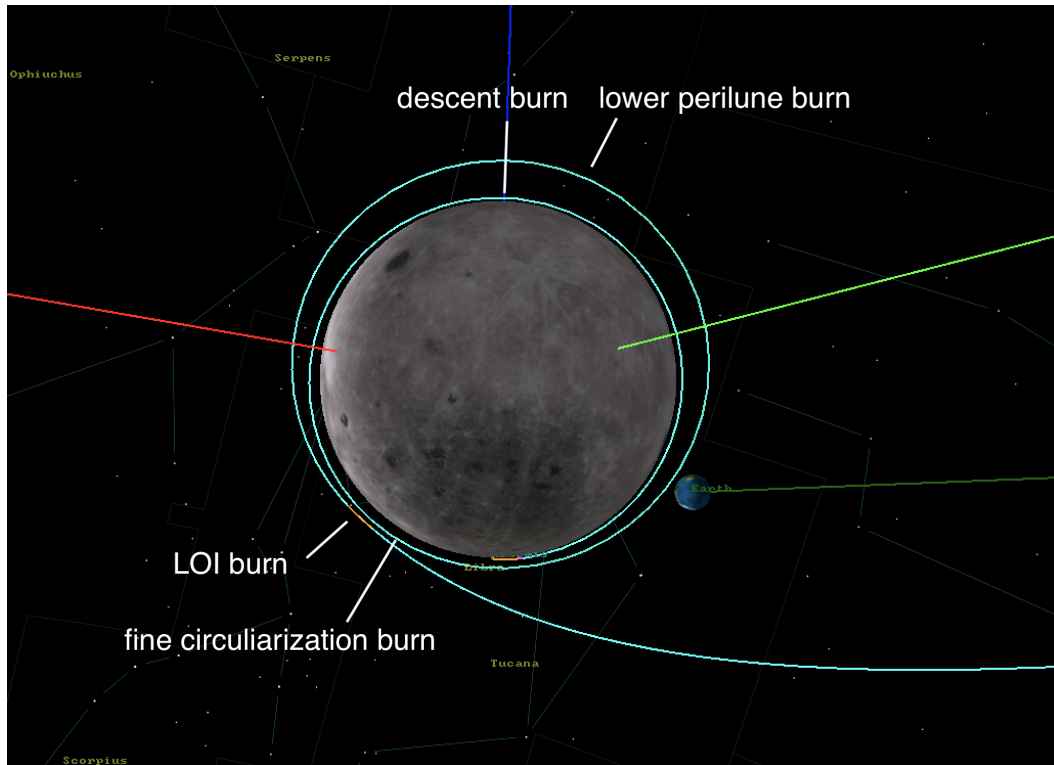
Figure 2.15: Algorithm phases 7 and 8

2.12.9   Phase 9: Final Approach

Solver Control Variables

- Approach duration

Solver Constraints

- Range from landing site = 250 km

2.12.10 Phase 10: Braking, Parabolic Free-fall, and Landing

Solver Control Variables

- B duration

- Free-fall duration

- L duration

Solver Constraints

- Free-fall surface tangential velocity @ 2.5 km = 10 m/s

- Post landing LCLF altitude = 0 m/s

- Post landing surface normal velocity = 0 m/s
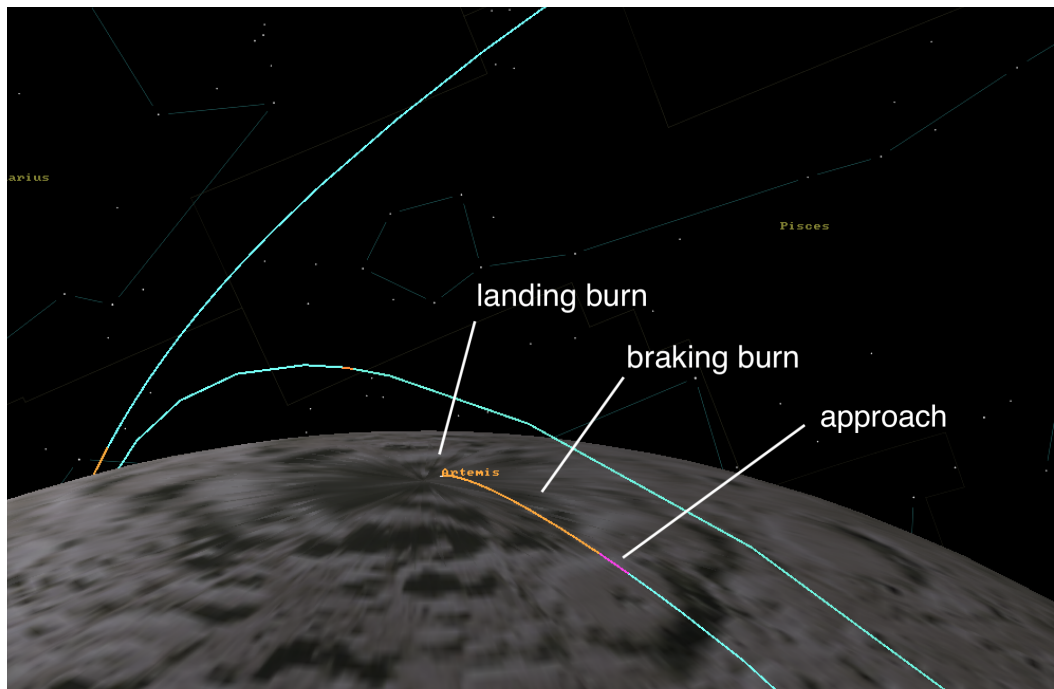
Figure 2.16: Algorithm phases 9 and 10

CHAPTER 3

RESULTS

3.1   Data Filtration and Indexing

3.1.1   PACE Output

The 2020 - 2038 analysis period with 2 day intervals provided a trajectory and mission data for 3397 independent epochs across the nodal cycle. This breadth of samples enabled the analysis of trends in mission performance due to the 18.6 year precession of the line of nodes, the 8.9 year translation of the line of apsides, the 1 year Earth orbit, the 7 month lunar eccentricity fluctuation, and the 27.3 day lunar orbit.

The 9 payload increments across a scale from 0 kg to 24 kg gave representation to a realistic suite of small satellite buses - from miniature 1U spacecraft used for technology validation, to 12U spacecraft capable of high value lunar science.

Flyby, orbit insertion, and landing trajectory profiles were computed, along with 7 lunar orbit inclinations between -135° and 135° to encompass prograde and retrograde orbits from equatorial to polar. This ensured representation of a detailed set of arrival conditions upon which propellant consumption and flight time were dependant.

The combination of these parameters resulted in 642,033 lunar trajectories run through the GMAT algorithm on PACE clusters. The output for each of these missions was a single line string exported by GMAT. This string encoded the input parameters, along with all output metrics that proved useful for comparative analysis, including departure orbital elements, arrival orbital elements, burn durations, propellant consumption, mission mass and flight time.

The Linux header script used to cycle the input parameters through the GMAT algorithm compiled the individual strings into three text files; one each for Flyby, Orbit Insertion, and Landing.

3.1.2   Filtering

The first step in post-processing the GMAT output was the identification and treatment of outliers. Numerous outliers observed as having high deviations from the running means in several parameters. Specifically, these anomalies manifested as mission mass extremums of μ +100/-0 kg, translunar flight time extremums of μ +600/-2 days, and arrival inclination extremums of μ +30/-30 °.
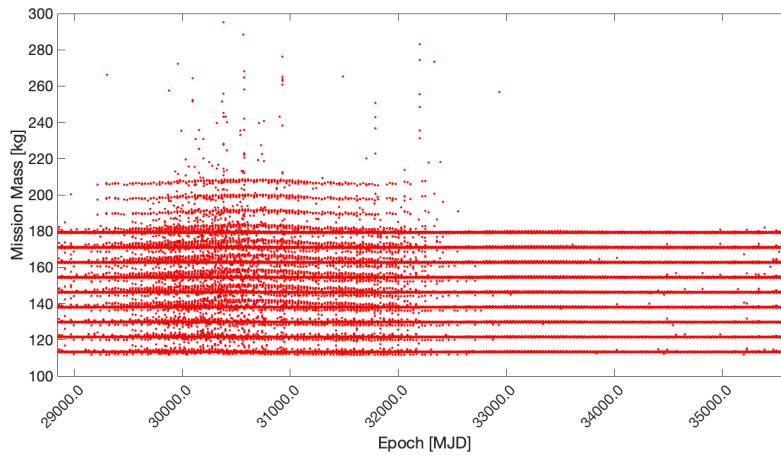
Figure 3.1: Pre-filtered GMAT data: Flyby mission mass

The above plot shows all raw flyby data for mission mass, flight time, and arrival inclination. Through figure 3.1, one can observe 9 distinct strata of mission mass values. These strata correspond to the 9 payload masses. Numerous data points lie irregularly spaced outside of these strata, in some cases by hundreds of kilograms. Figure 3.2 shows several extreme flight time outliers. These include flight times that are several hundreds of days longer, and several days shorter than adjacent data points. Figure 3.2 demonstrates 4 distinct strata in absolute arrival inclination, or for the flyby case, B-Vector angle. There represent the 0°, 45°, 90°, and 135°

96
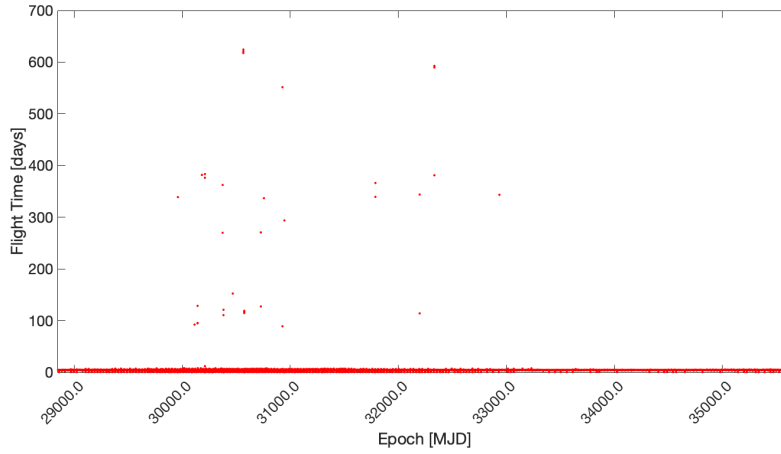
Figure 3.2: Pre-filtered GMAT data: Flyby flight time
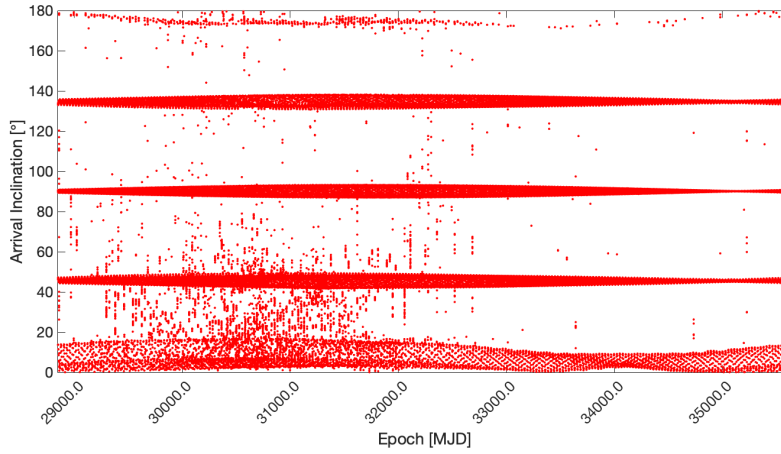
Figure 3.3: Pre-filtered GMAT data: Flyby arrival inclination

positive/negative pairs. However, there is also significant noise, where the target inclinations have not been achieved to within tolerance. These outliers translated to related metrics including Δv, burn duration, and propellant consumption mass.

A random sample of outliers was selected for singular test runs through the GMAT algorithm. All tested samples demonstrated convergence failures in one or more of the algorithms targeting sequences. This resulted in one of three behaviours.

First, when the finite TLI burn failed to converge on a correct arrival B-Vector angle, the arrival inclination error was large. To counter this error, the IAB burn

would require a long duration (therefore increased propellant) to actively alter the orbital plane. This case resulted in a high missions mass.

Second, when the parking orbit RAAN and AOP variations failed to converge upon an acceptable perilune during the finite burn phases, the targeting sequence would continually increase the burn duration in search of a solution. Without an upper bound, this would lead to a burn duration "run-away" in some cases. When the targeting sequence reached its maximum number of iterations, the subsequent targeting sequences would continue to completion, though the desired arrival inclination and perilune altitude could not be achieved. This case resulted in a short flight time, high mission mass, and high lunar orbit semi-major axis.

Third, in very rare cases, the coarse impulsive burn targeting sequences would fail to find the moon. After reaching the iteration limit without convergence, the fine adjustment segments would follow suite, sending the spacecraft into a highly elliptic Earth orbit until, eventually, a perilune condition (the closest approach within the LCI frame) was met. This case resulted in a long flight time.
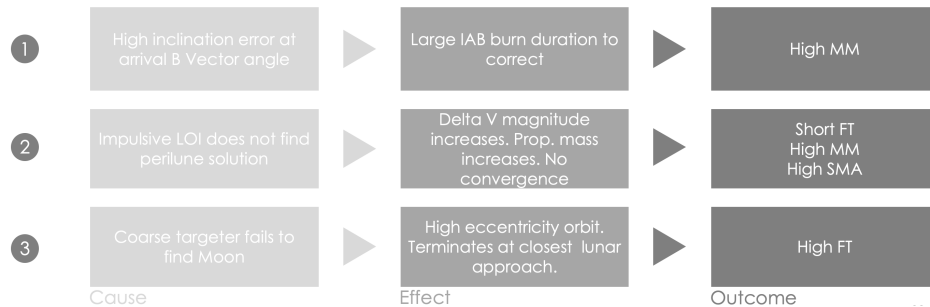
Figure 3.4: Root-cause analysis for GMAT convergence failures

None of these cases reflect a realistic scenario, but rather a failure of the algorithm to converge. As such, they can be filtered from the data without altering the validity of the overall sample.

After trial and error, it was found that the convergence failures could be eliminated through three simple filters applied to the result strings. First, perilune radius

was restricted to 2470 km (730 km altitude), translunar flight time was restricted to 3 - 6 days, and arrival inclination was restricted to +/- 10° from target. The post-filter results for the flyby trajctories can be observed in figures 3.5, 3.6, and 3.7.
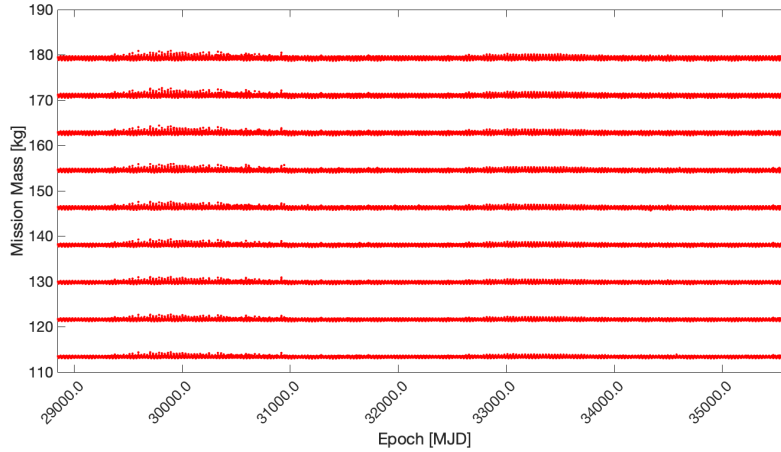
Figure 3.5: Post-filtered GMAT data: Flyby mission mass
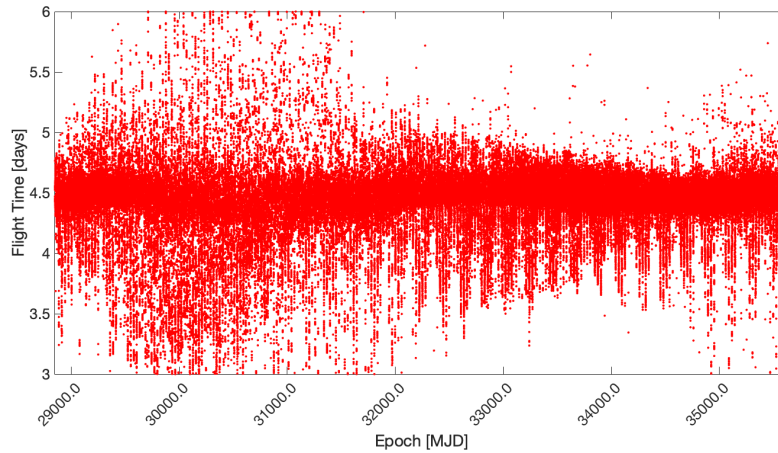
Figure 3.6: Post-filtered GMAT data: Flyby translunar flight time

3.1.3 Indexing

A series of MATLAB scripts were the written to process the filtered data from the text files into three epoch-ordered arrays; flyby (FB), orbit insertion (OI), and land-
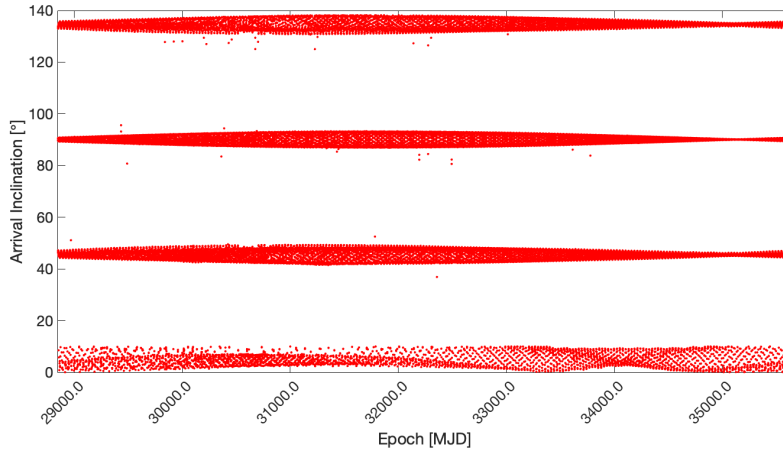
Figure 3.7: Post-filtered GMAT data: Flyby arrival inclination

ing (LN) profiles. The data within each array was structured by mission parameter, payload mass and arrival inclination.

$$GMAT\ strings\ FB\ \rightarrow\ MATLAB\ reader\ FB\ \rightarrow\ array\ FB$$

$$GMAT\ strings\ OI\ \rightarrow\ MATLAB\ reader\ OI\ \rightarrow\ array\ OI$$

$$GMAT\ strings\ LN\ \rightarrow\ MATLAB\ reader\ LN\ \rightarrow\ array\ LN$$

Where:

$$array\ FB\ =\ FB. < parameter > . < payload > . < inclination >$$

$$array\ OI\ =\ OI. < parameter > . < payload > . < inclination >$$

$$array\ LN\ =\ LN. < parameter > . < payload > . < inclination >$$

As an example, calling up an epoch-ordered vector of mission mass data for the 24 kg payload, -135° inclination orbit insertion case could be achieved through the following MATLAB commands:

$$>> OI.missionmass.p\_24.i\_n135$$

This form enabled simple handling and plotting of any metric within the output

100

string for analysis of patterns across the range of input parameters.

3.1.4 Analysis of Filtered Results

To allow detailed analysis of the filtered results, MATLAB was used to discretize and plot the indexed arrays by mission profile, payload, and inclination over short and long time scales to study emergent trends in the data. With 642,033 GMAT strings encoding several million output parameters, it was essential that data processing and trend recognition be done graphically. The open-source *Shape Language Modelling Toolbox* developed by John D'Errico was used prolifically for least-squares spline modelling to aid data visualization and trend identification.

3.2 Flyby

The first year (01 Jan 2020 - 01 Jan 2021) of flyby epoch and mission mass data was plotted for each payload and arrival inclination. The data was then spline fitted using the SLM toolbox as demonstrated by the 24 kg, 90° inclination sample in figure 3.8.
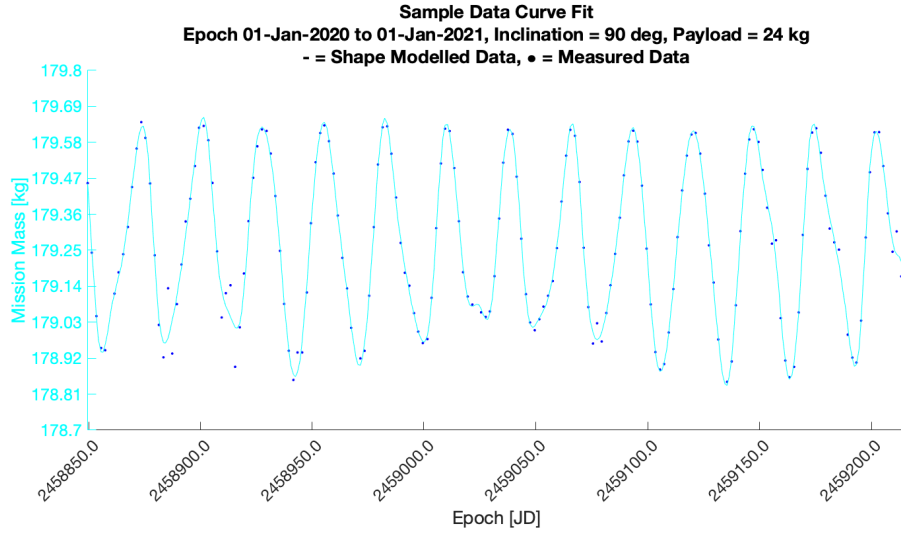
Figure 3.8: Flyby: Sample data curve fit

This sample (representative of the behaviors observed in all other payload/in-

clination sets) demonstrates two points of interest. The first is a clear epoch dependency. The mission mass oscillates between local maximum and minimum values with a period of approximately 27.3 days, or one lunar orbit. This observation implies a direct relationship between the lunar orbit true anomaly, and the amount of propellant, thereby the amount of energy required to reach it. Second, the magnitude of this dependency is small. Figure 3.8 demonstrates that for the largest payload mass of 24 kg, a favourable monthly departure epoch allows between 0.5 and 0.6 kg of mission mass reduction when compared to a worst-case epoch.

The SLM splines for all payload masses were then compiled to asses the effects of payload mass on mission mass. As demonstrated by the 90° inclination sample in figure 3.9, each consecutive 3 kg increase in payload mass corresponds to a near constant increase in mission mass of 8.2 kg incorporating both the additional payload itself, and the corresponding additional propellant.

Figure 3.9: Flyby: Sample mission mass across payload masses

This sample demonstrates that each 3 kg increment in payload mass has a significantly higher impact on flyby trajectories than departure epoch.

As with payload mass, SLM splines were compiled for all arrival inclinations to study the effects of arrival inclination upon mission mass. As demonstrated by

a 24 kg payload sample in figure 3.10, each arrival inclination demonstrates the same monthly oscillations. The lowest average mission mass is observed as corresponding to a 0° arrival (as highlighted i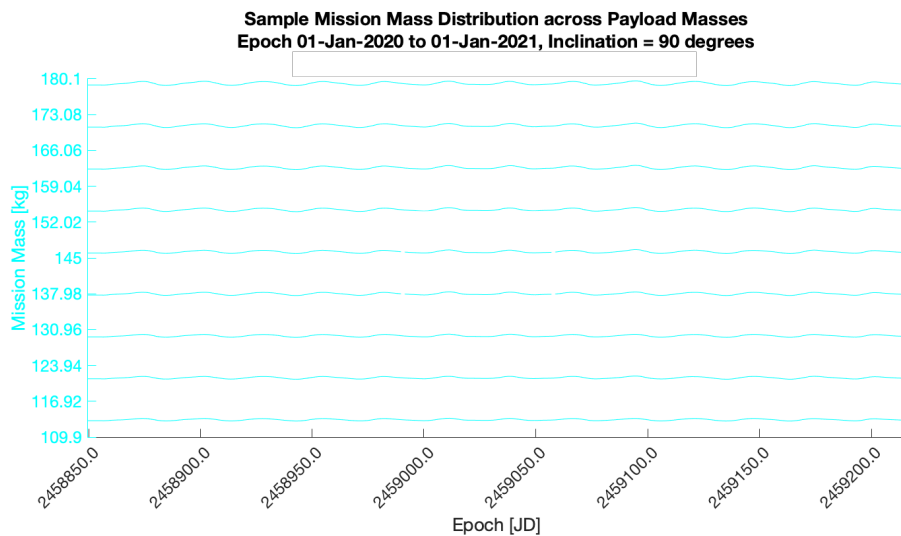n red). Epoch dependent variations in mission mass are observed to be very slight, in the order of 0.1 - 0.2 kg. As a result, flyby mission performance may be considered insensitive to departure epoch for the practical purposes of mission design.
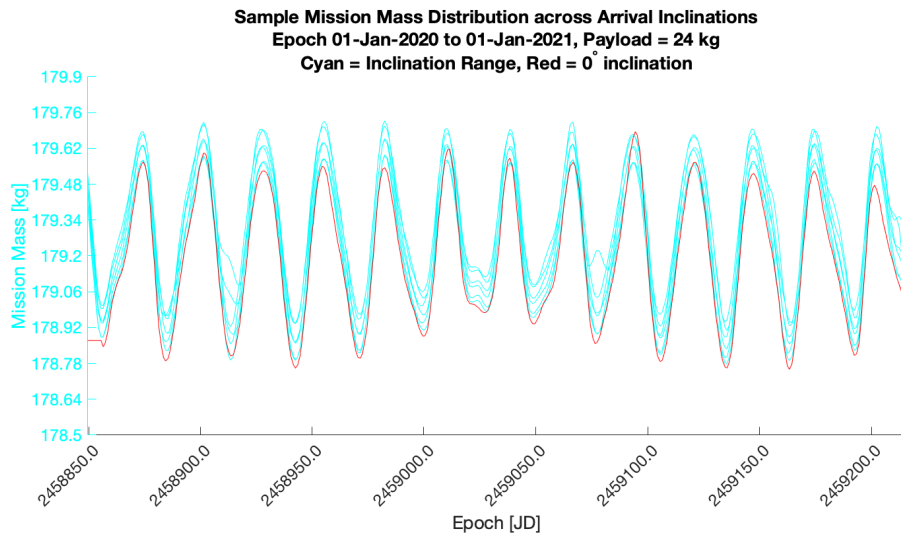
Figure 3.10: Flyby: Sample mission mass across arrival inclinations

To accurately characterize the distribution of mission metrics across the various inclinations, the mission mass values at the base of each oscillation were selected as points of interest. These minima represent optimal departures phasing for each month, thus, they are important in the design of efficient translunar trajectories. The data arrays for each mission profile were filtered for these minima, and the corresponding mission mass, epoch, flight time, and burn duration were catalogued for comparative analysis.

For the one year sample of a 24 kg payload mission, figure 3.11 demonstrates the statistical distribution of mission mass and flight time for optimal monthly departures across the inclination range. The bars of the histogram (quantified by the left axis) represent the mean mission mass of all 12 monthly minima within the

sample period of 01 Jan 2020 to 01 Jan 2021. Black error bars bound a single standard deviation range about the mean (+/- 1 σ) as an indication of variance. The magenta line (quantified by the right axis) denotes the mean flight time across the monthly minima with magenta arrows again bounding the +/- 1 σ.
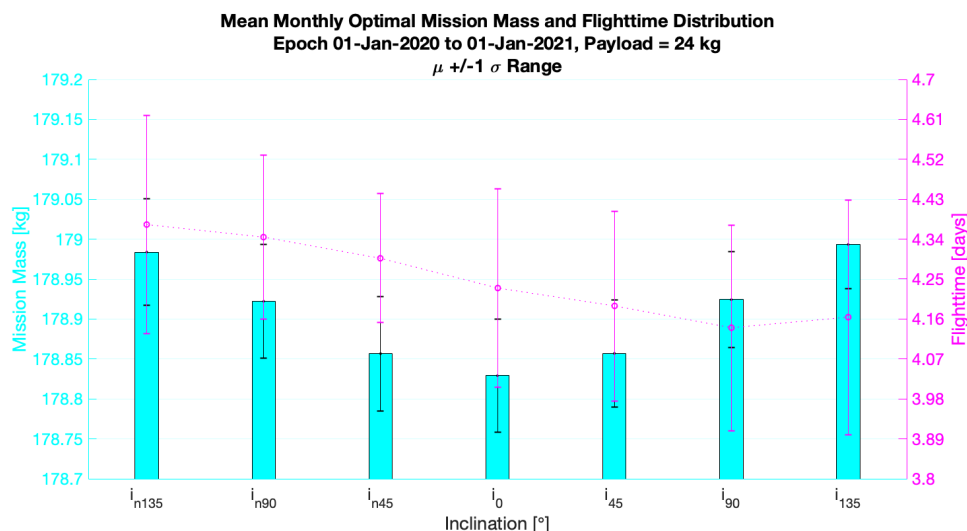
Figure 3.11: Flyby: Sample mean optimal mission mass and flight time distribution

The prograde equatorial arrival inclination of 0 corresponds to the lowest mean mission mass for optimal monthly departures. Mission mass is observed to increase for both higher and lower arrival inclinations, reaching its highest for the retrograde inclinations of +/-135°. The magnitude of the mission mass variation is very slight, with the lowest mean (178.83 kg for 0° inclination) only 0.16 kg lighter than highest mean (178.99 kg for 135° inclination). Therefore, flyby missions may be considered insensitive to arrival inclination for mission design purposes. With standard deviations of approximately 0.4 days, the mean flight times have a high variance, and therefore do not demonstrate a clear trend across inclinations. The +/- 1σ for all flight times fall between 4 and 4.6 days. As expected, this near-Hohmann transfer trajectory has a longer flight time than the more direct free-return trajectories of Apollo 10, 11, 12 (3.4, 3.3, and 3.7 days respectively) as catalogued in chapter 1.

Across the same 2020, 24 kg payload sample, figure 3.12 demonstrates the mean

monthly minimum burn duration of the 635 N main engine required to achieve TLI across the range of arrival inclinations (indicated by the magenta line). Magenta error bars bound the +/- 1° bounds for the monthly minimum sample. The green histogram and error bars (quantified by the left axis) represent the mean TLI Δv and +/- 1σ range computed by integrating the relationship between thrust and instantaneous mass over the corresponding burn duration:

$$\Delta v = \int_{t_0}^{t_{burn}} \frac{F_T}{m_{mission} - \dot{m}_{engine}t} dt \tag{3.1}$$

As expected, the mean Δv values match the trend in mission mass with a minimum at the prograde equatorial arrival inclination of 0, increasing at higher and lower inclinations, with a difference in extremums of only 2.8 m/s.
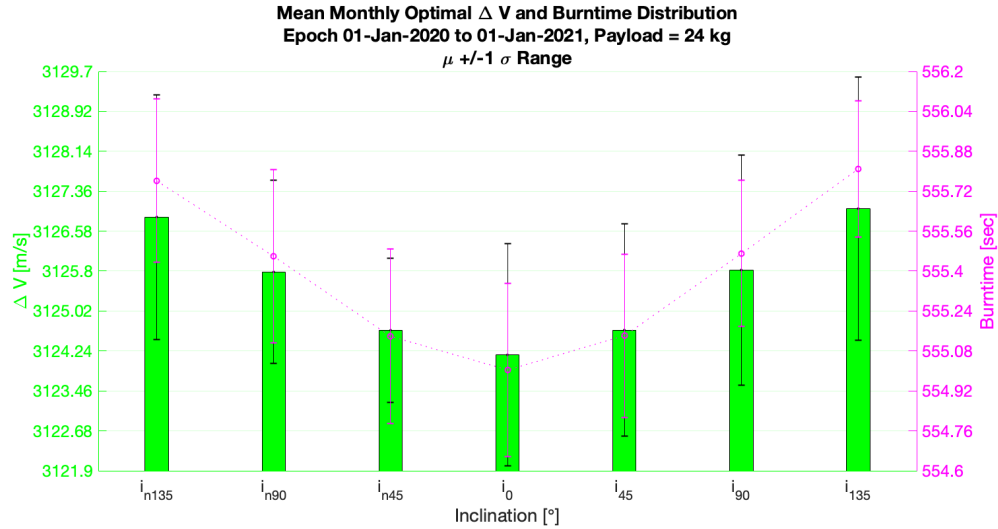
Figure 3.12: Flyby: Sample mean optimal ΔV and burn time distribution

A counter-intuitive result emerges upon comparison with the Apollo 10 Δv value from Chapter 1. Despite a lower parking orbit altitude of 160.3 km and a less efficient free-return trajectory, TLI was acheived with a Δv of 3049 m/s, less than the observed 3124.2 m/s required for a 0° inclination arrival from a 400 km parking orbit via a near-Hohmann transfer. This difference is due to the burn du-

ration. Using the powerful J2 H_2/O_2 engine of the S-IVB upper stage, Apollo 10 achieved TLI with a 343 s burn [8]. This short burn made use of the Oberth Effect, whereby a burn at or close to perigee (where the spacecraft is at its highest orbital velocity) imparts the greatest mechanical energy into the orbit per second, therefore, is more efficient. In contrast, the modelled trajectory achieved TLI after 555.1 s due to a lower thrust to weight ratio of the TLI stage. This translated to a steady decrease in efficiency as the spacecraft passed further from perigee along its burn.

To understand the observed (if very slight) epoch dependencies in flyby trajectory performance, a one year sample (01 Jan 2020 - 01 Jane 2021) for a 24 kg, 90° mission was plotted against periodic and secular cycles. First, the mission mass vs. epoch relationship was modelled with an SLM spline, and overlaid with the monthly optimal and worst case departures. Atop this data set, the lunar range over the sample period as generated by JPL Horizons was overlaid. A direct correlation can be clearly observed between the mission mass and lunar range approximately 4.3 days (the observed mean translunar flight time for a 24 kg, 90° mission) into the future. That is, the lunar range at the time of spacecraft arrival.
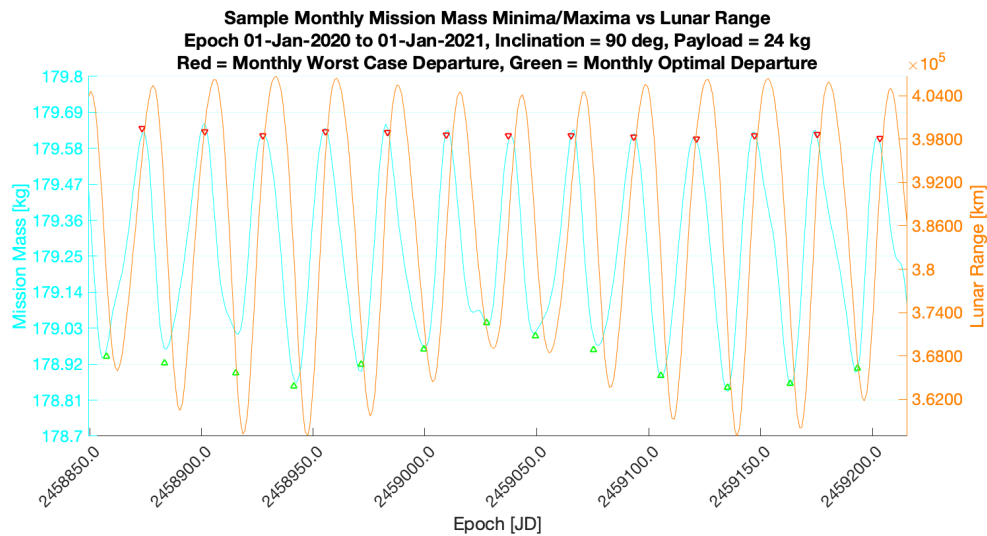
Figure 3.13: Flyby: Sample monthly optimal and worst case mission mass vs lunar range

The magnitude of each minimum is directly proportional to the magnitude of the monthly lunar perigee as it fluctuates due to a 7 month variation in lunar eccentricity caused by Earth tidal and third body gravitational effects. Thus, flyby mission performance was deemed highly correlated to range, though the magnitude of variation due to this correlation is so small that the performance is considered insensitive to the lunar orbit and eccentricity periodic cycles. No correlation was observed with lunar declination.

Similarly, performance was analysed against the secular cycles of Earth orbit, apisidal precession, and nodal precession. This is best demonstrated by viewing the monthly optimal and worst case mission mass values plotted for each arrival inclination over the full 18.6 year analysis period, where lunar inclination is included as a reference of major and minor standstills. No correlation to Earth orbit, apisidal precession or nodal precession was observed, therefore flyby mission performance was considered insensitive to secular cycles.

Figure 3.14: Flyby: Full nodal cycle monthly mission mass extremums vs lunar inclination

Figure 3.15: Flyby: Full nodal cycle monthly mission mass extremums vs lunar inclination

Figure 3.16: Flyby: Full nodal cycle monthly mission mass extremums vs lunar inclination
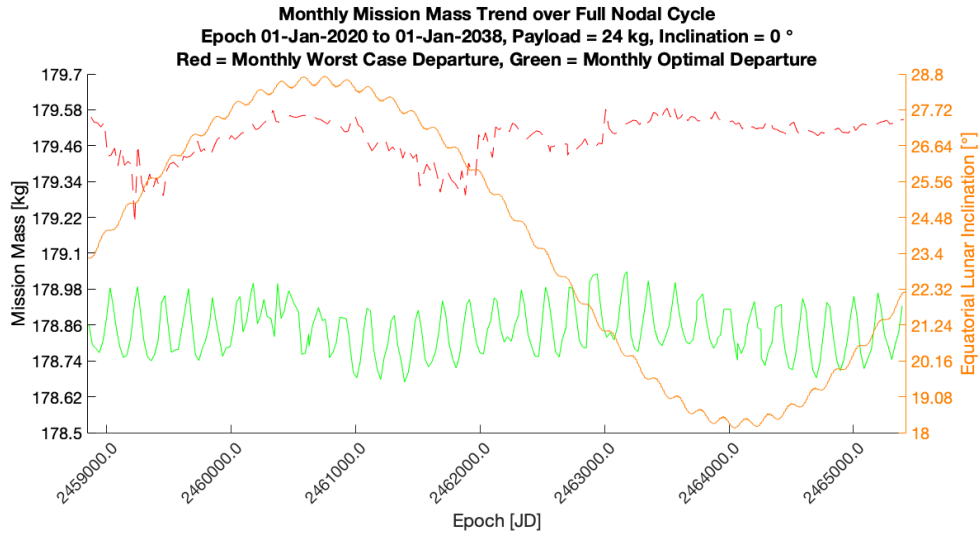
Figure 3.17: Flyby: Full nodal cycle monthly mission mass extremums vs lunar inclination
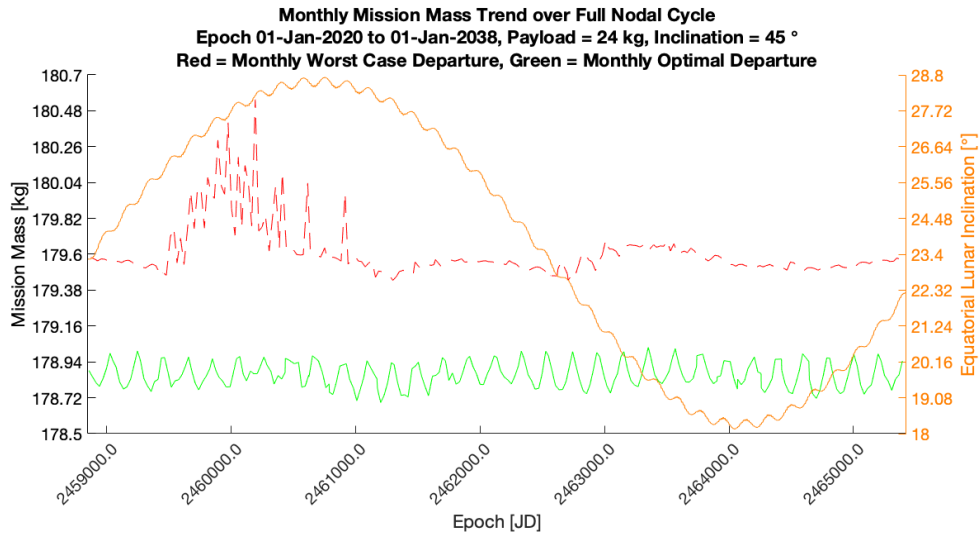
Figure 3.18: Flyby: Full nodal cycle monthly mission mass extremums vs lunar inclination
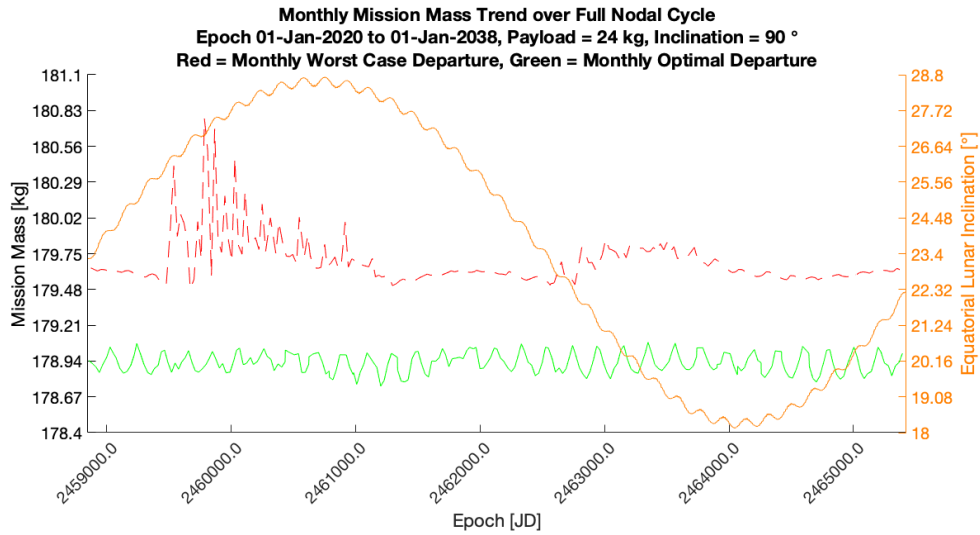
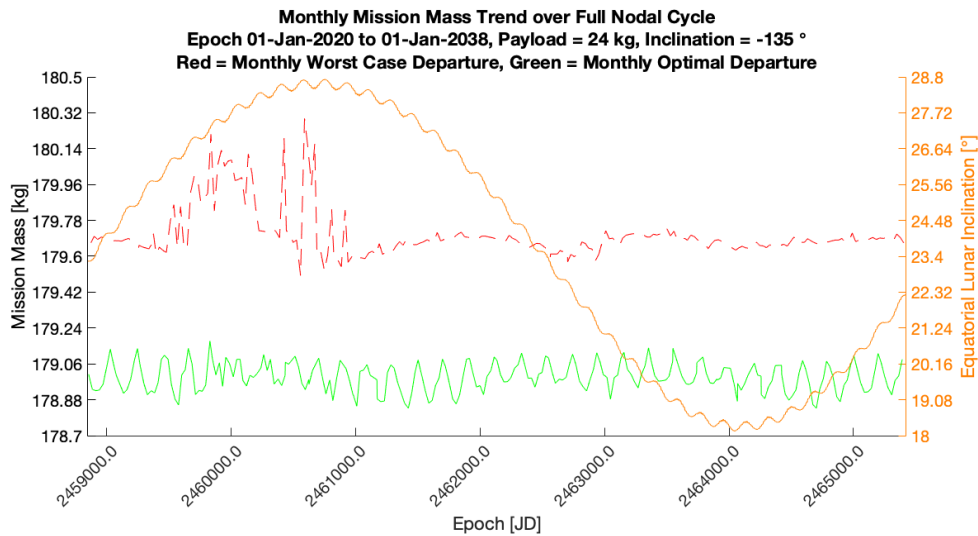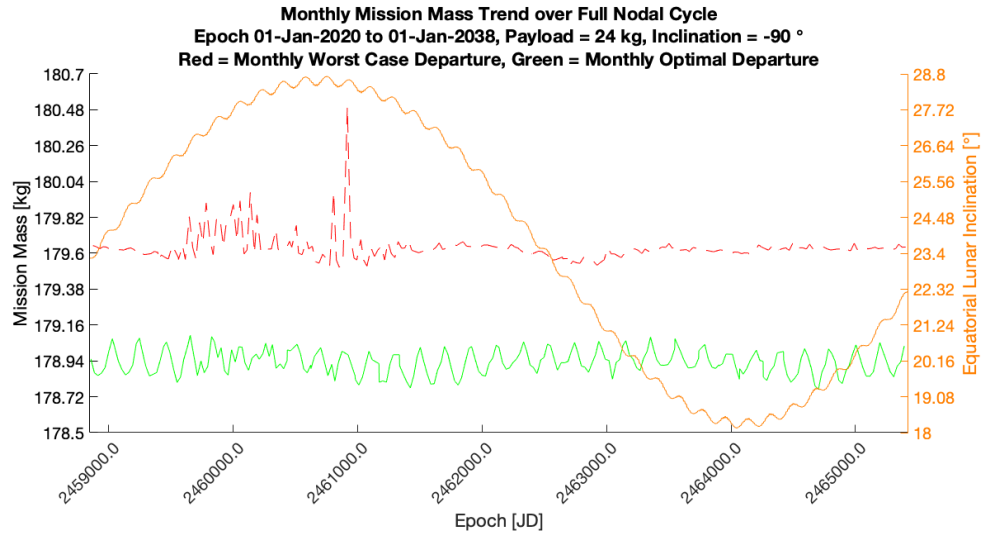Figure 3.19: Flyby: Full nodal cycle monthly mission mass extremums vs lunar inclination
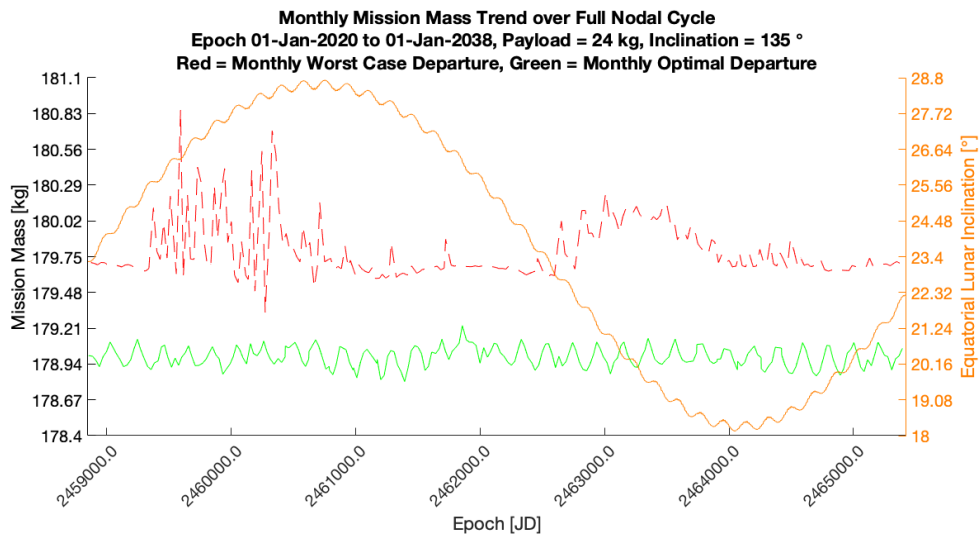
Figure 3.20: Flyby: Full nodal cycle monthly mission mass extremums vs lunar inclination
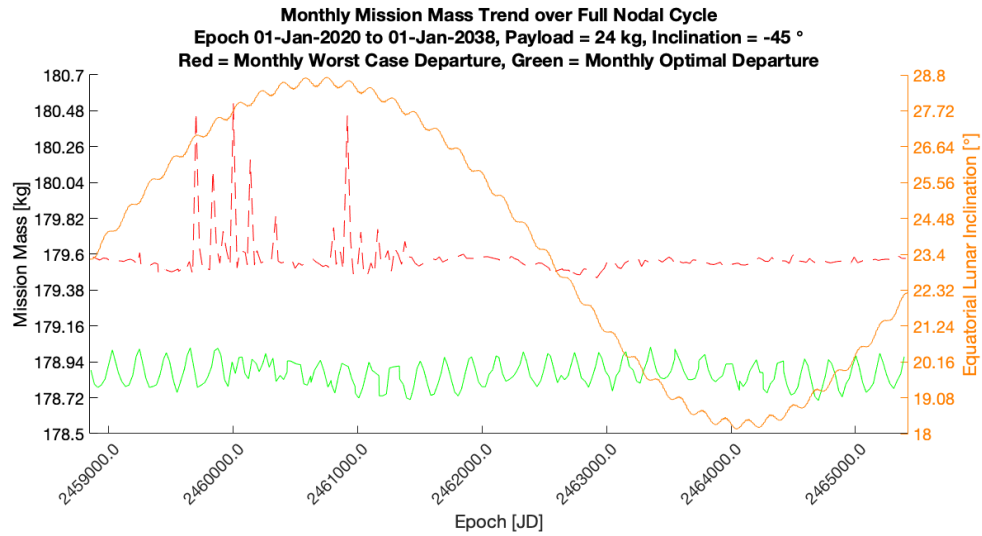
Assuming an optimal monthly departure time, the expected range in mission mass across the analysed payloads and arrival inclinations may be characterized statistically. Figure 3.21 provides the mission mass distribution for monthly minima across the full nodal cycle for a 0 kg payload mass. The inclination/payload set providing the lowest $\mu - 1\sigma$ mission mass across the entire sample space is 0°/0 kg at 113.05 kg.

Figure 3.21 provides the mission mass distribution for monthly minima across the full nodal cycle for a 24 kg payload mass. The inclination/payload set providing the highest $\mu + 1\sigma$ mission mass across the entire sample space is 135°/24 kg kg at 179.06 kg.

These two extremums provide the upper and lower bounds of the sample space, such that any combination of payload mass from 0-24 kg and arrival inclination from -135° to 135° will require a mission mass between 113.05 kg and 179.06 kg.

Whilst arrival inclination and departure epoch can be tuned for optimal performance, the overall mission mass is dominated by payload mass. Thus, for a given payload, flyby missions allow flexibility in launch date and arrival orbital elements without significant impact on the required launch vehicle capacity.

The statistical distributions for all monthly minima across the nodal cycle are provided for each payload mass within Appendices A (mission mass and flight time) and B (Δv and burn time). This data may prove a useful reference for lunar satellite mission designers in scoping launch vehicle capacity to suit targeted payload mass and arrival elements.
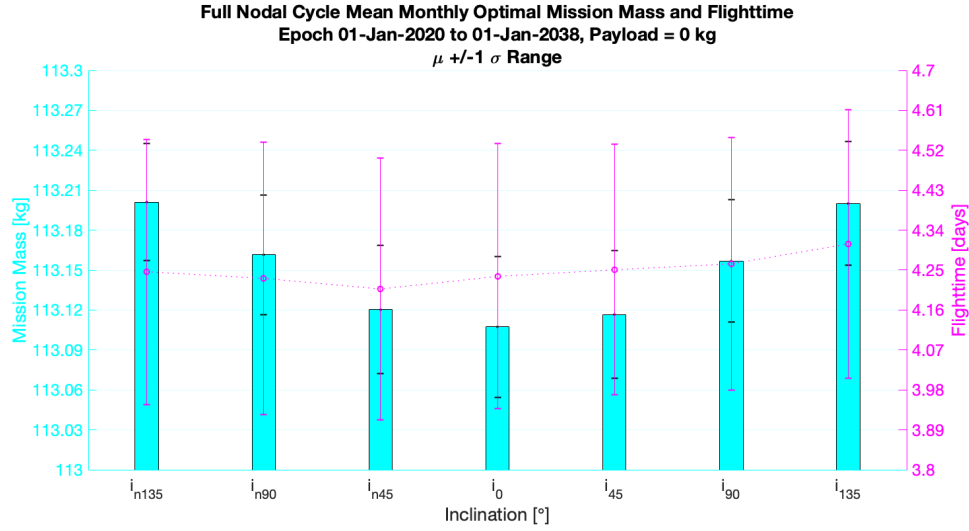
Figure 3.21: Flyby: Full nodal cycle mean optimal mission mass and flight time distribution, 0 kg Payload
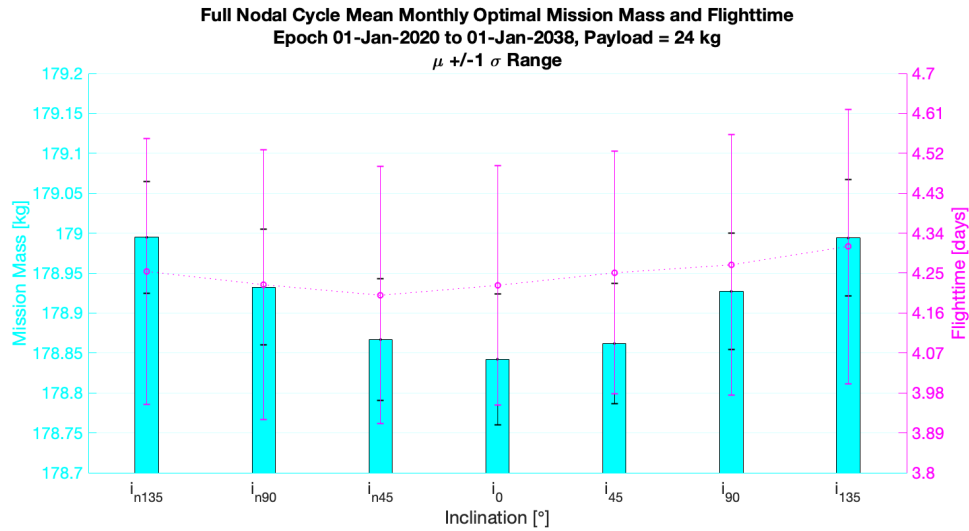
Figure 3.22: Flyby: Full nodal cycle mean optimal mission mass and flight time distribution, 24 kg Payload

3.3 Orbit Insertion

As with flyby, Shape Language Modeling was applied to the filtered orbit insertion mission mass data for the extrapolation of parameter dependent trends. A year long sample (01 Jan 2020 - 01 Jan 2021) for a 24 kg payload across all inclinations clearly demonstrates the monthly oscillation commensurate with lunar range.
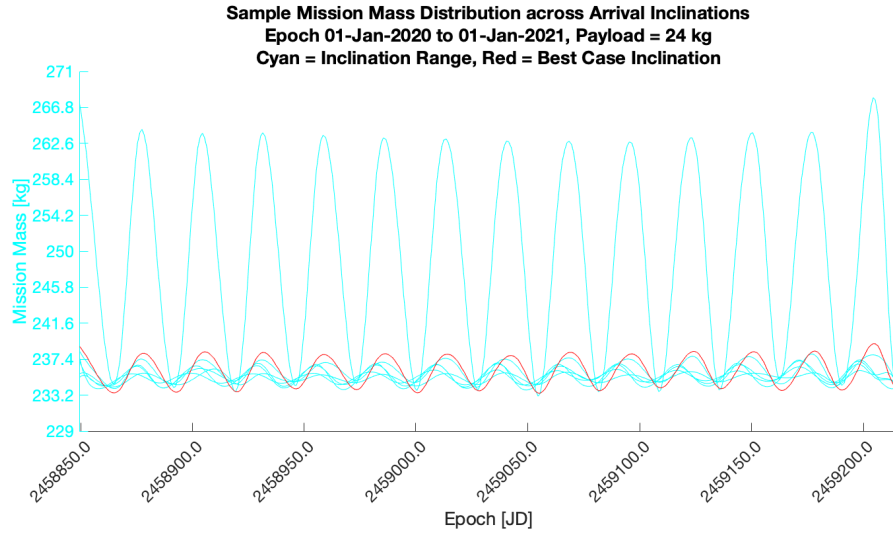
Figure 3.23: Orbit Insertion: Sample mission mass across lunar arrival inclinations

However, upon comparing the full range of arrival inclinations across the analysis period, one notes a significant variation in the corresponding mission mass extremums. All but one inclination shares a relatively consistent monthly minimum, with -45° (displayed in red) presenting the lowest mean value of monthly minima over a one year sample period.

Excepted from this consistency is the 0° case, for which greater minima variation and a notably large maxima (approximately 27 kg from the averaged maxima of all other inclinations) may be observed.

The oscillations between monthly mission mass extremums are approximately 5 kg for all higher inclination arrivals, and approximately 30 kg for 0° arrivals. As such, this sample demonstrates a significantly higher performance dependency

on both epoch and arrival inclination than the flyby case, for which the equivalent sample 3.10 showing an average oscillation between extremums of only 0.8 kg.

Figure 3.24 demonstrates a one year sample (01 Jan 2020 - 01 Jan 2021) at a 90° arrival inclination of mission mass payload dependencies. Each consecutive 3 kg increase in payload mass corresponds to a near constant increase in mission mass of 10.7 kg at the lower end of the payload scale, and 10.8 kg at the top end. This is a greater relative difference than the equivalent flyby sample for which a difference of 8.2 kg between increments was observed in figure 3.9. This result is expected, given the addition of LOI and IAB burns resulting in a longer total burn duration, therefore, more propellant must be carried for each additional kg of payload mass.
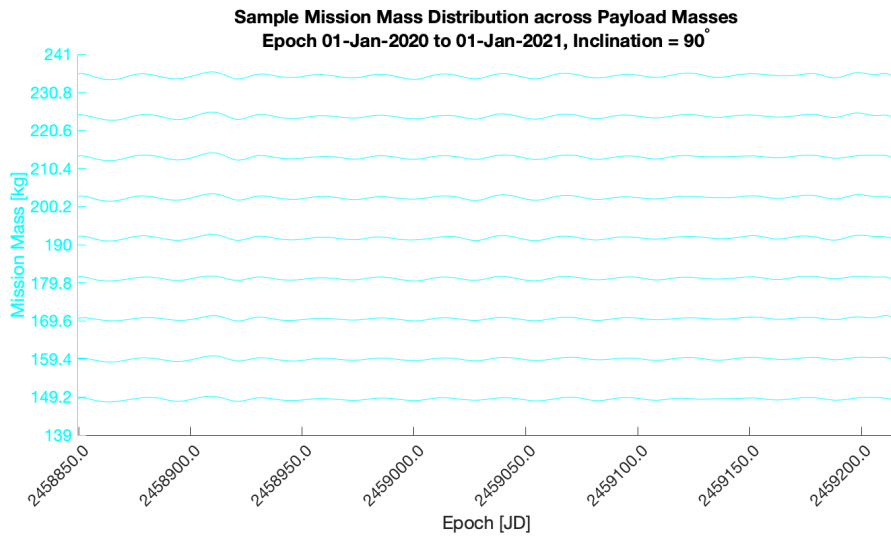
Figure 3.24: Orbit Insertion: Sample mission mass across payload masses

A factor that was not expected is the measurable variability in the mission mass increase/payload increment ratio (growing by 0.1 kg over the payload range). This result signifies a drop in efficiency as burn duration increases indicative of the Oberth Effect. As the burn is occurring progressively further from perigee (where the spacecraft is at its highest orbital velocity), the mechanical energy imparted upon the spacecraft is reducing.

An interesting point to note is that, while payload mass maintains a dominant

influence on mission mass for +/- 135°, 90°, and 45° arrival inclination, this is no longer true for 0° arrival. The year long samples showed a 10.8 kg mission mass delta between payload increments, and 30 kg mission mass delta between monthly departure extremums. Thus, the performance improvement made by optimal selection of departure epoch equates to a 7.43 kg increase in allowable payload mass when compared to worst case departure.

As with the flyby analysis, the data arrays for a one year orbit insertion sample were filtered for optimal monthly departures. For the one year sample of a 24 kg payload mission, figure 3.25 demonstrates the statistical distribution of mission mass and flight time for optimal monthly departures across the inclination range. Both mean and +/- 1σ ranges are presented.
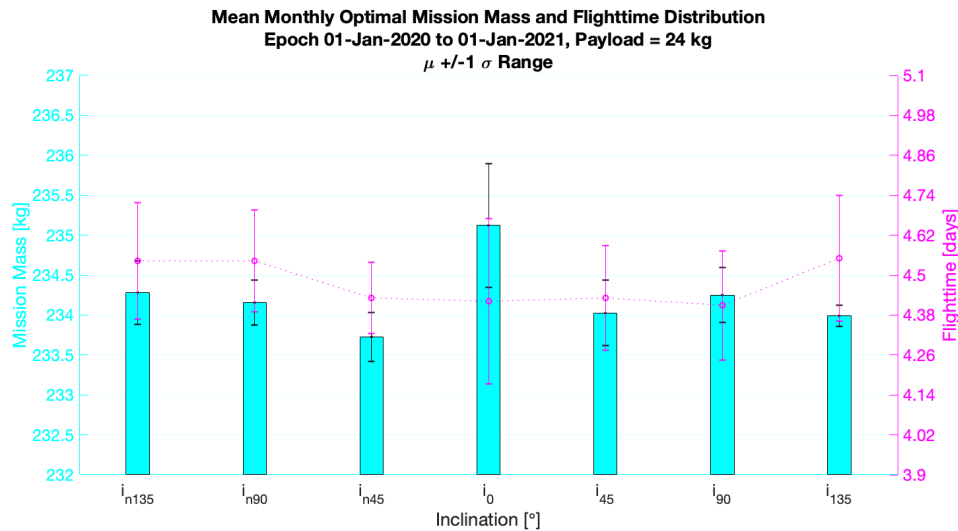
Figure 3.25: Orbit Insertion: Sample monthly optimal and worst case mission mass vs lunar range

The -45° arrival inclination corresponds to the lowest mean mission mass. Mission mass is observed to increase for the higher inclinations, though, rather uniquely, the +135° arrival has a lower mission mass than the +/- 90° cases for this sample. The largest mission mass mean and variance by a significant margin is that of the 0° degree arrival.

The magnitude of the mission mass variation is higher than for the flyby case, though still not large, with the lowest mean (233.55 kg for -45° inclination) being 1.55 kg lighter than highest mean (235.10 kg for 0° inclination). With standard deviations of approximately 0.2 days, the mean flight times have a high variance, and therefore do not demonstrate a clear trend across inclinations. The +/- 1σ for all flight times fall between 4.15 and 4.74 days. As expected, the near-Hohmann transfer trajectories have a longer duration than Apollo 10, 11, and 12, and are commensurate with the flyby equivalents.

Across the same 2020, 24 kg payload sample, figure 3.26 demonstrates optimal monthly departure total burn duration (TLI + LOI + IAB) with Δv mean values and +/- 1σ bounds across the inclination range.
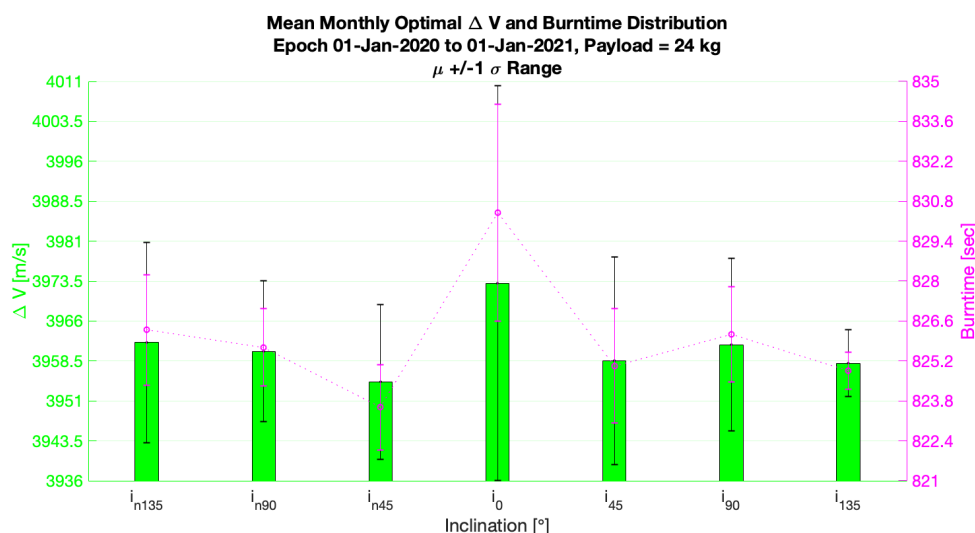
Figure 3.26: Orbit Insertion: Sample mean optimal ΔV and burn time distribution

As anticipated, the results are proportional to the mission mass magnitudes, with a Δv range from 3955 m/s to 3974 m/s from the 400 km Earth parking orbit to a circular 100 km lunar orbit. These may be compared to the Apollo 10 , 11, and 12 magnitudes of 4021 m/s (95.3 km x 98.2 km lunar orbit), 4131 m/s (86.6 km x 105.7 km lunar orbit), and 4155 m/s (87.4 km x 106.4 km orbit). It is intuitive that the overall Δv for the Apollo trajectories is slightly higher given the additional

LOI quotient required to remove the energy of the free-return approach as opposed to a less energetic near-Hohmann transfer. Upon lunar arrival, the thrust to weight ratio no longer provides a comparative Δv advantage to Apollo as it did during the TLI segment for two reasons. First, the LOI was performed by the Command and Service Module's Aerozine 50/Nitrogen Tetroxide main engine (as opposed to the more powerful S-IVB hydrolox engine that provided TLI), thus the thrust to weight ratio of Apollo was reduced. Second, the analysis spacecraft has spent the vast majority of it's fuel during the TLI burn, leaving only a small portion of the original mission mass for the 635 N main engine to decelerate, thus, it's thrust to weight ratio was increased.

The reason for the additional Δv required to achieve a low arrival inclination may be explained by visualizing the arrival vector within the LCI frame. For the near-Homann transfer achieved by the GMAT algorithm, the relative velocity to the moon upon arrival to the lunar sphere of influence is approximately 800 m/s (though the exact magnitude is obviously case dependent). For a $0°$ target inclination case, the spacecraft will arrive with some LCI Z-component velocity. The lunar gravity is not strong enough to alter the trajectory to remove this before striking the B-plane. As a result, a non-planar arrival with a B-Vector of 0 will still have Z-component velocity, and thus will be inserted into a slightly inclined orbit. This is evidenced by the unfiltered flyby data in figure 3.3 which shows a loose distribution in the arrival inclination at the 0 B-Vector target, while showing tight distributions (implying higher accuracy) for the higher inclinations.

The higher inclinations can be accessed with minimal inaccuracy as they provide additional degrees of freedom for tailoring the arrival vector. With slight adjustments in the TLI burn duration, AOP, and RAAN, these lunar arrival inclinations can be directly targeted provided they are higher than the relative inclination of the incoming transfer orbit, minimizing reliance upon lunar gravity for course correc-

tion.

To correct for inaccuracy in inclination upon arrival, the IAB burn must actively correct the inclination with a large plane change for low inclination arrivals. As orbital plane changes are prohibitively energy intensive, the $0°$ arrivals result in a larger overall Δv, and therefore a higher mission mass.

To study the epoch dependency of orbit insertion missions, a one year, 24 kg payload, $90°$ arrival sample of monthly extremums was compared to lunar range from JPL Horizons.
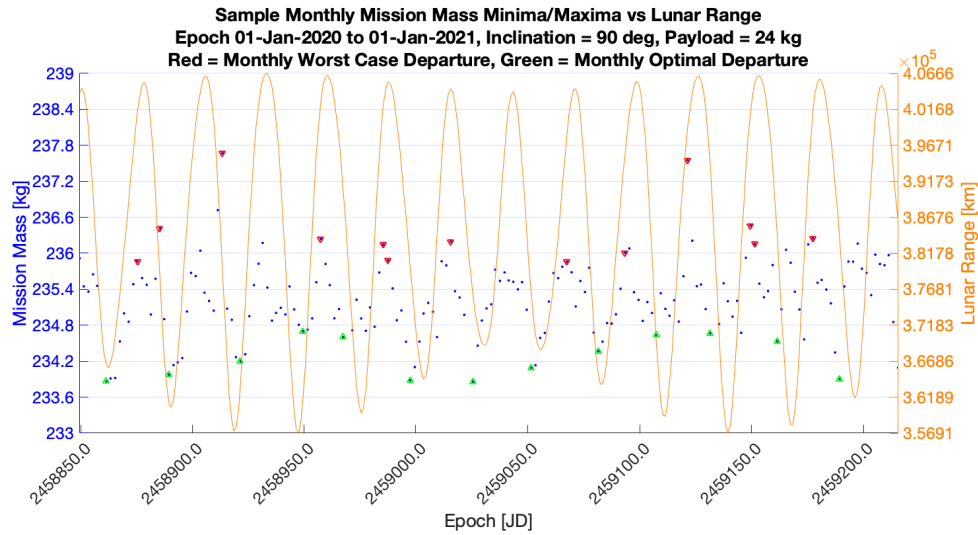
Figure 3.27: Orbit Insertion: Sample monthly optimal and worst case mission mass vs lunar range

From figure 3.34, it is immediately apparent that that the correlation between lunar range and monthly minima is weaker than the clear causal relationship manifested in the flyby results. Upon a similar superposition of lunar declination, no clear, singular periodic cycle aligned with the monthly extemums as the driving factor for mission performance. To characterize the epoch dependency due to secular cycles, the monthly maxima and minima mission mass values were plotted for each arrival inclination over the full 18.6 year nodal cycle.
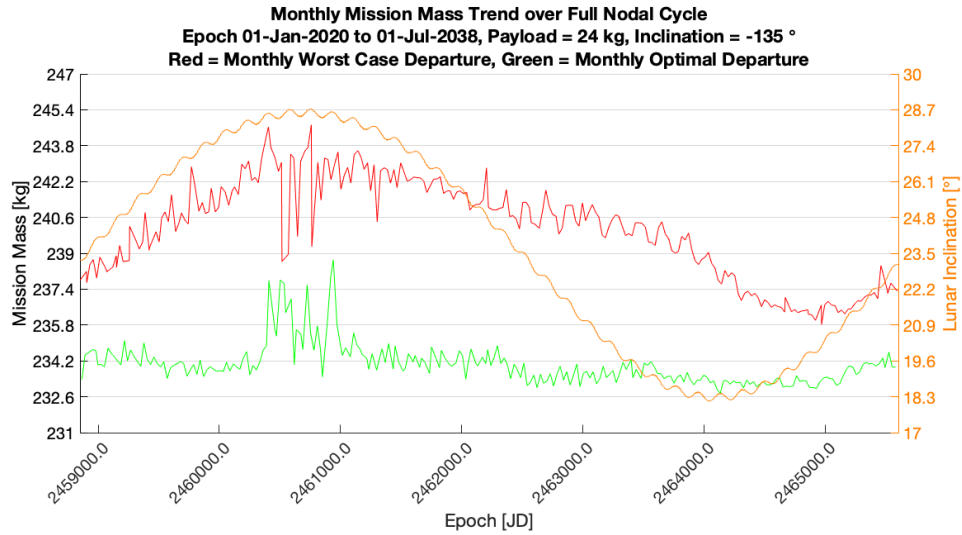
Figure 3.28: Orbit Insertion: Full nodal cycle monthly mission mass extremums vs lunar inclination
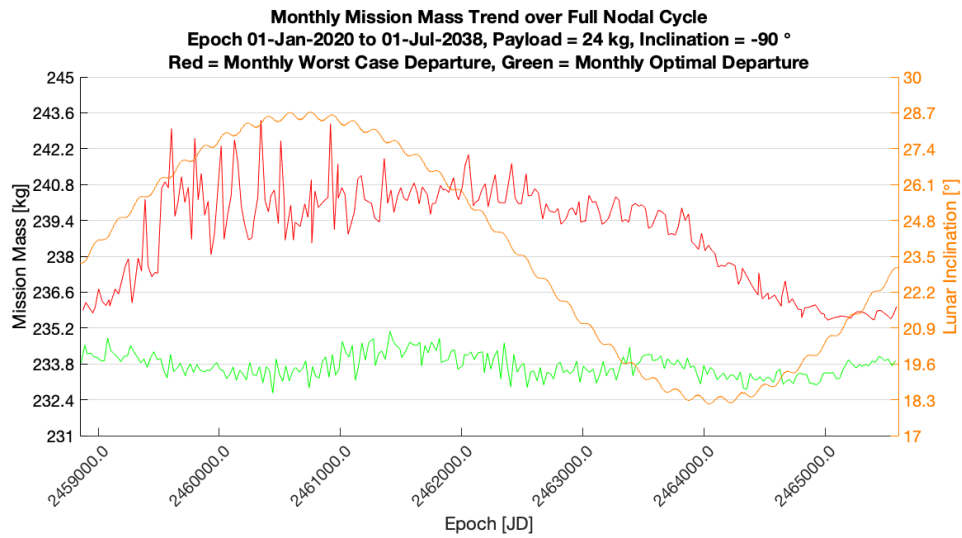
Figure 3.29: Orbit Insertion: Full nodal cycle monthly mission mass extremums vs lunar inclination
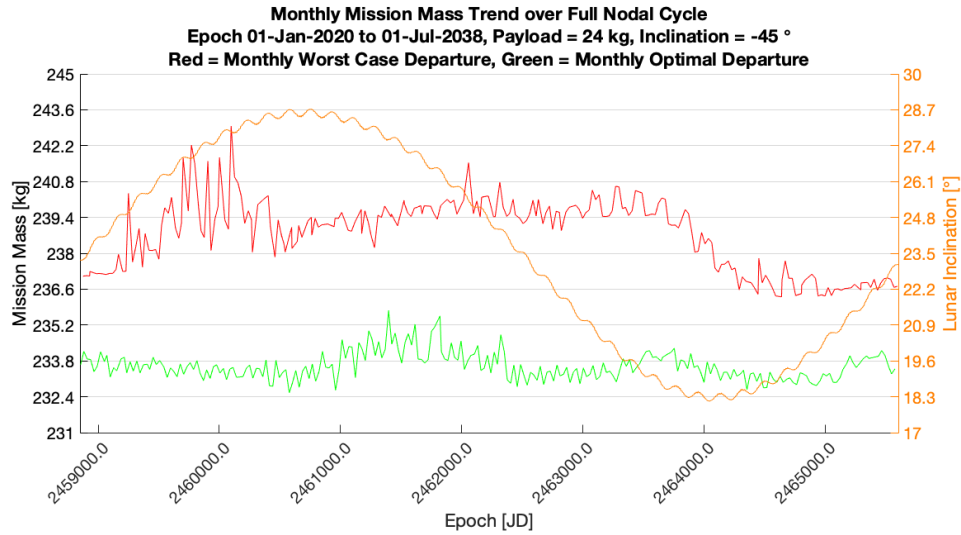
Figure 3.30: Orbit Insertion: Full nodal cycle monthly mission mass extremums vs lunar inclination
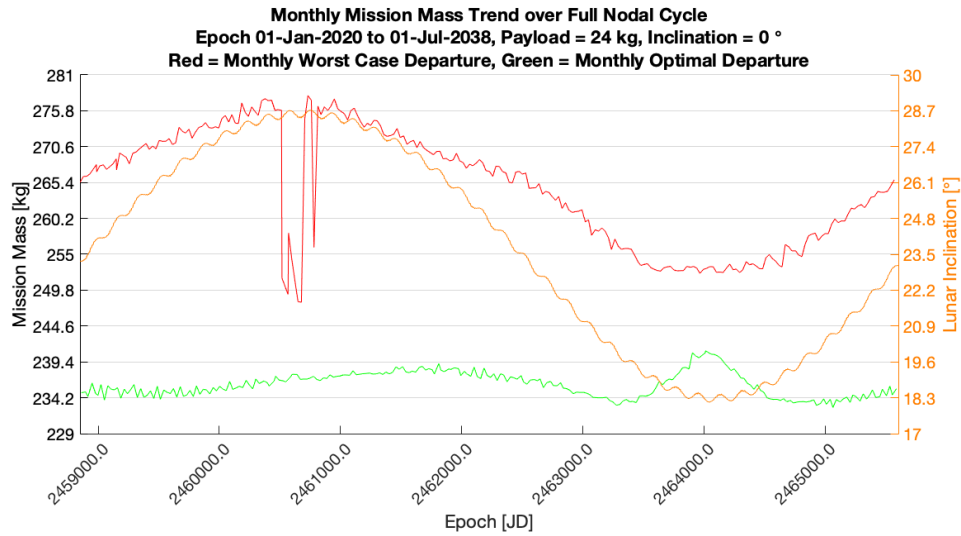
Figure 3.31: Orbit Insertion: Full nodal cycle monthly mission mass extremums vs lunar inclination
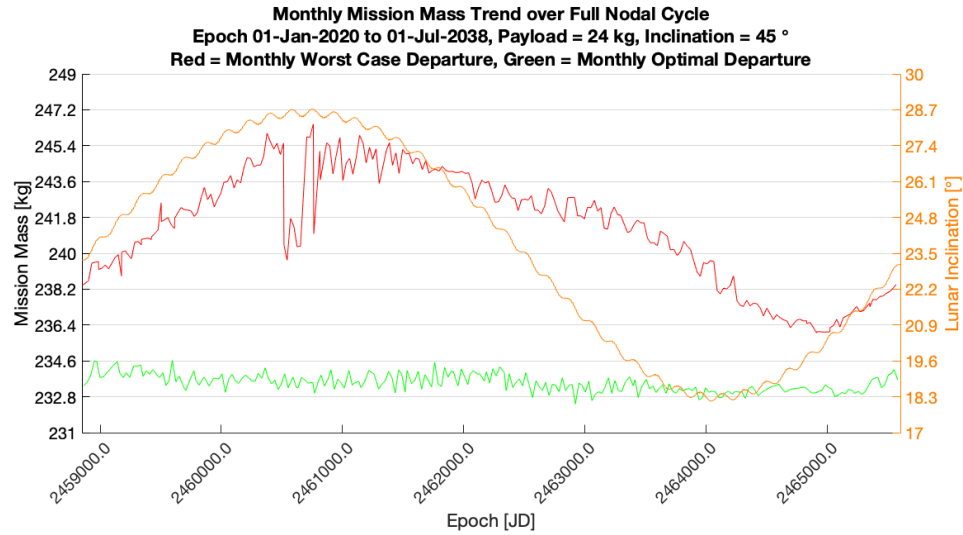
Figure 3.32: Orbit Insertion: Full nodal cycle monthly mission mass extremums vs lunar inclination
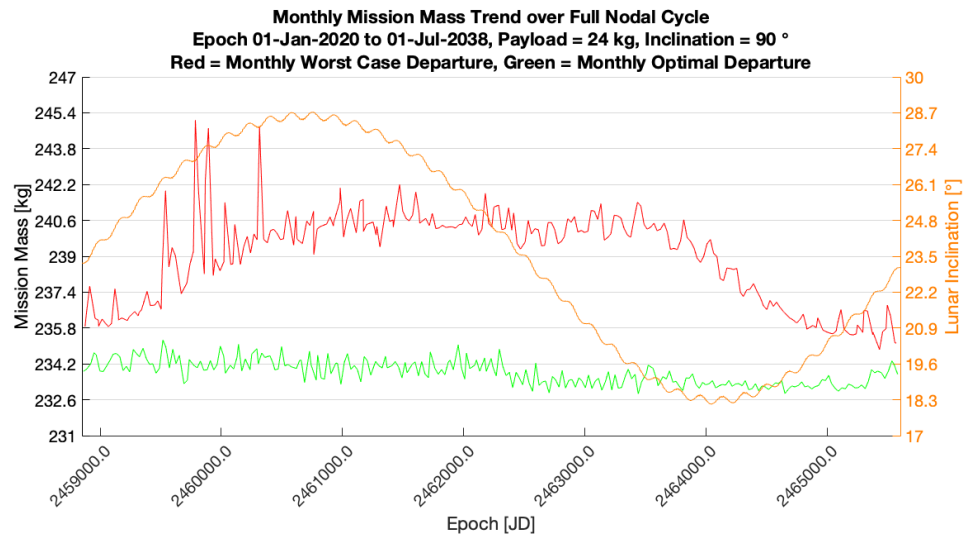
Figure 3.33: Orbit Insertion: Full nodal cycle monthly mission mass extremums vs lunar inclination
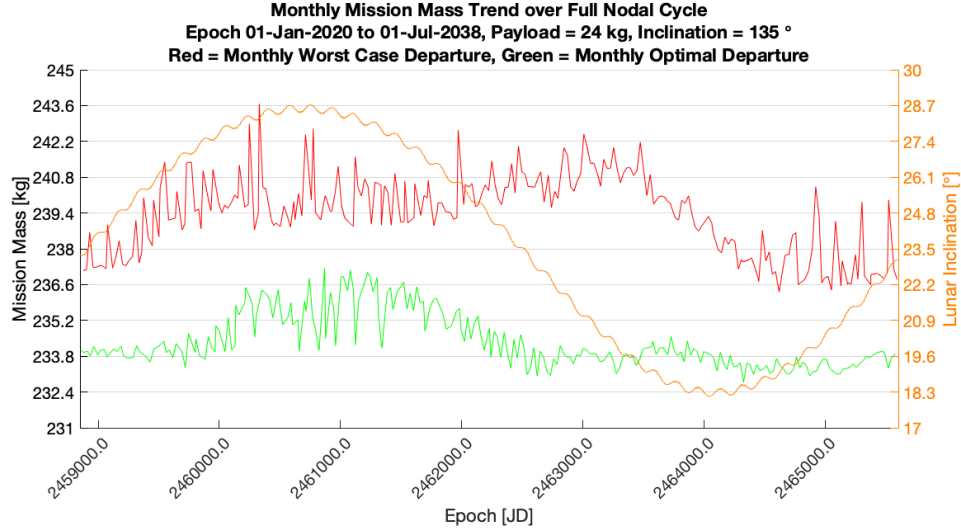
Figure 3.34: Orbit Insertion: Full nodal cycle monthly mission mass extremums vs lunar inclination

These plots allow one to visualize the effects of the complex relationship between performance and the combined effects of the various lunar cycles. The range at epoch is driven by the progress on the moon through its monthly orbit, and of the presecssion of the line of apisides. As demonstrated during the analysis of flyby results, it dictates the energy of the transfer orbit and thus the Δv required to achieve TLI.

Declination is driven by the progressing of the moon through its monthly orbit, the obliquity of Earth's polar axis, the lunar ecliptic inclination, and the precession of the lunar line of nodes. This characteristic drives the alignment of the parking orbit to the lunar position upon arrival. Thus, it dicates the relative velocity in the LCI frame. The lower the relative angle between the arrival vector and the lunar velocity vector, the lower the relative velocity upon arrival, thus the less energy is required for orbit insertion.

The trends seen above are the result of an ever changing combination of range and declination turning through the 27.3 day, 7 month, 1 year, 8.9 year and 18.6 year cycles of the Earth-Moon system.

In the study of these trends, several interesting observations can be made. First, despite significantly higher epoch sensitivity in mission performance when compared to the flyby case the monthly minima (designated in green) remains relatively stable throughout the entire nodal cycle for all inclinations with the exception of 0°. Though there is some noise around major standstill in the +/- 135° cases, the variations in optimally phased mission mass are limited to approximately 4 kg. It is the maxima that are observed as susceptible to the nodal cycle, trending towards a higher mission mass in the first half of the cycle, then consistently dropping off to converge to a minima near the end of the second half from 2030 to 2038. These observations are useful in the selection of optimal phasing. From them, one can observe that an efficient launch window may be selected each month throughout the entire nodal cycle, thus enabling lunar departure to be both frequent and adaptable to launch opportunities.

The 0° arrival case shows a variation of 40 kg at the point of maximum difference between extremums, however, interesting phenomena can be seen at the points of maximum and minimum lunar inclination. At major standstill, the lunar inclination briefly equals the parking orbit inclination of 28.5°. For this short time, the translunar coast is perfectly planar. Under this condition, a low arrival inclination may be accessed directly without a high IAB burn and the relative arrival inclination and velocity are low. These two factors reduce the mission mass of the monthly worst case departure.

At minor standstill, the difference in lunar and transfer orbit inclinations reaches a peak, and a very large IAB burn is required to achieve a 0° arrival and relative velocity is large. As a result, the mission mass of the monthly optimal departures spikes for several years.

Assuming an optimal monthly departure time, the expected range in mission mass across the analysed payloads and arrival inclinations may be characterized

statistically. Figure 3.35 provides the mission mass distribution for monthly minima across the full nodal cycle for a 0 kg payload mass. The inclination/payload set providing the lowest $\mu - 1\sigma$ mission mass across the entire sample space is -45°/0 kg at 147.30 kg.

Figure 3.36 provides the mission mass distribution for monthly minima across the full nodal cycle for a 24 kg payload mass. The inclination/payload set providing the highest $\mu + 1\sigma$ mission mass across the entire sample space is 0°/24 kg kg at 237.90 kg.

These two extremums provide the upper and lower bounds of the sample space, such that any combination of payload mass from 0-24 kg and arrival inclination from -135° to 135° will require a mission mass between 147.60 kg and 237.90 kg.

In contrast to flyby, the arrival inclination and departure epoch have a significant impact on overall performance and therefore must be selected carefully by mission designers to optimize mission mass for launch vehicle characterization.

The statistical distributions for all monthly minima across the Earth-Moon nodal cycle is provided for each payload mass within Appendices C (mission mass and flight time) and D (Δv and burn time).
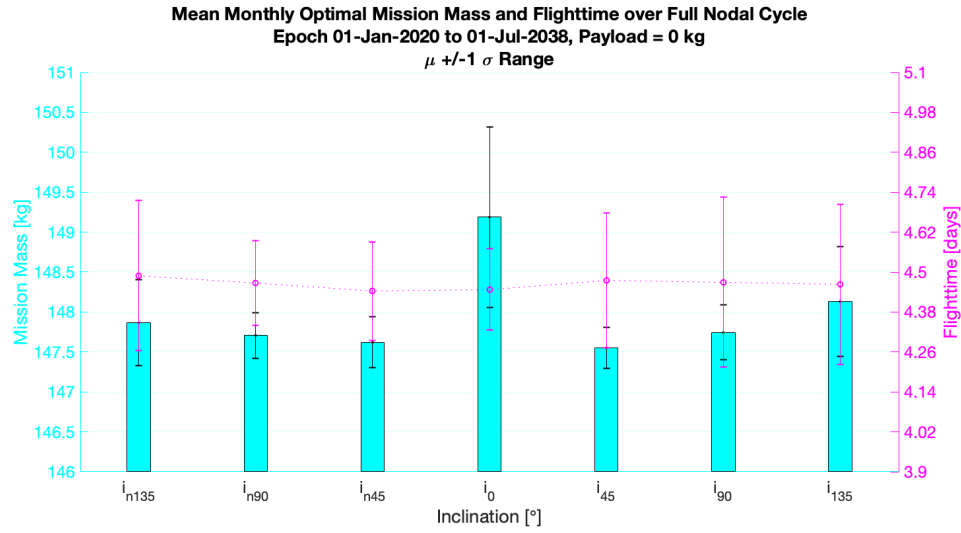
Figure 3.35: Orbit Insertion: Full nodal cycle mean optimal mission mass and flight time distribution, 0 kg Payload
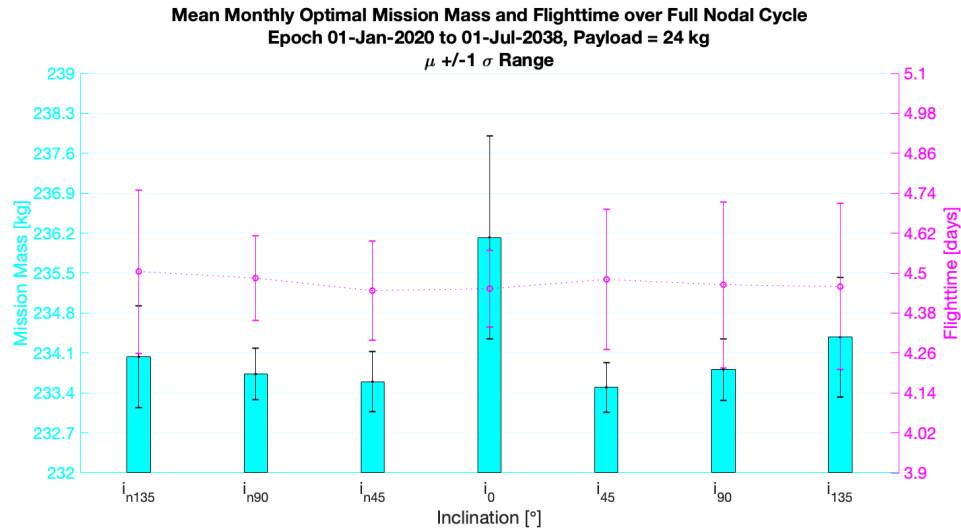
Figure 3.36: Orbit Insertion: Full nodal cycle mean optimal mission mass and flight time distribution, 24 kg Payload

3.4 Landing

Shape Language Modeling was applied to the filtered landing mission mass data for the extrapolation of parameter dependent trends. A year long sample (01 Jan 2020 - 01 Jan 2021) for a 24 kg payload across all inclinations clearly demonstrates the monthly oscillation as observed in the flyby and orbit insertion cases, though with significantly more noise in the sinusoidal profile.
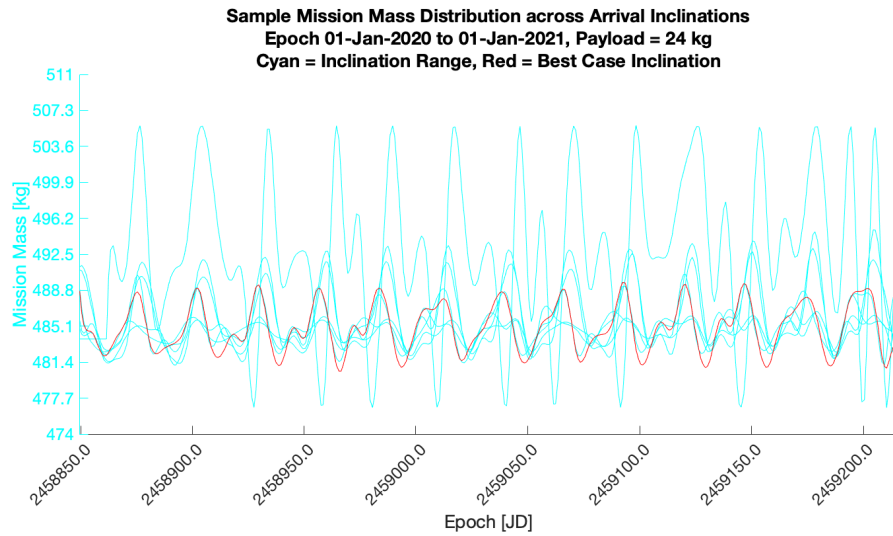
Figure 3.37: Landing: Sample mission mass across lunar arrival inclinations

This is due to the significant mass of landing propellant (from 53.1 kg to 63.7 kg depending on payload mass) that must be carried as payload throughout the TLI and LOI maneuvers. The increased vehicle mass amplifies variations in overall propellant consumption between data points. The sharp peaks at the extremums of the monthly cycle cause the SLM toolbox to produce an erroneous fit that does not accurately represent to the true form of the oscillations.

As a result, one must rely directly upon the filtered data to visualize monthly trends. Whilst this technique is conservative in characterizing the maxima and minima of the steep oscillations seen in the 0° arrival case, it provides a robust solution for all other arrival inclinations.

126
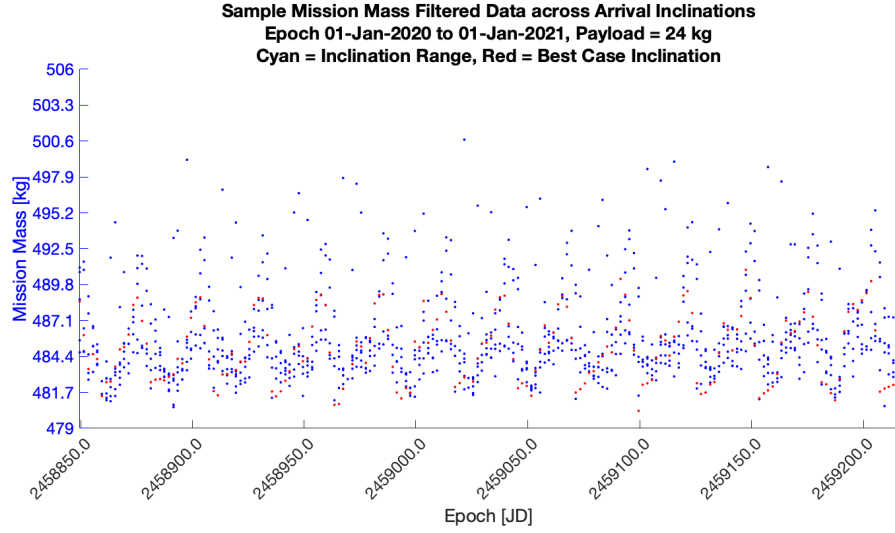
Figure 3.38: Landing: Sample mission mass filtered data

As discerned from a study of figure 3.38, the largest fluctuations between worst case and best case monthly departure epochs over the sample period for non-equatorial arrivals is approximately 10.8 kg of mission mass, compared to 5 kg and 0.8 kg seen in the equivalent orbit insertion and flyby samples respectively.

Figure 3.39 demonstrates a one year sample (01 Jan 2020 - 01 Jan 2021) at a 90° arrival inclination for payload mass dependency.
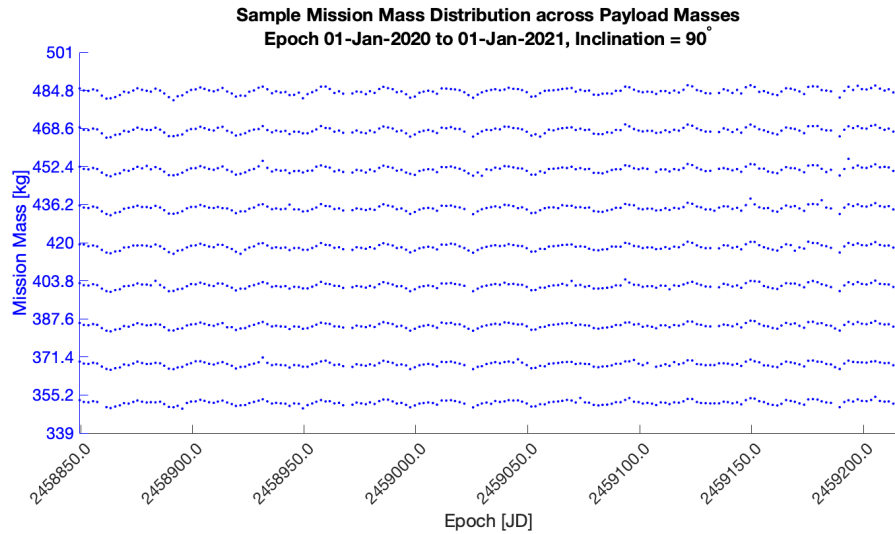
Figure 3.39: Landing: Sample mission mass across payload masses

A 3 kg increase in payload mass corresponds to a near constant increase in

127

mission mass of 16.0 kg at the lower end of the payload scale, and 16.3 kg at the top end. This is a greater relative difference than the equivalent orbit insertion and flyby samples for which respective differences of 10.8 kg and 8.2 kg between increments were observed. This result proves intuitive. As well as the additional 3 kg of payload, each increment requires approximately 1.3 kg of additional landing propellant. This combined 4.3 kg incremental step in dry + landing propellant mass requires additional propellant consumption to facilitate longer TLI, LOI, and IAB burns.

Like the orbit insertion case, landing missions demonstrate an efficiency reduction at longer burn durations due to the Oberth Effect. This efficiency drop manifests as a 0.3 kg growth in the mission mass increase per payload increment over the payload range.

Payload mass no longer dominates mission mass. For +/- 135°, 90°, and 45° arrival inclinations, the 10.8 kg variation between monthly departure extremums is comparable to the 16.5 kg variation between payload mass increments. Though not characterized by shape language modelling, one can expect the epoch dependency of the 0° arrival to be substantially higher still. This 0° arrival upper bound was not explored further. As any real-world lunar landing trajectories would be built around an optimal monthly departure, understanding the precise mission mass penalty of a worst case departure was not deemed critical.

The data arrays for a one year landing sample were filtered for the monthly minima. For the one year sample of a 24 kg payload mission, figure 3.40 demonstrates the statistical distribution of mission mass and flight time for optimal monthly departures across the inclination range. Both mean and +/- 1σ ranges are presented.

The -45° arrival inclination corresponds to the lowest mean mission mass for optimal monthly departures. Mission mass is observed to increase for the outer inclinations, though, as seen in the orbit insertion case, the +135° arrival has a lower

128
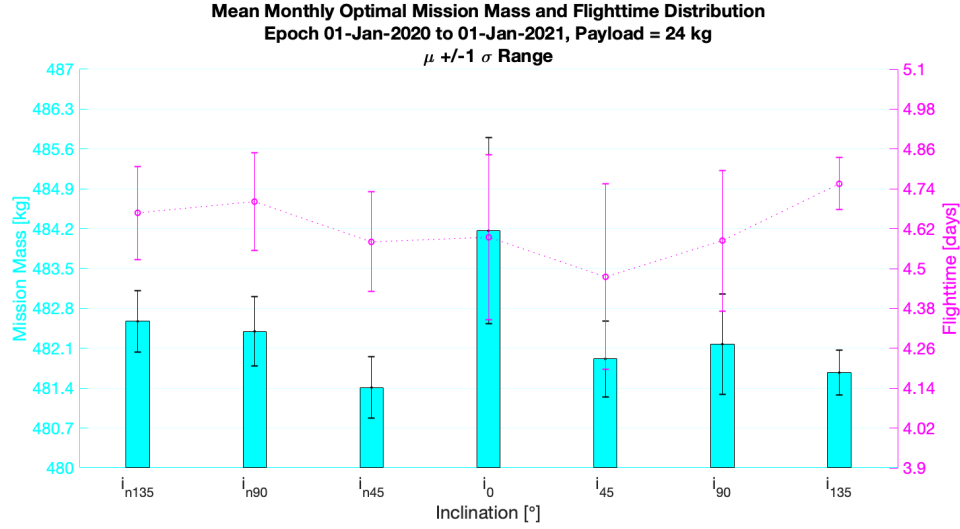
Figure 3.40: Landing: Sample mean optimal mission mass vs lunar range

mission mass than the +/- 90° cases for this particular sample. The largest mission mass mean and variance by a significant margin is that of the 0° degree arrival which exceeds that of the best case inclination by approximately 2.1 kg, compared to 0.2 kg and 1.4 kg observed in the flyby and orbit insertion cases respectively. One can conclude that landing trajectories have a substantially higher dependency on each of the input parameters than the orbit insertion profile. As with the flyby and orbit insertion missions, the mean flight times have a high variance, and therefore do not demonstrate a clear trend across inclinations. The +/- 1σ for all flight times fall between 4.22 and 4.86 days.

Across the same 2020, 24 kg payload sample, figure 3.41 demonstrates the monthly minima total burn duration (TLI + LOI + IAB + PL + C + DO + B + L) and Δv mean values and +/- 1σ bounds across the inclination range.

As expected, the results are proportional to mission mass magnitudes with a sample Δv range of 6201 m/s to 6219 m/s from the 400 km Earth parking orbit to touchdown on the lunar surface. These values are closely aligned with Apollo 11 and Apollo 12 Δv values of 6267 m/s and 6178 m/s respectively for similar descent profiles. The Δv increase at the 0° arrival inclination is again due to disproportion-
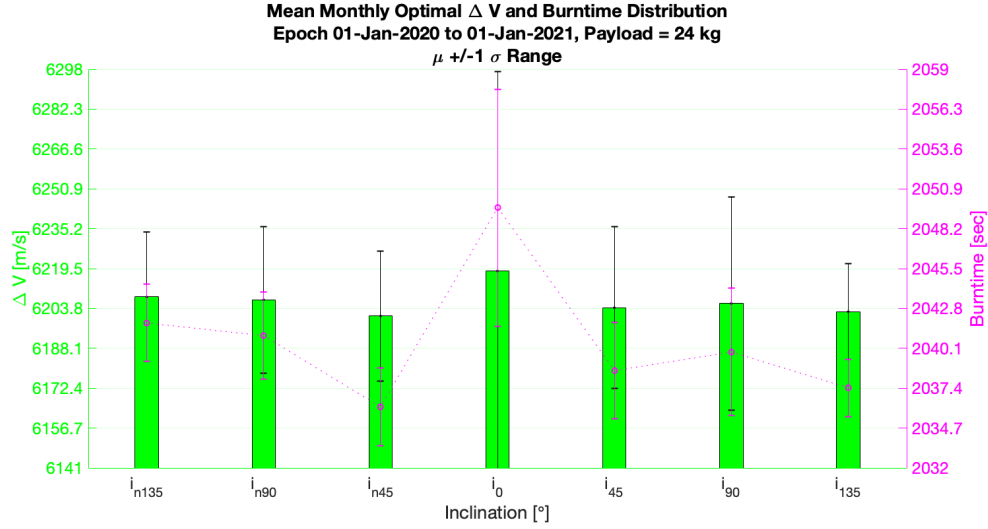
Figure 3.41: Landing: Sample mean optimal ΔV and burn time distribution

ately high IAB burn durations required for plane corrections.

To study the epoch dependency of orbit insertion missions, a one year, 24 kg payload, 90° arrival sample of monthly extremums was compared to lunar range from JPL Horizons.
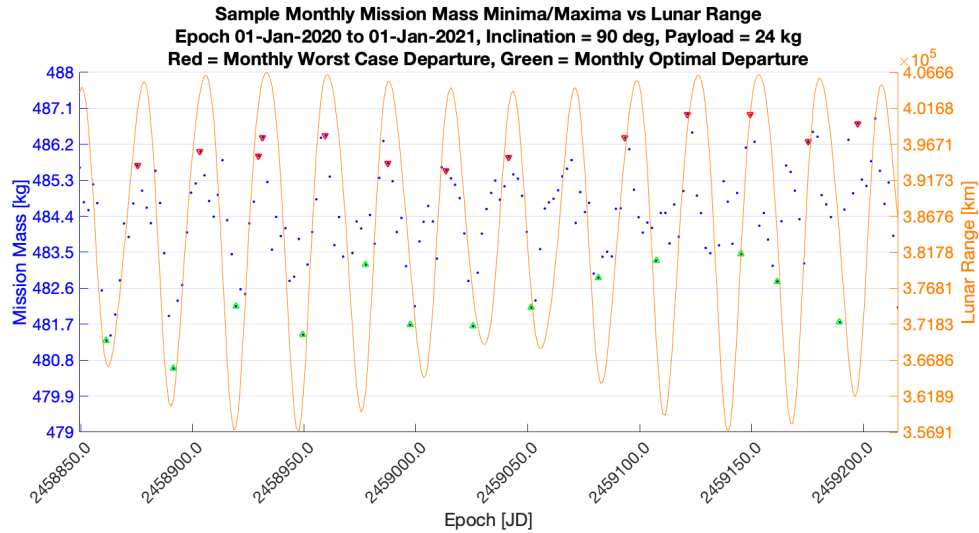
Figure 3.42: Landing: Sample monthly optimal and worst case mission mass vs lunar range

From figure 3.42, it is apparent that - as with the orbit insertion missions - no clear causal relationship can be observed between the individual periodic cycles,

and the monthly optimal departures. To characterize epoch dependency due to secular cycles, the monthly maxima and minima mission mass values was plotted for each arrival inclination over the full 18.6 year nodal cycle.

The blue line represents the maximum mission mass of 490 kg for which the configuration defined in chapter 2 is valid (a bound set by the propellant tank design). Mission mass values above this line are included graphically as an indication, though are omitted from statistical distributions presented herein.
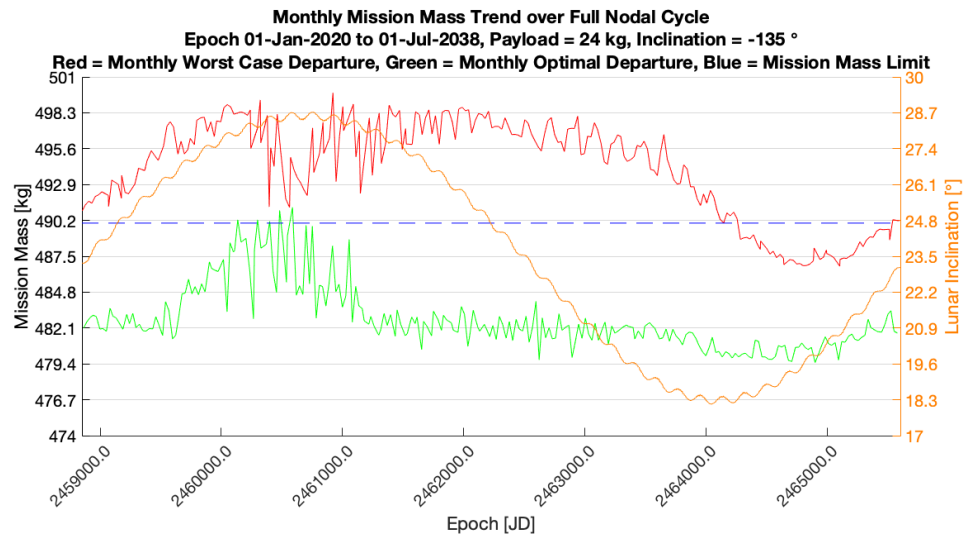
Figure 3.43: Landing: Full nodal cycle monthly mission mass extremums vs lunar inclination
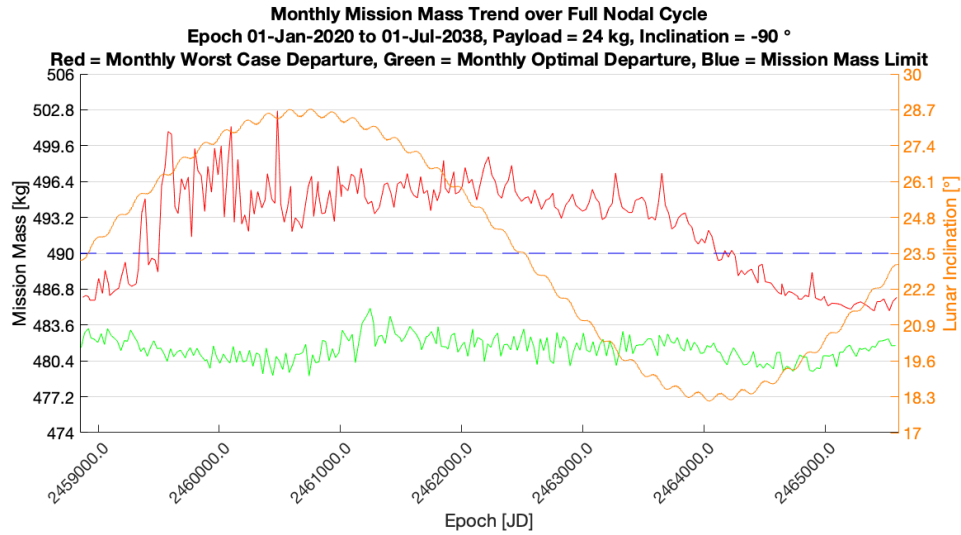
Figure 3.44: Landing: Full nodal cycle monthly mission mass extremums vs lunar inclination
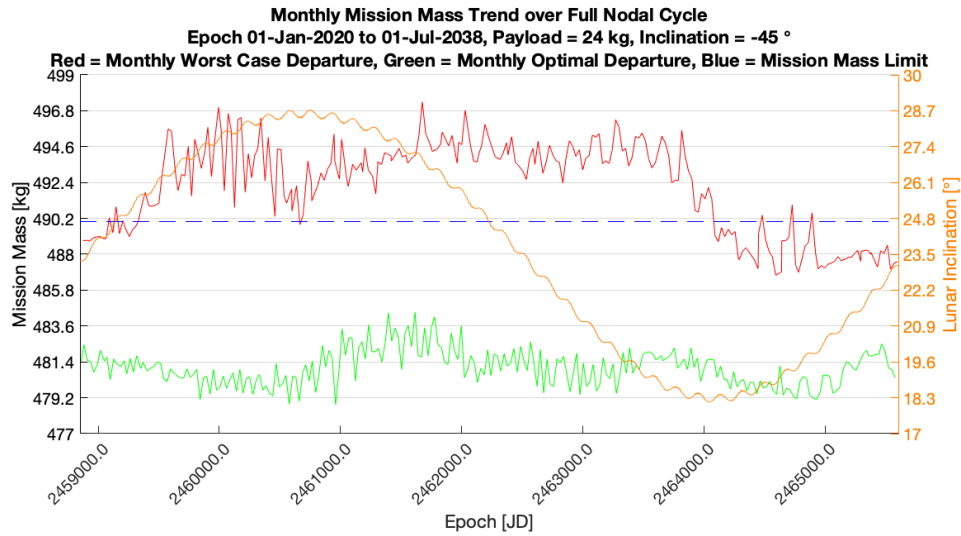
Figure 3.45: Landing: Full nodal cycle monthly mission mass extremums vs lunar inclination
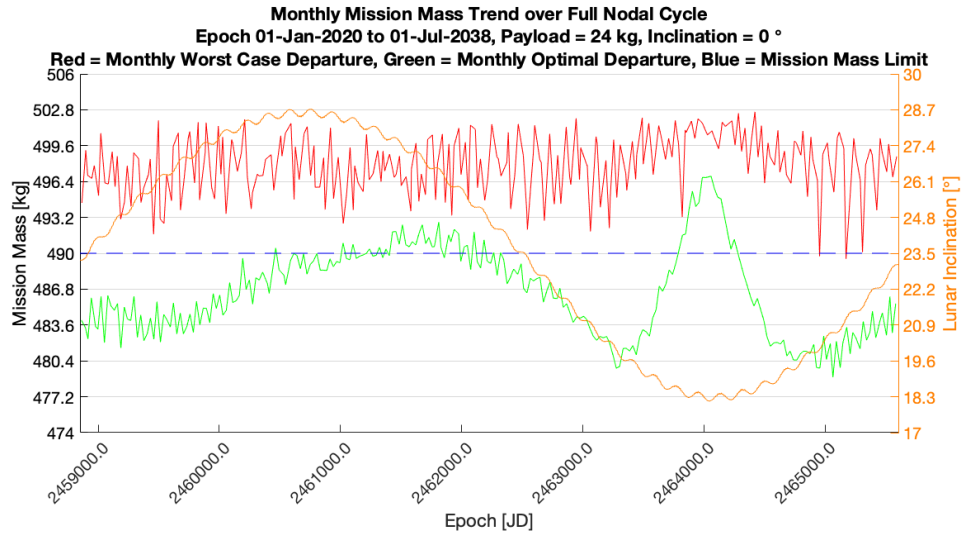
Figure 3.46: Landing: Full nodal cycle monthly mission mass extremums vs lunar inclination
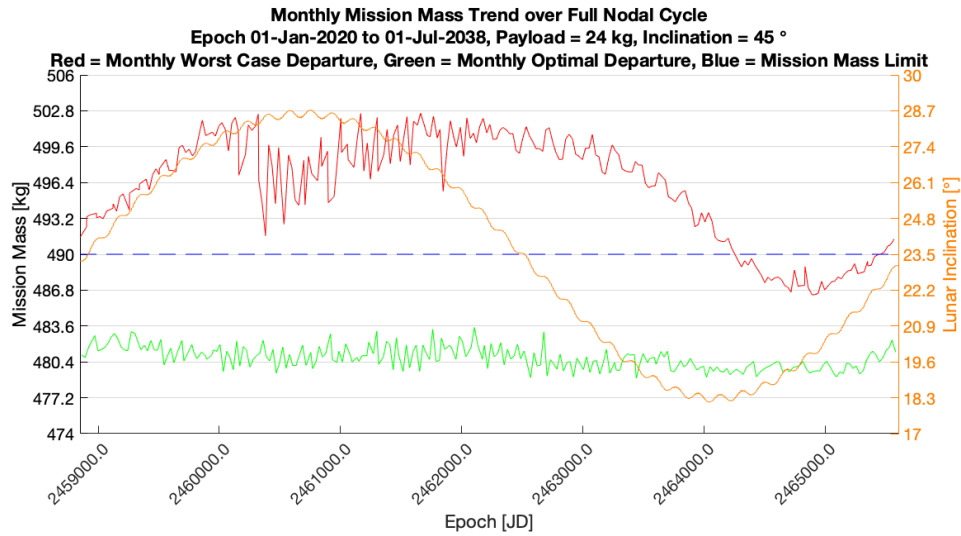
Figure 3.47: Landing: Full nodal cycle monthly mission mass extremums vs lunar inclination
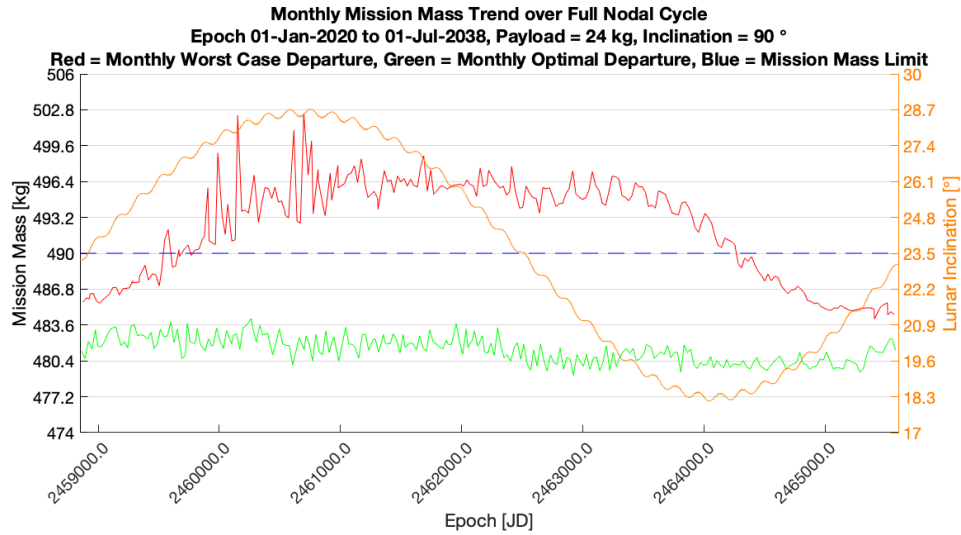
Figure 3.48: Landing: Full nodal cycle monthly mission mass extremums vs lunar inclination
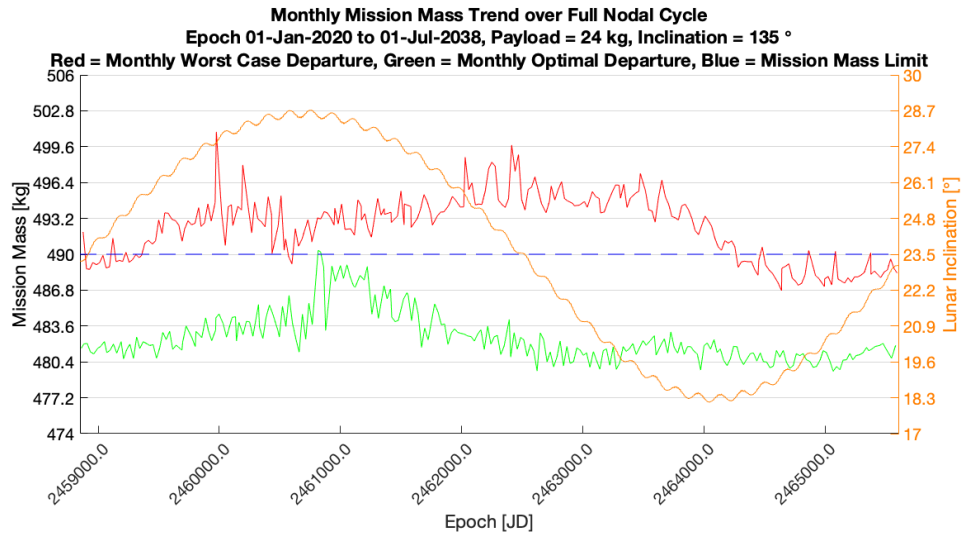
Figure 3.49: Landing: Full nodal cycle monthly mission mass extremums vs lunar inclination

Assuming an optimal monthly departure time, the expected range in mission mass across the analysed payloads and arrival inclinations may be characterized. Figure 3.50 provides the mission mass distribution for monthly minima across the full nodal cycle for a 0 kg payload mass. The inclination/payload set providing the lowest $\mu - 1\sigma$ mission mass across the entire sample space is 45°/0 kg at 348.60 kg.

Figure 3.36 provides the mission mass distribution for monthly minima across the full nodal cycle for a 24 kg payload mass. The inclination/payload set providing the highest $\mu + 1\sigma$ mission mass across the entire sample space is 0°/24 kg kg at 489.90 kg.

These two extremums provide the upper and lower bounds of the sample space, such that any combination of payload mass from 0-24 kg and arrival inclination from -135° to 135° will require a mission mass between 348.60 kg and 489.90 kg.

Given the additional propellant mass required for the multiple burns of the lunar landing segment, the arrival elements and departure epoch have a pronounced effect on overall performance - far more so than for flyby or orbit insertion missions. Therefore, these parameters must be selected carefully by mission designers to optimize mission mass for launch vehicle characterization.

The statistical distributions for all monthly minima across the nodal cycle is provided for each payload mass within Appendices E (mission mass and flight time) and F (Δv and burn time).
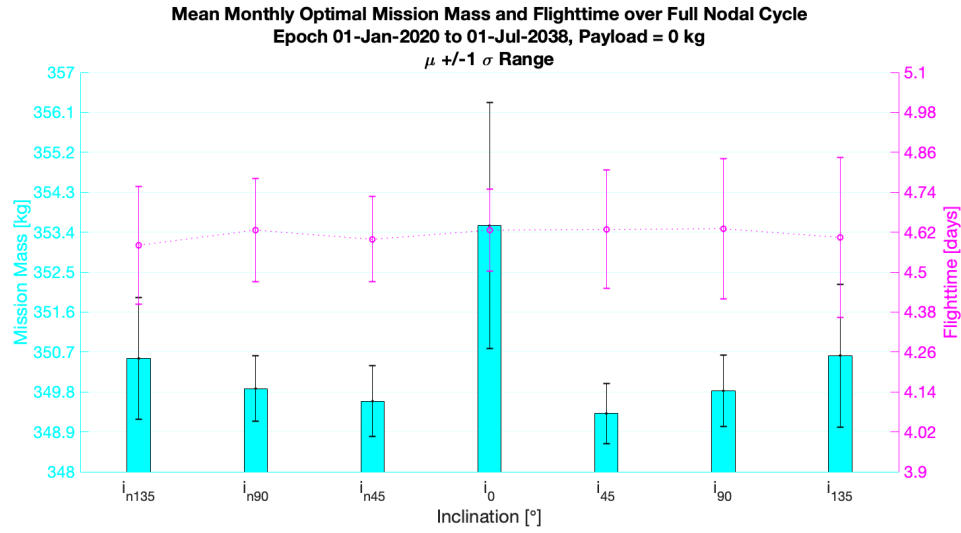
Figure 3.50: Landing: Full nodal cycle mean optimal mission mass and flight time distribution, 0 kg Payload
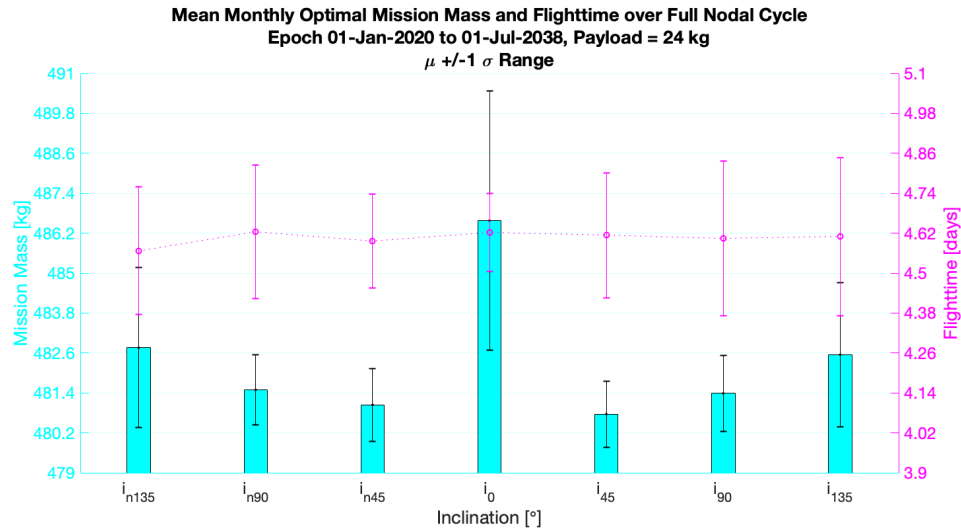
Figure 3.51: Landing: Full nodal cycle mean optimal mission mass and flight time distribution, 24 kg Payload

3.5 Phased Translunar Injection

The results presented above characterize the mission mass for a multitude of lunar missions based on a high thrust, direct injection translunar trajectory. As discussed in chapter 2, this architecture offers a sound "baseline" measure of the performance required to achieve cost competitive, high-cadence, lunar missions to useful range of lunar orbits and landing sites.

It does so by leveraging flight proven bi-propellant propulsion technology. Recognizing that navigation, communication, power, and environmental endurance are non-trivial factors beyond LEO, the fast transfer times associated with direct injection maximize scientific return over the finite life of the payload whilst minimizing Van Allen radiation exposure.
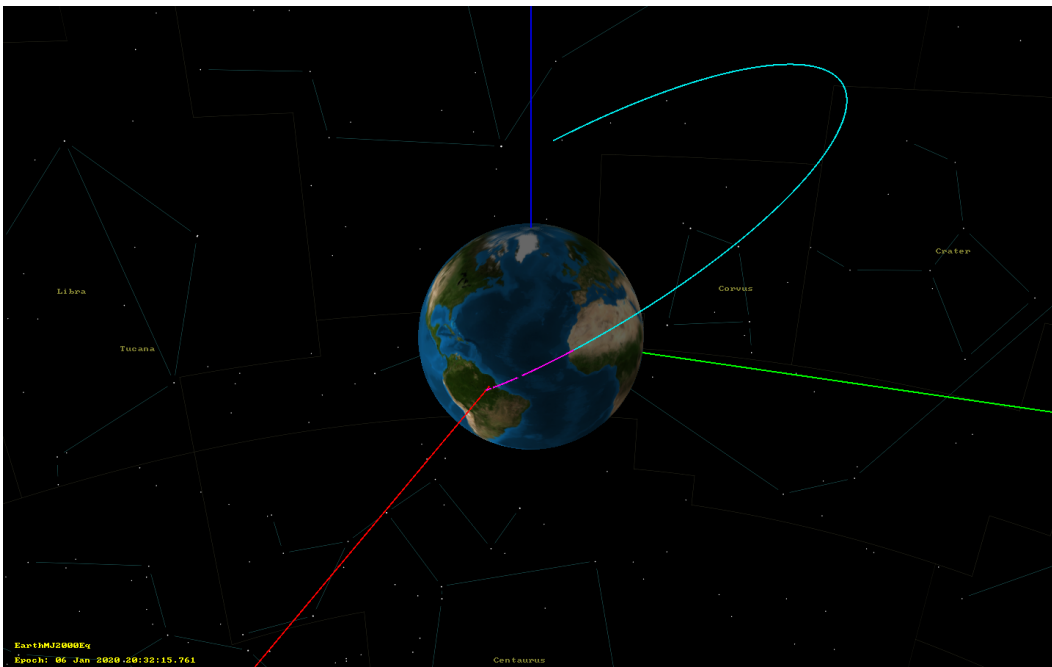
Figure 3.52: Direct injection profile

It is, however, interesting to consider the performance improvements that can be made through the application of phasing loops as applied to the recent Beresheet and Chandrayaan 2 missions.

These loops take advantage of the Oberth effect, whereby for a set thrust and burn duration, maximum mechanical energy may be imparted upon a spacecraft (and, correspondingly, the point of minimum mechanical energy imparted upon the exhaust gases) when the spacecraft is travelling at its highest orbital velocity. This occurs at periapsis passage.

For spacecraft with low thrust to weight ratios, burn duration required for translunar injection may be in the order of several hundred to several thousand seconds. At orbital speeds, this means that the majority of the TLI burn may occur far from perigee.

By partitioning the TLI burn into a series of short maneuvers that progressively raise the apogee altitude, each burn makes use of the Oberth effect for greater efficiency, thus reducing the overall thrust duration required to reach the same transfer orbit.
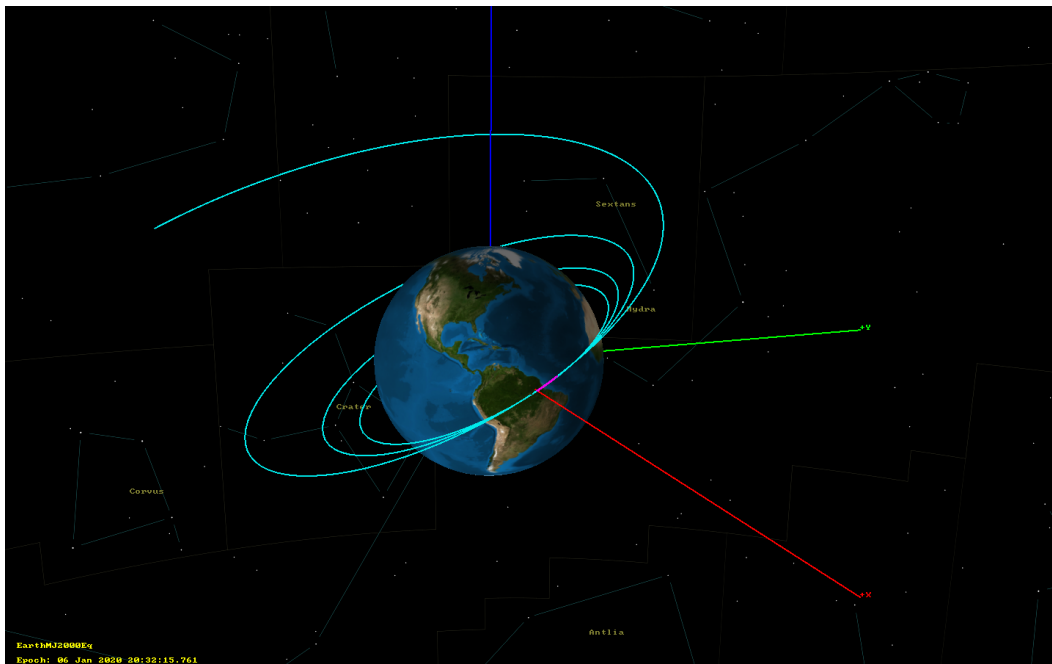
Figure 3.53: Phased injection profile

To model the performance advantages of phasing loops, a GMAT analysis was applied to compare direct and phased lunar flyby trajectories. The algorithm prop-

agated two spacecraft from an Earth parking orbit to an apogee of 403,898 km - the lunar radius at the analysis epoch of 01 Jan 2020, 00:00:00 UTC per JPL Horizons ephemerides. Spacecraft A applied a single TLI burn for a direct injection. Spacecraft B applied 3 phasing burns followed by a final TLI burn, each spaced evenly over the perigee of each successive orbit. The GMAT algorithm adjusted timings such that all four burns had equal duration at that the cumulative burn duration resulted in zero residual propellant mass. The variable parameter used in the targeting sequence was initial propellant mass. As a result, the trajectories produced are optimized to reach an apogee at lunar distance just as the propellant tanks are depleted, thus providing the minimum required mass ratio for TLI.

The assumptions for the TLI stage were the same as detailed in chapter 2. The main engine provided 635 N of thrust at an I_{sp} of 317 s. The propellants were 1021 kg/m^3 Hydrazine fuel and 1370 kg/m^3 MON oxidizer with a 0.541:0.459 o/f ratio. A payload mass of 24 kg (a 12U cube satellite) was applied.

The analysis results are summarized in table 3.1.

Table 3.1: Direct vs phased translunar injection, full thrust

Spacecraft	Direct, Full Thrust	Phased, Full Thrust
Dry Mass [kg]	65.50	65.50
Thrust [N]	635	635
I_{sp} [s]	317	317
Burn Duration [s]	552.61	545.77
Propellant Cons. [kg]	112.84	111.44
Mission Mass [kg]	178.34	176.94 (-1.40)
Flight Time [days]	5.37	5.81 (+0.44)

The use of the phasing loops offered a 1.4 kg reduction in mission mass for the TLI stage configuration applied throughout this study. The flight time increase due to the phasing loops is 0.44 days (assuming a single orbit between burns).

One might observe that with a 635 N thruster sized to enable lunar landing,

the thrust to weight ratio achieved with a flyby propellant load is high. For orbit insertion or landing missions, this thrust to weight ratio is greatly reduced by the propellant mass required upon lunar arrival - a mass that is effectively carried as payload throughout the TLI maneuvers. To emulate a lower thrust-to-weight, the same analysis was performed at a 50% thrust level of 318 N.

Table 3.2: Direct vs phased translunar injection, half thrust

Spacecraft	Direct, Half Thrust	Phased, Half Thrust
Dry Mass [kg]	65.50	65.50
Thrust [N]	318	318
I_{sp} [s]	317	317
Burn Duration [s]	1146.98	1092.49
Propellant Cons. [kg]	117.29	111.72
Mission Mass [kg]	182.78	177.21 (-5.57)
Flight Time [days]	5.38	5.85 (+0.47)

The results in table 3.2 demonstrate a 5.57 kg reduction in mission mass - a considerable quantity in the context of launch vehicle lift capacity. This performance difference is due to the efficiency losses of an increased burn duration required for TLI with a lower thrust-to-weight ratio (driven by the Oberth Effect). The direct approach will require the TLI burn end much farther from perigee, making the efficiency loss more pronounced. Flight time is increased by 0.47 days (assuming a single orbit between burns).

This analysis demonstrates the increasing advantage in phased TLI architectures as thrust-to-weight ratio reduces. Thus, mission designers may use phasing as a strategy to improve upon the baseline performance figures published in Appendices A - F given high payload and arrival propellant masses such as the orbit insertion and landing cases. However, phasing can only be applied in the specific case where the payload can tolerate increased translunar flight time and Van Allen exposure.

3.6 Low Thrust Propulsion

A prominent alternative to the high thrust, direct injection architecture is a low thrust translunar trajectory. The advantage of low thrust propulsion is a significant improvement in propellant mass efficiency due to high specific impulse. This mission architecture is fundamentally different to the one presented throughout this research, though it is interesting to quantify the mission mass and flight time differences for comparative analysis.
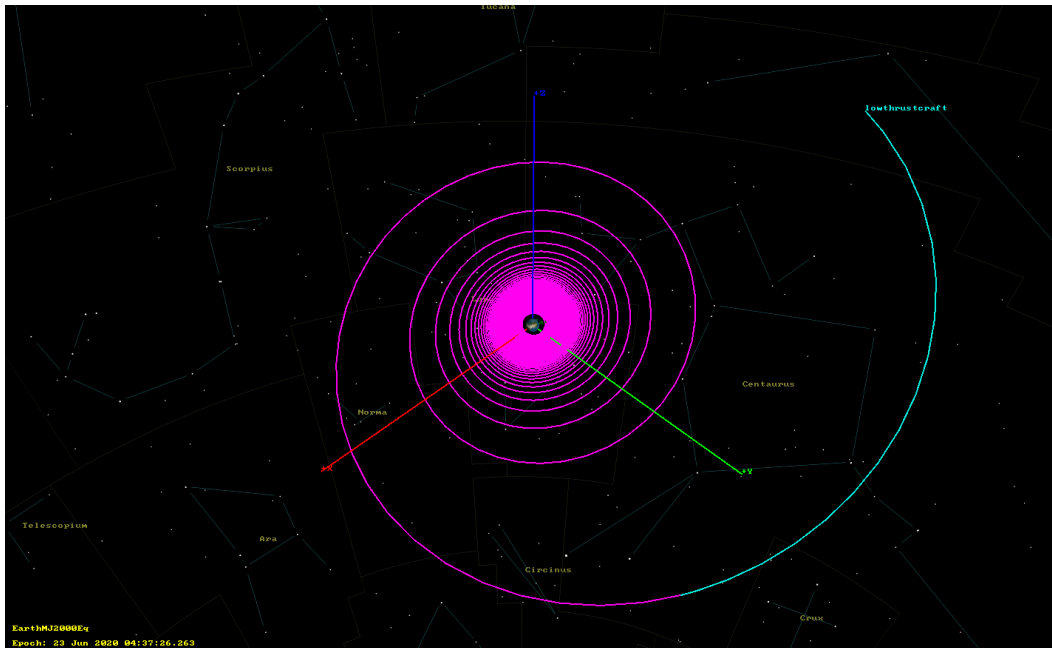
Figure 3.54: Low thrust lunar transfer

To this end, a GMAT algorithm was written to propagate a low thrust trajectory to the lunar orbital radius. This model was based upon a mature low-thrust engine - the Hall effect thruster.

This engine type generates an electro-magnetic field to ionize and accelerate a small quantity of gaseous propellant to produce a directed plume of very high velocity plasma. The Busek BHT-200 is a Hall effect thruster with proven flight heritage aboard TacSat-2 in 2006, FalconSat-5 in 2010, and FalconSat-6 in 2018.

Using Xenon as the gaseous propellant, the BHT-200 draws 200 W of electrical power (250 V at 0.8 A) to produce 13.2 mN of thrust at a specific impulse of 1390 s. The dry mass for a single BHT-200 module is 1100 g.[28].

Based on iterative GMAT test runs at progressively increasing thrust levels, a block of four BHT-200 thrusters was deemed necessary to lift a 24kg payload with appropriate subsystem mass modifications from a 400 km parking orbit to the lunar radius within one year.

To ensure robust results for meaningful comparison, the TLI stage systems designed in chapter 2 were reconfigured to reflect an electric, low thrust propulsion system. The original vehicle required 55.1 W to power the non-propulsive subsystems. Combined with four 200 W thrusters, the total power budget for the Hall thruster vehicle was considered 900 W (including margin). As before, battery capacity was scoped to provide full power for two hours to cover periods of eclipse, resulting in 1800 Wh.

To service these power demand and storage requirements, the same NanoPower BPX Li-ion batteries (154 Wh/kg) and MMA HaWK SolAero XJT solar cells (120 W/kg) as decribed in chapter 2 were used for their energy storage and generation density. Doubling the mass of the solar cells to account for deployables (driven by an increase in the required panel surface area), 11.68 kg of batteries and 14.94 kg of solar panels were added to the TLI stage. Per Larson and Wertz [20], the mass of the PCU was estimated as 2% of the total power consumption, or 18 kg.

The total mass of the system was derived from the chapter 2 vehicle mass, less the original propulsion and power system, with the new BHT-200 thrusters and power system then applied. Again per Larson and Wertz [20], margins of 10% and 2% of total system mass were applied to model structure and harnessing respectively. The resultant low thrust TLI stage was 82.82 kg.

This configuration was modelled in GMAT, assuming a 24 kg payload (repre-

senting a 12U spacecraft), a 10% annual decay on solar panel performance, and an anti-velocity drag area of 1.75 m based on the kW/m^2 performance of the SolAero XJT solar cells.

The same high fidelity Near Earth Propagator was used to apply a continuous thrust from a 400 km altitude, 28.5° inclination parking orbit to the mean lunar range over the nodal cycle, 385,014 km, as derived using JPL Horizons. The GMAT algorithm used a differential correction targeting sequence to optimize the mass of Xenon propellant required to achieve this trajectory, similar to the phasing loop analysis.

The algorithm converged with zero propellant residual to an optimal solution of 50.49 kg of Xenon, at a mission mass of 133.31 kg and flight time of 174.19 days. A direct performance comparison with an equivalent 24 kg payload high thrust flyby trajectory is provided in table 3.3.

Table 3.3: High thrust vs low thrust transfer

Spacecraft	High Thrust	Low Thrust
Main Engine	Bi-Prop. Chemical	Hall Effect
Propellant	N_2H_4, MON	Xenon
Dry Mass [kg]	65.50	82.82
Thrust [N]	635	0.0528
I_{sp} [s]	317	1390
Burn Duration [days]	0.01	167.78
Propellant Cons. [kg]	112.84	50.49
Mission Mass [kg]	178.34	133.31 (-45.03)
Flight Time [days]	5.37	174.19 (+168.82)

As expected, the low thrust model provides a significant mass saving (45.03 kg) due to a high specific impulse, and therefore propulsive efficiency. This is, however, balanced by a large increase in flight time (168.82 days) due to the additional time required to escape Earth's gravity well under low thrust.

The mass reductions associated with low thrust propulsion are certainly beneficial in broadening compatibility with different launch vehicles. However, it is important to note that a low thrust trajectory is a fundamentally different mission architecture. As discussed in chapter 1, the reduced complexity and flight times of direct, high thrust trajectories enable fast, iterative missions for technology validation and viable lunar science whilst limiting environmental endurance demands.

The additional operational complexity of a long duration passage through both the Van Allen Belts and translunar space requires increased thermal and radiation shielding, as well as redundant systems for adequate mission assurance. These steps are essential in justifying the operational commitment of a multi-month transfer for which the cost of maintaining a team of highly skilled operators and access translunar compatible ground stations is significant. The weight penalty of these modifications reduces the mass fraction of the primary payload, thus limiting the scientific outcomes available from a 24 kg bus. Furthermore, a lower tolerance to risk limits the use and validation of new, untried payload technologies - one of the primary value propositions of the mission model proposed by this thesis.

CHAPTER 4

CONCLUSIONS

The goal of this study was to use high-performance computing to characterize direct injection lunar trajectories over a broad parameter space, and in so doing, demonstrate the viability of cost-competitive, high-cadence lunar pathfinder missions using the near-future commercial launch market. The results are intended to provide lunar pathfinder mission designers with a provide a versatile reference for preliminary planning, including optimal departure epochs, and pertinent performance dependencies.

To characterize performance, this study focused on three mission metrics:

Translunar Flight Time: the elapsed time between TLI and passage through lunar periapsis (perilune).

Delta Velocity (Δv): the cumulative total velocity change required to achieve all maneuvers. Used for cross mission comparison.

Mission Mass: the cumulative total mass of payload, spacecraft, and propellant - the total mass that must be lifted into an Earth parking orbit by a launch vehicle. Used for vehicle scoping.

The 2020 - 2038 analysis period with 3397 independent epochs enabled an analysis of trends in mission performance due periodic and secular cycles within the Earth-Moon system, including the 18.6 year precession of the line of nodes, the 8.9 year precession of the line of apsides, the 1 year Earth orbit, the 7 month lunar eccentricity fluctuation, and the 27.3 lunar orbit.

The 9 payload increments from 0 kg to 24 kg gave representation to a realistic suite of small satellite buses - from miniature 1U buses used for technology validation, to 12U spacecraft capable of high value lunar science. As demonstrated by the

145

6U form factors planned for EM1 secondary payloads, this form factor range can enable viable lunar pathfinder missions.

Flyby, orbit insertion, and landing trajectory profiles were computed, along with 7 lunar orbit inclinations between -135° and 135° to encompass prograde and retrograde orbits from equatorial to polar. This ensured representation of a detailed set of arrival conditions upon which propellant consumption and flight time were dependant.

The combination of these parameters resulted in 642,033 lunar trajectories computed by a customized GMAT algorithm. This large sample size provided a global characterization of mission performance demands to answer the four research questions put forward in chapter 1.

4.1 Conclusion 1: Payload Mass Dependency

Research Question 1

What is the relationship between mission mass and payload mass for lunar flyby, orbit insertion, and landing trajectories?

Hypothesis 1

Based on the rocket equation, it is hypothesized that propellant consumption, and therefore mission mass, must increase in proportion to payload mass such that the wet/dry mass ratio is maintained.

Conclusion 1

For flyby missions requiring a single translunar injection burn, payload mass was observed to have the dominant impact on mission mass when compared to epoch and arrival elements. As hypothesized, mission mass increases proportionally with

payload mass at a proportionality coefficient of approximately 2.8 kg per 1 kg of payload (8.2 kg for each measured 3 kg payload increment).

For orbit insertion missions requiring translunar injection burn, lunar orbit insertion, and inclination adjustment burns, payload mass was observed to have the dominant impact on mission mass when compared to epoch and arrival elements, with the exception of the $0°$ arrival inclination (discussed in Conclusion 2). As hypothesized, mission mass increases proportionately with payload mass. However, an unanticipated result is that the proportionality coefficient between mission mass to payload is no longer constant. The coefficient begins at 10.7 kg from 0 - 3kg of payload, increasing to 10.8 kg for 21 - 24 kg of payload. Thus, for a longer cumulative burn duration, the efficiency of the burn is measurably reduced as it occurs further from perigee (the Oberth effect). This phenomenon increases the required mass ratio and demonstrates the importance of modelling finite burn durations as opposed to impulsive maneuvers for improved accuracy. The Oberth effect requires more propellant be consumed to achieve the same trajectory.

For landing missions requiring translunar injection, lunar orbit insertion, and inclination adjustment, perigee lowering, circularization, de-orbit, braking, and landing burns, payload mass was no longer observed to have a dominant impact on mission mass. Its effect was instead observed as comparable to departure epoch selection. The same variable proportionality coefficient observed in the orbit insertion case was seen again, though the magnitude of the variation was higher due to a longer cumulative burn time. The ratio began at 16.0 kg from 0 - 3 kg, increasing to 16.3 kg from 21 - 24 kg.

Thus, it is concluded that mission mass increases proportionately with payload mass, with the proportionality constant driven burn duration - a function of mass, thrust magnitude, and specific impulse. This disproved the hypothesis that the mission mass/payload mass ratio is driven purely by maintenance of the wet/dry ratio.

In the context of lunar mission planning, payload mass has the dominant impact on flyby mission performance. For orbit insertion, payload mass has a dominant impact compared with arrival inclination and epoch with the exception of the $0°$ arrival inclination case, whereby arrival inclination and epoch are comparable. For landing, the impact of payload mass is comparable with arrival inclination and departure epoch for all higher inclination cases, and is low compared to arrival inclination and departure for low inclination cases.

Payload mass has no observable impact on translunar flight time, with +/- 1σ bounds of 4.0 - 4.6 days for flyby, 4.1 - 4.7 days for orbit insertion, and 4.4 to 4.9 for landing.

4.2   Conclusion 2: Arrival Orbital Element Dependency

Research Question 2

What is the relationship between mission mass and the arrival LCLF inclination and right ascension of the ascending node for lunar flyby, orbit insertion, and landing trajectories?

Hypothesis 2

Arrival at a $0°$ inclination corresponds to entry into the lunar sphere of influence at the shortest possible orbital radius from Earth. Given this requires a marginally less energetic transfer orbit, it is hypothesized that a $0°$ arrival corresponds to the lowest propellant consumption, therefore mission mass, and that increasing or decreasing inclinations progressively increase mission mass. Upon insertion into a lunar orbit, it is predicted that a specific LCLF RAAN can be achieved by waiting for the moon to turn beneath the orbit over its 27.3 day rotation, thus RAAN has no effect on mission mass. RAAN is only defined upon orbit insertion, therefore does not pertain to flyby missions

Conclusion 2

For flyby missions, LCLF RAAN is undefined. Without an elliptical lunar orbit, there is no line of nodes. As the moon is tidally locked with Earth, the geography underneath the ground track was driven only by arrival inclination. LCLF RAAN, therefore, had no effect on mission mass for the flyby case as hypothesized, though the available regions of observation are limited.

For orbit insertion and landing missions, the 100 km circular lunar orbit was observed to be stable over the 27.3 day revolution of the Moon in inertial space with high fidelity orbital dynamics . Thus, any LCLF RAAN may be achieved by waiting for the Moon to rotate beneath the orbit without additional expenditure of energy. Upon the assumption that 27.3 days is an acceptable duration for a lunar small satellite in a stable orbit, LCLF RAAN was deemed to have no effect on mission mass for the orbit insertion and landing cases.

With respect to translunar flight time, LCLF RAAN has no impact on flyby, orbit insertion, or landing cases. Total flight time is, however, dictated by the holding period in lunar orbit for orbit insertion and landing cases. Depending in the departure epoch, orbit insertion and landing flight times range from 4.1 - 32.0 days and 4.4 - 32.2 days respectively.

For flyby missions, a 0° prograde arrival LCLF inclination yielded the lowest Δv and mission mass values relative for any given payload. These metrics increased with the absolute value of the inclination, peaking at the +/- 135° retrograde orbits. This effect was, however, small.

As hypothesized, the mission mass deviations were driven by the transfer orbit apogee radius required to place the spacecraft at the right position on the lunar sphere of influence for a correctly inclined approach. A 0° approach required the minimum apogee radius. This apogee radius increased with absolute inclination. However, a unique and unanticipated finding is that the +/- 1σ ranges are small. For

a 24 kg payload mass, the +/- 1σ monthly minimum mission mass range across all inclinations was only 178.76 kg to 179.06 kg.

Orbit insertion and landing missions were found to demonstrate a similar insensitivity to absolute inclinations greater than $45°$. For a 24 kg payload, the difference in monthly minimum mission mass between $45°$ and $135°$ was observed to be 0.8 kg for orbit insertion, and 1.9 kg for landing. However, these mission profiles were highly sensitive at low arrival inclinations. The equivalent mission mass differences between $45°$ and $0°$ was observed to be 2.8 kg and 5.9 kg.

This additional mission mass is a consequence of the inclination errors present at low inclination arrivals. A non-planar arrival to a B-Vector of 0 will retain an LCLF Z-component velocity, and thus will be inserted into a slightly inclined orbit. Lunar gravity is not enough to correct this inclination error passively. As a consequence, a $0°$ inclination cannot be directly accessed upon arrival to the lunar sphere of influence. To correct the error actively, the inclination adjustment burn must provide a large plane change. As orbital plane changes are energy intensive, $0°$ arrivals result in a larger overall Δv, and therefore a higher mission mass.

Higher inclinations can be directly achieved with minimal inaccuracy as they provide additional degrees of freedom for tailoring the arrival vector. With slight adjustments in the TLI burn duration, AOP, and RAAN, these lunar arrival inclinations can be targeted with minimal requirement for passive gravitational correction provided they are higher than the relative inclination of the incoming transfer orbit.

With respect to translunar flight time, LCLF inclination has no significant impact upon flyby, orbit insertion, of landing cases.

4.3   Conclusion 3: Departure Epoch Dependency

Research Question 3

What is the relationship between mission mass and the departure (TLI ignition) epoch for lunar flyby, orbit insertion, and landing trajectories?

Hypothesis 3

Transfer orbit energy is driven by lunar range (defining travel distance), and declination (defining relative inclination and velocity upon arrival). It is hypothesized that flyby mission mass is optimized at minimum lunar range, and that orbit insertion and landing mission mass is minimized at the lowest relative inclination between the transfer orbit and lunar orbit at major standstill (the point of highest lunar inclination with respect to the equator).

Conclusion 3

For flyby missions, performance demand was highly correlated to lunar range upon arrival as hypothesized. The mission mass was observed to oscillate in harmony with lunar range as the Moon travelled through the 27.3 day lunar orbit periodic cycle. Thus, the optimal monthly departure epoch consistently preceded lunar perigee passage by the translunar flight time - the point where lunar range was lowest upon arrival.

As the eccentricity of the lunar orbit changed due to gravitation effects of the Sun and Earth, the radius of perigee (and thus, the monthly optimal performance demand) fluctuated through a 7 month secular cycle.

No clear correlations were observed in either the periodic declination, or the longer term secular cycles of the Earth-Moon system. Furthermore, it was observed that the magnitudes of the range dependent performance oscillations were small -

approximately 0.8 - 0.9 kg for the 24 kg payload case.

It was therefore concluded that, though 27.3 day cycle dependencies were clearly observed, flyby mission performance has a low sensitivity to departure epoch in the context of mission design.

For orbit insertion missions, the departure epoch sensitivity was considerably more pronounced. Variations in optimal and worst case monthly departures was observed to be approximately 5.0 kg for 24 kg payload sample at higher inclinations, and 30 kg in the 0° case as discussed in Conclusion 2). Landing missions displayed similar behaviour with larger magnitudes of dependency, where variations between optimal and worst case monthly departures was observed to be 10.8 kg over the same sample for high inclination arrivals, and >30 kg for low inclinations.

The magnitude of these oscillations is due to the dependence of the orbit insertion and inclination adjustment burns upon the relative inclination and velocity upon arrival. The lower this relative velocity, the less energy is required to achieve the targeted lunar orbit. The relative velocity vector at arrival is a function of lunar range and declination at departure.

The optimal and worst case monthly performance for each arrival inclination was analysed over the full 18.6 year analysis period to characterize trends over the full breadth of range and declination combinations. Two notable conclusions were drawn.

First, in the 0° arrival inclination case, the major standstill event causes a sharp, short term drop in monthly maximum mission mass, while the minor standstill event causes a sharp, temporary increase in monthly minimum mission mass. These events coincide with the minimum and maximum offsets in transfer orbit inclinations. At major standstill, the orbits are temporarily co-planar, thus opening a window for efficient, low arrival inclinations without large inclination adjustment burns. At minor standstill, the incoming transfer and lunar orbits are at the great-

152

est planar offset, thus creating a temporary period where low inclination arrivals require substantially higher inclination adjustment burns to correct large LCLF Z-component velocities. While this behaviour was anticipated around major and minor standstill, it was expected to apply to all arrival inclinations, and manifest as a gradual trend throughout the lunar declination cycle. This hypothesis has been disproved.

Second, while mission mass oscillates between monthly extremums due to the periodic cycles, the performance demand of optimally phased monthly departures remain remarkably constant throughout the secular cycles of the Earth-Moon system. This trend is of particular importance in the context of mission design. It allows an optimal departure in any month of any year with minimal consequence to mission mass, with the exception of low arrival inclinations at minor stand-still.

It was concluded that the careful selection of optimal monthly departure times has a significant impact on both orbit insertion and landing missions.

With respect to transular flight time, no discernible epoch dependencies were observed.

4.4 Conclusion 4: Launch Vehicle Compatibility

Research Question 4

Are direct injection, translunar missions for 0 - 24 kg small satellite payloads compatible with cost-effective launch vehicles in the near-future commercial market?

Hypothesis 4

It is hypothesized that the mission mass required for all direct injection, translunar missions within the parameter space can be delivered to the required parking orbit by the SpaceX Falcon 9 and Blue Origin New Glenn heavy lift vehicles. Furthermore, it is hypothesized that smaller, low-cost commercial launch vehicles can

provide frequent, dedicated parking orbit delivery to a subset of translunar missions for flyby and orbit insertion missions at lower payload masses.

Conclusion 4

To gauge compatibility with the commercial launch market, the *FAA Annual Compendium of Commercial Space Transportation [21]* was used to characterize the cost and payload capacity to LEO of commercial launch vehicles for insertion of the payload and TLI stage into the 400 km, 28.5° inclination Earth parking orbit. This characterization included vehicles that currently launch from KSC, or are at an advanced stage of development and expected to launch from KSC in the near-future.

Noting that optimal monthly performance is remarkably constant across the Earth-Moon nodal cycle, these launch vehicle lift capacities were compared against the highest $\mu + 1\sigma$ optimal departure mission mass bound for each payload mass of the flyby, orbit insertion, and landing missions computed over the full 18.6 analysis period.

Compatibility was characterized by three classes. First, incompatible - a lift capacity below the required mission mass. Second, compatible as a primary customer. This was judged as a mission mass of greater than half the lift capacity of the vehicle, thus making the launch cost effective as a dedicated mission, or as the primary payload aboard a ride share mission. Such a scenario would allow selection of the launch window. Third, compatible as secondary customer. This was judged as a mission mass of less than half the lift capacity of the vehicle, thus making the launch cost effective as a secondary customer aboard a non-dedicated ride share mission.

A distinction was also made between flight proven launch vehicles, and vehicles that are currently at an advanced stage in development, but are yet to achieve orbit.

Mission mass results are mapped to launch vehicle lift capacity in tables 4.1, 4.2,

and 4.3. Against each combination of payload and vehicle, a launch cost estimate is provided using the quoted $/kg to LEO, and the mission mass. It should, however, be noted that these costs are based on data provided by the launch companies. They may be subject to variation from a wide range of factors including inflation, mission complexity, and licensing, amongst many others. Therefore, price values should be used for comparative analysis only. The cost of launch for New Glenn is currently undisclosed.

As hypothesized, the New Glenn and Falcon 9 are both amply powered to support the full suite of missions, as are the Minotaur C, Alpha, and LauncherOne. The Pegasus XL can support all except landing missions of greater than 15 kg. The Electron cannot support landing, but can support all flyby missions, and orbit insertion masses up to 18 kg.

As flyby missions have low sensitivity to departure epoch, they have the flexibility to be launched as a secondary customer aboard ride share flights. For this reason, it is concluded that the cost-optimal launch vehicle for this mission is the Falcon 9 with the lowest $/kg ratio for ride share customers.

Orbit insertion and landing missions are highly departure epoch sensitive. Thus, dedicated missions are preferable for optimal performance. It is therefore concluded that Electron is the optimal launch vehicle for orbit insertion payloads up to 18 kg by offering the lowest cost for a dedicated mission. Pegasus XL is considered optimal flight proven launch vehicle for payloads 21 - 24 kg.

Similarly, it was concluded that Pegasus XL is the optimal flight proven launch vehicle for landing payloads 0 - 15 kg. No flight proven vehicle is sized to support 18 - 24 kg as a primary ride share payload, thus additional costs may be required to dictate the launch window. The Alpha and LauncherOne, though unproven, would prove effective at supporting the full range of lunar landing missions at a competitive rate if the advertised payload capacity and cost prove true.

155

Company	Flyby Launch Vehicle	$/launch	$/kg	Payload Mass [kg]								
				0	3	6	9	12	15	18	21	24
				μ + 3σ Mission Mass [kg]								
				113.25	121.45	129.67	137.89	146.11	154.34	162.57	170.82	179.06
Blue Origin	New Glenn	-	-									
Space X	Falcon 9	62 M	2,719	308	330	353	375	397	420	442	465	487
Orbital ATK	Minotaur C	45 M	32,895	3,725	3,995	4,265	4,536	4,806	5,077	5,348	5,619	5,890
Firelfly	Alpha	10 M	10,000	1,133	1,215	1,297	1,379	1,461	1,543	1,626	1,708	1,791
Virgin Orbit	Launcher One	12 M	24,000	2,718	2,915	3,112	3,309	3,507	3,704	3,902	4,100	4,297
Orbital ATK	Pegasus XL	40 M	88,889	10,067	10,796	11,526	12,257	12,988	13,719	14,451	15,184	15,916
Rocket Lab	Electron	4.9 M	21,778	2,466	2,645	2,824	3,003	3,182	3,361	3,540	3,720	3,900

Launch Vehicle not flight proven
Launch Cost — Compatible, < 50% payload capacity, rideshare customer (Launch cost in 1000 x USD)
Launch Cost — Compatible, > 50% payload capacity, primary customer (Launch cost in 1000 x USD)
Incompatible

Figure 4.1: Flyby mission launch vehicle compatibility

Company	Orbit Insertion Launch Vehicle	$/launch	$/kg	Payload Mass [kg]								
				0	3	6	9	12	15	18	21	24
				μ + 3σ Mission Mass [kg]								
				150.3	161.25	172.2	183.1	194	205	215.9	226.9	237.9
Blue Origin	New Glenn	-	-									
Space X	Falcon 9	62 M	2,719	409	438	468	498	528	557	587	617	647
Orbital ATK	Minotaur C	45 M	32,895	4,944	5,304	5,664	6,023	6,382	6,743	7,102	7,464	7,826
Firelfly	Alpha	10 M	10,000	1,503	1,613	1,722	1,831	1,940	2,050	2,159	2,269	2,379
Virgin Orbit	Launcher One	12 M	24,000	3,607	3,870	4,133	4,394	4,656	4,920	5,182	5,446	5,710
Orbital ATK	Pegasus XL	40 M	88,889	13,360	14,333	15,307	16,276	17,244	18,222	19,191	20,169	21,147
Rocket Lab	Electron	4.9 M	21,778	3,273	3,512	3,750	3,988	4,225	4,464	4,702		

Launch Vehicle not flight proven
Launch Cost — Compatible, < 50% payload capacity, rideshare customer (Launch cost in 1000 x USD)
Launch Cost — Compatible, > 50% payload capacity, primary customer (Launch cost in 1000 x USD)
Incompatible

Figure 4.2: Orbit insertion mission launch vehicle compatibility

Company	Landing Launch Vehicle	$/launch	$/kg	Payload Mass [kg]								
				0	3	6	9	12	15	18	21	24
				μ + 3σ Mission Mass [kg]								
				356.35	372.9	389.5	405.88	423.3	440.1	456.7	473.6	489.9
Blue Origin	New Glenn	-	-									
Space X	Falcon 9	62 M	2,719	969	1,014	1,059	1,104	1,151	1,197	1,242	1,288	1,332
Orbital ATK	Minotaur C	45 M	32,895	11,722	12,266	12,813	13,351	13,924	14,477	15,023	15,579	16,115
Firelfly	Alpha	10 M	10,000	3,564	3,729	3,895	4,059	4,233	4,401	4,567	4,736	4,899
Virgin Orbit	Launcher One	12 M	24,000	8,552	8,950	9,348	9,741	10,159	10,562	10,961	11,366	11,758
Orbital ATK	Pegasus XL	40 M	88,889	31,676	33,147	34,622	36,078	37,627	39,120			
Rocket Lab	Electron	4.9 M	21,778									

Launch Vehicle not flight proven
Launch Cost — Compatible, < 50% payload capacity, rideshare customer (Launch cost in 1000 x USD)
Launch Cost — Compatible, > 50% payload capacity, primary customer (Launch cost in 1000 x USD)
Incompatible

Figure 4.3: Landing mission launch vehicle compatibility

4.5 Final Remarks

Fast, high frequency translunar pathfinder missions hold great promise for advancing NASA's scientific observation, prospecting, and technology validation objectives in translunar space, lunar orbit, and upon the lunar surface.

This thesis provides an accurate reference for pathfinder mission designers by demonstrating the dependencies between mission performance demand, and departure epoch, arrival elements, and payload mass.

Characterized herein are the mission masses, Δv and translunar flight times required to achieve optimally phased missions to a range of tailored lunar arrivals, for a range of small satellite payloads capable of supporting pathfinder objectives. This characterization is based upon a TLI stage with flight proven propulsion technology, high fidelity orbital dynamics, and direct injection flyby, orbit insertion and landing architectures compatible with both dedicated and ride share commercial launches.

To validate the solutions, the statistical distribution of optimally phased Δv demands was directly compared with the Δv records for Apollo 10, 11, and 12 as catalogued by the mission reports. The close alignment between this analysis and an independent source of empirical data provides confidence that the results are robust.

To demonstrate that the proposed architecture is compatible with the near-future launch market, the resultant performance demands were mapped against lift capacities for numerous cost-competitive commercial launch vehicles. This compatibility analysis also provides estimates for comparative launch costs.

Though the payload dependency and compatibility studies are specific to small satellite payloads from 0 - 24 kg, the epoch, arrival inclination, and arrival architecture dependencies are broadly applicable to any payload class that adopts a direct injection transfer.

157

It is hoped the metrics and algorithms found within the appendices of this thesis will serve as a useful guide for future mission designers in this exciting new era of lunar exploration.

Appendices

APPENDIX A

FLYBY: NODAL CYCLE PERFORMANCE DISTRIBUTION FOR
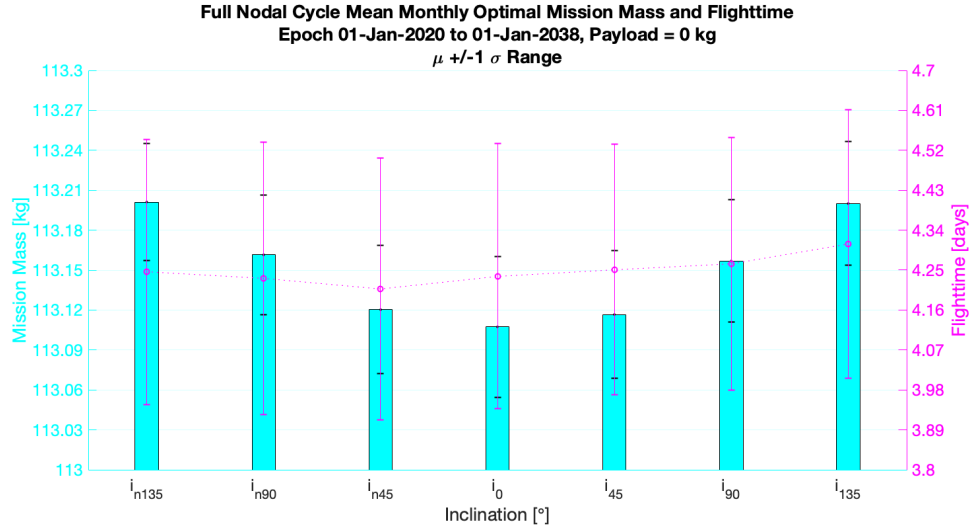
OPTIMAL DEPARTURES - MISSION MASS AND FLIGHT TIME

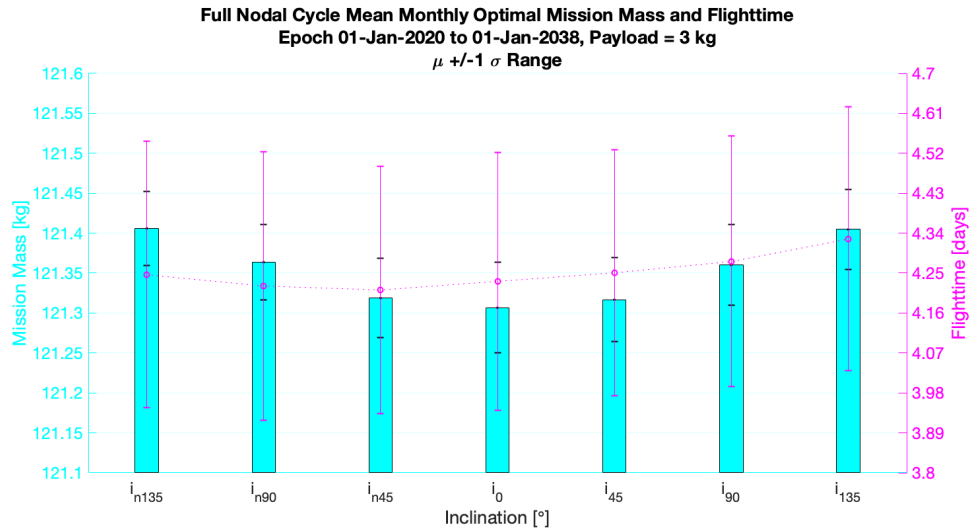Figure A.1: Flyby: Full nodal cycle mean monthly minimum mission mass and flight time distribution, 0 kg Payload

Figure A.2: Flyby: Full nodal cycle mean monthly minimum mission mass and flight time distribution, 3 kg Payload
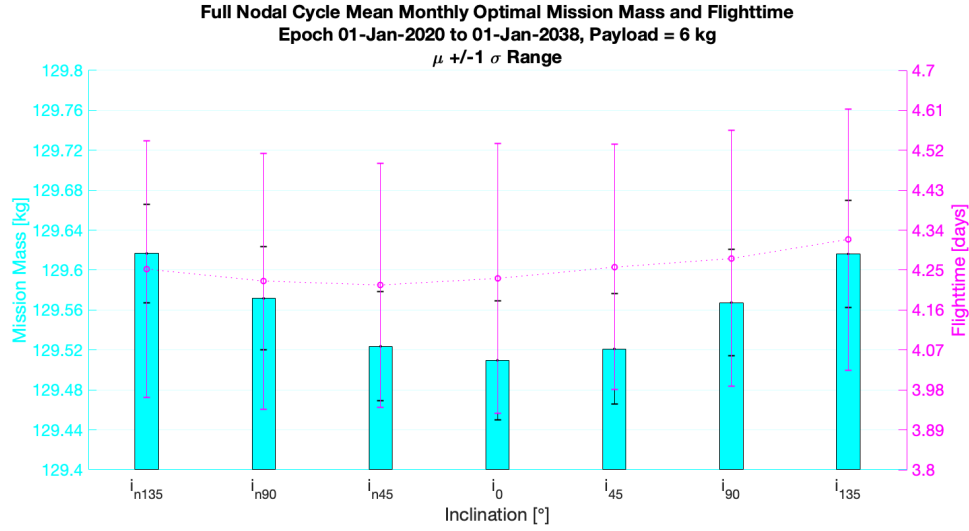
Figure A.3: Flyby: Full nodal cycle mean monthly minimum mission mass and flight time distribution, 6 kg Payload
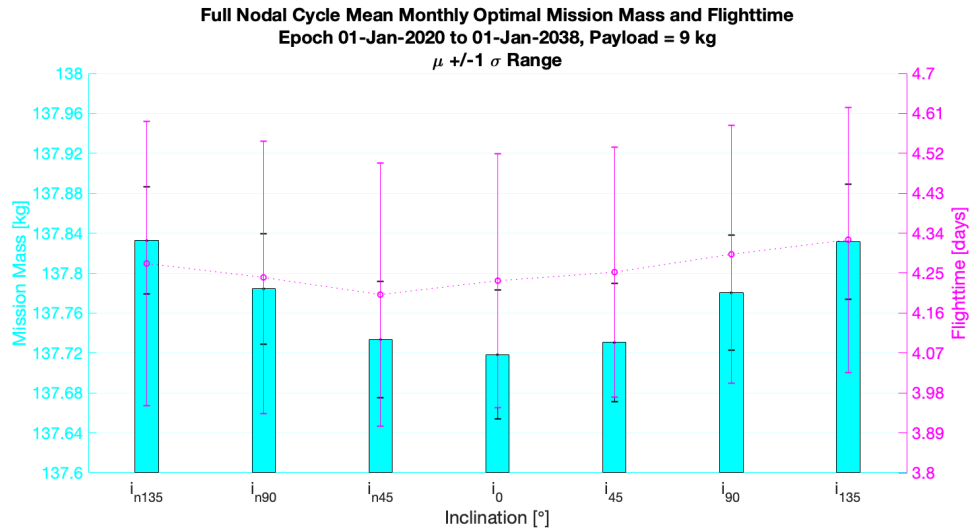

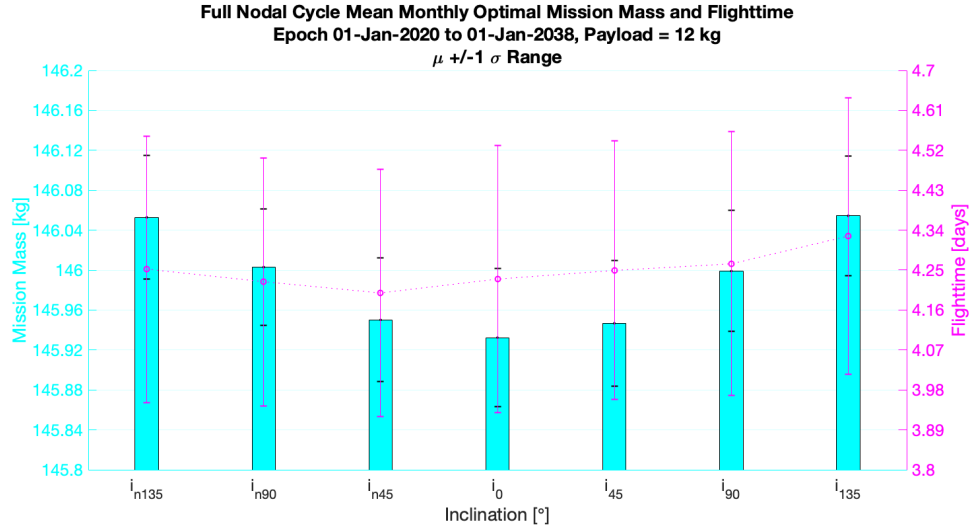Figure A.4: Flyby: Full nodal cycle mean monthly minimum mission mass and flight time distribution, 9 kg Payload

Figure A.5: Flyby: Full nodal cycle mean monthly minimum mission mass and flight time distribution, 12 kg Payload
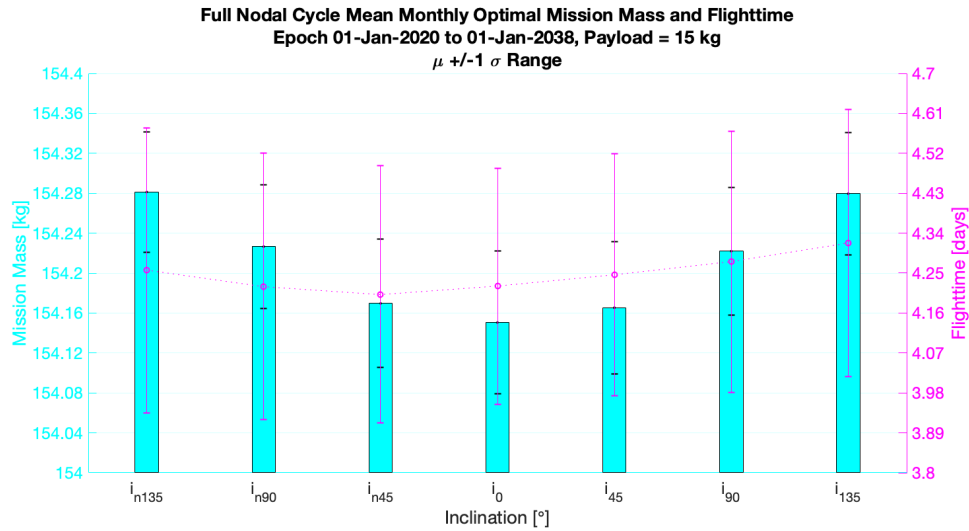

Figure A.6: Flyby: Full nodal cycle mean monthly minimum mission mass and flight time distribution, 15 kg Payload
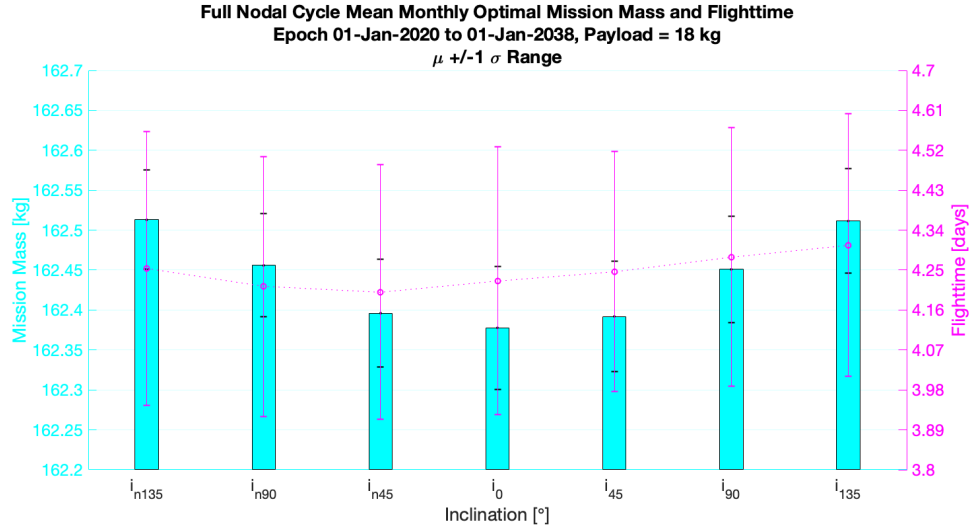
Figure A.7: Flyby: Full nodal cycle mean monthly minimum mission mass and flight time distribution, 18 kg Payload
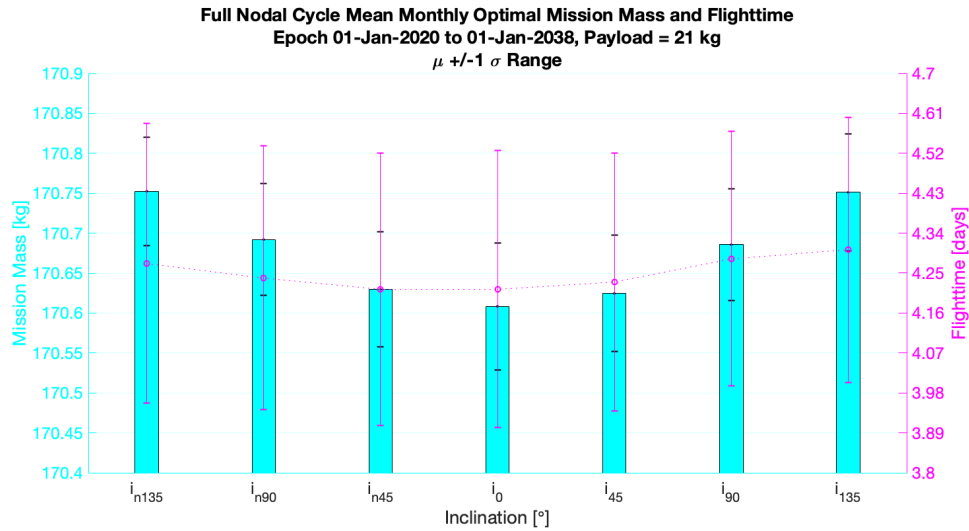

Figure A.8: Flyby: Full nodal cycle mean monthly minimum mission mass and flight time distribution, 21 kg Payload
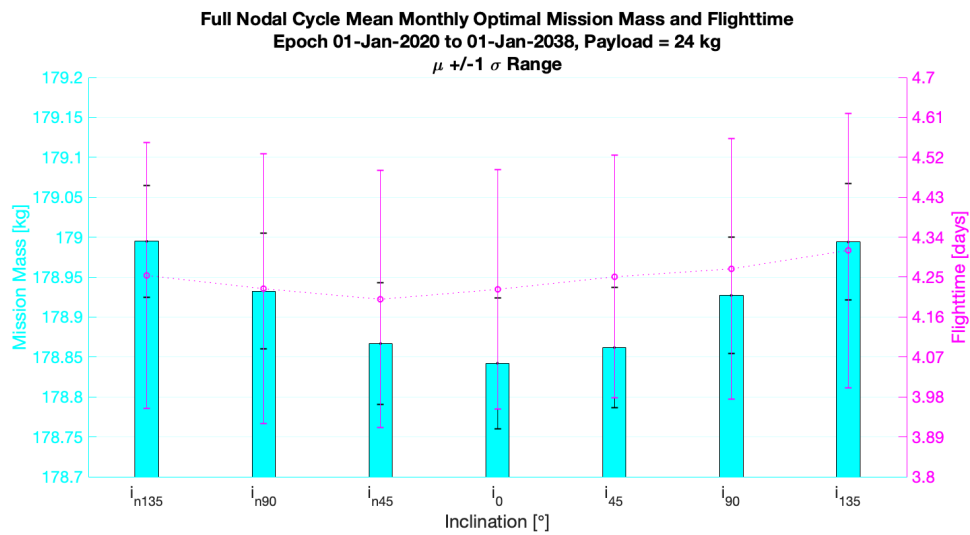
Figure A.9: Flyby: Full nodal cycle mean monthly minimum mission mass and flight time distribution, 24 kg Payload

APPENDIX B

FLYBY: NODAL CYCLE PERFORMANCE DISTRIBUTION FOR

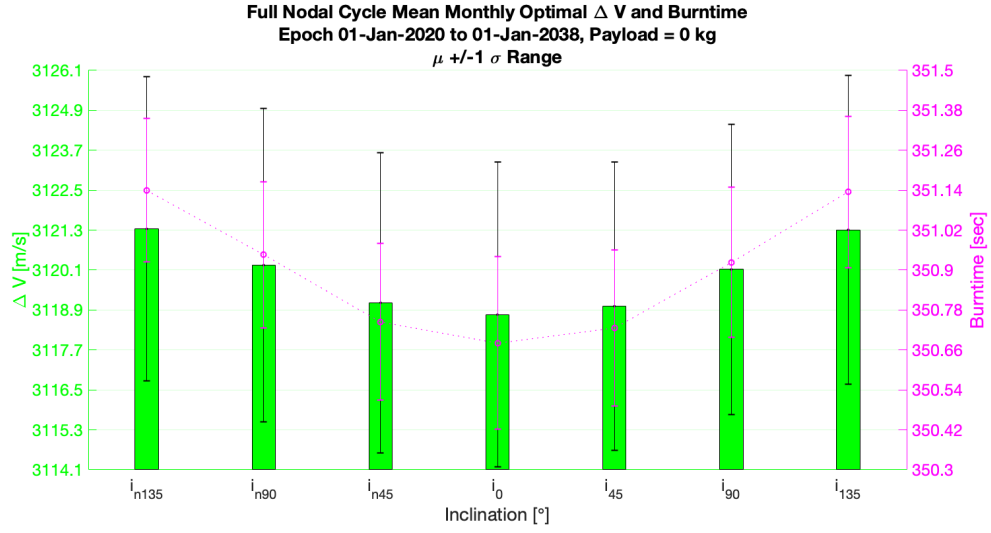# OPTIMAL DEPARTURES - △V AND BURN TIME

Figure B.1: Flyby: Full nodal cycle mean monthly minimum Δv and burn time distribution, 0 kg Payload

Figure B.2: Flyby: Full nodal cycle mean monthly minimum Δv and burn time distribution, 3 kg Payload

Figure B.3: Flyby: Full nodal cycle mean monthly minimum Δv and burn time distribution, 6 kg Payload

Figure B.4: Flyby: Full nodal cycle mean monthly minimum Δv and burn time distribution, 9 kg Payload
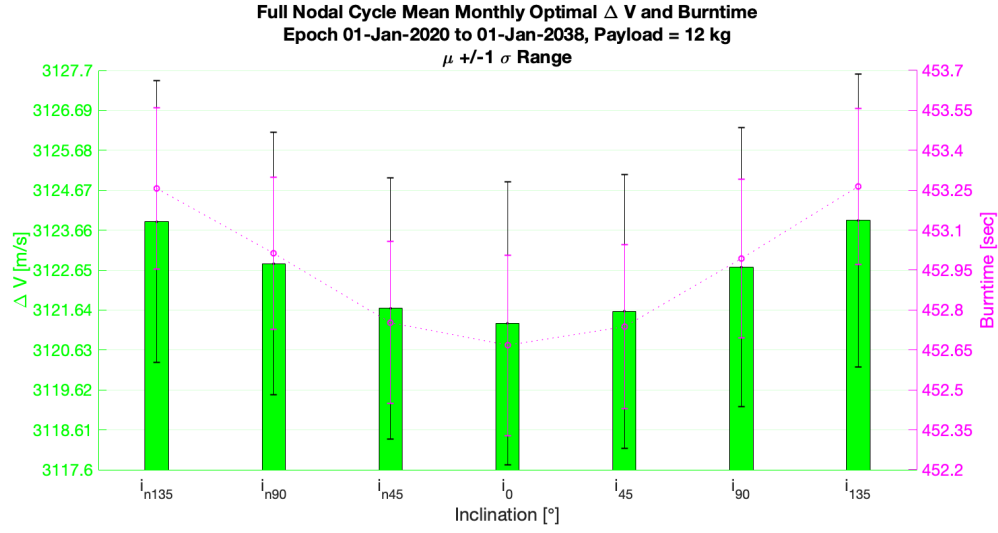
Figure B.5: Flyby: Full nodal cycle mean monthly minimum Δv and burn time distribution, 12 kg Payload
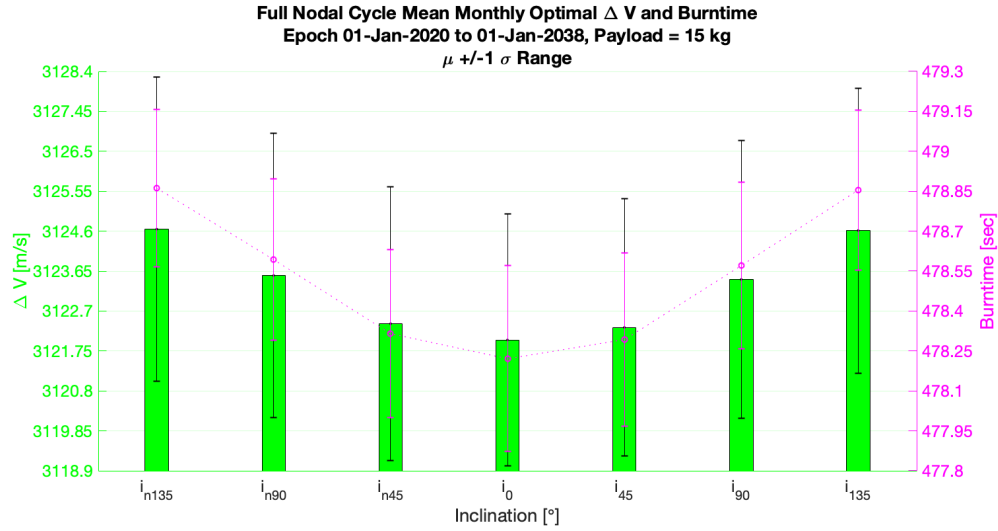
Figure B.6: Flyby: Full nodal cycle mean monthly minimum Δv and burn time distribution, 15 kg Payload
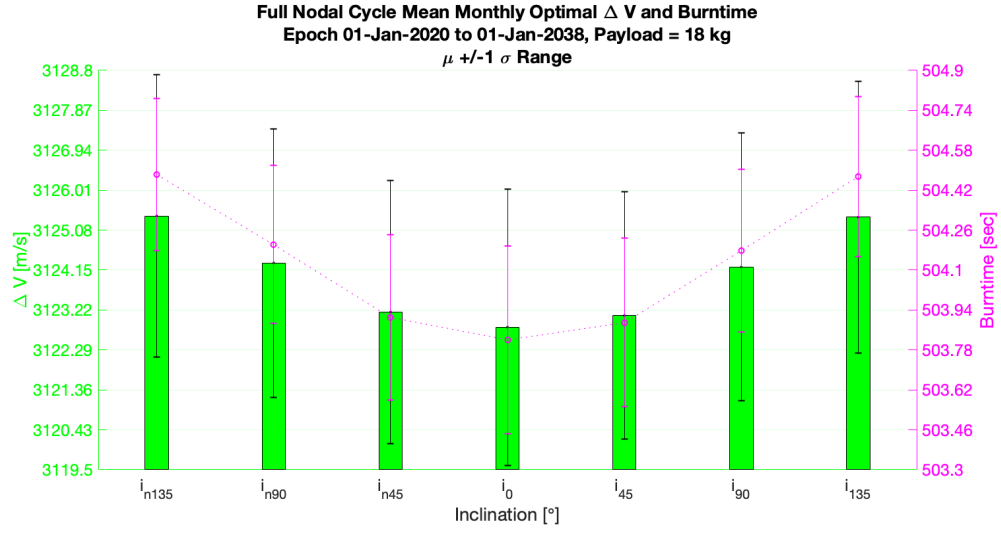
Figure B.7: Flyby: Full nodal cycle mean monthly minimum Δv and burn time distribution, 18 kg Payload
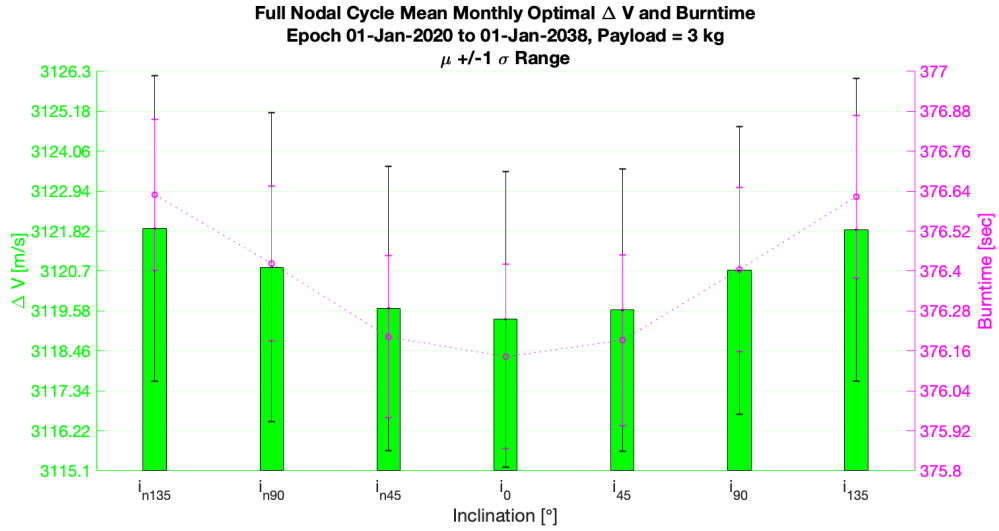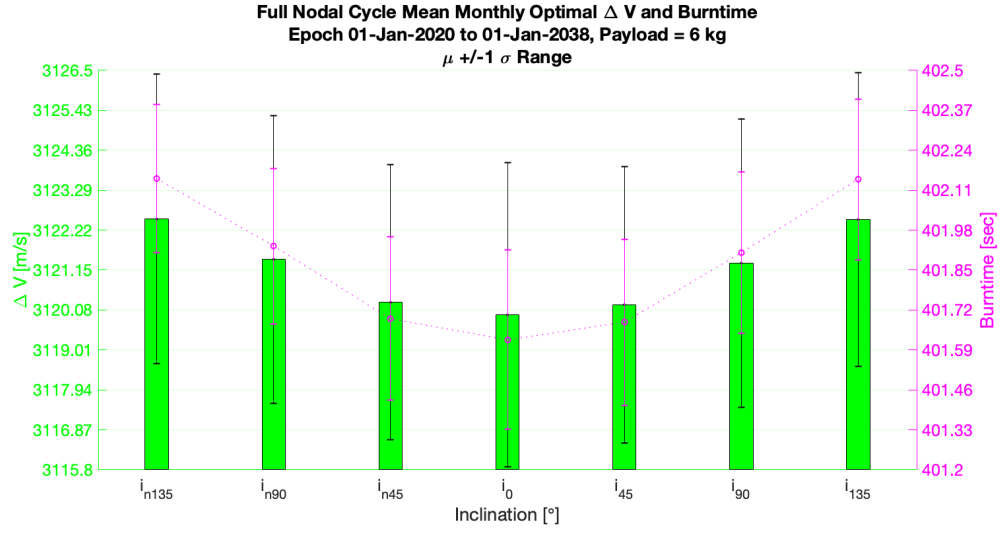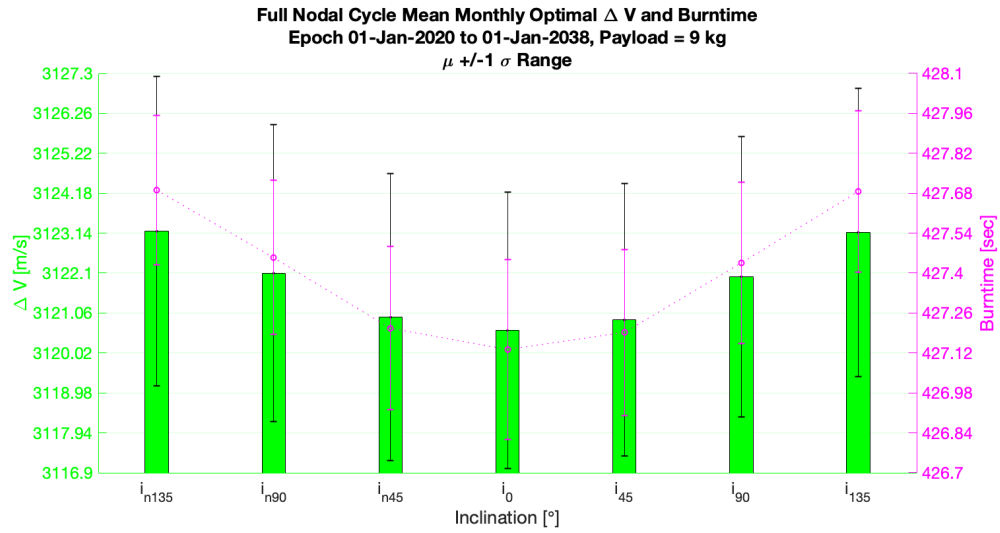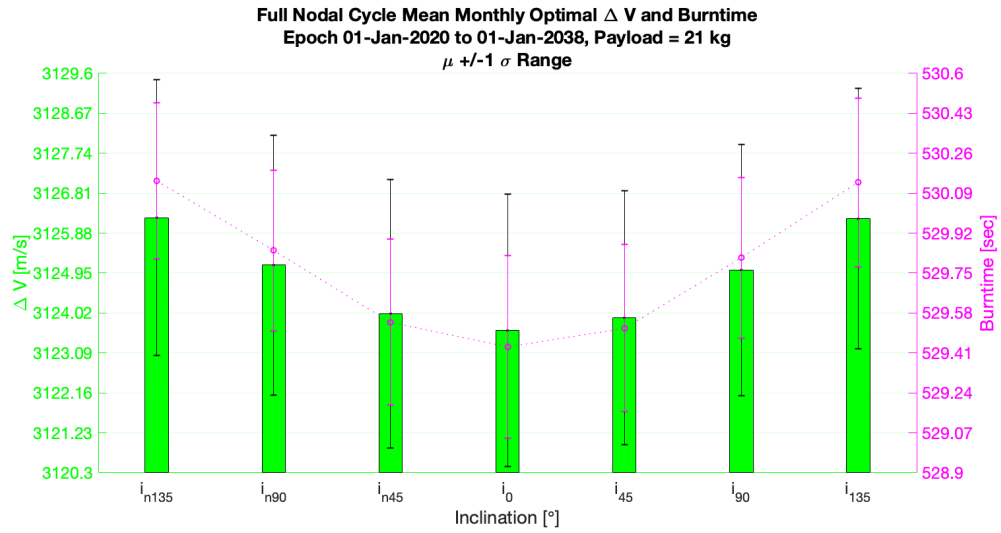

Figure B.8: Flyby: Full nodal cycle mean monthly minimum Δv and burn time distribution, 21 kg Payload
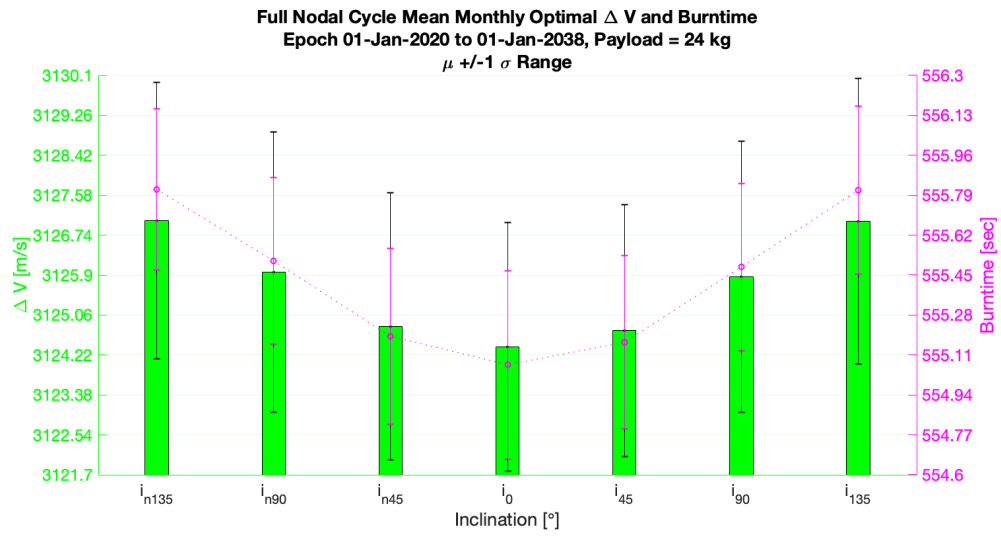
Figure B.9: Flyby: Full nodal cycle mean monthly minimum Δv and burn time distribution, 24 kg Payload

APPENDIX C

ORBIT INSERTION: NODAL CYCLE PERFORMANCE DISTRIBUTION

FOR OPTIMAL DEPARTURES - MISSION MASS AND FLIGHT TIME

Figure C.1: Orbit Insertion: Full nodal cycle mean monthly minimum mission mass and flight time distribution, 0 kg Payload

Figure C.2: Orbit Insertion: Full nodal cycle mean monthly minimum mission mass and flight time distribution, 3 kg Payload

Figure C.3: Orbit Insertion: Full nodal cycle mean monthly minimum mission mass and flight time distribution, 6 kg Payload

Figure C.4: Orbit Insertion: Full nodal cycle mean monthly minimum mission mass and flight time distribution, 9 kg Payload

Figure C.5: Orbit Insertion: Full nodal cycle mean monthly minimum mission mass and flight time distribution, 12 kg Payload

Figure C.6: Orbit Insertion: Full nodal cycle mean monthly minimum mission mass and flight time distribution, 15 kg Payload

Figure C.7: Orbit Insertion: Full nodal cycle mean monthly minimum mission mass and flight time distribution, 18 kg Payload

Figure C.8: Orbit Insertion: Full nodal cycle mean monthly minimum mission mass and flight time distribution, 21 kg Payload

Figure C.9: Orbit Insertion: Full nodal cycle mean monthly minimum mission mass and flight time distribution, 24 kg Payload

APPENDIX D

ORBIT INSERTION: NODAL CYCLE PERFORMANCE DISTRIBUTION

FOR OPTIMAL DEPARTURES - $\triangle$V AND BURN TIME
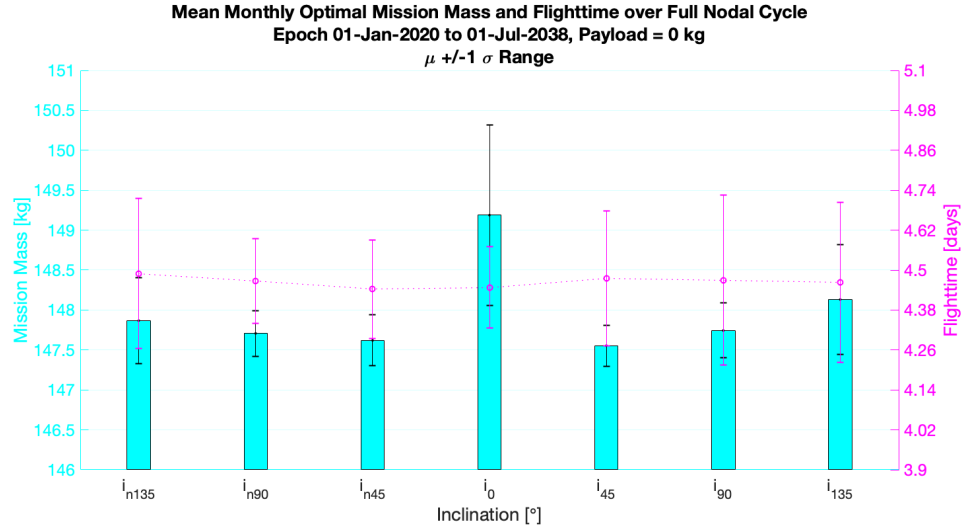
Figure D.1: Orbit Insertion: Full nodal cycle mean monthly minimum Δv and burn time distribution, 0 kg Payload
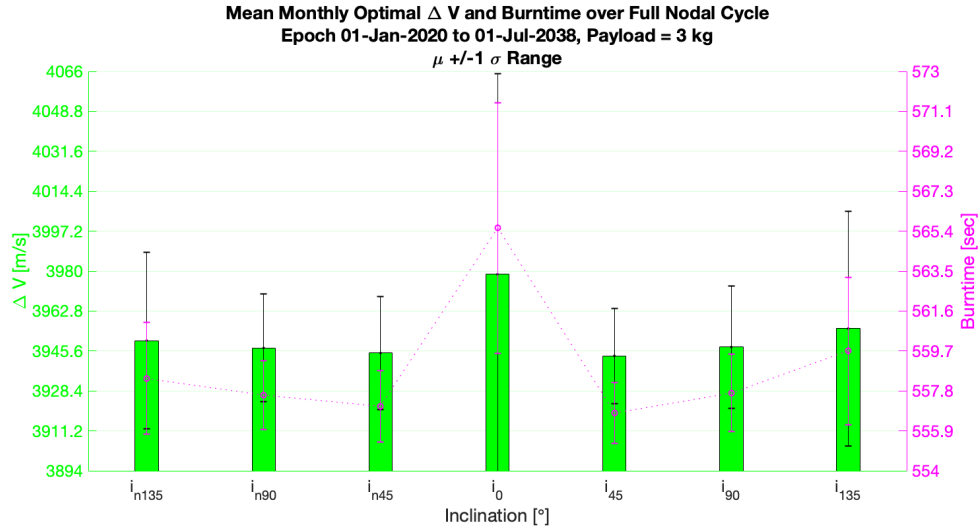
Figure D.2: Orbit Insertion: Full nodal cycle mean monthly minimum Δv and burn time distribution, 3 kg Payload

Figure D.3: Orbit Insertion: Full nodal cycle mean monthly minimum Δv and burn time distribution, 6 kg Payload
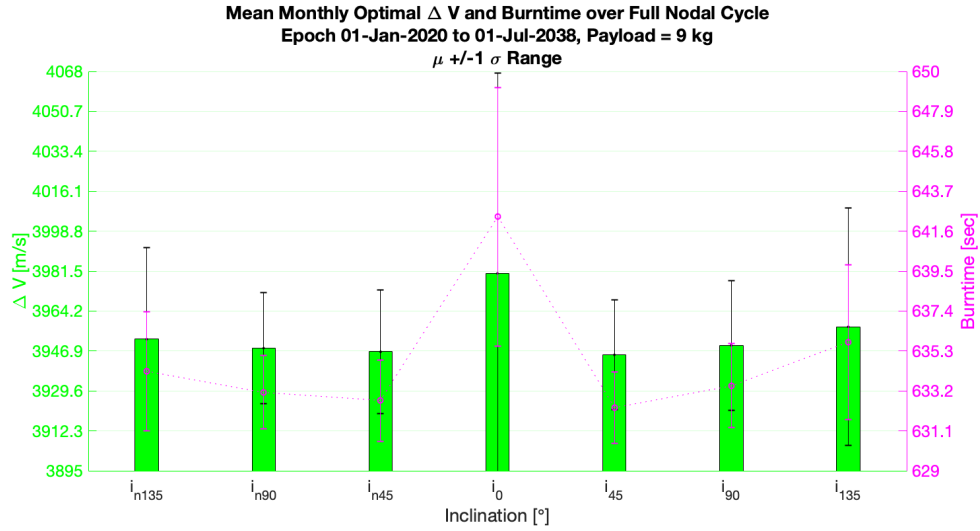
Figure D.4: Orbit Insertion: Full nodal cycle mean monthly minimum Δv and burn time distribution, 9 kg Payload
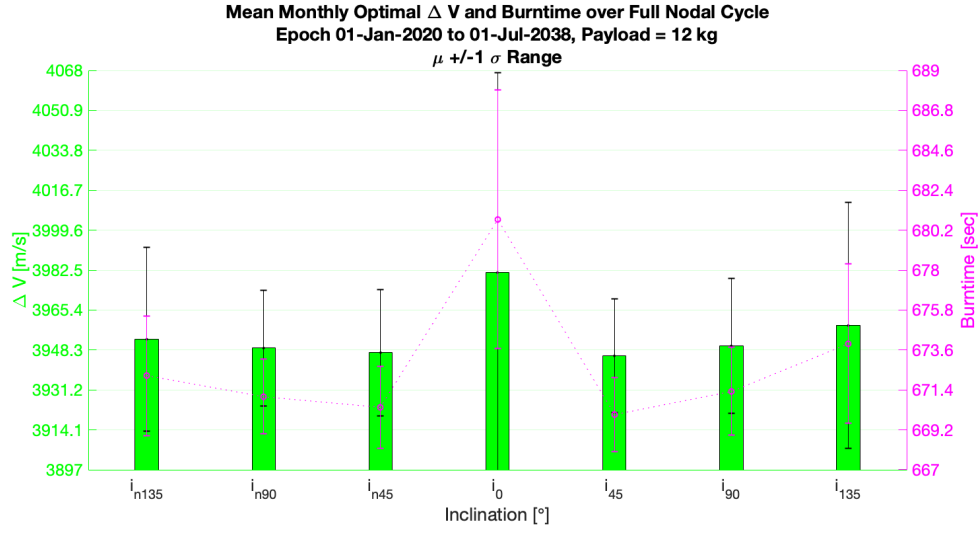
Figure D.5: Orbit Insertion: Full nodal cycle mean monthly minimum Δv and burn time distribution, 12 kg Payload
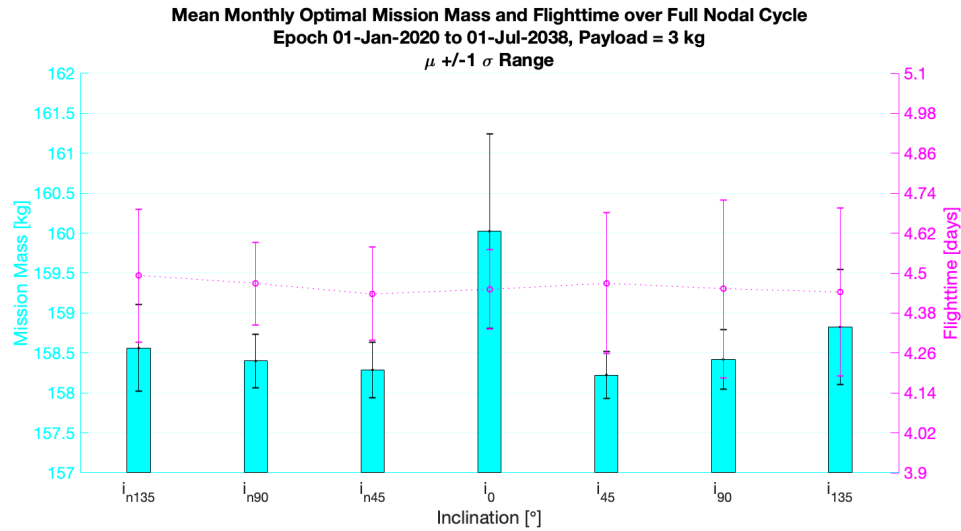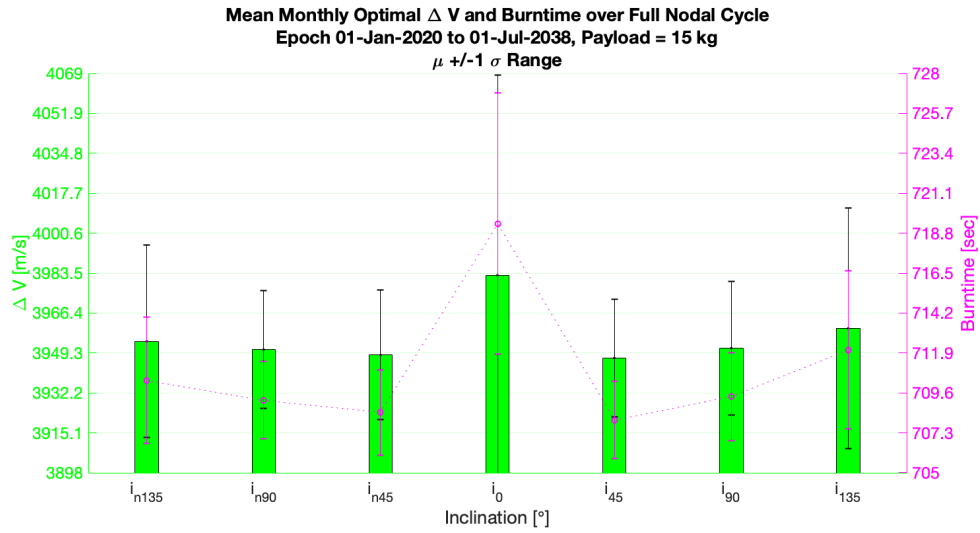

Figure D.6: Orbit Insertion: Full nodal cycle mean monthly minimum Δv and burn time distribution, 15 kg Payload
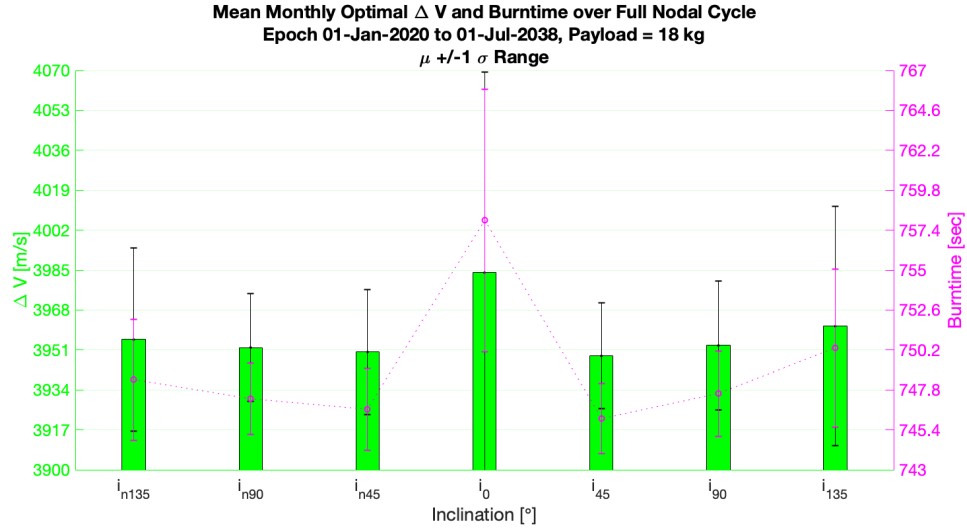
Figure D.7: Orbit Insertion: Full nodal cycle mean monthly minimum Δv and burn time distribution, 18 kg Payload

Figure D.8: Orbit Insertion: Full nodal cycle mean monthly minimum Δv and burn time distribution, 21 kg Payload
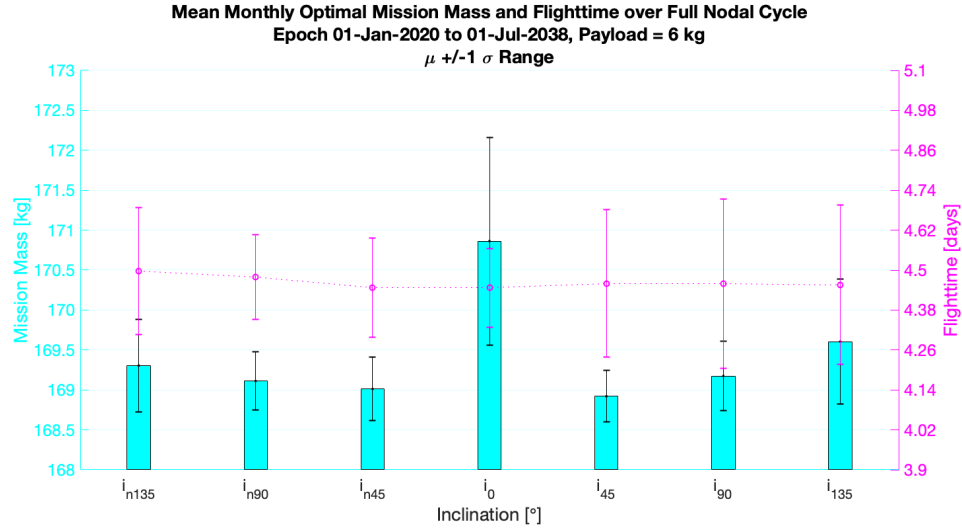
Figure D.9: Orbit Insertion: Full nodal cycle mean monthly minimum Δv and burn time distribution, 24 kg Payload

APPENDIX E

LANDING: NODAL CYCLE PERFORMANCE DISTRIBUTION FOR

OPTIMAL DEPARTURES - MISSION MASS AND FLIGHT TIME
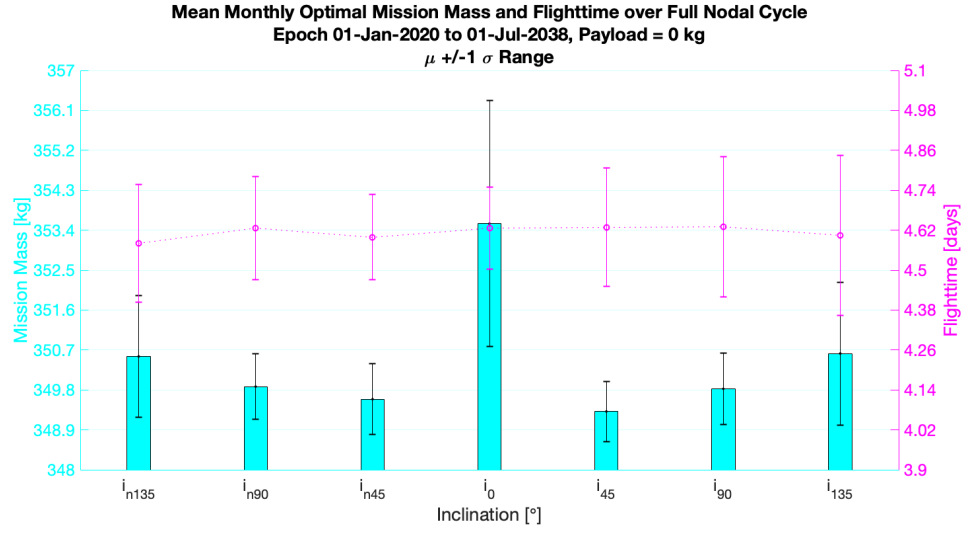
Figure E.1: Landing: Full nodal cycle mean monthly minimum mission mass and flight time distribution, 0 kg Payload
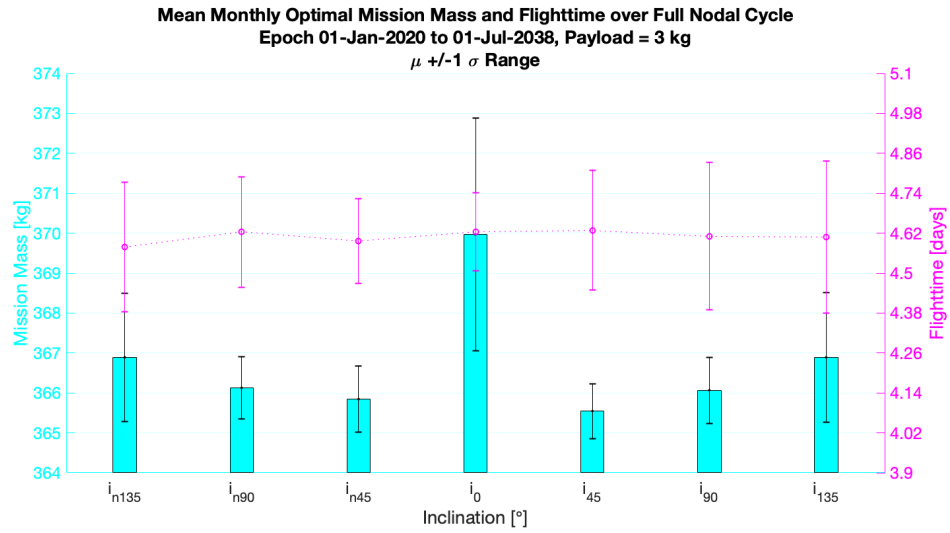
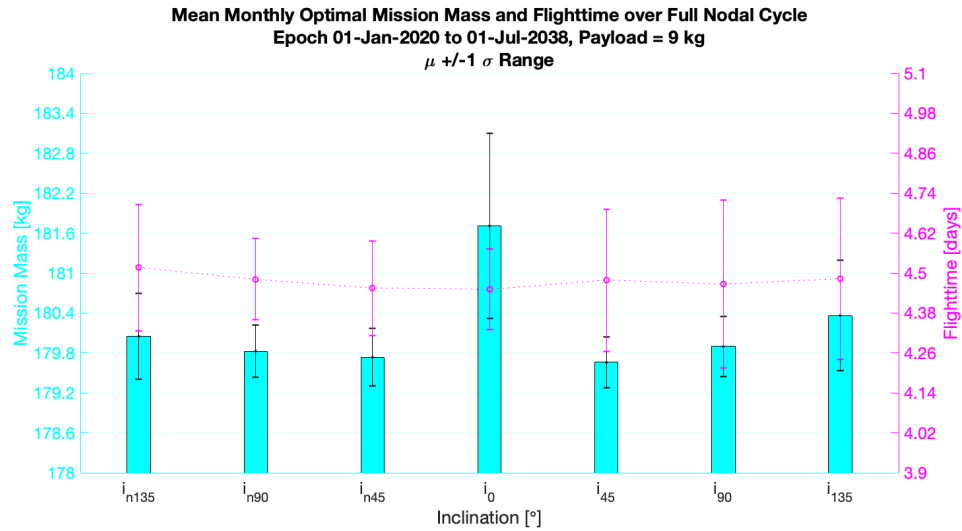Figure E.2: Landing: Full nodal cycle mean monthly minimum mission mass and flight time distribution, 3 kg Payload
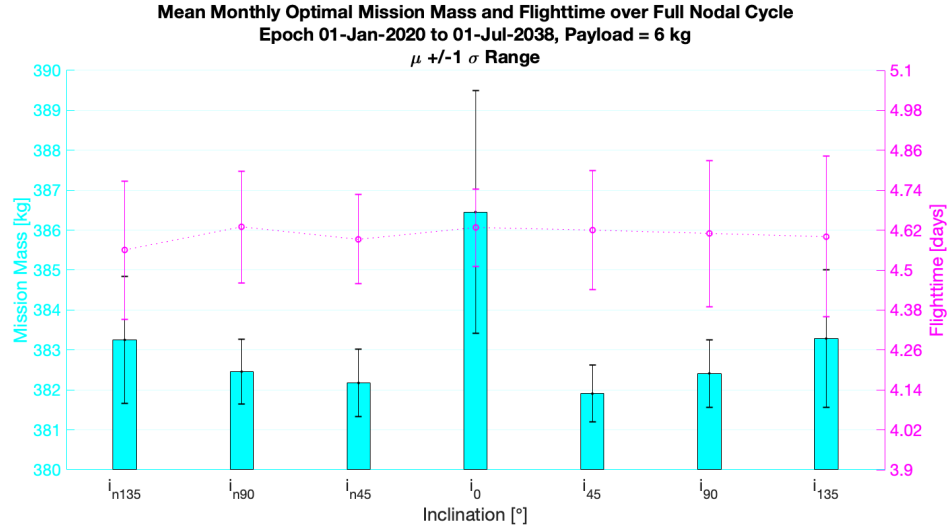
Figure E.3: Landing: Full nodal cycle mean monthly minimum mission mass and flight time distribution, 6 kg Payload
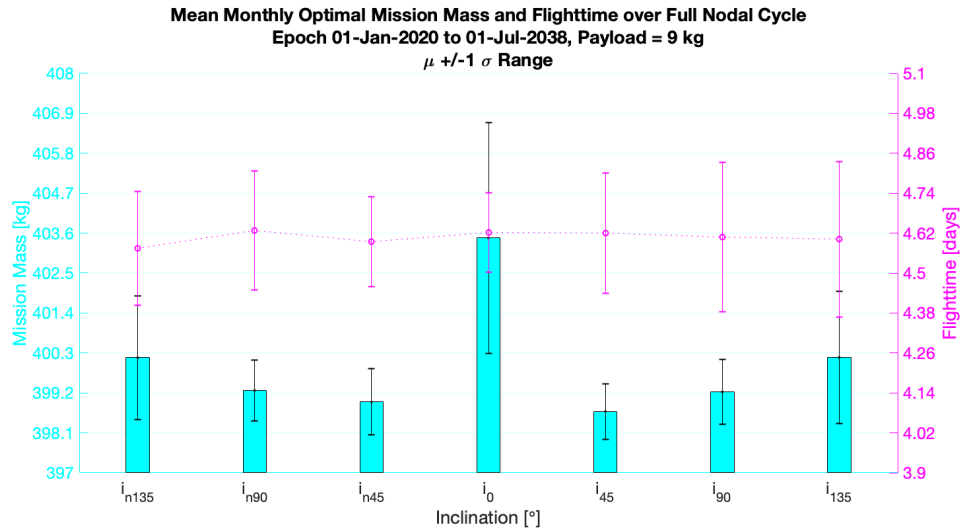
Figure E.4: Landing: Full nodal cycle mean monthly minimum mission mass and flight time distribution, 9 kg Payload
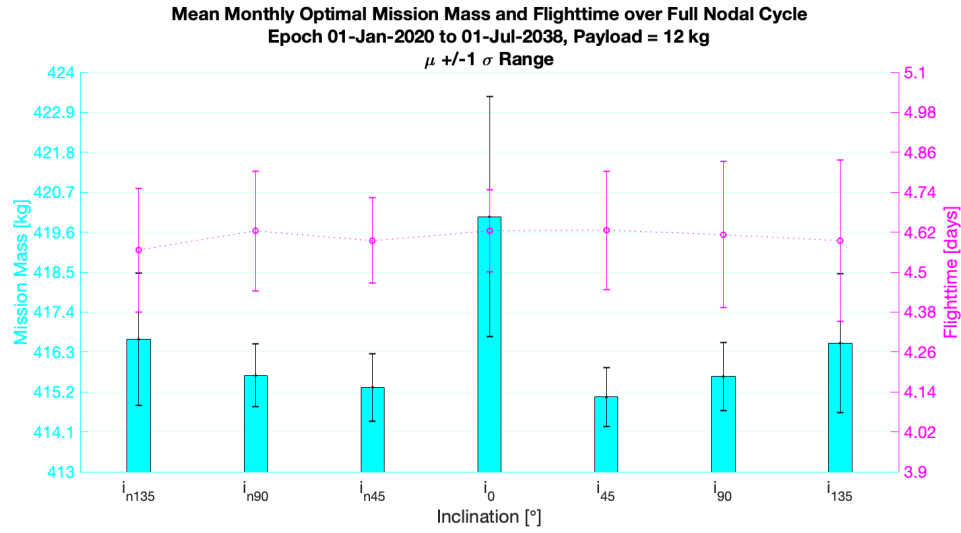
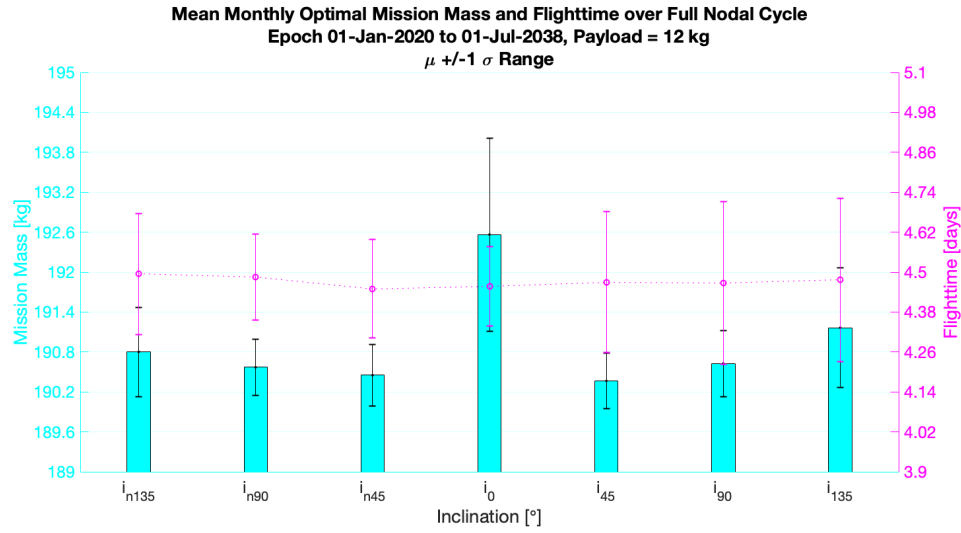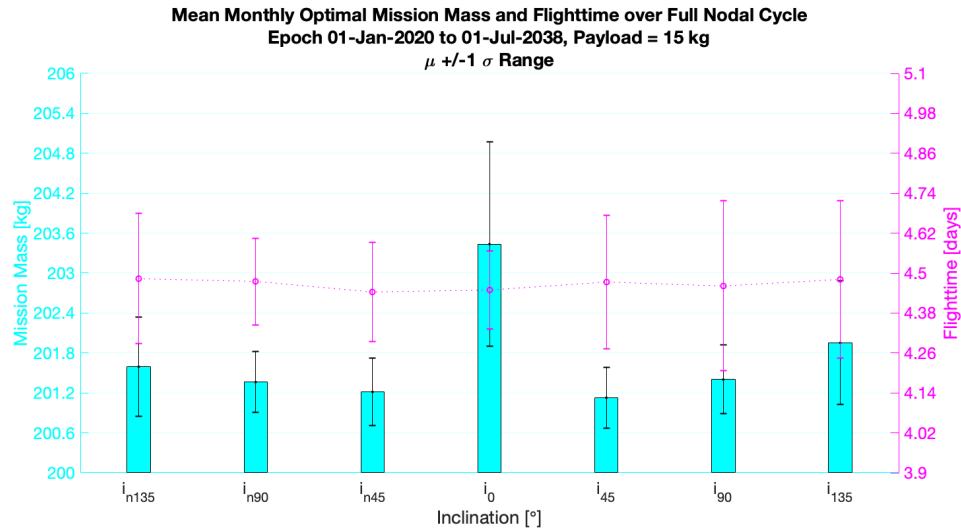Figure E.5: Landing: Full nodal cycle mean monthly minimum mission mass and flight time distribution, 12 kg Payload
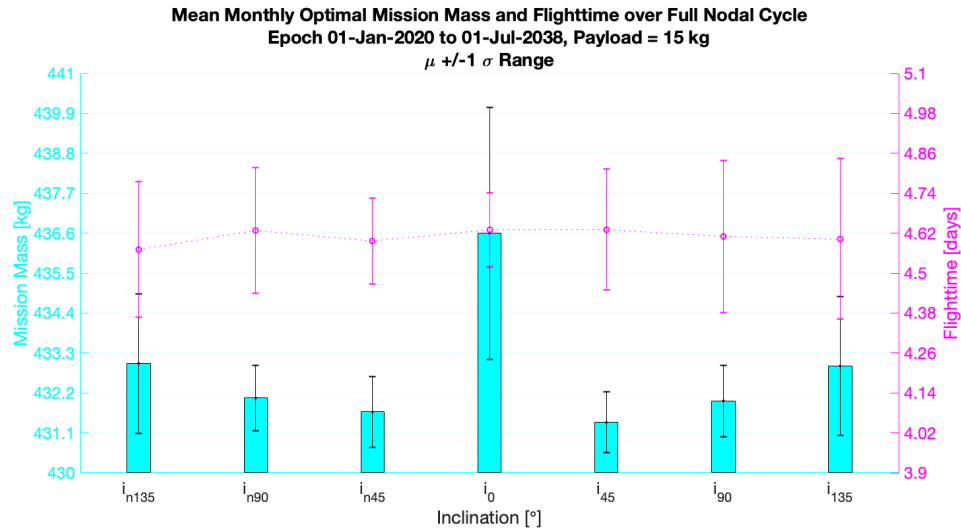
Figure E.6: Landing: Full nodal cycle mean monthly minimum mission mass and flight time distribution, 15 kg Payload
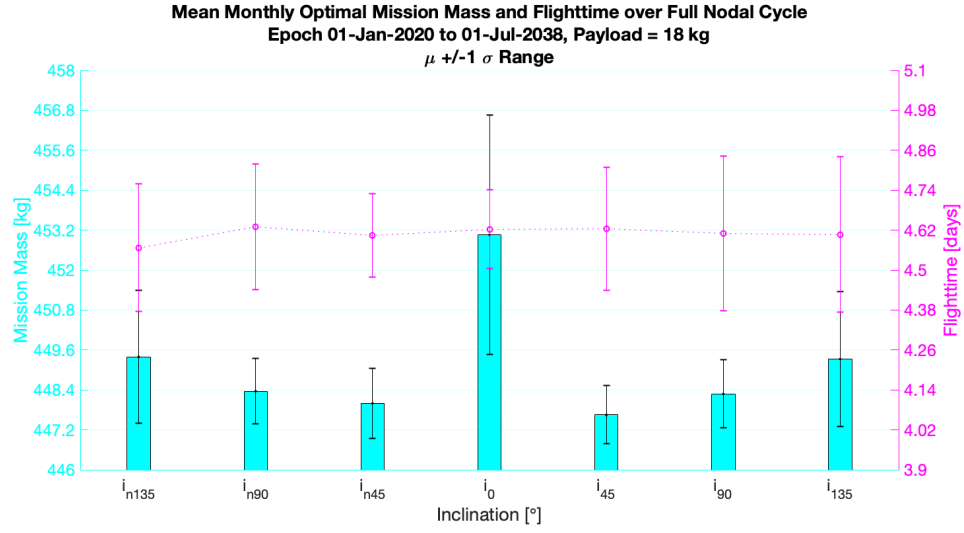
Figure E.7: Landing: Full nodal cycle mean monthly minimum mission mass and flight time distribution, 18 kg Payload
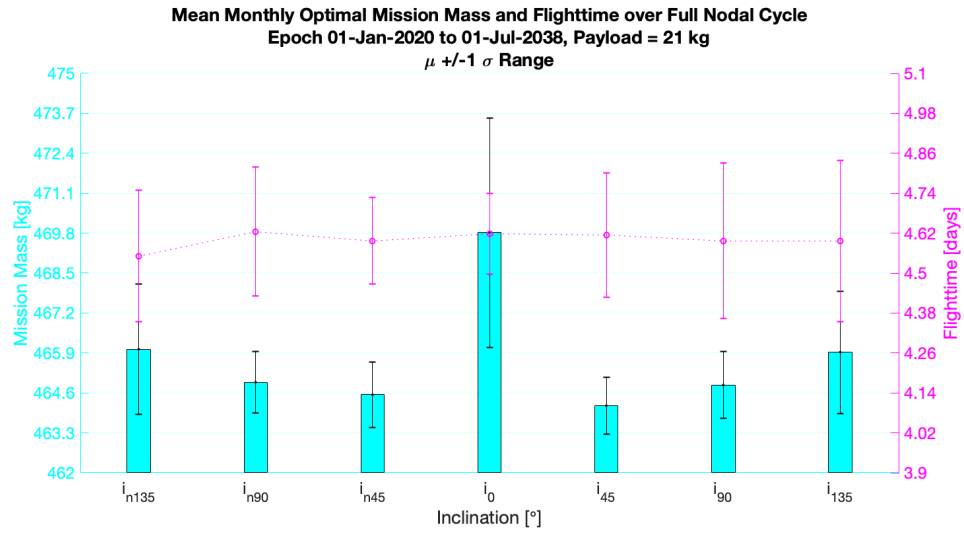
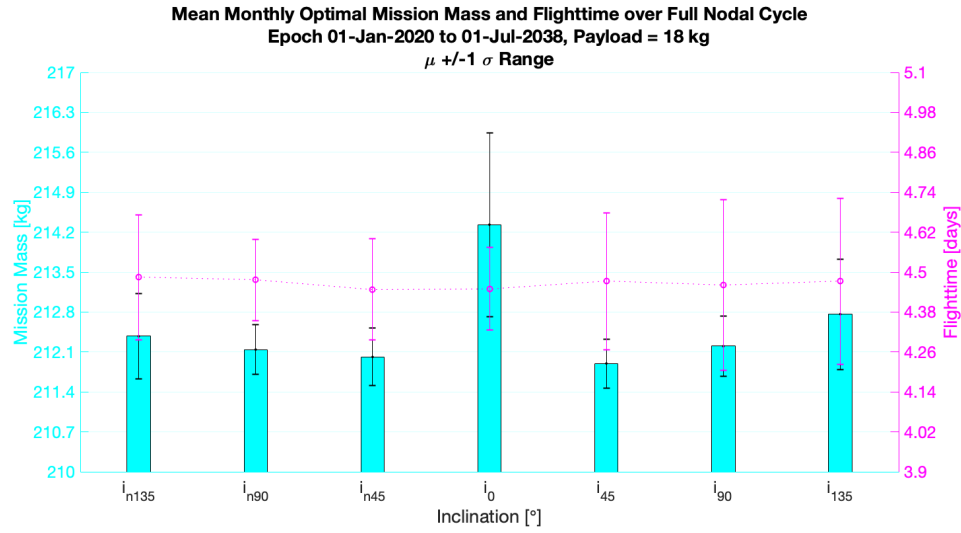Figure E.8: Landing: Full nodal cycle mean monthly minimum mission mass and flight time distribution, 21 kg Payload
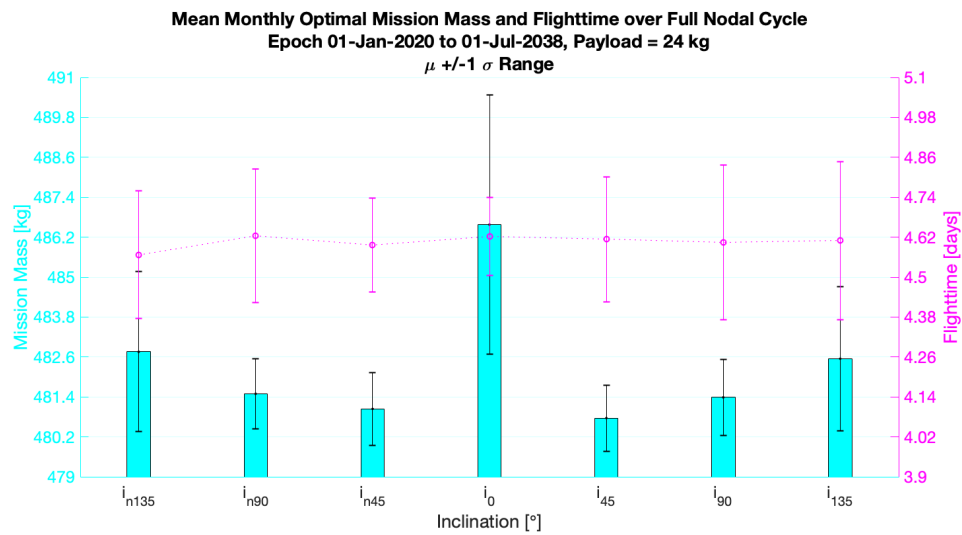
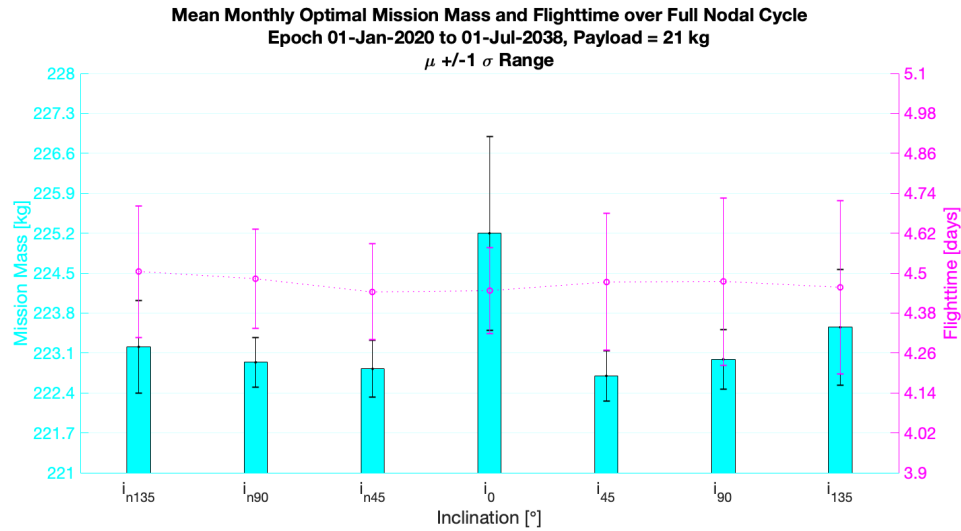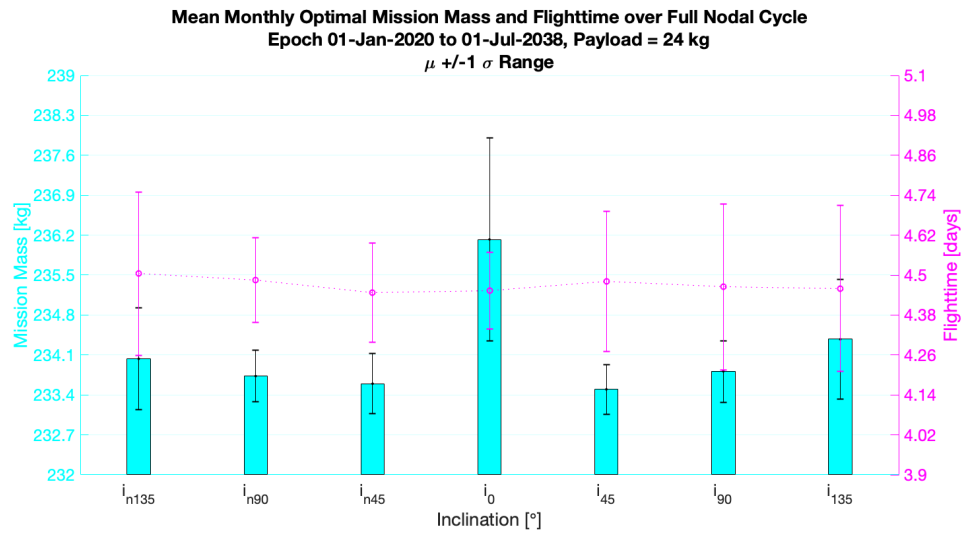Figure E.9: Landing: Full nodal cycle mean monthly minimum mission mass and flight time distribution, 24 kg Payload

APPENDIX F

LANDING: NODAL CYCLE PERFORMANCE DISTRIBUTION FOR

OPTIMAL DEPARTURES - $\triangle$V AND BURN TIME
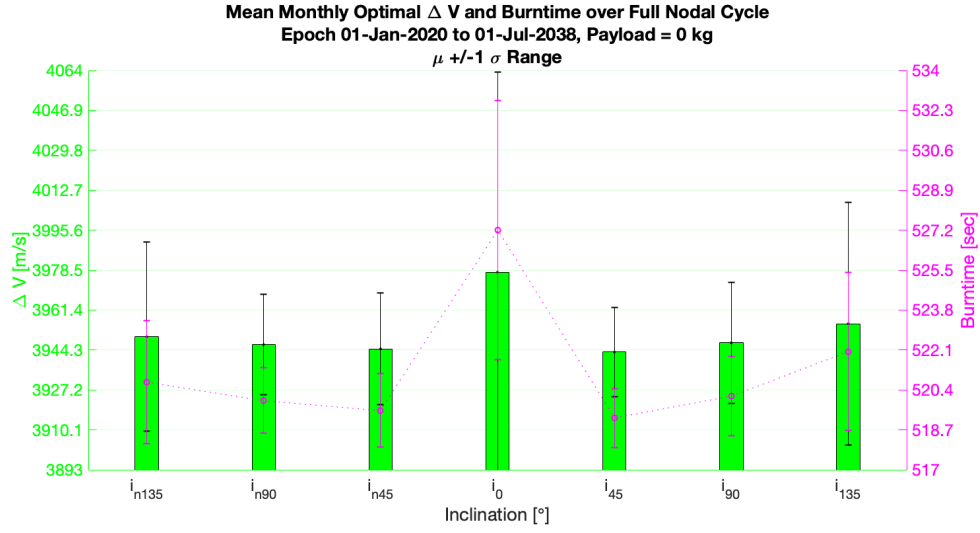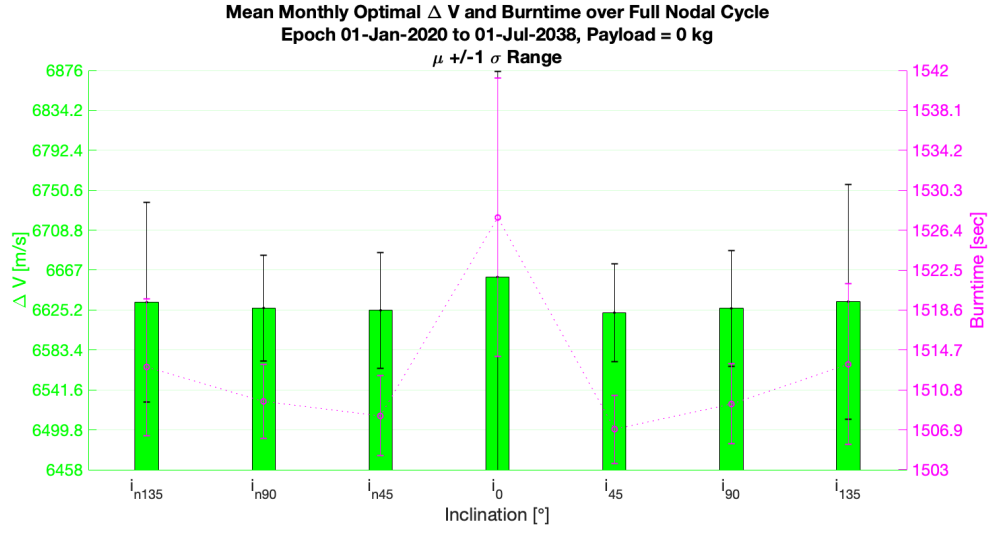
Figure F.1: Landing: Full nodal cycle mean monthly minimum Δv and burn time distribution, 0 kg Payload
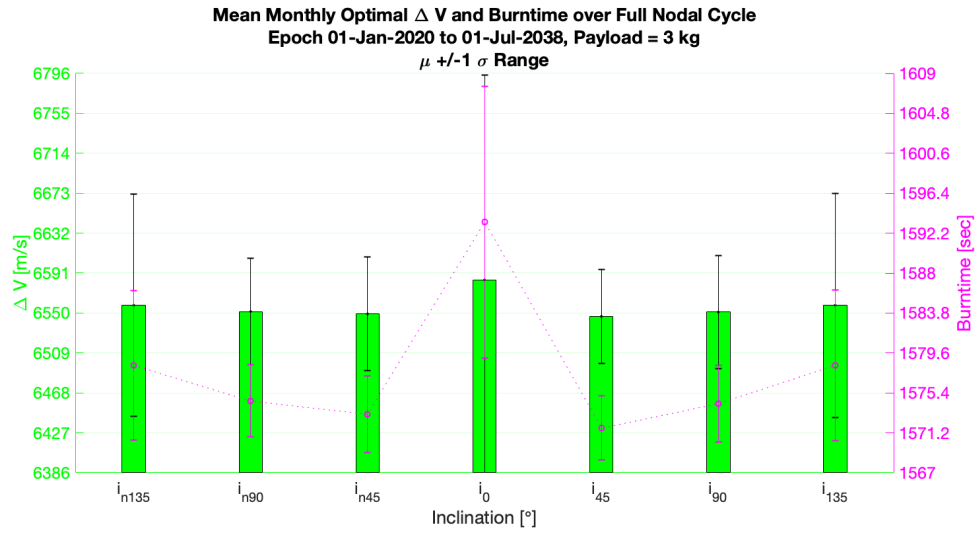
Figure F.2: Landing: Full nodal cycle mean monthly minimum Δv and burn time distribution, 3 kg Payload
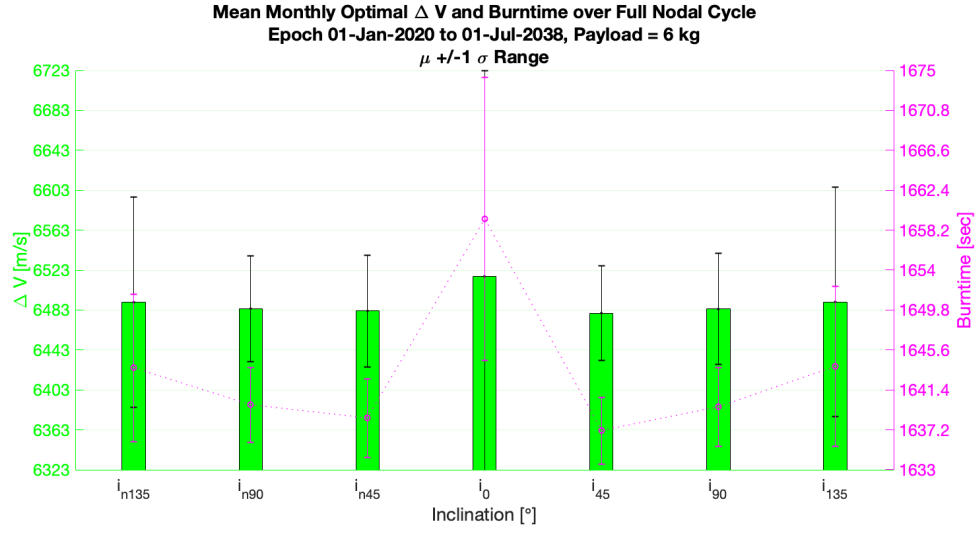
Figure F.3: Landing: Full nodal cycle mean monthly minimum Δv and burn time distribution, 6 kg Payload
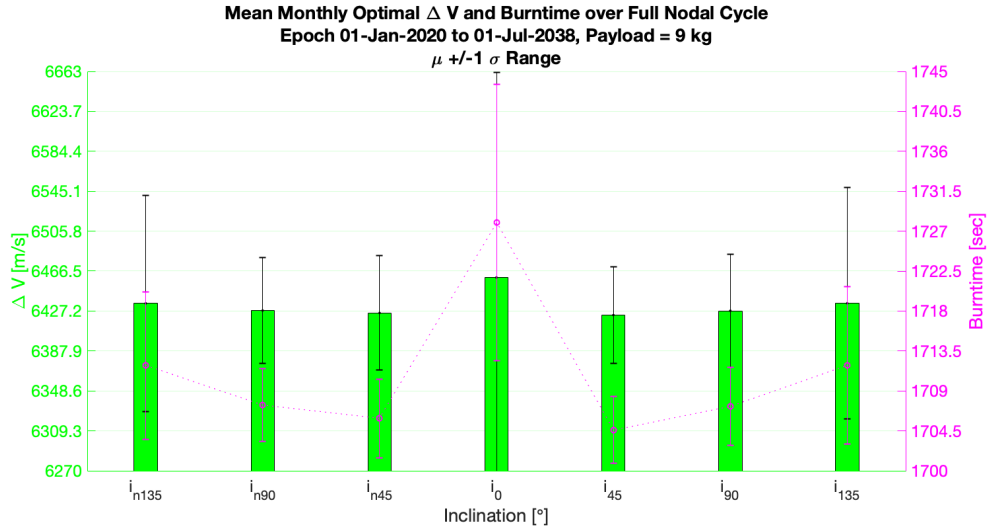
Figure F.4: Landing: Full nodal cycle mean monthly minimum Δv and burn time distribution, 9 kg Payload
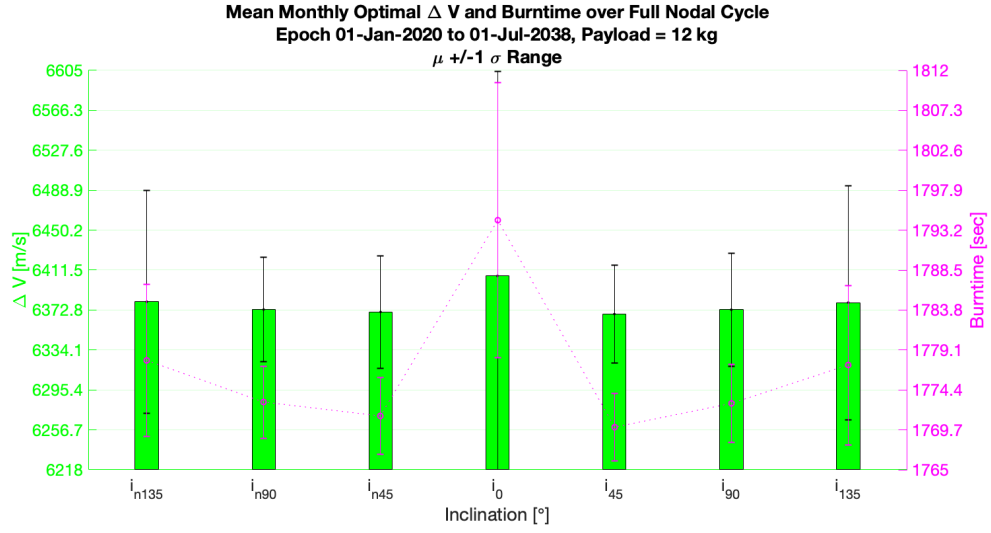
Figure F.5: Landing: Full nodal cycle mean monthly minimum Δv and burn time distribution, 12 kg Payload
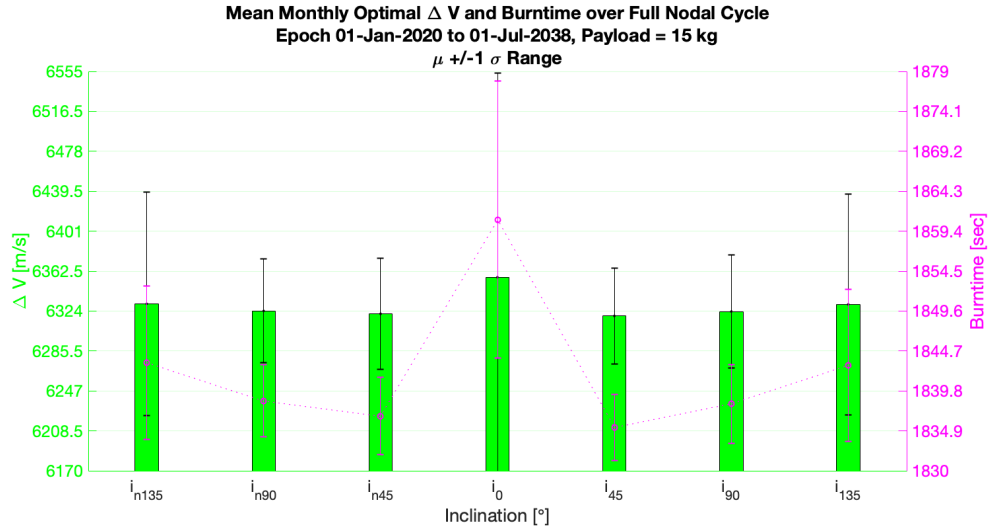
Figure F.6: Landing: Full nodal cycle mean monthly minimum Δv and burn time distribution, 15 kg Payload
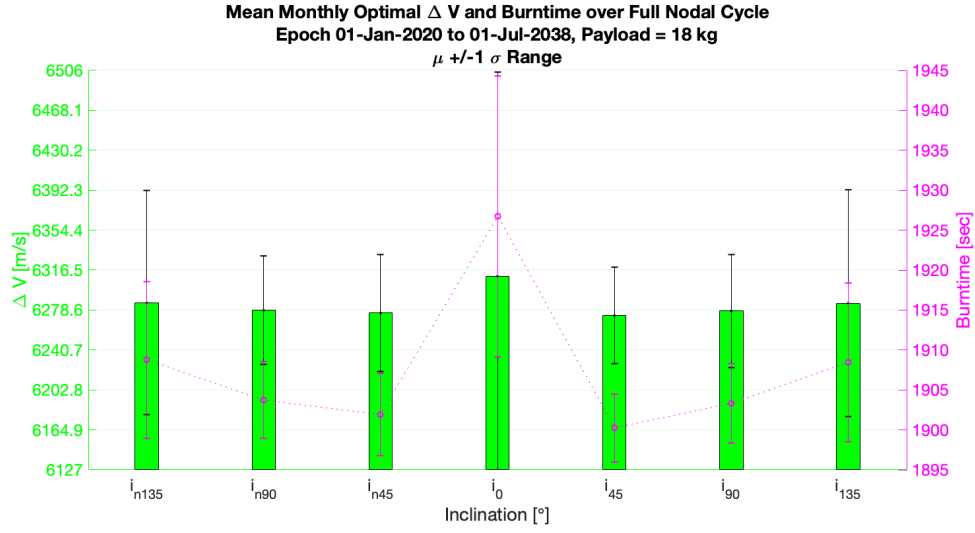
Figure F.7: Landing: Full nodal cycle mean monthly minimum Δv and burn time distribution, 18 kg Payload
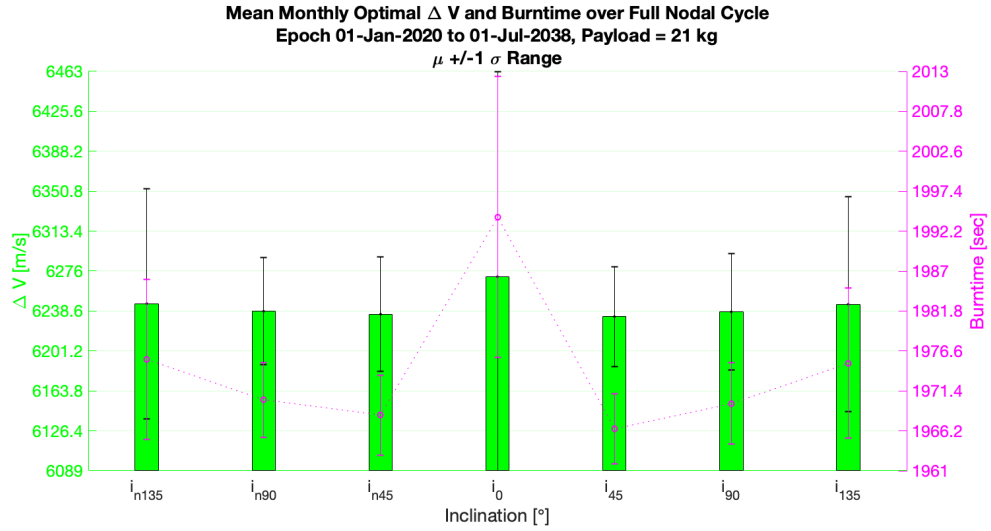
Figure F.8: Landing: Full nodal cycle mean monthly minimum Δv and burn time distribution, 21 kg Payload
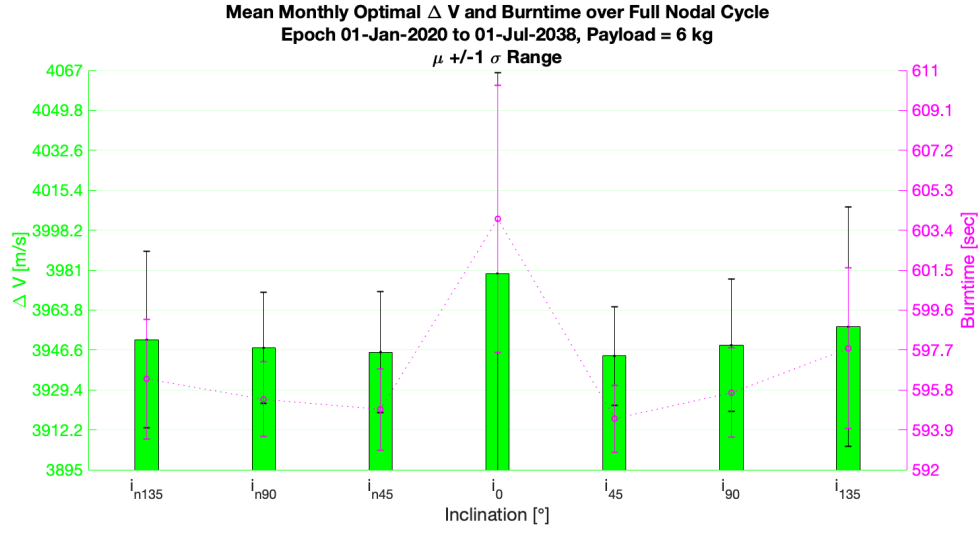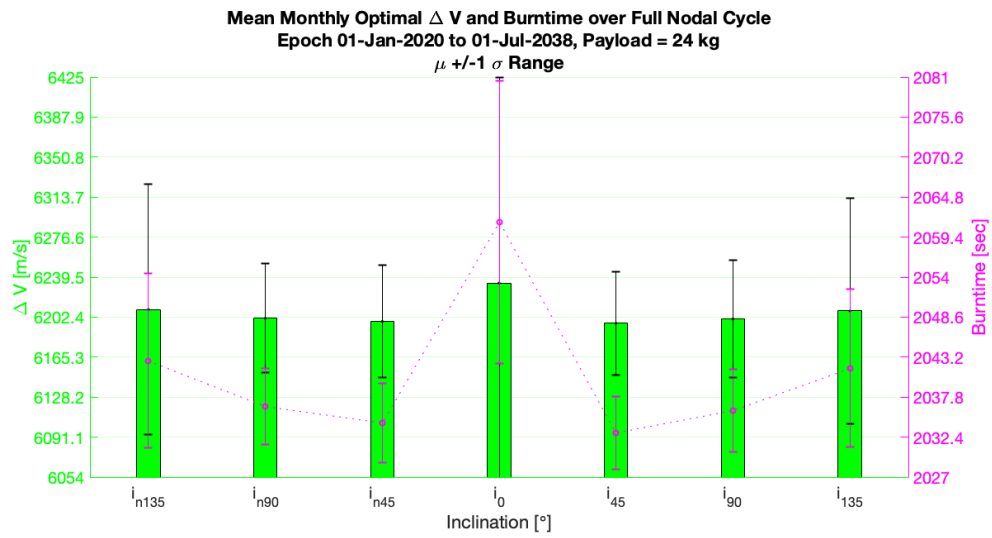
Figure F.9: Landing: Full nodal cycle mean monthly minimum Δv and burn time distribution, 24 kg Payload
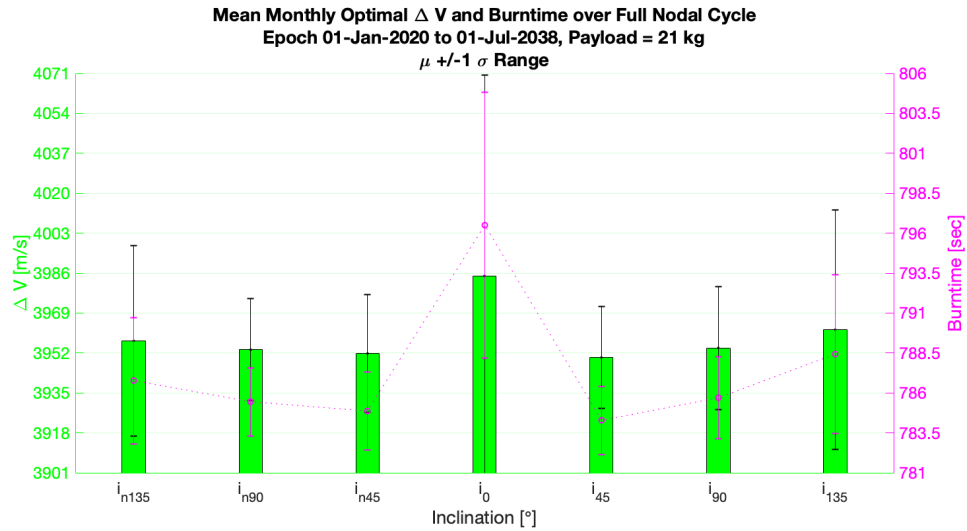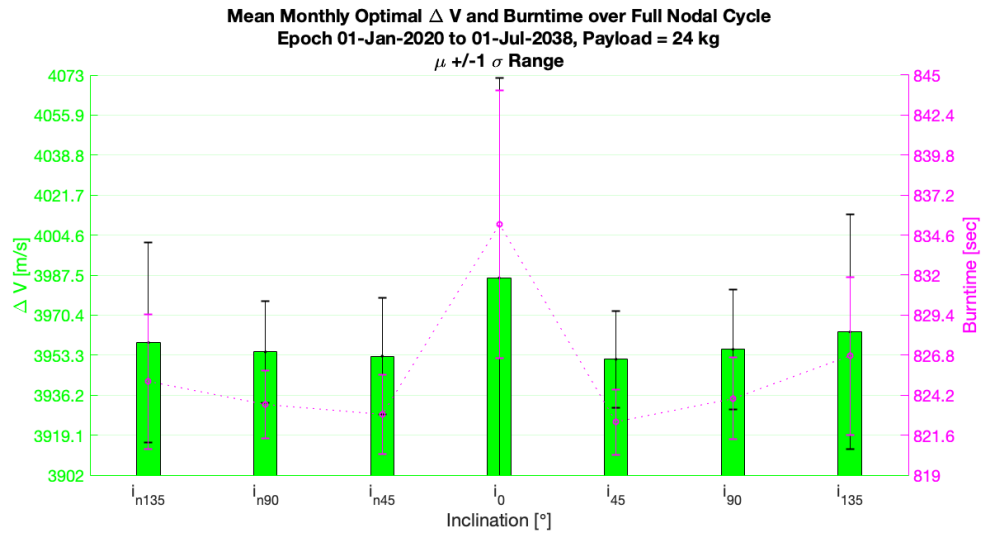
APPENDIX G

TRAJECTORY DESIGN ALGORITHM

```
%General Mission Analysis Tool(GMAT) Script
%Created: 2019 05 25 10:219:02
%Flyby, OrbitInsertion, Landing
%R A J Hunter


%
%            Spacecraft
%

Create Spacecraft Artemis;
GMAT Artemis.DateFormat = UTCModJulian;
GMAT Artemis.Epoch = '28849.5';
GMAT Artemis.CoordinateSystem = EarthMJ2000Eq;
GMAT Artemis.DisplayStateType = Keplerian;
GMAT Artemis.SMA = 6778.120000000001;
GMAT Artemis.ECC = 4.83305428361925e 16;
GMAT Artemis.INC = 0;
GMAT Artemis.RAAN = 0;
GMAT Artemis.AOP = 0;
GMAT Artemis.TA = 0;
GMAT Artemis.DryMass = 1;
GMAT Artemis.Cd = 2.2;
GMAT Artemis.Cr = 1.8;
GMAT Artemis.DragArea = 1;
GMAT Artemis.SRPArea = 1;
GMAT Artemis.Tanks = {HydrazineTank, MONTank};
GMAT Artemis.Thrusters = {LEROSThuster, LEROSThusterLOI, LEROSThusterIAB, LEROSThusterEAB};
GMAT Artemis.NAIFId = 123456789;
GMAT Artemis.NAIFIdReferenceFrame = 123456789;
GMAT Artemis.OrbitColor = Red;
GMAT Artemis.TargetColor = Teal;
GMAT Artemis.OrbitErrorCovariance = [ 1e+70 0 0 0 0 0 ; 0 1e+70 0 0 0 0 ; 0 0 1e+70 0 0 0 ; 0 0 0 1e+70 0 0 ;
      0 0 0 0 1e+70 0 ; 0 0 0 0 0 1e+70 ];
GMAT Artemis.CdSigma = 1e+70;
GMAT Artemis.CrSigma = 1e+70;
GMAT Artemis.Id = 'SatId';
GMAT Artemis.Attitude = CoordinateSystemFixed;
GMAT Artemis.SPADSRPScaleFactor = 1;
GMAT Artemis.ModelFile = '../data/vehicle/models/aura.3ds';
GMAT Artemis.ModelOffsetX = 0;
GMAT Artemis.ModelOffsetY = 0;
GMAT Artemis.ModelOffsetZ = 0;
GMAT Artemis.ModelRotationX = 0;
GMAT Artemis.ModelRotationY = 0;
GMAT Artemis.ModelRotationZ = 0;
GMAT Artemis.ModelScale = 0.00989999994635582;
GMAT Artemis.AttitudeDisplayStateType = 'Quaternion';
```

196

```
GMAT Artemis.AttitudeRateDisplayStateType = 'AngularVelocity';
GMAT Artemis.AttitudeCoordinateSystem = EarthMJ2000Eq;
GMAT Artemis.EulerAngleSequence = '321';


Create Spacecraft ArtemisFine;
GMAT ArtemisFine.DateFormat = TAIModJulian;
GMAT ArtemisFine.Epoch = '21545';
GMAT ArtemisFine.CoordinateSystem = EarthMJ2000Eq;
GMAT ArtemisFine.DisplayStateType = Cartesian;
GMAT ArtemisFine.X = 7100;
GMAT ArtemisFine.Y = 0;
GMAT ArtemisFine.Z = 1300;
GMAT ArtemisFine.VX = 0;
GMAT ArtemisFine.VY = 7.35;
GMAT ArtemisFine.VZ = 1;
GMAT ArtemisFine.DryMass = 850;
GMAT ArtemisFine.Cd = 2.2;
GMAT ArtemisFine.Cr = 1.8;
GMAT ArtemisFine.DragArea = 15;
GMAT ArtemisFine.SRPArea = 1;
GMAT ArtemisFine.NAIFId = 123456789;
GMAT ArtemisFine.NAIFIdReferenceFrame = 123456789;
GMAT ArtemisFine.OrbitColor = Green;
GMAT ArtemisFine.TargetColor = LightGray;
GMAT ArtemisFine.OrbitErrorCovariance = [ 1e+70 0 0 0 0 0 ; 0 1e+70 0 0 0 0 ; 0 0 1e+70 0 0 0 ; 0 0 0 1e+70 0
      0 ; 0 0 0 0 1e+70 0 ; 0 0 0 0 0 1e+70 ];
GMAT ArtemisFine.CdSigma = 1e+70;
GMAT ArtemisFine.CrSigma = 1e+70;
GMAT ArtemisFine.Id = 'SatId';
GMAT ArtemisFine.Attitude = CoordinateSystemFixed;
GMAT ArtemisFine.SPADSRPScaleFactor = 1;
GMAT ArtemisFine.ModelFile = '../data/vehicle/models/aura.3ds';
GMAT ArtemisFine.ModelOffsetX = 0;
GMAT ArtemisFine.ModelOffsetY = 0;
GMAT ArtemisFine.ModelOffsetZ = 0;
GMAT ArtemisFine.ModelRotationX = 0;
GMAT ArtemisFine.ModelRotationY = 0;
GMAT ArtemisFine.ModelRotationZ = 0;
GMAT ArtemisFine.ModelScale = 3;
GMAT ArtemisFine.AttitudeDisplayStateType = 'Quaternion';
GMAT ArtemisFine.AttitudeRateDisplayStateType = 'AngularVelocity';
GMAT ArtemisFine.AttitudeCoordinateSystem = EarthMJ2000Eq;
GMAT ArtemisFine.EulerAngleSequence = '321';


Create Spacecraft ArtemisFiniteBurn;
GMAT ArtemisFiniteBurn.DateFormat = TAIModJulian;
GMAT ArtemisFiniteBurn.Epoch = '21545';
GMAT ArtemisFiniteBurn.CoordinateSystem = EarthMJ2000Eq;
GMAT ArtemisFiniteBurn.DisplayStateType = Cartesian;
GMAT ArtemisFiniteBurn.X = 7100;
GMAT ArtemisFiniteBurn.Y = 0;
GMAT ArtemisFiniteBurn.Z = 1300;
GMAT ArtemisFiniteBurn.VX = 0;
GMAT ArtemisFiniteBurn.VY = 7.35;
GMAT ArtemisFiniteBurn.VZ = 1;
GMAT ArtemisFiniteBurn.DryMass = 850;
```

```
GMAT ArtemisFiniteBurn.Cd = 2.2;
GMAT ArtemisFiniteBurn.Cr = 1.8;
GMAT ArtemisFiniteBurn.DragArea = 15;
GMAT ArtemisFiniteBurn.SRPArea = 1;
GMAT ArtemisFiniteBurn.NAIFId = 10004001;
GMAT ArtemisFiniteBurn.NAIFIdReferenceFrame = 9004001;
GMAT ArtemisFiniteBurn.OrbitColor = Blue;
GMAT ArtemisFiniteBurn.TargetColor = DimGray;
GMAT ArtemisFiniteBurn.OrbitErrorCovariance = [ 1e+70 0 0 0 0 0 ; 0 1e+70 0 0 0 0 ; 0 0 1e+70 0 0 0 ; 0 0 0 1e
      +70 0 0 ; 0 0 0 0 1e+70 0 ; 0 0 0 0 0 1e+70 ];
GMAT ArtemisFiniteBurn.CdSigma = 1e+70;
GMAT ArtemisFiniteBurn.CrSigma = 1e+70;
GMAT ArtemisFiniteBurn.Id = 'SatId';
GMAT ArtemisFiniteBurn.Attitude = CoordinateSystemFixed;
GMAT ArtemisFiniteBurn.SPADSRPScaleFactor = 1;
GMAT ArtemisFiniteBurn.ModelFile = 'aura.3ds';
GMAT ArtemisFiniteBurn.ModelOffsetX = 0;
GMAT ArtemisFiniteBurn.ModelOffsetY = 0;
GMAT ArtemisFiniteBurn.ModelOffsetZ = 0;
GMAT ArtemisFiniteBurn.ModelRotationX = 0;
GMAT ArtemisFiniteBurn.ModelRotationY = 0;
GMAT ArtemisFiniteBurn.ModelRotationZ = 0;
GMAT ArtemisFiniteBurn.ModelScale = 1;
GMAT ArtemisFiniteBurn.AttitudeDisplayStateType = 'Quaternion';
GMAT ArtemisFiniteBurn.AttitudeRateDisplayStateType = 'AngularVelocity';
GMAT ArtemisFiniteBurn.AttitudeCoordinateSystem = EarthMJ2000Eq;
GMAT ArtemisFiniteBurn.EulerAngleSequence = '321';


Create Spacecraft ArtemisFiniteCoarse;
GMAT ArtemisFiniteCoarse.DateFormat = TAIModJulian;
GMAT ArtemisFiniteCoarse.Epoch = '21545';
GMAT ArtemisFiniteCoarse.CoordinateSystem = EarthMJ2000Eq;
GMAT ArtemisFiniteCoarse.DisplayStateType = Cartesian;
GMAT ArtemisFiniteCoarse.X = 7100;
GMAT ArtemisFiniteCoarse.Y = 0;
GMAT ArtemisFiniteCoarse.Z = 1300;
GMAT ArtemisFiniteCoarse.VX = 0;
GMAT ArtemisFiniteCoarse.VY = 7.35;
GMAT ArtemisFiniteCoarse.VZ = 1;
GMAT ArtemisFiniteCoarse.DryMass = 850;
GMAT ArtemisFiniteCoarse.Cd = 2.2;
GMAT ArtemisFiniteCoarse.Cr = 1.8;
GMAT ArtemisFiniteCoarse.DragArea = 15;
GMAT ArtemisFiniteCoarse.SRPArea = 1;
GMAT ArtemisFiniteCoarse.NAIFId = 10004001;
GMAT ArtemisFiniteCoarse.NAIFIdReferenceFrame = 9004001;
GMAT ArtemisFiniteCoarse.OrbitColor = Blue;
GMAT ArtemisFiniteCoarse.TargetColor = DimGray;
GMAT ArtemisFiniteCoarse.OrbitErrorCovariance = [ 1e+70 0 0 0 0 0 ; 0 1e+70 0 0 0 0 ; 0 0 1e+70 0 0 0 ; 0 0 0
      1e+70 0 0 ; 0 0 0 0 1e+70 0 ; 0 0 0 0 0 1e+70 ];
GMAT ArtemisFiniteCoarse.CdSigma = 1e+70;
GMAT ArtemisFiniteCoarse.CrSigma = 1e+70;
GMAT ArtemisFiniteCoarse.Id = 'SatId';
GMAT ArtemisFiniteCoarse.Attitude = CoordinateSystemFixed;
GMAT ArtemisFiniteCoarse.SPADSRPScaleFactor = 1;
GMAT ArtemisFiniteCoarse.ModelFile = 'aura.3ds';
```

```
GMAT ArtemisFiniteCoarse.ModelOffsetX = 0;
GMAT ArtemisFiniteCoarse.ModelOffsetY = 0;
GMAT ArtemisFiniteCoarse.ModelOffsetZ = 0;
GMAT ArtemisFiniteCoarse.ModelRotationX = 0;
GMAT ArtemisFiniteCoarse.ModelRotationY = 0;
GMAT ArtemisFiniteCoarse.ModelRotationZ = 0;
GMAT ArtemisFiniteCoarse.ModelScale = 1;
GMAT ArtemisFiniteCoarse.AttitudeDisplayStateType = 'Quaternion';
GMAT ArtemisFiniteCoarse.AttitudeRateDisplayStateType = 'AngularVelocity';
GMAT ArtemisFiniteCoarse.AttitudeCoordinateSystem = EarthMJ2000Eq;
GMAT ArtemisFiniteCoarse.EulerAngleSequence = '321';


%
%           Hardware Components
%

Create ChemicalThruster LEROSThuster;
GMAT LEROSThuster.CoordinateSystem = Local;
GMAT LEROSThuster.Origin = Earth;
GMAT LEROSThuster.Axes = VNB;
GMAT LEROSThuster.ThrustDirection1 = 1;
GMAT LEROSThuster.ThrustDirection2 = 0;
GMAT LEROSThuster.ThrustDirection3 = 0;
GMAT LEROSThuster.DutyCycle = 1;
GMAT LEROSThuster.ThrustScaleFactor = 1;
GMAT LEROSThuster.DecrementMass = true;
GMAT LEROSThuster.Tank = {HydrazineTank, MONTank};
GMAT LEROSThuster.MixRatio = [ 0.541 0.459 ];
GMAT LEROSThuster.GravitationalAccel = 9.81;
GMAT LEROSThuster.C1 = 635;
GMAT LEROSThuster.C2 = 0;
GMAT LEROSThuster.C3 = 0;
GMAT LEROSThuster.C4 = 0;
GMAT LEROSThuster.C5 = 0;
GMAT LEROSThuster.C6 = 0;
GMAT LEROSThuster.C7 = 0;
GMAT LEROSThuster.C8 = 0;
GMAT LEROSThuster.C9 = 0;
GMAT LEROSThuster.C10 = 0;
GMAT LEROSThuster.C11 = 0;
GMAT LEROSThuster.C12 = 0;
GMAT LEROSThuster.C13 = 0;
GMAT LEROSThuster.C14 = 0;
GMAT LEROSThuster.C15 = 0;
GMAT LEROSThuster.C16 = 0;
GMAT LEROSThuster.K1 = 317;
GMAT LEROSThuster.K2 = 0;
GMAT LEROSThuster.K3 = 0;
GMAT LEROSThuster.K4 = 0;
GMAT LEROSThuster.K5 = 0;
GMAT LEROSThuster.K6 = 0;
GMAT LEROSThuster.K7 = 0;
GMAT LEROSThuster.K8 = 0;
GMAT LEROSThuster.K9 = 0;
GMAT LEROSThuster.K10 = 0;
GMAT LEROSThuster.K11 = 0;
```

```
GMAT LEROSThuster.K12 = 0;
GMAT LEROSThuster.K13 = 0;
GMAT LEROSThuster.K14 = 0;
GMAT LEROSThuster.K15 = 0;
GMAT LEROSThuster.K16 = 0;


Create ChemicalTank HydrazineTank;
GMAT HydrazineTank.AllowNegativeFuelMass = true;
GMAT HydrazineTank.FuelMass = 1;
GMAT HydrazineTank.Pressure = 2600;
GMAT HydrazineTank.Temperature = 20;
GMAT HydrazineTank.RefTemperature = 20;
GMAT HydrazineTank.Volume = 0.2;
GMAT HydrazineTank.FuelDensity = 1021;
GMAT HydrazineTank.PressureModel = PressureRegulated;


Create ChemicalTank MONTank;
GMAT MONTank.AllowNegativeFuelMass = true;
GMAT MONTank.FuelMass = 1;
GMAT MONTank.Pressure = 2600;
GMAT MONTank.Temperature = 20;
GMAT MONTank.RefTemperature = 20;
GMAT MONTank.Volume = 0.2;
GMAT MONTank.FuelDensity = 1370;
GMAT MONTank.PressureModel = PressureRegulated;


%
%          Hardware Components
%

Create ChemicalThruster LEROSThusterLOI;
GMAT LEROSThusterLOI.CoordinateSystem = Local;
GMAT LEROSThusterLOI.Origin = Luna;
GMAT LEROSThusterLOI.Axes = VNB;
GMAT LEROSThusterLOI.ThrustDirection1 = 1;
GMAT LEROSThusterLOI.ThrustDirection2 = 0;
GMAT LEROSThusterLOI.ThrustDirection3 = 0;
GMAT LEROSThusterLOI.DutyCycle = 1;
GMAT LEROSThusterLOI.ThrustScaleFactor = 1;
GMAT LEROSThusterLOI.DecrementMass = true;
GMAT LEROSThusterLOI.Tank = {HydrazineTank, MONTank};
GMAT LEROSThusterLOI.MixRatio = [ 0.541 0.459 ];
GMAT LEROSThusterLOI.GravitationalAccel = 9.81;
GMAT LEROSThusterLOI.C1 = 635;
GMAT LEROSThusterLOI.C2 = 0;
GMAT LEROSThusterLOI.C3 = 0;
GMAT LEROSThusterLOI.C4 = 0;
GMAT LEROSThusterLOI.C5 = 0;
GMAT LEROSThusterLOI.C6 = 0;
GMAT LEROSThusterLOI.C7 = 0;
GMAT LEROSThusterLOI.C8 = 0;
GMAT LEROSThusterLOI.C9 = 0;
GMAT LEROSThusterLOI.C10 = 0;
GMAT LEROSThusterLOI.C11 = 0;
GMAT LEROSThusterLOI.C12 = 0;
GMAT LEROSThusterLOI.C13 = 0;
```

```
GMAT LEROSThusterLOI.C14 = 0;
GMAT LEROSThusterLOI.C15 = 0;
GMAT LEROSThusterLOI.C16 = 0;
GMAT LEROSThusterLOI.K1 = 317;
GMAT LEROSThusterLOI.K2 = 0;
GMAT LEROSThusterLOI.K3 = 0;
GMAT LEROSThusterLOI.K4 = 0;
GMAT LEROSThusterLOI.K5 = 0;
GMAT LEROSThusterLOI.K6 = 0;
GMAT LEROSThusterLOI.K7 = 0;
GMAT LEROSThusterLOI.K8 = 0;
GMAT LEROSThusterLOI.K9 = 0;
GMAT LEROSThusterLOI.K10 = 0;
GMAT LEROSThusterLOI.K11 = 0;
GMAT LEROSThusterLOI.K12 = 0;
GMAT LEROSThusterLOI.K13 = 0;
GMAT LEROSThusterLOI.K14 = 0;
GMAT LEROSThusterLOI.K15 = 0;
GMAT LEROSThusterLOI.K16 = 0;


%
%          Hardware Components
%

Create ChemicalThruster LEROSThusterIAB;
GMAT LEROSThusterIAB.CoordinateSystem = Local;
GMAT LEROSThusterIAB.Origin = Luna;
GMAT LEROSThusterIAB.Axes = VNB;
GMAT LEROSThusterIAB.ThrustDirection1 = 0;
GMAT LEROSThusterIAB.ThrustDirection2 = 1;
GMAT LEROSThusterIAB.ThrustDirection3 = 0;
GMAT LEROSThusterIAB.DutyCycle = 1;
GMAT LEROSThusterIAB.ThrustScaleFactor = 1;
GMAT LEROSThusterIAB.DecrementMass = true;
GMAT LEROSThusterIAB.Tank = {HydrazineTank, MONTank};
GMAT LEROSThusterIAB.MixRatio = [ 0.541 0.459 ];
GMAT LEROSThusterIAB.GravitationalAccel = 9.81;
GMAT LEROSThusterIAB.C1 = 635;
GMAT LEROSThusterIAB.C2 = 0;
GMAT LEROSThusterIAB.C3 = 0;
GMAT LEROSThusterIAB.C4 = 0;
GMAT LEROSThusterIAB.C5 = 0;
GMAT LEROSThusterIAB.C6 = 0;
GMAT LEROSThusterIAB.C7 = 0;
GMAT LEROSThusterIAB.C8 = 0;
GMAT LEROSThusterIAB.C9 = 0;
GMAT LEROSThusterIAB.C10 = 0;
GMAT LEROSThusterIAB.C11 = 0;
GMAT LEROSThusterIAB.C12 = 0;
GMAT LEROSThusterIAB.C13 = 0;
GMAT LEROSThusterIAB.C14 = 0;
GMAT LEROSThusterIAB.C15 = 0;
GMAT LEROSThusterIAB.C16 = 0;
GMAT LEROSThusterIAB.K1 = 317;
GMAT LEROSThusterIAB.K2 = 0;
GMAT LEROSThusterIAB.K3 = 0;
```

```
GMAT  LEROSThusterIAB . K4  =  0;
GMAT  LEROSThusterIAB . K5  =  0;
GMAT  LEROSThusterIAB . K6  =  0;
GMAT  LEROSThusterIAB . K7  =  0;
GMAT  LEROSThusterIAB . K8  =  0;
GMAT  LEROSThusterIAB . K9  =  0;
GMAT  LEROSThusterIAB . K10  =  0;
GMAT  LEROSThusterIAB . K11  =  0;
GMAT  LEROSThusterIAB . K12  =  0;
GMAT  LEROSThusterIAB . K13  =  0;
GMAT  LEROSThusterIAB . K14  =  0;
GMAT  LEROSThusterIAB . K15  =  0;
GMAT  LEROSThusterIAB . K16  =  0;


%
%              Hardware  Components
%


Create  ChemicalThruster  LEROSThusterEAB ;
GMAT  LEROSThusterEAB . CoordinateSystem  =  Local ;
GMAT  LEROSThusterEAB . Origin  =  Luna ;
GMAT  LEROSThusterEAB . Axes  =  VNB ;
GMAT  LEROSThusterEAB . ThrustDirection1  =   1;
GMAT  LEROSThusterEAB . ThrustDirection2  =  0;
GMAT  LEROSThusterEAB . ThrustDirection3  =  0;
GMAT  LEROSThusterEAB . DutyCycle  =  1;
GMAT  LEROSThusterEAB . ThrustScaleFactor  =  1;
GMAT  LEROSThusterEAB . DecrementMass  =  true ;
GMAT  LEROSThusterEAB . Tank  =  {HydrazineTank ,  MONTank };
GMAT  LEROSThusterEAB . MixRatio  =  [  0.541  0.459  ];
GMAT  LEROSThusterEAB . GravitationalAccel  =  9.81 ;
GMAT  LEROSThusterEAB . C1  =  635;
GMAT  LEROSThusterEAB . C2  =  0;
GMAT  LEROSThusterEAB . C3  =  0;
GMAT  LEROSThusterEAB . C4  =  0;
GMAT  LEROSThusterEAB . C5  =  0;
GMAT  LEROSThusterEAB . C6  =  0;
GMAT  LEROSThusterEAB . C7  =  0;
GMAT  LEROSThusterEAB . C8  =  0;
GMAT  LEROSThusterEAB . C9  =  0;
GMAT  LEROSThusterEAB . C10  =  0;
GMAT  LEROSThusterEAB . C11  =  0;
GMAT  LEROSThusterEAB . C12  =  0;
GMAT  LEROSThusterEAB . C13  =  0;
GMAT  LEROSThusterEAB . C14  =  0;
GMAT  LEROSThusterEAB . C15  =  0;
GMAT  LEROSThusterEAB . C16  =  0;
GMAT  LEROSThusterEAB . K1  =  317;
GMAT  LEROSThusterEAB . K2  =  0;
GMAT  LEROSThusterEAB . K3  =  0;
GMAT  LEROSThusterEAB . K4  =  0;
GMAT  LEROSThusterEAB . K5  =  0;
GMAT  LEROSThusterEAB . K6  =  0;
GMAT  LEROSThusterEAB . K7  =  0;
GMAT  LEROSThusterEAB . K8  =  0;
GMAT  LEROSThusterEAB . K9  =  0;
```

```
GMAT LEROSThusterEAB.K10 = 0;
GMAT LEROSThusterEAB.K11 = 0;
GMAT LEROSThusterEAB.K12 = 0;
GMAT LEROSThusterEAB.K13 = 0;
GMAT LEROSThusterEAB.K14 = 0;
GMAT LEROSThusterEAB.K15 = 0;
GMAT LEROSThusterEAB.K16 = 0;


%
%                ForceModels
%


Create ForceModel NearMoonProp_ForceModel;
GMAT NearMoonProp_ForceModel.CentralBody = Luna;
GMAT NearMoonProp_ForceModel.PrimaryBodies = {Luna};
GMAT NearMoonProp_ForceModel.PointMasses = {Earth, Jupiter, Mars, Saturn, Sun, Venus};
GMAT NearMoonProp_ForceModel.Drag = None;
GMAT NearMoonProp_ForceModel.SRP = On;
GMAT NearMoonProp_ForceModel.RelativisticCorrection = On;
GMAT NearMoonProp_ForceModel.ErrorControl = RSSStep;
GMAT NearMoonProp_ForceModel.GravityField.Luna.Degree = 10;
GMAT NearMoonProp_ForceModel.GravityField.Luna.Order = 10;
GMAT NearMoonProp_ForceModel.GravityField.Luna.StmLimit = 100;
GMAT NearMoonProp_ForceModel.GravityField.Luna.PotentialFile = 'LP165P.cof';
GMAT NearMoonProp_ForceModel.GravityField.Luna.TideModel = 'None';
GMAT NearMoonProp_ForceModel.SRP.Flux = 1367;
GMAT NearMoonProp_ForceModel.SRP.SRPModel = Spherical;
GMAT NearMoonProp_ForceModel.SRP.Nominal_Sun = 149597870.691;


%
%                ForceModels
%


Create ForceModel NearEarthProp_ForceModel;
GMAT NearEarthProp_ForceModel.CentralBody = Earth;
GMAT NearEarthProp_ForceModel.PrimaryBodies = {Earth};
GMAT NearEarthProp_ForceModel.PointMasses = {Jupiter, Luna, Mars, Saturn, Sun, Venus};
GMAT NearEarthProp_ForceModel.SRP = On;
GMAT NearEarthProp_ForceModel.RelativisticCorrection = On;
GMAT NearEarthProp_ForceModel.ErrorControl = RSSStep;
GMAT NearEarthProp_ForceModel.GravityField.Earth.Degree = 10;
GMAT NearEarthProp_ForceModel.GravityField.Earth.Order = 10;
GMAT NearEarthProp_ForceModel.GravityField.Earth.StmLimit = 100;
GMAT NearEarthProp_ForceModel.GravityField.Earth.PotentialFile = 'JGM3.cof';
GMAT NearEarthProp_ForceModel.GravityField.Earth.TideModel = 'None';
GMAT NearEarthProp_ForceModel.SRP.Flux = 1367;
GMAT NearEarthProp_ForceModel.SRP.SRPModel = Spherical;
GMAT NearEarthProp_ForceModel.SRP.Nominal_Sun = 149597870.691;
GMAT NearEarthProp_ForceModel.Drag.AtmosphereModel = JacchiaRoberts;
GMAT NearEarthProp_ForceModel.Drag.HistoricWeatherSource = 'ConstantFluxAndGeoMag';
GMAT NearEarthProp_ForceModel.Drag.PredictedWeatherSource = 'ConstantFluxAndGeoMag';
GMAT NearEarthProp_ForceModel.Drag.CSSISpaceWeatherFile = 'SpaceWeather All v1.2.txt';
GMAT NearEarthProp_ForceModel.Drag.SchattenFile = 'SchattenPredict.txt';
GMAT NearEarthProp_ForceModel.Drag.F107 = 150;
GMAT NearEarthProp_ForceModel.Drag.F107A = 150;
GMAT NearEarthProp_ForceModel.Drag.MagneticIndex = 3;
```

```
GMAT NearEarthProp_ForceModel.Drag.SchattenErrorModel = 'Nominal';
GMAT NearEarthProp_ForceModel.Drag.SchattenTimingModel = 'NominalCycle';


%
%          Propagators
%

Create Propagator NearMoonProp;
GMAT NearMoonProp.FM = NearMoonProp_ForceModel;
GMAT NearMoonProp.Type = PrinceDormand78;
GMAT NearMoonProp.InitialStepSize = 60;
GMAT NearMoonProp.Accuracy = 9.999999999999999e 12;
GMAT NearMoonProp.MinStep = 0;
GMAT NearMoonProp.MaxStep = 86400;
GMAT NearMoonProp.MaxStepAttempts = 50;
GMAT NearMoonProp.StopIfAccuracyIsViolated = true;


%
%          Propagators
%

Create Propagator NearEarthProp;
GMAT NearEarthProp.FM = NearEarthProp_ForceModel;
GMAT NearEarthProp.Type = PrinceDormand78;
GMAT NearEarthProp.InitialStepSize = 60;
GMAT NearEarthProp.Accuracy = 9.999999999999999e 12;
GMAT NearEarthProp.MinStep = 0;
GMAT NearEarthProp.MaxStep = 86400;
GMAT NearEarthProp.MaxStepAttempts = 50;
GMAT NearEarthProp.StopIfAccuracyIsViolated = true;


%
%          Burns
%

Create ImpulsiveBurn TLI;
GMAT TLI.CoordinateSystem = Local;
GMAT TLI.Origin = Earth;
GMAT TLI.Axes = VNB;
GMAT TLI.Element1 = 3.08;
GMAT TLI.Element2 = 0;
GMAT TLI.Element3 = 0;
GMAT TLI.DecrementMass = false;
GMAT TLI.Isp = 318;
GMAT TLI.GravitationalAccel = 9.81;


Create FiniteBurn FiniteTLICoarse;
GMAT FiniteTLICoarse.Thrusters = {LEROSThuster};
GMAT FiniteTLICoarse.ThrottleLogicAlgorithm = 'MaxNumberOfThrusters';


Create ImpulsiveBurn LOI;
GMAT LOI.CoordinateSystem = Local;
GMAT LOI.Origin = Luna;
GMAT LOI.Axes = VNB;
GMAT LOI.Element1 = 0.5;
GMAT LOI.Element2 = 0;
```

```
GMAT LOI. Element3 = 0;
GMAT LOI. DecrementMass = false;
GMAT LOI. Isp = 300;
GMAT LOI. GravitationalAccel = 9.81;

Create FiniteBurn FiniteLOI;
GMAT FiniteLOI. Thrusters = {LEROSThusterLOI};
GMAT FiniteLOI. ThrottleLogicAlgorithm = 'MaxNumberOfThrusters';

Create FiniteBurn FiniteTLI;
GMAT FiniteTLI. Thrusters = {LEROSThuster};
GMAT FiniteTLI. ThrottleLogicAlgorithm = 'MaxNumberOfThrusters';

Create ImpulsiveBurn IAB;
GMAT IAB. CoordinateSystem = Local;
GMAT IAB. Origin = Luna;
GMAT IAB. Axes = VNB;
GMAT IAB. Element1 = 0;
GMAT IAB. Element2 = 0.1;
GMAT IAB. Element3 = 0;
GMAT IAB. DecrementMass = false;
GMAT IAB. Isp = 300;
GMAT IAB. GravitationalAccel = 9.81;

Create FiniteBurn FiniteIAB;
GMAT FiniteIAB. Thrusters = {LEROSThusterIAB};
GMAT FiniteIAB. ThrottleLogicAlgorithm = 'MaxNumberOfThrusters';

Create FiniteBurn FiniteEAB;
GMAT FiniteEAB. Thrusters = {LEROSThusterEAB};
GMAT FiniteEAB. ThrottleLogicAlgorithm = 'MaxNumberOfThrusters';

%
%          Coordinate Systems
%

Create CoordinateSystem EarthMoonRot;
GMAT EarthMoonRot. Origin = Earth;
GMAT EarthMoonRot. Axes = ObjectReferenced;
GMAT EarthMoonRot. XAxis = R;
GMAT EarthMoonRot. ZAxis = N;
GMAT EarthMoonRot. Primary = Earth;
GMAT EarthMoonRot. Secondary = Luna;

Create CoordinateSystem LunaInertial;
GMAT LunaInertial. Origin = Luna;
GMAT LunaInertial. Axes = BodyInertial;

Create CoordinateSystem LunaFixed;
GMAT LunaFixed. Origin = Luna;
GMAT LunaFixed. Axes = BodyFixed;

%
%          Solvers
%
```

```
Create DifferentialCorrector DC1;
GMAT DC1.ShowProgress = true;
GMAT DC1.ReportStyle = Normal;
GMAT DC1.ReportFile = 'DifferentialCorrectorDC1.data';
GMAT DC1.MaximumIterations = 150;
GMAT DC1.DerivativeMethod = ForwardDifference;
GMAT DC1.Algorithm = NewtonRaphson;


%
%            Subscribers
%


Create OrbitView EarthMoonRotatingFrame;
GMAT EarthMoonRotatingFrame.SolverIterations = Current;
GMAT EarthMoonRotatingFrame.UpperLeft = [ 0.2541666666666667 0.4988888888888889 ];
GMAT EarthMoonRotatingFrame.Size = [ 0.3951388888888889 0.47 ];
GMAT EarthMoonRotatingFrame.RelativeZOrder = 5;
GMAT EarthMoonRotatingFrame.Maximized = false;
GMAT EarthMoonRotatingFrame.Add = {Artemis, Earth, Luna};
GMAT EarthMoonRotatingFrame.CoordinateSystem = EarthMoonRot;
GMAT EarthMoonRotatingFrame.DrawObject = [ true true true ];
GMAT EarthMoonRotatingFrame.DataCollectFrequency = 1;
GMAT EarthMoonRotatingFrame.UpdatePlotFrequency = 50;
GMAT EarthMoonRotatingFrame.NumPointsToRedraw = 0;
GMAT EarthMoonRotatingFrame.ShowPlot = false;
GMAT EarthMoonRotatingFrame.MaxPlotPoints = 20000;
GMAT EarthMoonRotatingFrame.ShowLabels = true;
GMAT EarthMoonRotatingFrame.ViewPointReference = Earth;
GMAT EarthMoonRotatingFrame.ViewPointVector = [ 10000 0 30000 ];
GMAT EarthMoonRotatingFrame.ViewDirection = Earth;
GMAT EarthMoonRotatingFrame.ViewScaleFactor = 40;
GMAT EarthMoonRotatingFrame.ViewUpCoordinateSystem = EarthMoonRot;
GMAT EarthMoonRotatingFrame.ViewUpAxis = X;
GMAT EarthMoonRotatingFrame.EclipticPlane = Off;
GMAT EarthMoonRotatingFrame.XYPlane = Off;
GMAT EarthMoonRotatingFrame.WireFrame = Off;
GMAT EarthMoonRotatingFrame.Axes = Off;
GMAT EarthMoonRotatingFrame.Grid = Off;
GMAT EarthMoonRotatingFrame.SunLine = Off;
GMAT EarthMoonRotatingFrame.UseInitialView = On;
GMAT EarthMoonRotatingFrame.StarCount = 7000;
GMAT EarthMoonRotatingFrame.EnableStars = On;
GMAT EarthMoonRotatingFrame.EnableConstellations = On;


Create OrbitView LunaInertialFrame;
GMAT LunaInertialFrame.SolverIterations = Current;
GMAT LunaInertialFrame.UpperLeft = [ 0.6513888888888889 0.04111111111111111 ];
GMAT LunaInertialFrame.Size = [ 0.3416666666666667 0.4466666666666667 ];
GMAT LunaInertialFrame.RelativeZOrder = 15;
GMAT LunaInertialFrame.Maximized = false;
GMAT LunaInertialFrame.Add = {Artemis, Luna, Earth};
GMAT LunaInertialFrame.CoordinateSystem = LunaInertial;
GMAT LunaInertialFrame.DrawObject = [ true true true ];
GMAT LunaInertialFrame.DataCollectFrequency = 1;
GMAT LunaInertialFrame.UpdatePlotFrequency = 50;
GMAT LunaInertialFrame.NumPointsToRedraw = 150;
```

```
GMAT LunaInertialFrame.ShowPlot = false;
GMAT LunaInertialFrame.MaxPlotPoints = 20000;
GMAT LunaInertialFrame.ShowLabels = true;
GMAT LunaInertialFrame.ViewPointReference = Luna;
GMAT LunaInertialFrame.ViewPointVector = [ 10000 10000 10000 ];
GMAT LunaInertialFrame.ViewDirection = Luna;
GMAT LunaInertialFrame.ViewScaleFactor = 1.5;
GMAT LunaInertialFrame.ViewUpCoordinateSystem = EarthMJ2000Eq;
GMAT LunaInertialFrame.ViewUpAxis = Z;
GMAT LunaInertialFrame.EclipticPlane = Off;
GMAT LunaInertialFrame.XYPlane = On;
GMAT LunaInertialFrame.WireFrame = Off;
GMAT LunaInertialFrame.Axes = On;
GMAT LunaInertialFrame.Grid = Off;
GMAT LunaInertialFrame.SunLine = Off;
GMAT LunaInertialFrame.UseInitialView = On;
GMAT LunaInertialFrame.StarCount = 7000;
GMAT LunaInertialFrame.EnableStars = On;
GMAT LunaInertialFrame.EnableConstellations = On;

Create OrbitView FarEarthInertialFrame;
GMAT FarEarthInertialFrame.SolverIterations = Current;
GMAT FarEarthInertialFrame.UpperLeft = [ 0.6513888888888889 0.4988888888888889 ];
GMAT FarEarthInertialFrame.Size = [ 0.3423611111111111 0.47 ];
GMAT FarEarthInertialFrame.RelativeZOrder = 10;
GMAT FarEarthInertialFrame.Maximized = false;
GMAT FarEarthInertialFrame.Add = {Artemis, Earth, Luna};
GMAT FarEarthInertialFrame.CoordinateSystem = EarthMJ2000Eq;
GMAT FarEarthInertialFrame.DrawObject = [ true true true ];
GMAT FarEarthInertialFrame.DataCollectFrequency = 1;
GMAT FarEarthInertialFrame.UpdatePlotFrequency = 50;
GMAT FarEarthInertialFrame.NumPointsToRedraw = 0;
GMAT FarEarthInertialFrame.ShowPlot = false;
GMAT FarEarthInertialFrame.MaxPlotPoints = 20000;
GMAT FarEarthInertialFrame.ShowLabels = true;
GMAT FarEarthInertialFrame.ViewPointReference = Earth;
GMAT FarEarthInertialFrame.ViewPointVector = [ 0 0 30000 ];
GMAT FarEarthInertialFrame.ViewDirection = Earth;
GMAT FarEarthInertialFrame.ViewScaleFactor = 45;
GMAT FarEarthInertialFrame.ViewUpCoordinateSystem = EarthMJ2000Eq;
GMAT FarEarthInertialFrame.ViewUpAxis = Z;
GMAT FarEarthInertialFrame.EclipticPlane = Off;
GMAT FarEarthInertialFrame.XYPlane = Off;
GMAT FarEarthInertialFrame.WireFrame = Off;
GMAT FarEarthInertialFrame.Axes = On;
GMAT FarEarthInertialFrame.Grid = Off;
GMAT FarEarthInertialFrame.SunLine = Off;
GMAT FarEarthInertialFrame.UseInitialView = On;
GMAT FarEarthInertialFrame.StarCount = 7000;
GMAT FarEarthInertialFrame.EnableStars = On;
GMAT FarEarthInertialFrame.EnableConstellations = On;

Create ReportFile FlybyReport;
GMAT FlybyReport.SolverIterations = All;
GMAT FlybyReport.UpperLeft = [ 0 0 ];
GMAT FlybyReport.Size = [ 0 0 ];
```

```
GMAT FlybyReport.RelativeZOrder = 0;
GMAT FlybyReport.Maximized = false;
GMAT FlybyReport.Filename = 'FlybyReport.txt';
GMAT FlybyReport.Precision = 6;
GMAT FlybyReport.WriteHeaders = true;
GMAT FlybyReport.LeftJustify = On;
GMAT FlybyReport.ZeroFill = Off;
GMAT FlybyReport.FixedWidth = true;
GMAT FlybyReport.Delimiter = ' ';
GMAT FlybyReport.ColumnWidth = 10;
GMAT FlybyReport.WriteReport = true;


Create OrbitView CloseEarthInertialFrame;
GMAT CloseEarthInertialFrame.SolverIterations = Current;
GMAT CloseEarthInertialFrame.UpperLeft = [ 0.2527777777777778 0.04111111111111111 ];
GMAT CloseEarthInertialFrame.Size = [ 0.3958333333333333 0.4533333333333333 ];
GMAT CloseEarthInertialFrame.RelativeZOrder = 23;
GMAT CloseEarthInertialFrame.Maximized = false;
GMAT CloseEarthInertialFrame.Add = {Artemis, Earth, Luna};
GMAT CloseEarthInertialFrame.CoordinateSystem = EarthICRF;
GMAT CloseEarthInertialFrame.DrawObject = [ true true true ];
GMAT CloseEarthInertialFrame.DataCollectFrequency = 1;
GMAT CloseEarthInertialFrame.UpdatePlotFrequency = 50;
GMAT CloseEarthInertialFrame.NumPointsToRedraw = 0;
GMAT CloseEarthInertialFrame.ShowPlot = false;
GMAT CloseEarthInertialFrame.MaxPlotPoints = 20000;
GMAT CloseEarthInertialFrame.ShowLabels = true;
GMAT CloseEarthInertialFrame.ViewPointReference = Earth;
GMAT CloseEarthInertialFrame.ViewPointVector = [ 0 0 40000 ];
GMAT CloseEarthInertialFrame.ViewDirection = Earth;
GMAT CloseEarthInertialFrame.ViewScaleFactor = 1;
GMAT CloseEarthInertialFrame.ViewUpCoordinateSystem = EarthMJ2000Eq;
GMAT CloseEarthInertialFrame.ViewUpAxis = Z;
GMAT CloseEarthInertialFrame.EclipticPlane = Off;
GMAT CloseEarthInertialFrame.XYPlane = Off;
GMAT CloseEarthInertialFrame.WireFrame = Off;
GMAT CloseEarthInertialFrame.Axes = Off;
GMAT CloseEarthInertialFrame.Grid = Off;
GMAT CloseEarthInertialFrame.SunLine = Off;
GMAT CloseEarthInertialFrame.UseInitialView = On;
GMAT CloseEarthInertialFrame.StarCount = 7000;
GMAT CloseEarthInertialFrame.EnableStars = On;
GMAT CloseEarthInertialFrame.EnableConstellations = On;


Create EphemerisFile Ephemeris;
GMAT Ephemeris.UpperLeft = [ 0 0 ];
GMAT Ephemeris.Size = [ 0 0 ];
GMAT Ephemeris.RelativeZOrder = 0;
GMAT Ephemeris.Maximized = false;
GMAT Ephemeris.Spacecraft = Artemis;
GMAT Ephemeris.Filename = 'FlybyEphemeris.txt';
GMAT Ephemeris.FileFormat = STK TimePosVel;
GMAT Ephemeris.EpochFormat = UTCModJulian;
GMAT Ephemeris.InitialEpoch = InitialSpacecraftEpoch;
GMAT Ephemeris.FinalEpoch = FinalSpacecraftEpoch;
GMAT Ephemeris.StepSize = IntegratorSteps;
```

208

```
GMAT Ephemeris . Interpolator = Lagrange ;
GMAT Ephemeris . InterpolationOrder = 7;
GMAT Ephemeris . CoordinateSystem = EarthMJ2000Eq ;
GMAT Ephemeris . OutputFormat = LittleEndian ;
GMAT Ephemeris . WriteEphemeris = false ;
GMAT Ephemeris . DistanceUnit = Kilometers ;
GMAT Ephemeris . IncludeEventBoundaries = true ;


Create ReportFile FlybyString ;
GMAT FlybyString . SolverIterations = Current ;
GMAT FlybyString . UpperLeft = [ 0 0 ];
GMAT FlybyString . Size = [ 0 0 ];
GMAT FlybyString . RelativeZOrder = 0;
GMAT FlybyString . Maximized = false ;
GMAT FlybyString . Filename = 'FlybyString . txt ';
GMAT FlybyString . Precision = 16;
GMAT FlybyString . WriteHeaders = false ;
GMAT FlybyString . LeftJustify = On;
GMAT FlybyString . ZeroFill = Off ;
GMAT FlybyString . FixedWidth = false ;
GMAT FlybyString . Delimiter = '   ';
GMAT FlybyString . ColumnWidth = 23;
GMAT FlybyString . WriteReport = true ;


Create OrbitView LunaFixedFrame ;
GMAT LunaFixedFrame . SolverIterations = Current ;
GMAT LunaFixedFrame . UpperLeft = [ 0.05 0.1522222222222222 ];
GMAT LunaFixedFrame . Size = [ 0.5451388888888888 0.6144444444444445 ];
GMAT LunaFixedFrame . RelativeZOrder = 383;
GMAT LunaFixedFrame . Maximized = false ;
GMAT LunaFixedFrame . Add = { Artemis , Earth , Luna };
GMAT LunaFixedFrame . CoordinateSystem = LunaFixed ;
GMAT LunaFixedFrame . DrawObject = [ true true true ];
GMAT LunaFixedFrame . DataCollectFrequency = 1;
GMAT LunaFixedFrame . UpdatePlotFrequency = 50;
GMAT LunaFixedFrame . NumPointsToRedraw = 0;
GMAT LunaFixedFrame . ShowPlot = false ;
GMAT LunaFixedFrame . MaxPlotPoints = 20000;
GMAT LunaFixedFrame . ShowLabels = true ;
GMAT LunaFixedFrame . ViewPointReference = Luna ;
GMAT LunaFixedFrame . ViewPointVector = [ 10000 10000 10000 ];
GMAT LunaFixedFrame . ViewDirection = Luna ;
GMAT LunaFixedFrame . ViewScaleFactor = 1;
GMAT LunaFixedFrame . ViewUpCoordinateSystem = LunaFixed ;
GMAT LunaFixedFrame . ViewUpAxis = Z;
GMAT LunaFixedFrame . EclipticPlane = Off ;
GMAT LunaFixedFrame . XYPlane = On;
GMAT LunaFixedFrame . WireFrame = Off ;
GMAT LunaFixedFrame . Axes = On;
GMAT LunaFixedFrame . Grid = Off ;
GMAT LunaFixedFrame . SunLine = Off ;
GMAT LunaFixedFrame . UseInitialView = On;
GMAT LunaFixedFrame . StarCount = 7000;
GMAT LunaFixedFrame . EnableStars = On;
GMAT LunaFixedFrame . EnableConstellations = On;
```

```
Create GroundTrackPlot LunaGroundTrackPlot;
GMAT LunaGroundTrackPlot.SolverIterations = Current;
GMAT LunaGroundTrackPlot.UpperLeft = [ 0.4861111111111111 0.3711111111111111 ];
GMAT LunaGroundTrackPlot.Size = [ 0.4083333333333333 0.4611111111111111 ];
GMAT LunaGroundTrackPlot.RelativeZOrder = 375;
GMAT LunaGroundTrackPlot.Maximized = false;
GMAT LunaGroundTrackPlot.Add = {Artemis, Earth};
GMAT LunaGroundTrackPlot.DataCollectFrequency = 1;
GMAT LunaGroundTrackPlot.UpdatePlotFrequency = 50;
GMAT LunaGroundTrackPlot.NumPointsToRedraw = 0;
GMAT LunaGroundTrackPlot.ShowPlot = false;
GMAT LunaGroundTrackPlot.MaxPlotPoints = 20000;
GMAT LunaGroundTrackPlot.CentralBody = Luna;
GMAT LunaGroundTrackPlot.TextureMap = 'Moon_HermesCelestiaMotherlode.jpg';


%
%          Arrays, Variables, Strings
%
Create Variable RAAN AOP BurnCoarse Thrust Isp g c TLIdV mdry mdot;
Create Variable mprop mwet mratio t tlimit FullTankMass TLIEmptyTankMass TLIPropConsMass MissionMass mpayload;
Create Variable msubsys mengine ArrRA TA tinitial DepartEpoch ArriveEpoch FlightTime I Adjt;
Create Variable LOIdV MissiondV BurnLOI LOIEmptyTankMass LOIPropConsMass tLOI AdjtLOI TotalPropConsMass
      Inclination BurnTotal;
Create Variable InitialTA Burn TLICoarsePropConsMass BurnINC INCTarget absINCTarget Bvector IABdV BurnIAB
      IABEmptyTankMass;
Create Variable IABPropConsMass Period100km TransLunarTime PeriluneEpoch LunarSidereal;
%GMAT RAANTargetArray(1, 2) = 30;
%GMAT RAANTargetArray(1, 3) = 60;
%GMAT RAANTargetArray(1, 4) = 90;
%GMAT RAANTargetArray(1, 5) = 120;
%GMAT RAANTargetArray(1, 6) = 150;
%GMAT RAANTargetArray(1, 7) = 180;
%GMAT RAANTargetArray(1, 8) = 210;
%GMAT RAANTargetArray(1, 9) = 240;
%GMAT RAANTargetArray(1, 10) = 270;
%GMAT RAANTargetArray(1, 11) = 300;
%GMAT RAANTargetArray(1, 12) = 330;
GMAT RAAN = 0;
GMAT AOP = 0;
GMAT BurnCoarse = 0;
GMAT Thrust = 635;
GMAT Isp = 317;
GMAT g = 9.81;
GMAT c = 0;
GMAT TLIdV = 0;
GMAT mdry = 0;
GMAT mdot = 0;
GMAT mprop = 0;
GMAT mwet = 0;
GMAT mratio = 0;
GMAT t = 0;
GMAT tlimit = 2520;
GMAT FullTankMass = 0;
GMAT TLIEmptyTankMass = 0;
GMAT TLIPropConsMass = 0;
GMAT MissionMass = 0;
```

```
GMAT mpayload = PAYLOAD;
GMAT msubsys = 37;
GMAT mengine = 4.5;
GMAT ArrRA = 0;
GMAT TA = 0;
GMAT tinitial = 0;
GMAT DepartEpoch = EPOCH;
GMAT ArriveEpoch = 0;
GMAT FlightTime = 0;
GMAT Adjt = 0;
GMAT LOIdV = 0;
GMAT MissiondV = 0;
GMAT BurnLOI = 0;
GMAT LOIEmptyTankMass = 0;
GMAT LOIPropConsMass = 0;
GMAT tLOI = 0;
GMAT AdjtLOI = 0;
GMAT TotalPropConsMass = 0;
GMAT Inclination = INCLINATION;
GMAT BurnTotal = 0;
GMAT Burn = 0;
GMAT TLICoarsePropConsMass = 0;
GMAT BurnINC = 0;
GMAT INCTarget = TARGETINCLINATION;
GMAT absINCTarget = 0;
GMAT Bvector = 0;
GMAT IABdV = 0;
GMAT BurnIAB = 0;
GMAT IABEmptyTankMass = 0;
GMAT IABPropConsMass = 0;
GMAT Period100km = 14140;
GMAT TransLunarTime = 0;
GMAT PeriluneEpoch = 0;
GMAT LunarSidereal = 655.728;


%
%          Mission Sequence
%

BeginMissionSequence;
GMAT 'Find mdry' mdry = msubsys+mengine+mpayload;
GMAT 'Set Dry Mass' Artemis.DryMass = mdry;
GMAT 'Set Epoch' Artemis.Epoch = DepartEpoch;
GMAT 'Set Inclination' Artemis.INC = Inclination;

GMAT 'Store Placeholder Fine' ArtemisFine = Artemis;
GMAT 'Store Placeholder Finite Coarse' ArtemisFiniteCoarse = Artemis;
GMAT 'Store Placeholder Finite' ArtemisFiniteBurn = Artemis;

Toggle 'Turn Off Selected Plots' Ephemeris LunaFixedFrame LunaGroundTrackPlot Off;

Target 'Coarse Lunar Target' DC1 {SolveMode = Solve, ExitMode = DiscardAndContinue, ShowProgressWindow = false
     };

   Vary 'Vary RAAN' DC1(Artemis.RAAN = 0, {Perturbation = .00001, Lower = 1e300, Upper = 1e300, MaxStep = 10,
          AdditiveScaleFactor = 0.0, MultiplicativeScaleFactor = 1.0});
```

```
    Vary 'Vary AOP' DC1(Artemis.AOP = 0, {Perturbation = .00001, Lower = 1e300, Upper = 1e300, MaxStep = 5,
        AdditiveScaleFactor = 0.0, MultiplicativeScaleFactor = 1.0});
    Maneuver 'Apply TLI' TLI(Artemis);

    GMAT 'Save RAAN' RAAN = Artemis.RAAN;
    GMAT 'Save AOP' AOP = Artemis.AOP;

    Propagate 'Prop To Moon' NearEarthProp(Artemis) {Artemis.Earth.Apoapsis, Artemis.ElapsedDays = 4.5};

    Achieve 'RA = 0' DC1(Artemis.EarthMoonRot.RA = 0, {Tolerance = 1});
    Achieve 'DEC = 0' DC1(Artemis.EarthMoonRot.DEC = 0, {Tolerance = 1});

EndTarget;  % For targeter DC1

GMAT 'Initilaze SC Fine' Artemis = ArtemisFine;

Target 'Fine Lunar Target' DC1 {SolveMode = Solve, ExitMode = DiscardAndContinue, ShowProgressWindow = false};

    Vary 'Vary RAAN' DC1(Artemis.RAAN = RAAN, {Perturbation = .00001, Lower = 9.999999e300, Upper = 9.999999
        e300, MaxStep = 10, AdditiveScaleFactor = 0.0, MultiplicativeScaleFactor = 1.0});
    Vary 'Vary AOP' DC1(Artemis.TA = AOP, {Perturbation = 0.00001, Lower = 1e300, Upper = 1e300, MaxStep = 10,
        AdditiveScaleFactor = 0.0, MultiplicativeScaleFactor = 1.0});
    Vary 'Vary TLI' DC1(TLI.Element1 = TLI.Element1, {Perturbation = .0000001, Lower = 9.999999e300, Upper =
        9.999999e300, MaxStep = .01, AdditiveScaleFactor = 0.0, MultiplicativeScaleFactor = 1.0});

    Maneuver 'Apply TLI' TLI(Artemis);

    GMAT 'Save TLIdV' TLIdV = TLI.Element1;
    GMAT 'Save RAAN' RAAN = Artemis.RAAN;
    GMAT 'Save AOP' TA = Artemis.TA;
    GMAT 'Save TA' TA = Artemis.TA;
    Propagate NearEarthProp(Artemis) {Artemis.Luna.Periapsis, Artemis.ElapsedDays = 6};
    Achieve 'Achieve BvectorAngle' DC1(Artemis.LunaInertial.BVectorAngle = INCTarget, {Tolerance = 1});
    Achieve 'Achieve Altitude' DC1(Artemis.Luna.Altitude = 100, {Tolerance = 1});

EndTarget;  % For targeter DC1

GMAT 'Set ArrRA' ArrRA = Artemis.RA;

%Target 'Orbit Insertion Impulse' DC1 {SolveMode = Solve, ExitMode = DiscardAndContinue, ShowProgressWindow =
        false};
%    Vary 'Vary LOI' DC1(LOI.Element1 = LOI.Element1, {Perturbation = 0.0001, Lower = 1e300, Upper = 1e300,
        MaxStep = 0.01, AdditiveScaleFactor = 0.0, MultiplicativeScaleFactor = 1.0});
%    Maneuver 'Apply LOI' LOI(Artemis);
%    GMAT 'Save LOIdV' LOIdV = LOI.Element1;
%    Achieve 'Achieve ECC' DC1(Artemis.Luna.ECC = 0, {Tolerance = 0.01});
%EndTarget;  % For targeter DC1

%Propagate 'Prop Z = 0' NearMoonProp(Artemis) {Artemis.LunaFixed.Z = 0};

GMAT 'Find absLatTarget' absINCTarget = abs(INCTarget);

%Target 'Inclination Adjustment Impulse' DC1 {SolveMode = Solve, ExitMode = DiscardAndContinue,
        ShowProgressWindow = false};
%    Vary 'Vary IAB' DC1(IAB.Element2 = 0.5, {Perturbation = 0.0001, Lower = 1e300, Upper = 1e300, MaxStep =
        0.1, AdditiveScaleFactor = 0.0, MultiplicativeScaleFactor = 1.0});
```

```
%      Maneuver 'Apply IAB' IAB(Artemis);
%      GMAT 'Set IABdV' IABdV = IAB.Element2;
%      Achieve 'Achieve INC' DC1(Artemis.LunaFixed.INC = absINCTarget, {Tolerance = 0.01});
%EndTarget;   % For targeter DC1


%GMAT 'Find MissiondV' MissiondV = (abs(TLI.Element1) + abs(LOI.Element1) + abs(IAB.Element2))*1000;
GMAT 'Find MissiondV' MissiondV = abs(TLIdV)*1000;


GMAT 'Initialize SC Finite' Artemis = ArtemisFiniteCoarse;
GMAT 'Set RAAN' Artemis.RAAN = RAAN;
GMAT 'Set TA' Artemis.TA = AOP;
GMAT 'Find c' c = g*Isp;
GMAT 'Find mdry' mdry = Artemis.DryMass;
GMAT 'Find mdot' mdot = Thrust/c;
GMAT 'Find mratio' mratio = exp(MissiondV/c);
GMAT 'Find mwet' mwet = mratio*mdry;
GMAT 'Find mprop' mprop = mwet    mdry;


%GMAT 'Find t' t = (TLIdV*1000/MissiondV)*mprop/mdot;
GMAT 'Find t' t = mprop/mdot;


GMAT 'Fill Hydrazine tank with 3% margin' Artemis.HydrazineTank.FuelMass = (0.541)*mprop + 0.03*(0.541)*mprop;
GMAT 'Fill MON tank with 3% margin' Artemis.MONTank.FuelMass = (0.459)*mprop + 0.03*(0.459)*mprop;
GMAT 'Set FuelTankMass' FullTankMass = Artemis.HydrazineTank.FuelMass + Artemis.MONTank.FuelMass;


Report FlybyReport DepartEpoch;
Report FlybyReport mpayload;
Report FlybyReport Inclination;
Report FlybyReport INCTarget;
Report FlybyReport TLI.Element1 TLI.Element2 TLI.Element3;
%Report FlybyReport LOI.Element1 LOI.Element2 LOI.Element3;
%Report FlybyReport IAB.Element1 IAB.Element2 IAB.Element3;
Report FlybyReport MissiondV;
Report FlybyReport mdry mratio mwet mprop;
Report FlybyReport FullTankMass;


Target 'Finite TLI Coarse' DC1 {SolveMode = Solve, ExitMode = DiscardAndContinue, ShowProgressWindow = false};
    Vary 'Vary Burn' DC1(BurnCoarse = t, {Perturbation = 0.0001, Lower = 0.0, Upper = 1e300, MaxStep = 10,
        AdditiveScaleFactor = 0.0, MultiplicativeScaleFactor = 1.0});
    Vary 'Vary TA' DC1(Artemis.TA = Artemis.TA, {Perturbation = 0.0001, Lower = 1e300, Upper = 1e300, MaxStep
        = 5, AdditiveScaleFactor = 0.0, MultiplicativeScaleFactor = 1.0});
    GMAT 'Save TA' TA = Artemis.TA;
    BeginFiniteBurn 'Begin TLI Coarse' FiniteTLICoarse(Artemis);
    Propagate 'Prop BurnCoarse' NearEarthProp(Artemis) {Artemis.ElapsedSecs = BurnCoarse, OrbitColor = [253 160
        23]};
    EndFiniteBurn 'End TLI Coarse' FiniteTLICoarse(Artemis);
    Propagate 'Prop to Apoapsis' NearEarthProp(Artemis) {Artemis.Earth.Apoapsis};
    Achieve 'Achieve RA' DC1(Artemis.EarthMJ2000Eq.RA = ArrRA, {Tolerance = 0.1});
    Achieve 'Achieve RMAG' DC1(Artemis.Earth.RMAG = 350000, {Tolerance = 0.1});
EndTarget;   % For targeter DC1


GMAT 'Set Burn' Burn = BurnCoarse;
GMAT 'Initialize SC Finite' Artemis = ArtemisFiniteBurn;
GMAT 'Set RAAN' Artemis.RAAN = RAAN;
GMAT 'Set AOP' Artemis.AOP = AOP;
GMAT 'Set TA' Artemis.TA = TA;
```

```
GMAT 'Fill Hydrazine Tank' Artemis.HydrazineTank.FuelMass = 0.541*FullTankMass;
GMAT 'Fill MON Tank' Artemis.MONTank.FuelMass = 0.459*FullTankMass;


Toggle LunaFixedFrame On;


Target 'Finite TLI Fine' DC1 {SolveMode = Solve, ExitMode = DiscardAndContinue, ShowProgressWindow = false};
    Vary 'Vary Burn' DC1(Burn = Burn, {Perturbation = 0.0001, Lower = t, Upper = tlimit, MaxStep = 1,
        AdditiveScaleFactor = 0.0, MultiplicativeScaleFactor = 1.0});
    Vary 'Vary TA' DC1(Artemis.TA = Artemis.TA, {Perturbation = 0.0001, Lower = 1e300, Upper = 1e300, MaxStep
        = 1, AdditiveScaleFactor = 0.0, MultiplicativeScaleFactor = 1.0});
    BeginFiniteBurn 'Begin TLI Fine' FiniteTLI(Artemis);
    Propagate 'Prop Burn' NearEarthProp(Artemis) {Artemis.ElapsedSecs = Burn, OrbitColor = [251 0 15]};
    EndFiniteBurn 'End TLI Fine' FiniteTLI(Artemis);
    Propagate 'Prop to Moon' NearEarthProp(Artemis) {Artemis.Luna.Periapsis, OrbitColor = [32 255 254]};
    Achieve 'Achieve RadPer' DC1(Artemis.Luna.RadPer = 1837.4, {Tolerance = 0.1});
    Achieve 'Achieve BvectorAngle' DC1(Artemis.LunaInertial.BVectorAngle = INCTarget, {Tolerance = 0.1});
    Achieve 'Achieve RA' DC1(Artemis.EarthMJ2000Eq.RA = ArrRA, {Tolerance = 1});
EndTarget;  % For targeter DC1


GMAT 'Save TLIEmptyTankMass' TLIEmptyTankMass = Artemis.HydrazineTank.FuelMass + Artemis.MONTank.FuelMass;
GMAT 'Find TLIPropConsMass' TLIPropConsMass = FullTankMass    TLIEmptyTankMass;


% GMAT 'Find tLOI' tLOI = abs(LOIdV*1000/MissiondV)*mprop/mdot;


Report FlybyReport Burn;
Report FlybyReport TLIEmptyTankMass TLIPropConsMass;
Report FlybyReport Artemis.LunaFixed.INC;
Report FlybyReport Artemis.LunaFixed.RAAN;
Report FlybyReport Artemis.Luna.SMA;
Report FlybyReport Artemis.Luna.ECC;
Report FlybyReport Artemis.LunaFixed.AOP;



GMAT 'Find TotalPropConsMass' TotalPropConsMass = TLIPropConsMass;
GMAT 'Find MissionMass' MissionMass = TotalPropConsMass + mdry;
GMAT 'Find ArriveEpoch' ArriveEpoch = Artemis.UTCModJulian;
GMAT 'Find FlightTime' FlightTime = ArriveEpoch    DepartEpoch;


Report FlybyReport TotalPropConsMass MissionMass;
Report FlybyReport ArriveEpoch FlightTime;
Report FlybyString DepartEpoch mpayload Inclination INCTarget TLI.Element1 TLI.Element2 TLI.Element3 MissiondV
        mdry mratio mwet mprop FullTankMass Burn TLIEmptyTankMass TLIPropConsMass Artemis.LunaFixed.INC Artemis
        .LunaFixed.RAAN Artemis.Luna.SMA Artemis.Luna.ECC Artemis.LunaFixed.AOP TotalPropConsMass MissionMass
        ArriveEpoch FlightTime;


Stop;


Target 'Finite LOI' DC1 {SolveMode = Solve, ExitMode = DiscardAndContinue, ShowProgressWindow = false};
    Vary 'Vary BurnLOI' DC1(BurnLOI = AdjtLOI, {Perturbation = 0.0001, Lower = 0, Upper = tlimit, MaxStep = 2,
        AdditiveScaleFactor = 0.0, MultiplicativeScaleFactor = 1.0});
    BeginFiniteBurn 'Begin Finite LOI' FiniteLOI(Artemis);
    Propagate 'Prop BurnLOI' NearMoonProp(Artemis) {Artemis.ElapsedSecs = BurnLOI, OrbitColor = [233 29 254]};
    EndFiniteBurn 'End Finite LOI' FiniteLOI(Artemis);
    Achieve 'Achieve ECC' DC1(Artemis.Luna.ECC = 0, {Tolerance = 0.05});
EndTarget;  % For targeter DC1
```

```
GMAT 'Find LOIEmptyTankMass' LOIEmptyTankMass = Artemis.HydrazineTank.FuelMass + Artemis.MONTank.FuelMass;
GMAT 'Find LOIPropConsMass' LOIPropConsMass = TLIEmptyTankMass    LOIEmptyTankMass;
Propagate 'Prop to Z = 0' NearMoonProp(Artemis) {Artemis.LunaFixed.Z = 0};
If 'If INC +/ ' Artemis.LunaInertial.INC > absINCTarget
   GMAT 'Set N Thust Direction 1' Artemis.LEROSThusterIAB.ThrustDirection2 =  1;


EndIf;
Target 'Finite IAB' DC1 {SolveMode = Solve, ExitMode = DiscardAndContinue, ShowProgressWindow = false};
   Vary 'Vary BurnIAB' DC1(BurnIAB = 0, {Perturbation = 0.0001, Lower = 0.0, Upper = 1e300, MaxStep = 1,
         AdditiveScaleFactor = 0.0, MultiplicativeScaleFactor = 1.0});
   BeginFiniteBurn 'Begin Finite IAB' FiniteIAB(Artemis);
   Propagate 'Prop BurnIAB' NearMoonProp(Artemis) {Artemis.ElapsedSecs = BurnIAB, OrbitColor = [253 183 30]};
   EndFiniteBurn 'End Finite IAB' FiniteIAB(Artemis);
   Achieve 'Achieve INC' DC1(Artemis.LunaFixed.INC = absINCTarget, {Tolerance = 1});
EndTarget;  % For targeter DC1
GMAT 'Find IABEmptyTankMass' IABEmptyTankMass = Artemis.HydrazineTank.FuelMass + Artemis.MONTank.FuelMass;
GMAT 'Find IABPropConsMass' IABPropConsMass = LOIEmptyTankMass    IABEmptyTankMass;
GMAT 'Find TotalPropConsMass' TotalPropConsMass = TLIPropConsMass + LOIPropConsMass + IABPropConsMass;
GMAT 'Find MissionMass' MissionMass = mdry + TotalPropConsMass;
GMAT 'Set PeriluneEpoch' PeriluneEpoch = Artemis.UTCModJulian;
GMAT 'Find TranslunarTime' TransLunarTime = PeriluneEpoch DepartEpoch;
GMAT 'Find BurnTotal' BurnTotal = Burn + BurnLOI + BurnIAB;
For 'For I' I = 1:1:12;
%   If 'If RAANTarget < RAAN' RAANTargetArray(I) < Artemis.LunaFixed.RAAN
%       GMAT 'Find Coast Time' CoastArray(I) = (Artemis.LunaFixed.RAAN    RAANTargetArray(I))/360*LunarSidereal
         /24;
%   Else
%       GMAT 'Find Coast Time' CoastArray(I) = (360    RAANTargetArray(I) + Artemis.LunaFixed.RAAN)/360*
         LunarSidereal/24;
%   EndIf;
%   GMAT 'Find Flight Time' FlightTimeArray(I) = TransLunarTime + CoastArray(I);
%   GMAT 'Find Arrive Epoch' ArriveEpochArray(I) = DepartEpoch + FlightTimeArray(I);
EndFor;
Report FlybyReport BurnLOI;
Report FlybyReport LOIEmptyTankMass LOIPropConsMass;
Report FlybyReport BurnIAB;
Report FlybyReport IABEmptyTankMass IABPropConsMass;
Report FlybyReport BurnTotal;
Report FlybyReport Artemis.LunaFixed.INC;
Report FlybyReport Artemis.LunaFixed.RAAN;
Report FlybyReport Artemis.Luna.SMA;
Report FlybyReport Artemis.Luna.ECC;
Report FlybyReport Artemis.LunaFixed.AOP;
Report FlybyReport TotalPropConsMass MissionMass;
Report FlybyReport PeriluneEpoch TransLunarTime;
%Report OrbitReport CoastArray;
%Report OrbitReport FlightTimeArray;
%Report OrbitReport ArriveEpochArray;
%Report OrbitString DepartEpoch mpayload Inclination INCTarget TLI.Element1 TLI.Element2 TLI.Element3 LOI.
     Element1 LOI.Element2 LOI.Element3 IAB.Element1 IAB.Element2 IAB.Element3 MissiondV mdry mratio mwet
     mprop FullTankMass Burn TLIEmptyTankMass TLIPropConsMass BurnLOI LOIEmptyTankMass LOIPropConsMass
     BurnIAB IABEmptyTankMass IABPropConsMass BurnTotal Artemis.LunaFixed.INC Artemis.LunaFixed.RAAN Artemis.
     Luna.SMA Artemis.Luna.ECC Artemis.LunaFixed.AOP TotalPropConsMass MissionMass PeriluneEpoch
     TransLunarTime CoastArray(1,1) CoastArray(1,2) CoastArray(1,3) CoastArray(1,4) CoastArray(1,5)
     CoastArray(1,6) CoastArray(1,7) CoastArray(1,8) CoastArray(1,9) CoastArray(1,10) CoastArray(1,11)
```

CoastArray(1,12) FlightTimeArray(1,1) FlightTimeArray(1,2) FlightTimeArray(1,3) FlightTimeArray(1,4)

FlightTimeArray(1,5) FlightTimeArray(1,6) FlightTimeArray(1,7) FlightTimeArray(1,8) FlightTimeArray(1,9)

FlightTimeArray(1,10) FlightTimeArray(1,11) FlightTimeArray(1,12) ArriveEpochArray(1,1)

ArriveEpochArray(1,2) ArriveEpochArray(1,3) ArriveEpochArray(1,4) ArriveEpochArray(1,5) ArriveEpochArray

(1,6) ArriveEpochArray(1,7) ArriveEpochArray(1,8) ArriveEpochArray(1,9) ArriveEpochArray(1,10)

ArriveEpochArray(1,11) ArriveEpochArray(1,12);

REFERENCES

[1] National Aeronautics and Space Administration, *NASA Strategic Plan, 2018*. NASA Headquarters, 2018.

[2] Committee of the Planetary Science Decadal Survey, Space Studies Board, National Research Council, *Vision and Voyages for Planetary Science in the Decade 2013-2022*. The National Academies Press, 2011.

[3] Sacksteder, K.,Sanders, G., "In-Situ Resource Utilization for Lunar and Mars Exploration," *45th AIAA Aerospace Sciences Meeting and Exhibit*, 2007.

[4] M. Stancati, M. M. Jacobs, and G. Rauwolf, "LANTR/ISPP-based Space Transportation for Moon/Mars Missions II - Results," *36th AIAA/ ASME/ SAE/ ASEE Joint Propulsion Conference and Exhibit*, 2000.

[5] Mission Design Division, *Small Spacecraft Technology State of the Art*. NASA Ames Research Center, 2015.

[6] Prussing, J, Conway, B., *Orbital Mechanics, Second Edition*. Oxford University Press, 2013.

[7] Mission Evaluation Team, *Apollo 10 Mission Report*. NASA Manned Spaceflight Center, 1969.

[8] Mission Evaluation Team, *Apollo 11 Mission Report*. NASA Manned Spaceflight Center, 1969.

[9] Mission Evaluation Team, *Apollo 12 Mission Report*. NASA Manned Spaceflight Center, 1970.

[10] Dawn, T., Gutkowski, J., Batcha, A., Williams, J., Pedrotty, S., "Trajectory Design Considerations for Exploration Mission 1," *28th AIAA/ AAS Space Flight Mechanics Meeting*, 2018.

[11] Oberth H., *Wege zur Raumschiffahrt (Ways to Spaceflight)*. Oldenbourg, Munchen (English translation: NASA TT F-622), 1929.

[12] Parker J., Anderson, R., *Low Energy Lunar Trajectory Design*. Jet Propulsion Laboratory, 2013.

217

[13] Hughes, S.,Qureshi, R.,Cooley, S.,Parker, J.,Grubb, T., "Verification and Validation of the General Mission Analysis Tool (GMAT)," *2014 AIAA/AAS Astrodynamics Specialist Conference*, 2014.

[14] Montenbruck O., Gill E., *Satellite Orbits, Models, Methods, and Applications, 4th Edition*. Springer, 2012.

[15] National Aeronautics and Space Administration, *General Mission Analysis Tool (GMAT) Mathematical Specification, Release R2018a*. NASA Goddard Spaceflight Center, 2018.

[16] Standish E., *Interoffice Memorandum: JPL Planetary and Lunar Ephemerides DE405/LE405*. Jet Propulsion Laboratory, 1998.

[17] S. Pines, "A Uniform Representation of Gravitational Potential and its Derivatives," *AIAA Journal*, vol. 11, pp. 1508–1511, 11 1973.

[18] Lundberg J., "Recursion Formulas for Legendre Functions for Use with Non-Singular Geopotential Models," *Journal of Guidance, Control, and Dynamics*, vol. 11, pp. 31–38, 1 1998.

[19] Long A., et. al., *Goddard Trajectory Determination System Mathematical Theory, Revision 1*. Computer Sciences Corporation, 1989.

[20] Larson, W., Wertz, J., *Space Mission Analysis and Design, Second Edition*. Microcosm, Inc., Kluwer Academic Publishers, 1992.

[21] Federal Aviation Administration, *The Annual Compendium of Commercial Space Transportation, 2018*. FAA Office of Commercial Space Transportation, 2018.

[22] Wiley S.,Dommer K, Mosher L., "MESSENGER Propulsion System Flight Performance," *42nd Joint Propulsion Conference, American Institute of Aeronautics and Astronautics/American Society of Mechanical Engineers/Society of Automotive Engineers/American Society for Engineering Education*, vol. AIAA 2006-4389, 2006.

[23] Wilson, M. N., Engelbrecht, C. S., and Trela, M. D., "Flight Performance of the MESSENGER Propulsion System from Launch to Orbit Insertion," *48th Joint Propulsion Conference and Exhibit, American Institute of Aeronautics and Astronautics/American Society of Mechanical Engineers/Society of Automotive Engineers/American Society for Engineering Education,*, vol. AIAA 2012–4333, 2012.

[24] Wiley S.,Dommer K, Mosher L., "Design and Development of the Messenger Propulsion System," *36th AIAA/ ASME/ SAE/ ASEE Joint Propulsion Conference and Exhibit*, vol. AIAA-2003-5078, 2003.

[25] Domingue, D. and Russell, C., *The Messenger Mission to Mercury*. Springer, 2007.

[26] Baker A., "Chemical Propulsion Systems for Mars Sample Return," *ESA 4th International Spacecraft Propulsion Conference*, 2004.

[27] Hodges R., Chahat N., Hoppe D., Vacchione J., "A deployable high-gain antenna bound for mars: Developing a new folded-panel reflectarray for the first cubesat mission to mars," *IEEE Antennas and Propagation Magazine*, 2017.

[28] Kamhawi, H., Haag, T., Benavides, G., Hickman, T. , Smith, T. , Williams, G. , Myers, J., Polzin, K., Dankanich, J., Byrne, L., "Overview of Iodine Propellant Hall Thruster Development Activities at NASA Glenn Research Center," *52nd AIAA/ SAE/ ASEE Joint Propulsion Conference*, 2016.